AN EXPERIMENTAL STUDY INTO THE BEHAVIOUR OF SULFUR DURING MARTIAN DIFFERENTIATION

William Nash

Linacre College & The Department of Earth Sciences

University of Oxford

Thesis submitted for the degree of Doctor of Philosophy

October 2016

Supervisor: Professor Bernie J. Wood



Declaration of originality

The contents of this thesis are all my own work, except where otherwise stated. The views and opinions expressed are mine, and not necessarily those of any other person unless attributed.

Acknowledgements

This thesis could not have been completed without the generous help and support of my friends, family and colleagues.

Grateful thanks are extended to Bernie Wood for supervising me throughout the process. Sincere thanks are further owed to Ashley Norris, Jon Wade and Duane Smythe, for their substantial support both personally and professionally. In addition, I have benefitted from enlightening discussions and moral support from (in particular order): Andrew Matzen, Helen Ashcroft, Melissa Murphy, David Byrne, Brendan Dyck, Mike Stock, Yu Zhou, Donald Fraser, Norman Charnley, Ben Buse, Stuart Kearns, Afsaneh Mohammadzaheri, Hale Harding, Bertrand Nortier, Alex Lawrence, Thomas Czertowicz and Freddie Nash.

I owe a debt of gratitude to Tina Geraki and Konstantin Ignatyev for their assistance collecting XANES spectra from the synchrotron; to John Craven for his extremely dedicated and professional management of the SIMS instrument at Edinburgh; to Ben Buse and Stuart Kearns for their help manning the Bristol microprobe; and to Jamie Long for the support of his workshop. Thanks also to Elizabeth Cowley for being such great company, and for looking past my deplorable attitude to the return of library books.

Special thanks are due to my housemates at 28 Temple Street: Anja Mizdrak, Jing Hu, Sam Blake, Jon Foxwell (honoured guest) and SmackDealer the dog. In a similar vein, I thank the department Frisbee team for some essential and thoroughly enjoyable recreation, the staff at Café Crème and Najar's Place for some fantastic wraps, and the bands Dire Straits and Pink Floyd for their uplifting acoustical motivation.

Through almost the entire stretch I have benefited from the company and care of my girlfriend Solfa Carlile. Thank you Solfa for making this such a happy time, and for enriching my life with your dependable cheer and good humour.

Finally, I wish to thank my parents Mark and Caroline, for their unwavering love and support during the past 27 years. It would be impossible to exaggerate the importance of your generosity and encouragement on my life and my work. For this, and for so many wonderful things, thank you.

To all of these people, and to any others whom I have neglected to name here, thank you so much for making my PhD such a colourful and rewarding experience.

ABSTRACT

A series of experiments related to igneous processes within Mars are presented, with a particular emphasis on the behaviour of sulfur during Martian magmatism.

Of most significance are a series of one-atmosphere experiments conducted on a broad range of silicate melt compositions, under oxygen fugacity (fO_2) conditions ranging from FMQ-1.67 to FMQ+1.6: a range which brackets much of the variation observed in Terrestrial and Martian igneous rocks. Quenched glasses from these experiments have been analysed by X-ray absorption Near Edge Spectroscopy (XANES) and Secondary Ion Mass Spectrometry (SIMS) to determine the speciation of their dissolved sulfur, as well as its overall concentration. The XANES spectra collected indicate the presence of the sulfide and sulfate species, and the progressive replacement of the former by the latter as fO_2 increases. Clear differences are observed between the $S^{6+}/\Sigma S$ ratios of different silicate melts equilibrated under the same fO_2 conditions, demonstrating that the major-element composition of a silicate melt has some measureable influence over sulfur speciation. The component most closely correlated with this change is FeO, whose presence in the silicate melt shifts the exchange between sulfide and sulfate towards higher fO_2 conditions. This is interpreted as an outcome of coupling between sulfur and iron in the melts, and on this basis a quantitative relationship between log $S^{6+}/\Sigma S$ and log (Fe_2O_3/FeO^2) is proposed. Such a relationship potentially provides an alternative to direct measurement of $S^{6+}/\Sigma S$, but warrants further study to establish its generality. SIMS analyses of the most oxidized melts indicate a strong inverse correlation between their sulfate concentration and the abundance of the tetrahedrally co-ordinated cations Si and Ti, suggesting that sulfate solubility is governed by competition for tetrahedral sites in silicate melts.

Additional experiments performed at 1.5GPa establish the sulfur concentration at sulfide saturation (SCSS) of a putative Martian primary melt at 1400°C. Experiments performed at the same pressure but under more oxidizing conditions constrain the sulfide-sulfate transition to between -1.5 and +0.8 log units relative to the Fayalite-Magnetite-Quartz (FMQ) buffer. This inference is supported by XANES spectra for these experiments, which show no evidence for mixed speciation. In addition to sulfur, the elements Sc, Y and a selection of REEs were also investigated at 1.5GPa. Partitioning coefficients were measured for these elements between a likely primary Martian melt, and three phases believed to be present in the Martian mantle: high- and low- calcium pyroxene and Fo_{76} olivine. The values obtained closely approximate those predicted by the lattice-strain

model, suggesting that these elements partitioning behaviour is unaffected by the unusually Fe-rich chemistry of this melt. REE profiles generated by a simple partial melting model demonstrate the complexity of Martian meteorites' petrogenesis, including the need for chemically separate reservoirs within Mars' mantle.

To assist in further investigations of Martian magmatism, in particular those involving sulfur, a method is presented for the manufacture of polycrystalline olivine capsules. These are suitable as containers for olivine-saturated melts in one-atmosphere experiments, and permit studies involving a wider range of melt compositions than those allowed by natural olivines (the presently used alternative). The equipment required for manufacture is readily available in most experimental petrology laboratories. Use of these capsules avoids common problems associated with using wire loops, such as their propensity to absorb iron, or to react with the sulfur in the experimental charge.

EXTENDED ABSTRACT

The differentiation of planets, and the resulting distribution of elements between their major reservoirs (core, mantle, crust, and atmosphere) is of fundamental importance to the geological sciences. Crust-mantle differentiation in particular plays a key role in determining the chemical composition and topography of planetary surfaces. On Earth, the primary mechanism for this process is partial melting of the mantle at mid-ocean ridges, and the recycling of altered oceanic through the mantle at subduction zones. In addition, melts are extracted from the terrestrial mantle at convergent margins and "hot-spots". Martian volcanism is less well understood, since far fewer samples are available, and tectonic evidence for a process analogous to mid-ocean ridge spreading is highly circumstantial. The shape and distribution of Martian volcanoes instead implies a process more akin to ocean-island or "hotspot" volcanism. Whatever the geometry, it is clear from the geochronology of Martian meteorites that volcanism continued until the relatively recent past, and over its lifetime, generated a considerably thick crust.

Chemical information about Mars' crust is available from Martian meteorites and analyses made in-situ by robotic spacecraft. Large contrasts in sulfur abundance have been reported for these, which correlate with estimates for their fO_2 of equilibration. Since sulfur is redox sensitive, it can dissolve in melts as either the sulfide or sulfate ion, and these species exhibit different solubilities. Therefore, the concentrations in Martian samples potentially provide information about the fO_2 conditions under which they separated from the Mantle. The speciation and solubility of sulfur is well stuied in terrestrial melts, but poorly studied in the considerably more FeO rich basalts characteristic of Martian magmatism. Motivated by this need to establish sulfur's redox behaviour in Fe-rich systems, a study has been made into the influence of silicate melt chemistry over the speciation of dissolved sulfur.

Six silicate melt compositions were studied, which together represent a broad range of commonly occurring natural magmas. A chemically primitive and a more enriched MORB were studied, to represent end-members of terrestrial mantle melting. These were complemented by two Martian melts, believed to represent low and high melt fractions of the putative Martian mantle. Finally, an andesite and a dacite were included to represent melts more typical of terrestrial calc-alkaline volcanism. Each of these melts was equilibrated with a series of CO-CO_2-SO_2 gas mixtures to impose oxygen fugacities ranging from FMQ-1.67 to FMQ+1.6. All experiments were conducted at 1300°C in a one-atmosphere gas-mixing furnace. To ensure that all of the intensive parameters

besides melt chemistry were invariant, the six melts were run simultaneously in each of the gas mixtures, hanging from a chandelier in the furnace.

Almost all experimental products are sulfur-undersaturated, and contain varying amounts of dissolved sulfur (from ~1000ppm to ~1 ppm). The valence of this sulfur was determined for each glass by X-ray Absorption Near Edge Spectroscopy (XANES), which indicated the presence of the sulfide ion at low fO_2, and the sulfate ion under more oxidizing conditions. Despite high levels of noise in the spectra of the most oxidized glasses (an outcome of the low sulfur concentrations imposed by gas-mixture limitations), the transition from sulfide- to sulfate- domination is evident for every melt studied, except for the dacite, for which only one spectrum is available. Crucially however, comparisons between the spectra of glasses equilibrated under identical fO_2 conditions reveal clear differences in their $S^{6+}/\Sigma S$ ratio, demonstrating a control over sulfur speciation by silicate melt chemistry. Furthermore, these differences correlate with contrasts in the glasses' FeO concentrations, implying that Fe exerts the dominant control over speciation.

As an alternative method of determining sulfur speciation, bulk sulfur analyses were made of each glass using SIMS, and for each melt-type, speciation was inferred indirectly from trends in their sulfur concentration plotted against their fS_2/fO_2 ratio. Although successful at positively identifying sulfide in each melt, no quantitative data on the position of the crossover could be obtained due to Fe-loss that affected experiments conducted above FMQ+0.13. These latter experiments were supported by platinum loops, and despite pre-saturation, Fe-loss introduced uneven variation into the composition of each of the six melt types.

Despite the absence of supplementary SIMS data, the following quantitative findings may be drawn from the XANES spectra. The sulfide-sulfate "crossover" position (the fO_2 at which both species are equally abundant) for the andesite and the primitive MORB is very close to FMQ, whereas that for the Martian basalts and the Primitive MORB is half a log unit higher. These two groups contain around 10wt% and 18wt% FeO respectively. Assuming the dacite's "crossover width" is equal to those of the other rocks, its crossover position can be extrapolated from the single $S^{6+}/\Sigma S$ ratio obtained at FMQ-1.67. The resulting value is approximately FMQ-1.5: at least 1.5 log units lower than for all of the other melts. With an FeO concentration of around 5wt%, this is also consistent with the notion that Fe is the principal determinant of speciation.

One reasonable explanation for the influence of Fe on sulfur valence is that these species are somehow coupled within the silicate melt. Such a coupling might be expressed by the following equilibrium between sulfide and hematite, and sulfate and wustite:

$$S^{2-} + 4\,Fe_2O_3 = SO_4^{2-} + 8\,FeO$$

The XANES-derived $S^{6+}/\Sigma S$ ratios, fO_2 conditions and major-element compositions of the melts studied here permit a test of this relationship. Using modelled Fe^{3+}/Fe^{2+} ratios for each melt, the parameters log S^{6+}/S^{2-} and log $Fe_2O_3/(FeO^2)$ are plotted against one another, and exhibit a reasonable linear correlation. Furthermore, the data form a trend with the gradient and intercept predicted from the stoichiometry of the equilibrium above, and the component's standard state Gibbs energies. The R-squared value is 0.75, and although the SIMS-derived data introduce considerable scatter to the data, they do not weaken this index of correlation. The agreement between these two independent and complementary measures of sulfur speciation suggest that this is a robust relationship, and that chemical equilibrium between the various species of iron and sulfur is realized in silicate melts (at least above 1300°C).

Despite their limited use as speciation sensors (they were only useful under relatively oxidizing conditions) the SIMS analyses did enable a useful assessment of the sulfide and sulfate capacities of the six melts. Consistent with previous studies, and with the above described extension of sulfide stability to higher fO_2 in Fe-poor melts, sulfide capacities correlate positively with FeO. More interesting however, is the inverse relation observed between the log of the sulfate capacities and the mole fractions of Si + Ti: the tetrahedrally co-ordinated cations present in the melts. This relationship, combined with spectroscopic evidence for tetrahedral bonding with oxygen of the S^{6+} ion, suggests that competition for these tetrahedral sites determines the sulfate capacity of silicate melts.

A useful extension to these one-atmosphere experiments would be re-equilibration of similar melts under sulfide or sulfate saturated conditions, so that their sulfide and sulfate solubilities could be established. Repetition of those experiments that experienced iron loss to their platinum loops would also be desirable. To assist such an extension, a method for manufacturing polycrystalline olivine capsules was developed, requiring only equipment that is readily available in most experimental petrology laboratories. Use of olivine capsules prevents loss of iron to (or reaction of sulfur with) the metal loops used to suspend melts in the furnace. Use of olivine as a capsule material to overcome these difficulties is not new, but is currently restricted by the (generally forsteritic) compositions of natural olivines. The manufacture method described here therefore extends the range of melt compositions that can be studied in this way.

The chief obstacle to melt retention was absorption of the melts by the capsule walls, owing to the extreme wetting of olivine by iron-rich silicate melts. This was overcome by performing the

crystallization of the olivine from its constituent oxides, and the annealing of this olivine into an appropriate shape, as separate processes. In addition, cycles of heating were found to be necessary for manufacturing more magnesian olivines. Ultimately, impermeable capsules were produced in this way, and shown to retain large melt pools for 24 hours. A further advantage of olivine as a capsule material is the ability to create large, separate volumes of melt and olivine, which permit analysis of components present within them at very low concentrations (such as is frequently necessary for studies of element partitioning or isotopic fractionation). Further work is probably worthwhile to investigate the feasibility of capsules formed from other common rock-forming minerals, so that melts undersaturated with olivine can be studied.

In addition to the sulfur-bearing experiments performed at one-atmosphere pressure, experiments were conducted on the same putative Martian primary melt at 1.5GPa using a piston-cylinder apparatus. An attempt was made to obtain sulfur-bearing glasses of this composition at a range of fO_2 conditions, so that the sulfide-sulfate crossover position could be determined at pressures more relevant to Martian mantle melting. This was attempted by varying both capsule compositions and the redox chemistry of the starting materials, but only two clusters of fO_2 conditions were achieved, at FMQ-1.5 and FMQ+0.8. XANES analysis of glasses from these clusters showed no evidence for mixed oxidation. The melts at FMQ-1.5 contain separate sulfide phases, and are therefore sulfide saturated. Thus their 4010ppm sulfur concentrations provide a measurement of the sulfur concentration at sulfide saturation (SCSS) for Martian melts. This compares favourably to models for this parameter available in the literature. The comparatively low sulfur concentrations in Martian meteorites, combined with negative dependence of SCSS on pressure, imply that either these rocks experienced considerable sulfur degassing en-route to the surface, or that they did not leave the Martian mantle sulfide-saturated.

Finally, trace element partitioning coefficients were determined for Sc, Y and a selection of Rare Earth Elements (REEs), between a similar Martian primary melt, and three phases expected to reside in Mars' mantle. These included high- and low-calcium pyroxenes, and a fayalitic olivine. The partitioning behaviour was found to conform rigidly to the expectations of the elastic strain model, with each mineral's site radii and elasticity accurately predicting the position and shape of the parabolas described by the data. This extends the elastic strain model to more Fe-rich compositions, and further implies that the melt composition plays a negligible role in element partitioning. The REE partitioning coefficients obtained were used to model equilibrium melting of Mars' mantle. Two generations of melting were explored, with the residue from the first melting

event was used as the mantle-input for the second. Besides generating a large contrast in LREE/HREE depletion, this modelling failed to reproduce the variation in REE-profile observed among the Martian meteorites. This failure demonstrates the complexity of Martian mantle evolution, and in particular highlights the need for melting in the presence of a phase capable of generating the inflection observed in these profiles between praseodymium and gadolinium.

Table of Contents

Chapter 1: Introduction to Martian Geology 1

1.1 - INTRODUCTION TO MARTIAN GEOLOGY 2
1.1.1 Overview 2
1.1.2 Topography and the Interior 2
1.1.3 Constraints on the composition of Mars' Crust 5
1.1.4 Constraints on Mars' bulk composition 11
1.1.5 Martian mantle mineralogy 14
1.1.6 A sulfur-rich planet? 16
1.1.7 Sulfur as a monitor for mantle fO_2 18

1.2 – CONTRIBUTIONS OF THE THESIS 19

1.3 – REFERENCES 20

Chapter 2: Manufacture of synthetic olivine capsules for use in experiments . 25

2.1 – ABSTRACT 26

2.2 – INTRODUCTION AND MOTIVATION 27

2.3 – THE MANUFACTURE METHOD 28

2.4 – METHOD DEVELOPMENT 30

2.5 – CAPSULE EVALUATION 34
2.5.1 Time Series experiments 34
2.5.2 Diffusion profiles and approach to equilibrium 34
2.5.3 An attempt to measure Cr-isotope fractionation 36
2.5.4 Capsules at high pressure 38

2.6 – CONCLUSIONS AND IMPLICATIONS 38

2.7 – REFERENCES 39

Chapter 3: Control of sulfur capacity and speciation by silicate melt chemistry 40

3.1 – ABSTRACT 41

3.2 – INTRODUCTION AND MOTIVATION 42

3.3 – PREVIOUS WORK 44

3.3.1 Sulfur dissolution in silicates: A brief and broadly chronological review 44
3.3.1 Early determination of speciation by indirect measures 44
3.3.1 Spectroscopic observations of speciation, and its dependence on fO_2 46

3.4 – EXPERIMENTAL METHODS 54
3.4.1 Choice of melt compositions 54
3.4.2 Experimental procedure 54
3.4.3 Control of temperature and oxygen fugacity 58
3.4.4 Choice of gas flux 59
3.4.5 Experimental uncertainties 61
3.4.6 Attainment of equilibrium 63

3.5 – ANALYTICAL METHODS 54
3.5.1 Overview 65
3.5.2 Imaging of glasses by SEM 65
3.5.3 Major element analysis by WDS 66
3.5.4 Analysis of sulfur by XANES 67
3.5.4.1 Overview 67
3.5.4.2 Introduction to X-ray absorption spectroscopy (XAS) 67
3.5.4.3 Interpretation of X-ray absorption spectra 70
3.5.4.4 XANES Analytical Procedure for the sulfur-bearing glasses 72
3.5.4.5 Spectrum normalization 73
3.5.5 Determination of total sulfur concentration by SIMS 74
3.5.5.1 Overview 74
3.5.5.2 Analytical routine 75
3.5.5.3 Sample preparation 76
3.5.5.4 Standardization 76
3.5.5.5 Errors in Sulfur Concentration 78

3.6 – ANALYTICAL RESULTS 80
3.6.1 Major-Element chemistry by WDS 80
3.6.2 Sulfur Speciation from XANES 82
3.6.2.1 Reference Materials and Peak Interpretation 82
3.6.2.2 Qualitative Interpretation of XANES Spectra 84
3.6.2.3 Estimating Redox Ratios by Linear Combination Fitting 99
3.6.2.4The sulfide-sulfate crossover position 102
3.6.2.5 Differences in speciation at constant fO_2 106
3.6.2.6 Comparisons with previous recearchers' results 107
3.6.3 Sulfur concentrations determined by SIMS 108
3.6.3.1 Speciation implied by the relationship with *log* fS_2/fO_2 108
3.6.3.2 Estimating sulfur speciation from concentration data 116
3.6.4 Evaluation of SIMS results, and comparison with XANES 122

3.7 – DISCUSSION 123
3.7.1 A possible explanation for the observations: Fe-S coupling 123
3.7.2 A compositional control over sulfate capacity 128
3.7.3 The importance of quench effects 130

3.8 – CONCLUSIONS 131
3.8.1 Summary of findings 131

3.9 – REFERENCES 132

Chapter 4: High Pressure experiments related to partial melting of the Martian mantle 137

4.1 – ABSTRACT 138

4.2 – INTRODUCTION AND MOTIVATION 139
4.2.1 Sulfur in Martian meteorites 139
4.2.2 REE elements in Martian meteorites 139

4.3 – PREVIOUS WORK 141
4.3.1 A brief introduction to trace-element partitioning 141
4.3.2 Sulfide solubility in magmas 143

4.4 – EXPERIMENTAL METHODS 146
4.4.1 Choice of melt compositions 146
4.4.2 Experimental procedure 147
4.4.3 Measurement of oxygen fugacity 150
4.4.4 Run conditions and objectives of Sulfur-bearing experiments 151
4.4.5 Attainment of equilibrium 152

4.5 – ANALYTICAL METHODS 153
4.5.1 Overview 153
4.5.2 Imaging of run products by SEM 153
4.5.3 Major-element chemistry and Fe-Ir bleb composition by WDS 154
4.5.3.1 Analysis of major-elements 154
4.5.3.2 Analysis of Fe-Ir blebs 154
4.5.3.3 Analysis of sulfur 155
4.5.4 REE concentrations determined by Mass Spectrometry 156
4.5.5 Sulfur valence determined by XANES 156

4.6 – RESULTS 158
4.6.1 REE partitioning experiments 158
4.6.2 Sulfur-bearing experiments 163

4.7 – DISCUSSION 169
4.7.1 Evaluation of models for SCSS 169
4.7.2 A review of Mars' status as a sulfur-rich planet 170
4.7.3 REE partitioning during Martian mantle melting 172

4.7 – REFERENCES 175

Chapter 5: Concluding Remarks and Directions for future research.....179

5.1 – OVERVIEW 180

5.2 – IMPLICATIONS..... 180
5.2.1 The origin of surficial Martian sulfur..... 180
5.2.2 The oxidation state of the Martian mantle..... 181
5.2.3 Origins of the Shergottite REE profiles..... 184

5.3 – DIRECTIONS FOR FUTURE WORK..... 185
5.3.1 Spectroscopic determination of sulfur speciation..... 185
5.3.2 Measurement of fO_2 with the Fe-Ir sensor..... 186
5.3.3 The role of garnet in the petrogenesis of the Shergottites 186

5.4 – REFERENCES 187

Appendices.....189

Appendix 1: Mass Flow Controller: principles of operation 190

Appendix 2: Gas mixture calculations..... 191

Appendix 3: A brief introduction to Secondary Ion Mass Spectrometry (SIMS) 192

Appendix 3: Calculation of sulfide concentrations with the model of Smythe et al. (2017)……. 196

Chapter 1

Introduction to Martian Geology

1.1 – INTRODUCTION TO MARTIAN GEOLOGY

1.1.1 Overview

The study of Martian geology, as a serious discipline, was initiated by the spacecraft Mariner 4 as it made the first flyby of the red planet in 1964. In the half-century or so that has followed, Mars has been the subject of a feverish research effort, motivated primarily by its potential for harbouring life. An additional – and slightly more realistic – impetus for this interest has been the opportunity Mars offers to test the models developed to understand our own planet. Earth's present character is accredited to the operation of processes such as accretion, core-mantle differentiation, partial melting, fractional crystallization, volcanism, out-gassing, plate tectonics, crustal deformation, erosion and sedimentation. As an independent instance of planetary formation, Mars presents us with the opportunity to test the relevance of these processes on a body formed from a broadly similar inventory of material, but with 11% of Earth's mass, and one third (~0.37) of its gravitational field strength; an irresistible natural experiment.

Of these processes, this thesis focuses on the igneous process of partial melting, and the role it has played in determining the crust-mantle distribution of sulfur within Mars. This avenue of inquiry is motivated by the extraordinary abundance of sulfur observed on the Martian surface; a feature that is in striking contrast with the surface of the Earth. The experiments presented in this thesis address the question of what can be inferred from this remarkable enrichment of sulfur, given the other information that is available on Mars' composition and internal structure. A rather grander long-term aim – towards which this thesis makes a tiny contribution – is to understand the relationship between an arbitrary planet's chemical constitution, its differentiation into discrete layers, and the consequences this has for its surface environment.

This chapter serves as an introduction to the major characteristics of Mars, with particular emphasis on those relevant to igneous processes and the sulfur cycle.

1.1.2 Topography and the Interior

Mariner 4's historic flyby revealed a cratered, moon-like surface beneath a thin (~7mbar pressure) atmosphere, dashing contemporary hopes for oceans and canals (Lowell 1906). Subsequent encounters by better-equipped spacecraft have reinforced the view that Mars is now geologically inactive. Seismometers carried by the Viking landers during the 1970s detected no seismic activity

(Goins *et al.* 1979), and periodic observations of the surface reveal a dry and static landscape, modified only by dust-storms (Gierasch 1974), landslides (Spagnuolo *et al.* 2011), and seasonal glaciation near the poles (Levy *et al.* 2014). These superficial changes aside, present-day Mars appears to be geologically dead.

Structures on the surface however, attest to a planet that was formerly more dynamic, possibly even in the recent past. Variations in impact crater density imply a large range of surface ages, from >3 Ga right up to the present (Hartmann and Neukum 2001). Radiometric ages determined for igneous Martian meteorites span almost the full history of the solar system, and indicate that magmatism persisted until as recently as 175Ma (Nyquist *et al.* 2001). Layered sediments and fans record extensive sedimentation, and while still circumstantial, a strengthening case for lakes and even oceans is emerging from data gathered in-situ by NASA's Mars Science Laboratory (Arvidson, 2016). Finally, chronicling crustal deformation and volcanic activity on an epic scale are a ~1km contrast in elevation between the northern and southern hemispheres, a graben larger than the United States, and some monumental shield volcanoes.

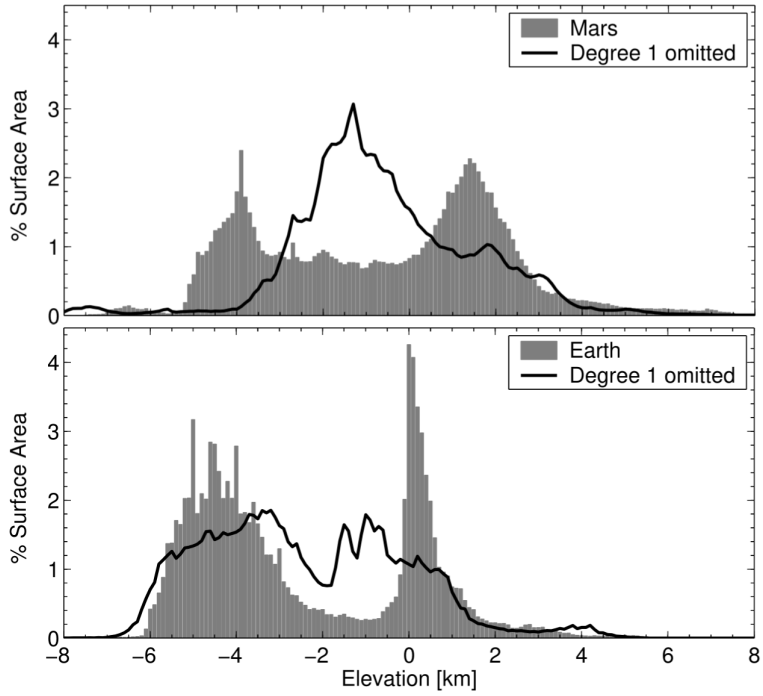
These large surficial features indicate that processes endogenous to Mars have reshaped its surface, driven – as on Earth – by heat escaping from its interior. Measurements of Mars' solar tide[1] (Yoder *et al.* 2003) indicate that its core remains at least partially molten, consistent with a history of protracted magmatism. But beyond establishing the reality of such processes, little is known about the details of their operation; in particular, the relation between the chemistry of the mantle that generated the crustal rocks, and the geometry of their expression at the surface. On Earth, surface topography is dominated by plate tectonics, which manufactures two distinct crustal lithologies whose contrasting densities cause them to float at different heights in the mantle, thereby maintaining a bimodal distribution of crustal elevation (see figure 1.1.2). Intriguingly, surface elevation distributions for Mars are also bimodal, with the Northern hemisphere lying at a uniformly lower elevation than the southern hemisphere (fig 1.1.2, Aharonson *et al.* 2001). Could this prominent 'crustal dichotomy' be the result of a (now defunct) process similar to plate tectonics? Magnetic stripes preserved in the southern highlands (Acuna *et al.* 1999) and the conspicuous smoothness of the northern lowlands (Sleep 1994) have been cited as evidence for horizontal motions of the crust. Hemispherical differences in age and composition are also

[1] The solar tide refers to the deformation of Mars' surface in response to changing gravitational field gradient. The size of this deformation depends on the viscoelastic properties of Mars' interior, so such measurements can be used to distinguish between solid and molten material even at great depth.

suggestive; the northern lowlands are significantly younger and more silica-rich (Christensen *et al.* 2001, McSween *et al.* 2003). Nonetheless, there are plausible alternative explanations for the dichotomy, including one or more massive impacts (Golabek *et al.* 2011, Frey and Schultz 1988) and degree-1 mantle convection[2] (Zhong and Zuber 2001).

This fundamental question about the dynamics of planetary resurfacing and its dependence on bulk chemistry is central to the planetary sciences in general, since it provides the link between the 'initial conditions' of a planet's formation, and the environmental conditions that will ultimately prevail on its surface. Understanding this relationship in the case of Mars will require knowledge of its past surface conditions, and the chemistry of its crust, mantle and core.

Figure 1.1.2: Histogram of surface elevation for Mars (top) and Earth (bottom), adapted from Aharonson *et al.* (2001). The grey bars indicate the proportion of the surface area at a given elevation. The black lines are residual distributions from further data processing, and may be ignored. Earth's bimodal profile is an outcome of the divergent melting and fractionation paths permitted in different tectonic environments. Is the Martian profile also indicative of plate tectonics?

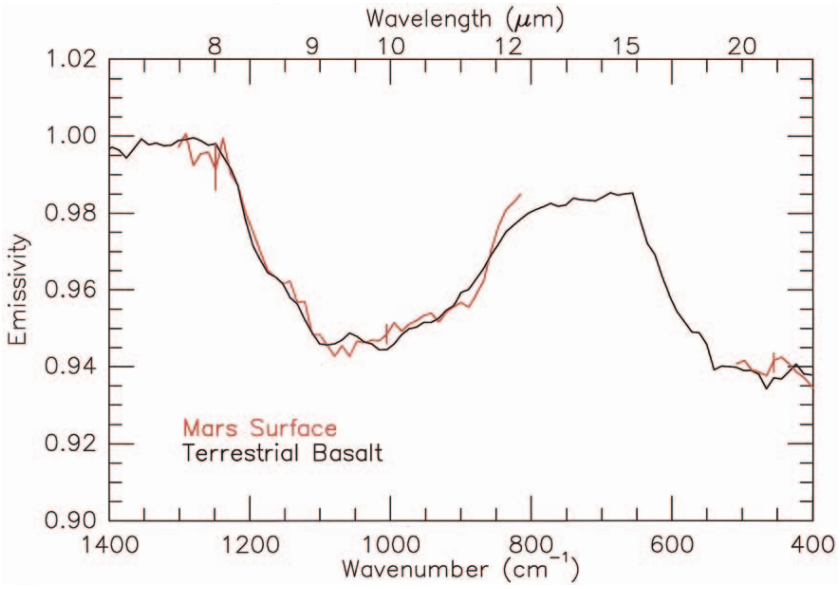


[2] Degree-1 convention is a configuration where single upwelling and downwelling structures occupy opposite hemispheres of a planetary mantle.

1.1.3 Constraints on the composition of Mars' Crust

The composition of Mars' crust has been characterized by combining remote-sensing data from orbiting spacecraft with analyses of individual samples; both meteorites on Earth and rocks studied in-situ by rovers on the surface. Global maps of surface mineralogy have been obtained using the Thermal Emission Spectrometer (TES) aboard the Mars Global Surveyor spacecraft. Comparisons between IR spectra collected using this instrument and spectra representing common rock-forming minerals indicate the presence of pyroxene, plagioclase and (minor) olivine in the regions least obscured by topsoil (Christensen *et al.* 2001). Thus a predominantly basaltic composition is implied for the igneous rocks forming the crust (see figure 1.1.3a). These conclusions are supported by a second global dataset: element abundances determined by the Gamma Ray Spectrometer (GRS) aboard the Mars Odyssey spacecraft. Concentrations of the major elements (such as Si, Ca, Fe) determined by GRS also imply a basaltic crust, but with an FeO concentration approximately double that exhibited by terrestrial MORBs (~18 wt% rather than ~9 wt%). This enrichment in iron has since become a defining feature of Martian magmatism, whose causes and consequences remain controversial (see section 1.1.4).

Figure 1.1.3a: The pyroxene-plagioclase mineralogy of Martian bedrock, indicated by the close match between IR-spectra for the Cimmeria Terra terrain (Mars) and the Deccan flood basalts (Earth). The spectra match closely despite the fact that no scaling, contrast enhancement or continuum removal have been applied to either of them. Figure from Christensen *et al.* (2001).



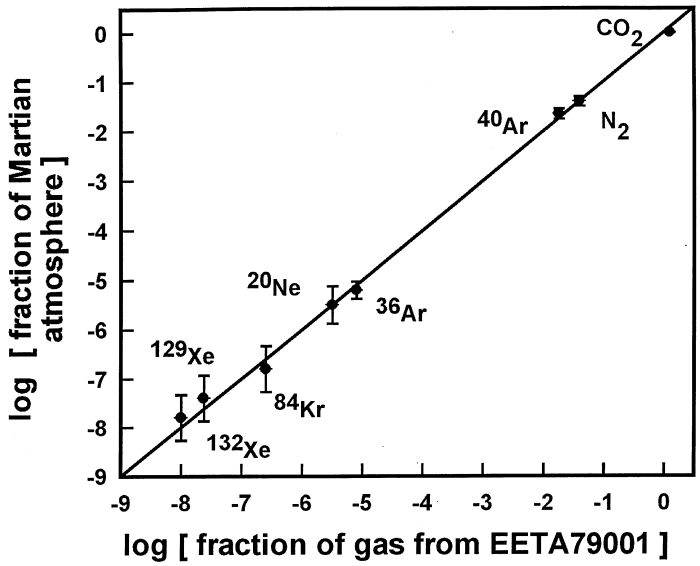
Supplementing these global surveys, and providing a broader range of analysis type (such as minor element concentrations and isotopic ratios) are the data collected on individual samples of Martian crust. Such samples have been examined either in-situ by rovers on the surface, or in a laboratory after their fortuitous natural delivery to Earth as meteorites. Igneous rocks analyzed in-situ are overwhelmingly basaltic, with compositions that generally resemble the GRS data in terms of their concentrations of alkalis and silica (see the TAS diagram in fig 1.1.3d), as well as their normative mineralogy. The bulk of these analyses have been made by the Spirit Rover at Gusev crater (McSween *et al.* 2004), and their similarity to the remote-sensing data (in particular their super-terrestrial FeO concentrations) lend support to the notion that they are representative of the Martian crust generally.

Martian meteorites permit more detailed analysis than rocks in-situ, and offer a unique view beneath Mars' surface since many (indeed most) are clearly intrusive igneous rocks. Consequently, they have formed the basis for most studies of Martian magmatism. They are formally termed the Shergottite-Nakhlite-Chassignite (SNC) meteorites after the three 'founding' meteorites groups in the association, which were initially distinguished on the basis of their mineralogy. The Shergottites (the most populous group) include basalts, olivine-phyric basalts and lherzolites; and exhibit a wide and nearly continuous range of Mg numbers (0.25-0.72) implying various degrees of fractional crystallization. Most are considered to be mixtures of melt and cumulus olivine, although a small number of the olivine-phyric types may represent primary melts of Mars' mantle. The Nakhlite group are clinopyroxenites, generally considered to be cumulates resulting from fractional crystallization. Chassigny is a dunite with a genesis likely similar to the Nakhlites. In addition to these 'classical' SNCs, there are the orthopyroxenite ALH84001, and the recently identified basalt NWA7034, which is remarkable for its strongly alkalic chemistry and high water content compared with the other Shergottites (Agee *et al.* 2013). In aggregate then, the SNC meteorites are samples from a crust with similar mineralogy and igneous textures to the mid/lower oceanic crust of Earth.

A common origin for the SNCs was first suggested by their oxygen isotope ratios, which are extremely similar to one another but distinct from the Earth and Moon (Franchi *et al.* 1999). That they originate from a large and differentiated planetary body is demonstrated by their layered mafic mineralogy (McSween 1984), their depleted trace element geochemistry (Bridges and Warren 2006) and their exceptionally young crystallization ages (Nyquist *et al.* 2001). The identity of this body was ultimately revealed by the isotopic ratios of gases trapped inside the meteorites,

which are an impressive match to those measured in the Martian atmosphere by the Viking landers (Pepin 1985, McSween 1985).

Figure 1.1.3b: log-log plot of gas isotope abundance for the Martian atmosphere against the Shergottite EETA79001. The agreement is striking, and confirms Mars as the SNC source beyond reasonable doubt. Figure taken from Treiman *et al.* (2000)

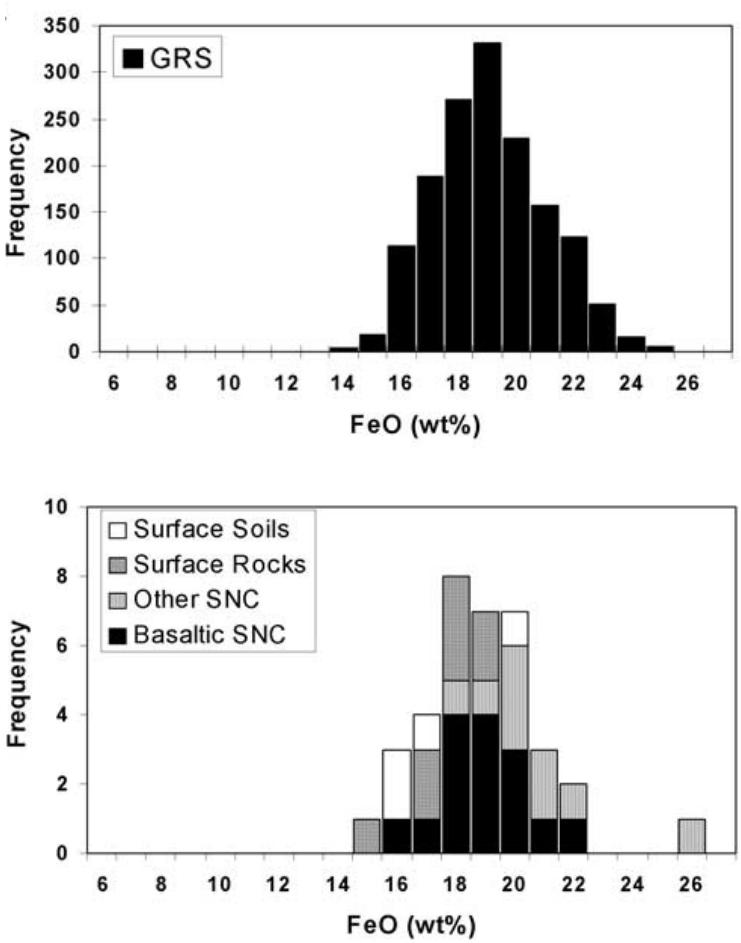


The range of ages calculated for the SNCs span almost the entire length of Mars' history. Many different isotope systems (K-Ar, ^{39}Ar-^{40}Ar, Rb-Sr, Sm-Nd and U-Th-Pb) have been used to calculate crystallization ages, and these are reviewed in detail by Nyquist *et al.* (2001), from whom the ages quoted here are taken. The ages fit into five discrete clusters, demonstrating that the SNCs provide windows onto different periods in Mars' history. The Shergottites are all relatively young (165-475 Ma), while the Nakhlites and Chassigny are much older (~1.3Ga). The most ancient rocks are ALH84001 (~4.5Ga), and NWA7034 (~4.4Ga, Cartwright *et al.* 2014). By comparison, the ages of rocks analyzed in-situ are known with significantly less precision, since they can only be estimated from the crater densities of their surrounding surfaces. Nonetheless, the aforementioned Gusev crater basalts – the outcrop most comprehensively sampled in-situ – are known to be much older than any of the Shergottites or Nakhlites, having an estimated age of ~3.5Ga (Balta and McSween 2013).

Because the Shergottites represent melt compositions rather than cumulates (albeit with varying degrees of olivine contamination), they have received more attention from studies of crustal

composition than the other SNC groups. Their mineralogy is dominated by pyroxene and vitrified plagioclase feldspar ('maskelynite') which frequently show a preferred orientation (McSween 1994), commonly attributed to either compaction or flow. Their major-element chemistry is comparable with terrestrial tholeiites, although their FeO concentration is extreme, averaging ~18.5 wt% (MetBase 2015). This key finding demonstrates that the FeO enrichment reported by GRS is not an artefact of contamination by surface soil, but is indeed a true feature of the igneous rocks forming Mars' crust (see figure 1.1.3c).

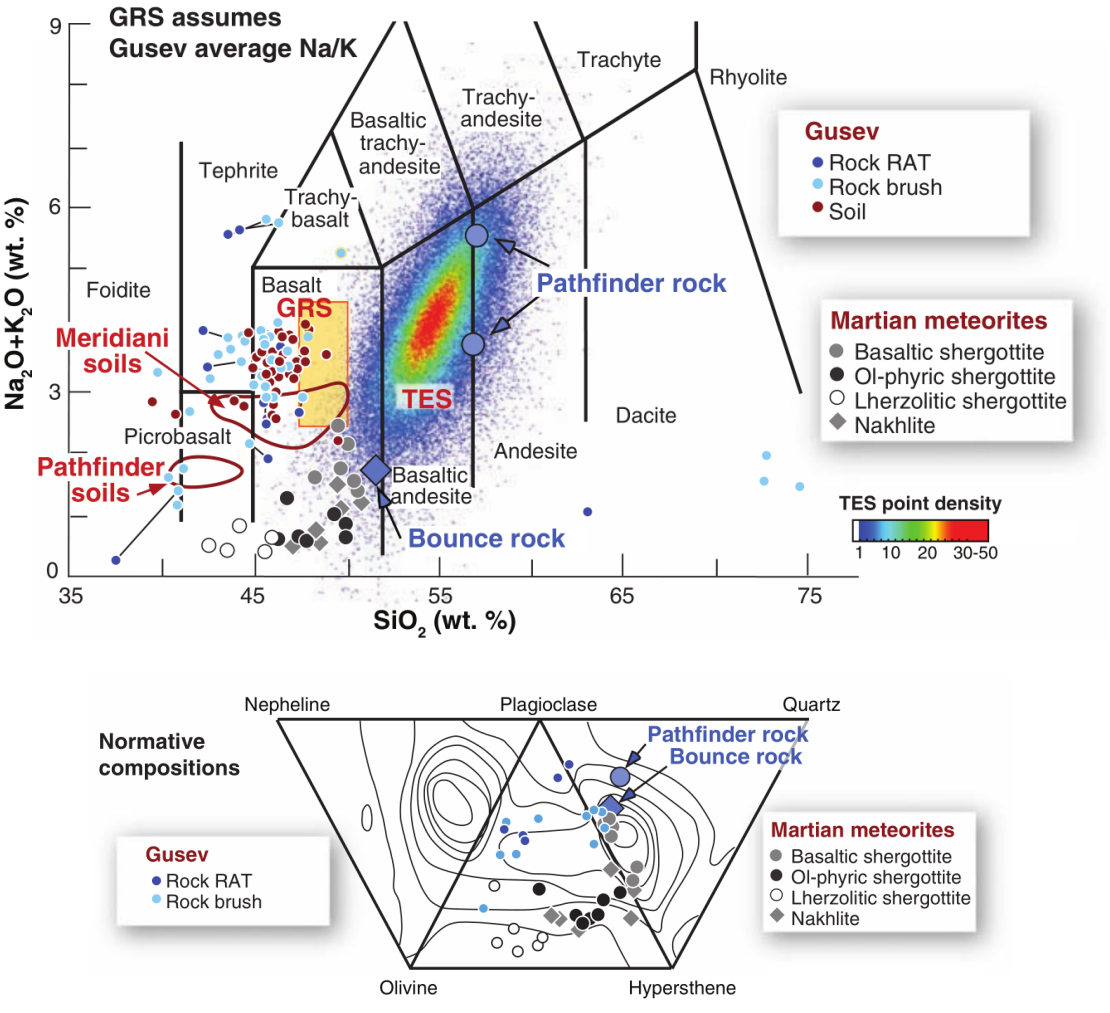
Figure 1.1.3c: FeO concentrations measured by Gamma Ray Spectroscopy (GRS) (top), compared with surface and meteorite samples (bottom). Figure from Taylor *et al.* (2006).



The three sources of data – remote-sensing data, meteorites, and in-situ analyses – are combined in figures 1.1.3d and 1.1.3e. Figure 1.1.3d displays total alkalis vs silica; an extremely common scheme for classifying terrestrial igneous rocks (note that the various fields are named). The GRS data, Gusev crater basalts, and meteorites all lie inside the basalt field. The agreement between

the data from the GRS and the Gusev crater basalts in particular is extremely close. The Gusev rocks are considerably richer in alkalis than the meteorites, and their similarity to the GRS data suggests that they better represent the average Martian crust. The TES data imply a more silicic composition than the GRS data (lying in the basaltic-andesite field), and the offset between these two datasets is attributed to the contrasting penetration depths of their parent techniques (submillimetre and decimetre for TES and GRS respectively). Thus a silica-rich topsoil is inferred for large tracts of Mars' surface, overlying bedrock with an alkali-basaltic composition. In addition to the Gusev basalts, exceptionally fresh samples encountered at other landing sites are labelled ('Bounce Rock' and 'Pathfinder Rock'). These demonstrate some variety, but still remain in the basalt or basaltic-andesite fields.

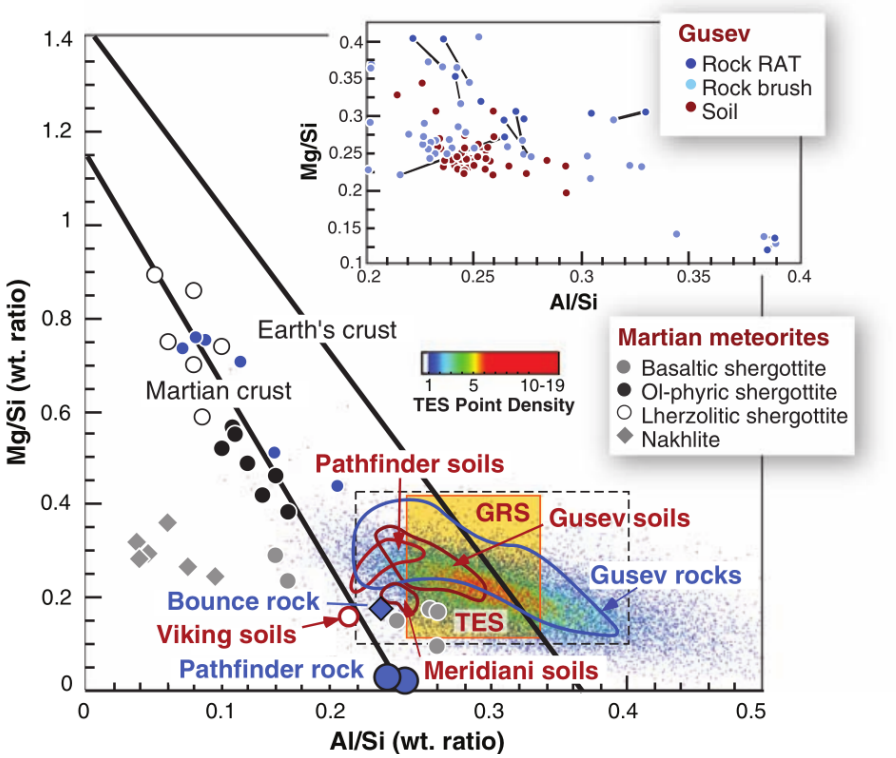
Figure 1.1.3d: Compilation of all data on the composition of Mars' crust, from McSween *et al.* (2009). Of the Gusev analyses, 'Rock brush' (light blue circles) refer to analyses made on surfaces with soil brushed away, and 'Rock RAT' (dark blue circles) refer to analyses made on the insides of small drill cores (these analyses are assumed to be less weathered).



At the bottom of fig1.1.3d is shown the normative mineralogy of the meteorites and Gusev basalts. The contours indicate relative abundances of terrestrial basalts. The majority of samples are quartz under-saturated, and concentrations of olivine vary greatly.

Figure 1.1.3e compares Mg/Si (a common index of differentiation) against Al/Si. Two important features are expressed by this diagram. First, the meteorites define a reasonably convincing slope (labelled 'Martian crust') which is markedly displaced from that of Terrestrial basalts ('Earth's crust'), highlighting a significant depletion in Aluminium. Secondly, this depletion is less pronounced for the GRS data and most of the Gusev crater basalts, suggesting (weathering alteration aside) that these rocks either have different liquid-lines of descent from the meteorites, or that they originated from a separate reservoir in Mars' mantle. This exciting possibility is explored further in the next section.

Figure 1.1.3e: Mg/Si v Al/Si for all Martian compositions. Martian meteorites contain significantly less Al than terrestrial basalts with equivalent olivine enrichment – an effect that is less pronounced in the GRS data. Figure taken from McSween *et al.* (2009).



To summarize very briefly, data on the Martian crust consistently suggest a basaltic mineralogy (with varying degrees of alkali enrichment), strongly enriched in Fe and depleted in Al with respect to the crust of the Earth. But what can this crust composition tell us about the interior?

1.1.4 Constraints on Mars' bulk composition

Inferring the composition of Mars' interior is a significantly more involved task than studying the crust, requiring us to extend our attention to other objects in the solar system, and place our trust in particular scenarios for its early evolution. As we'll see, the bulk composition and early evolution of a planet cannot be considered in isolation.

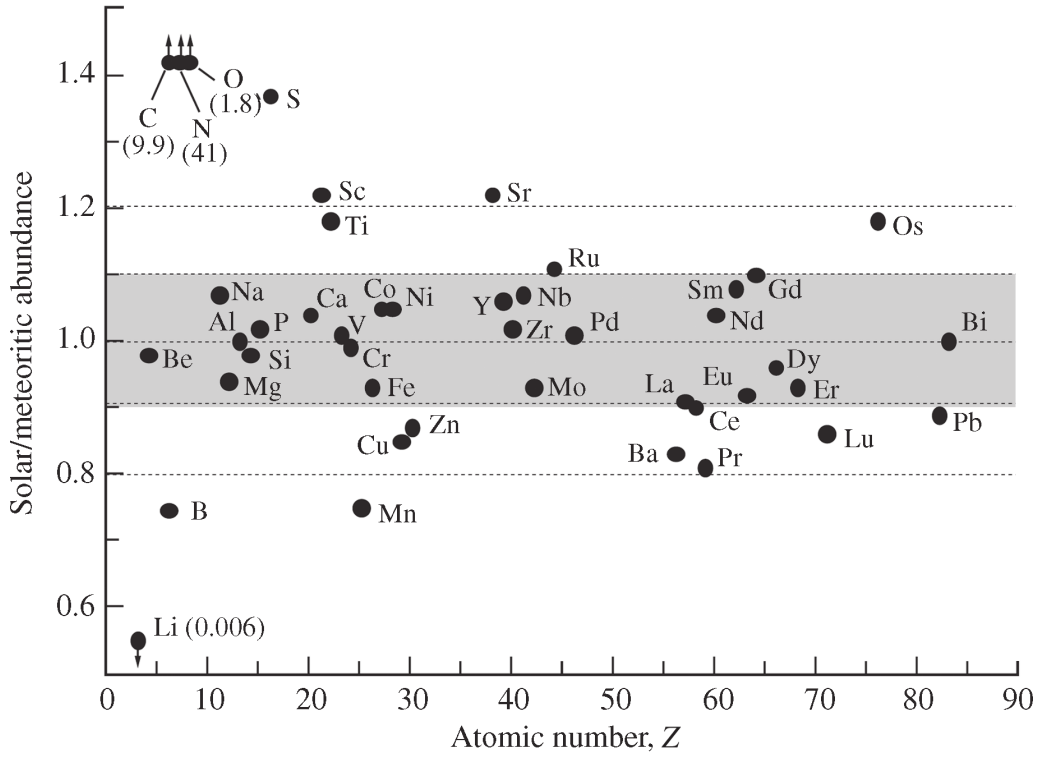
Since planets are rather large and opaque, their bulk compositions may only be determined indirectly; by using any available samples to estimate a bulk silicate (mantle plus crust) composition, and then adding to this an inventory of core material consistent with the planet's volume, density and moment of inertia. As an additional constraint, the phases conjectured to occupy these regions must be thermodynamically stable at the expected temperatures and pressures, and have mechanical properties consistent with the observed passage of seismic waves (if these can be observed). Carrying out this procedure for the Earth has yielded a bulk composition that is strikingly similar to that of the carbonaceous chondrite meteorites (Palme and O'Neill 2014), and also to the non-volatile elements detected spectroscopically in the Sun (Palme and Jones 2003, Fig 1.1.4). This grossly underrated discovery suggests that all of the bodies in the Solar System accreted from a common reservoir of near-uniform material, today preserved only by the chondrites[3]. Having established this 'chondritic' inventory for the early Solar System (at least in terms of the major rock-forming elements), it is reasonable to suggest that Mars' bulk composition be at least approximately chondritic, and check the consistency of this model against samples of Mars' crust (especially the meteorites); a sort of null hypothesis approach. This was the approach taken by Dreibus and Wanke (1988, 1994) in their model for the bulk silicate composition of Mars (hereafter BSM).

To estimate the composition of BSM, Dreibus and Wanke combined element ratios from both the chondrites and the SNC meteorites with knowledge about these elements' geochemical behaviour.

[3] It should be stressed that this 'chondritic model' is an approximation, rather than an exact statement about all of the elements in the periodic table.

In their model (commonly referred to as "DW"), the refractory elements (Si, Mg, Al, Ca, Fe etc.) are assumed to reside in the BSM in chondritic relative abundances, since their partitioning behaviour does not permit significant fractionation during condensation from the solar nebula. Despite being similarly refractory, Fe is not necessarily expected to occur in the mantle in chondritic proportions due to its participation in the core forming process, and its mantle abundance must be determined using some other method. In the absence of precise estimates for the size of Mars' core, Dreibus and Wanke estimated the BSM Fe abundance using the SNC's Mn/Fe ratio. This approach derives its validity from the constancy of the Mn/Fe ratio in all of the silicate materials of the known planetary bodies (Laul *et al.* 1972), a consequence of iron and manganese having very similar mineral-melt partition coefficients (Humayan *et al.* 2004). This part of the model represents an inversion of the partial melting process assumed to generate melts from Mars' mantle (it assumes knowledge of the directions which element ratios are expected to change during partial melting).

Figure 1.1.4: Solar/Chondritic element ratios. Note that the abundances of the major rock-forming elements (Si, Mg, Al, Ca, Fe) coincide to within 10%. Figure taken from Palme and Jones (2003).



The FeO abundance obtained by Dreibus and Wanke is 17.9 wt%, which is reassuringly close to the value observed by Mars Odyssey's GRS (Figure 1.1.3c). This FeO abundance is approximately twice the terrestrial value, and has important implications for the way in which the Martian mantle convects and melts to produce the crust. More crucially however, it places constraints on the size

and composition of Mars' core, if a chondritic abundance of Fe relative to the other refractory elements is assumed.

Models for the core that are consistent with Mars' FeO-rich mantle can involve adjustments in size, or in composition, or a combination of both. Obviously, a smaller core (comprising a smaller fraction of the total planet) must give rise to a more FeO-rich mantle. However, such a small size cannot be assumed arbitrarily, since the core diameter is constrained by Mars' moment of inertia factor and density (Bertka and Fei 1998). Alternatively, the presence of a large fraction of light elements in the core can give rise to an FeO-rich mantle by lowering the core's activity of metallic Fe. This assumes that the mantle and core are in the following equilibrium:

$$\mathrm{Fe}^{metal} + \tfrac{1}{2}\mathrm{O}_2 = \mathrm{FeO}^{silicate} \quad (1.1)$$

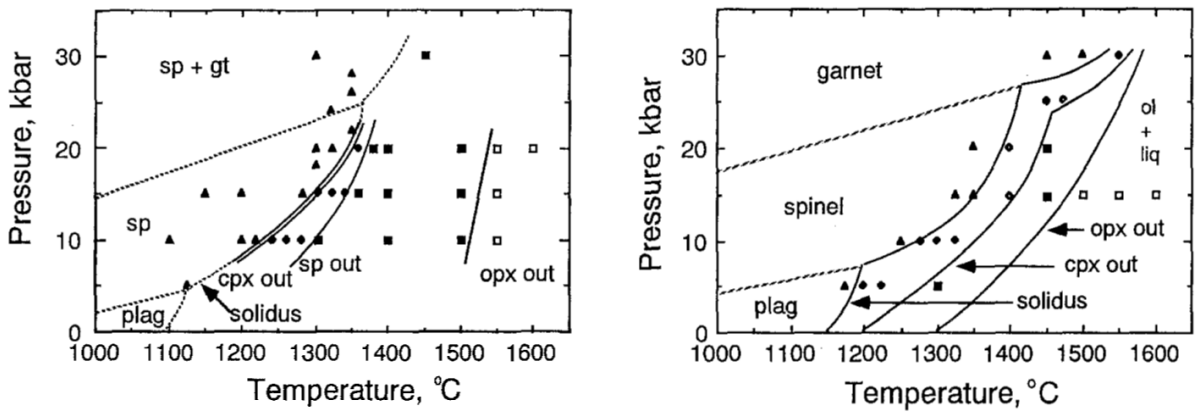
To maintain this equilibrium at constant fO_2, the activities of Fe and FeO must change sympathetically, rising and falling together. Presently, in the absence of precise measurements of core diameter, the actual combination of these alternatives (small size v light-element enriched composition) remains unknown. However, a leading candidate is a large, low-density core, with sulfur as the dominant light element (Stewart *et al.* 2007), since this satisfies both the measured density, and the requirement that the core be at least partially molten (since sulfur markedly depresses the melting point of Fe).

Returning to estimates for BSM, Lodders and Fegley (1997) proposed a different composition to DW by suggesting that the SNC's oxygen isotope ratios lie on a mixing line between those of various different chondrite groups. They found that the $^{18}O/^{16}O$ ratios in the SNCs could be reproduced by a mixture of 85% H-, 11% CV- and 4% CI-chondritic material, and the composition they obtained is very similar to DW; with an FeO abundance of 17.22 wt%, but around twice the abundance of alkalis. The similarity of this model to the DW composition (despite the indifference of the former to any data from the SNCs) lends support to the notion that Mars' composition is broadly chondritic, and further suggests that both provide reasonable (albeit imprecise) approximations to the major-elements chemistry of BSM.

1.1.5 Martian mantle mineralogy

The element abundances in Mars' mantle constitute valuable information, but are insufficient by themselves for addressing our long-term aim of understanding the relationship between planetary chemistry and resurfacing geometry. This is governed by the mantle's physical properties, which in turn depend on its mineralogy. Inferences can be made from geochemical trends among the SNC meteorites, which suggest an abundance of olivine and pyroxene, and perhaps also garnet (to explain their depletion in Al). However, far more information is available from piston-cylinder[4] experiments performed on the expected inventory of elements at mantle pressures and temperatures. The most comprehensive such study was undertaken by Bertka and Holloway (1994a, 1994b), who provisionally accepted the element abundances of the DW model, and experimentally determined its subsolidus mineralogy (1994a), and the composition of its primary melts (1994b) at various temperatures. Their results are summarized in the left-hand phase diagram of figure 1.1.5a, with the equivalent terrestrial diagram to the right. All of Bertka and Holloway's experiments were conducted at an fO_2 just below the Fayalite-Magnetite-Quartz (FMQ) redox buffer, which is broadly similar to estimates for the fO_2 calculated for the crystallization of the SNCs (Wadhwa 2001, Herd *et al.* 2003).

Figure 1.1.5: Stable phase assemblages for the DW and terrestrial mantles (left and right respectively), determined by Bertka and Holloway (1994a). The general shape of the Martian phase diagram is similar to Earth's, but with a ~50°C lower solidus temperature.



[4] This is a hydraulic compressor equipped with a conduction heater, which allows large and precisely chosen pressures and temperatures to be imposed on a studied material.

The DW mantle's phase relations display many similarities to Earth's mantle. The overall shape of both phase diagrams is broadly alike, with particular phase boundaries occupying the same relative positions in P-T space. Between 0.5 and 2.4GPa both compositions exhibit the same spinel lherzolite subsolidus assemblage (olivine + orthopyroxene + clinopyroxene + spinel), and in this pressure range the modal abundances of the constituent minerals are similar too, DW having around 10% more orthopyroxene and 10% less olivine than Earth.

There are also important differences however. The DW solidus is displaced to a temperature ~50°C lower than Earth's, consistent with the well-known asymmetric shape of the Forsterite-Fayalite binary phase diagram. At solidus temperatures, the spinel-garnet stability transition occurs at a similar pressure for both mantles, with the effects of elevated FeO and Cr_2O_3 within DW (known to elevate and depress the pressure of this boundary respectively) cancelling one another almost exactly. The pyroxenes are extremely Ca-poor with respect to the Earth's mantle, the stable clinopyroxene being a pigeonite (rather than an augite). This difference is interpreted to be responsible for the DW mantle's narrower temperature interval between the solidus and the clinopyroxene-out boundary (<20°C rather than ~60°C). Finally, the orthopyroxene + olivine melting interval is much larger for DW than for the terrestrial mantle (200°C versus 100°C respectively).

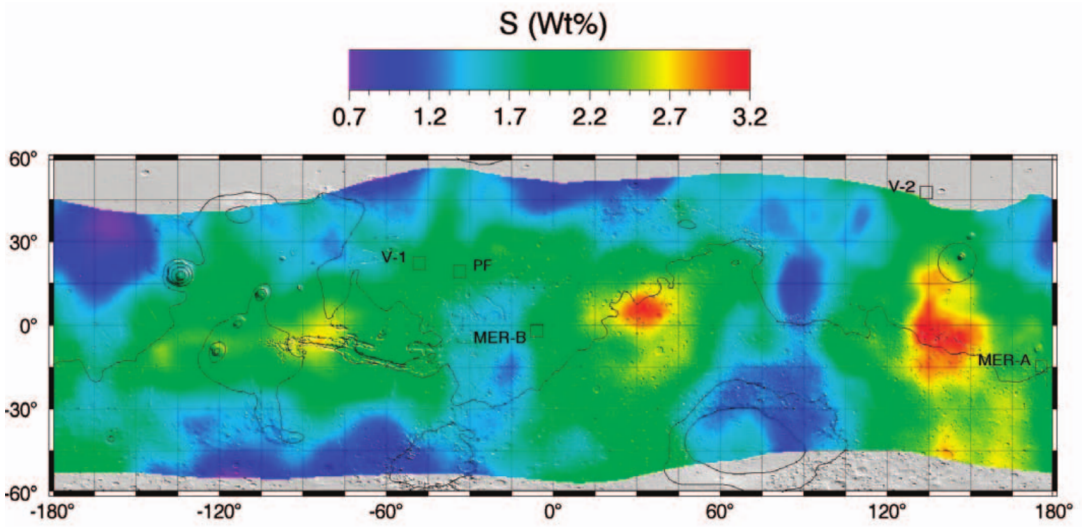
This phase diagram provides an excellent starting point for speculation into the depth and extent of the melting responsible for the SNC's source rocks, and the expected compositions of Martian primary melts. The melts obtained by Bertka and Holloway (1994b) are considered as the most reasonable approximation to a Martian primary melt, and therefore used for the sulfur-bearing experiments performed later.

Finally, a conspicuous feature of the Shergottite meteorites that is relevant to the mineralogy of Mars' mantle are their superchondritic CaO/Al_2O_3 ratios. Since partial melting and fractional crystallization of pyroxene and plagioclase are both expected to lower this ratio in melts, Agee and Draper (2004) suggested that it must be a feature of the Shergottite source region, which must therefore differ from Mars' mantle as a whole (for which chondritic ratios are assumed for all refractory lithophile elements). Agee and Draper (2004) demonstrated experimentally that melting of a DW-like source at high pressure (~5GPa) might take place in the presence of garnet, which would deplete any melts formed in aluminium. These melts could then serve as the source regions of the Shergottites. This is compelling evidence for the presence of garnet in the deep Martian mantle.

1.1.6 A sulfur-rich planet?

One of the most noteworthy features of Mars' surface, as revealed by GRS data, is its extraordinary high abundance of sulfur. A surface concentration map is shown in figure 1.1.6 (McLennan *et al.* 2010), which reveals an average concentration of 1.76 wt%, never falling below 0.7 wt%. By way of comparison, an equivalent map for the Earth (with the oceans drained) would exhibit concentrations hundreds of parts per million on average; more than a hundred times lower. Does this remarkable quantity of surficial sulfur reflect an excess for Mars as a whole (and therefore a deviation from the terrestrial or chondritic element inventories)? Or has it arisen solely through some concentrating process operating near the surface? To distinguish between these alternatives, it is necessary to determine the form of sulfur present at the surface (its mineralogy and origin), the abundance of sulfur in more deep-seated (indisputably igneous) rocks, and sulfur's geochemical behaviour during igneous processes. The first two of these areas are explored further in the following text, and the last is addressed experimentally in chapters 3 and 4, and forms the main object of this thesis.

Figure 1.1.6: Sulfur surface distribution map obtained by the Gamma Ray Spectrometer aboard NASA's Mars Odyssey spacecraft (McLennan et al. 2010). The sulfur abundance is extraordinary by comparison with the surface of the Earth.



Both remote-sensing data and in-situ analyses indicate a sedimentary origin for almost all of Mars' surficial sulfur. Visible/IR spectrometers carried by NASA's Mars Reconnaissance Orbiter and ESA's Mars Express spacecraft have identified various different types of oxidized, sulfur-rich sediments. In

particular, layered sulfate deposits have been located in graben walls and the interior rims of craters, gypsum flats have been observed in the northern polar regions, and jarosite-bearing siliceous layered deposits crop out around Valles Marineris (Murchie *et al.* 2009, Gendrin *et al.* 2005). Many of these deposits are hydrated, and almost all require the former presence of water for their formation. As on Earth, dissolution of sulfur from igneous rocks and subsequent precipitation in the near surface has clearly operated to concentrate sulfur. But by how much? And can these familiar mechanisms square the observed quantities with the integrated flux from Mars' mantle via volcanism?

Abundances of sulfur in unequivocally igneous samples are also high by the standards of equivalent terrestrial rocks. Concentrations average 1067 ppm in the SNC meteorites (Ding *et al.* 2015); most of this sulfur being hosted by sulfides. The Gusev crater basalts contain yet more sulfur (>3000 ppm, McSween *et al.* 2004), although it is unknown how much of this is primary. However, these concentrations measured in igneous rocks do not include sulfur lost by degassing en route to the surface (assuming this has taken place). Unless leaching and weathering sulfur from basalts on Mars are significantly more efficient processes than on Earth, the most probably origin for Mars' surficial sulfur is magma degassing. For this reason, the maximum sulfide concentrations (solubilities) of mantle melts are of interest, because these allow the difference between initial and measured concentrations to be calculated. This difference, expressed as an integrated mass for the whole crust, may then be compared with estimates for the total mass of surficial sulfur determined by remote sensing. If the former is larger than the latter, then there is no need to appeal to an external source of sulfur in order to explain Mars' sulfur-rich surface.

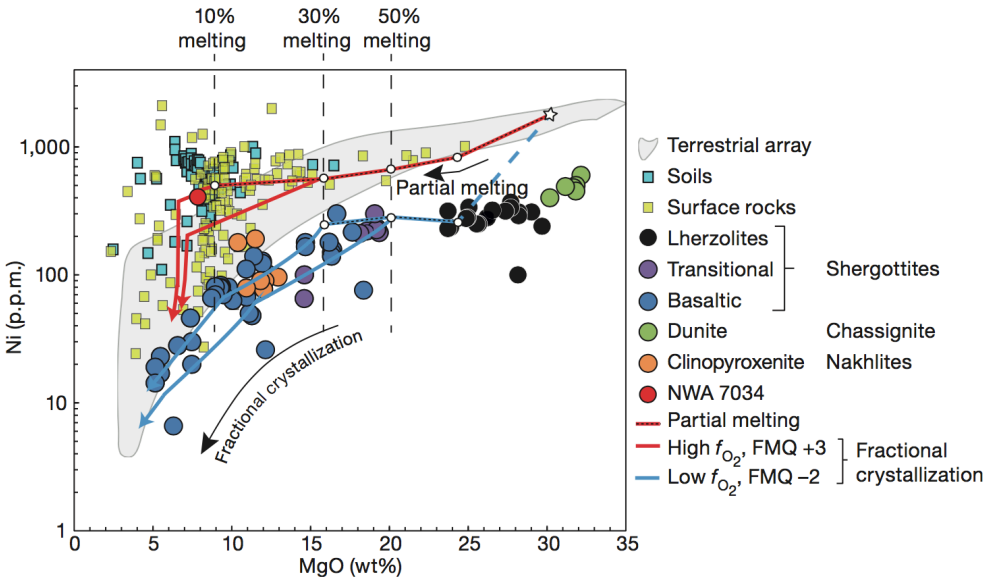
Finally, indirect measures of the Mars' bulk sulfur concentration are largely unavailable. The chondritic sulfur abundance is 5.41% (Dreibus *et al.* 1999), a figure that closely matches the solar abundance (as expressed as a ratio over silicon). However, being a volatile element, sulfur is not expected to undergo complete condensation from the solar nebula during planetary accretion. Therefore, the chondritic model is of little help in determining planetary abundances for sulfur, except perhaps as an upper limit[5]. A more promising route is to work backwards from the concentrations observed in melting products of the mantle.

[5] Superchondritic sulfur abundances would require external delivery of sulfur as a "late-veneer", which is considered unlikely, but cannot be ruled out.

1.1.7 Sulfur as a monitor for mantle fO_2

An important complication to the behaviour of sulfur during igneous processes is its exhibition of several redox states, which have very different solubilities in terrestrial silicate melts (Jugo *et al.* 2005). This potentially makes the concentrations of sulfur – or chalcophile elements – in Martian rocks useful sensors for their fO_2 of equilibration with the Martian mantle. Such differences in sulfur concentration have been noted by previous researchers (McSween *et al.* 2004), and used to make inferences about their host rocks' conditions of melting. The most revealing contrast (because it involves a comparison between similar rock types) is between the Shergottite meteorites and the basalts analyzed in-situ by NASA's Spirit Rover at Gusev crater. In addition to containing significantly more sulfur than the SNCs, the Gusev crater basalts contain an order of magnitude more Ni (McSween *et al.* 2004). Tuff *et al.* (2013) proposed that this contrast in Ni abundance reflected a difference in the fO_2 at which these rocks were last in equilibrium with their source regions. In this scheme, the relatively low concentrations of Ni on the Shergottites (originally thought to indicate a planet-wide scarcity) represents retention by sulfides present in their source regions. Conversely, the high concentrations in the Gusev basalts are taken to indicate an absence of sulfide in their source regions, which in turn requires that they be more oxidized. The modelled concentrations of Ni for these two rocks are illustrated in figure 1.1.7, superimposed on the concentrations measured in real samples.

Figure 1.1.7: Modelled Ni concentrations for putative Martian primary melts separated from their sources at high and low fO_2. Ni concentration here serves as a proxy for fO_2: low Ni contents correspond to retention of Ni by sulfide the source, and high Ni concentrations indicate the stability of sulfate rather than sulfide, so that Ni follows sulfur into the melt. Figure taken from Tuff *et al.* (2013).



If this contrast in Ni abundance does indeed result from the presence or absence of sulfide, it permits a lower limit to be placed on the fO_2 of the Gusev basalts' source region. However, the model is dependent on knowledge of the conditions at which sulfur changes its oxidation state between sulfide and sulfate. The modelling carried out by Tuff *et al.* (2013) used the sulfide-sulfate crossover fO_2 as determined for terrestrial rocks (Jugo *et al.* 2010), assuming the Martian ones to be no different. However, spectroscopic studies of sulfur speciation have reported evidence for control over sulfur speciation by silicate melt chemistry, in particular by Fe (Klimm *et al.* 2012b). This is potentially very significant because, as we have seen, a characteristic feature of Mars' mantle is its elevated FeO content. A more thorough understanding of the relationship between major-element chemistry and sulfur valence state is therefore required, to obtain quantitative information on fO_2 from these observations. Gaining such an understanding is the major objective of this project.

1.2 – CONTRIBUTIONS OF THE THESIS

The following three chapters describe work intended to assist studies of sulfur's behaviour during Martian igneous processes, as well as comparisons with igneous processes on Earth.

Chapter 2 is a methods chapter, which describes a procedure for manufacturing olivine capsules with lower forsterite numbers than are presently available from natural olivines. Chapter 3 (the longest chapter by a large margin) describes a series of experiments which establish the speciation of sulfur for different melts under varying conditions of oxygen fugacity. The results of this series of experiments place a lower limit on the oxygen fugacity of one of Mars' inferred mantle reservoirs (that of the aforementioned Gusev crater basalts). Chapter 4 describes an assortment of high pressure experiments, intended to complement the sulfur speciation study of chapter 2, but also to verify the solubility of sulfur in Martian magmas, and to investigate the partitioning behaviour of Rare Earth Elements during partial melting of Mars' mantle.

1.3 - REFERENCES

Acuna, M.H., Connerney, J.E.P., Ness, N.F., Lin, R.P., Mitchell, D., Carlson, C.W., McFadden, J., Anderson, K.A., Reme, H., Mazelle, C., Vignes, D., Wasilweski, P. and Cloutier, P. (1999). Global Distribution of Crustal Magnetization Discovered by the Mars Global Surveyor MAG/ER Experiment. *Science*, 284, pp.790-793.

Agee, C.B. and Draper, D.S. (2004). Experimental constraints on the origin of Martian meteorites and the composition of the Martian mantle. *Earth and Planetary Science Letters*, 224, pp.415-429.

Aharonson, O, Zuber, M.T. and Rothman, D.H. (2001). Statistics of Mars' topography from the Mars Orbiter Laser Altimeter: Slopes, correlations, and physical models. *Journal of Geophysical Research*, 106(E10), pp.23,723-23,735.

Arvidson, R.E. (2016). Aqueous history of Mars as inferred from landed mission measurements of rocks, soils, and water ice. *Journal of Geophysical Research: Planets*, 121, pp.1602-1626.

Balta, J.B., and McSween, H.Y. (2013). Water and the composition of Martian magmas. *Geology*, 41.10 (2013), pp.1,115-1,118.

Bertka, C.M. and Fei,Y. (1998). Desnsity profile of an SNC model Martian interior and the moment-of-inertia factor of Mars. *Earth and Planetary Science Letters*, 157, pp.79-88.

Bertka, C.M. and Holloway, J.R. (1994a). Anhydrous partial melting of an iron-rich mantle I: subsolidus phase assemblages and partial melting phase relations at 10 to 30 kbar. *Contributions to Mineralogy and Petrology*, 115(3), pp.313–322.

Bertka, C.M. and Holloway, J.R. (1994b). Anhydrous partial melting of an iron-rich mantle II: primary melt compositions at 15 kbar. *Contributions to Mineralogy and Petrology*, 115(3), pp.323–338.

Borg, L.E., Nyquist, L.E., Wiesmann, H., Shih, and C-Y, Reese, Y. (2003). The age of Dar al Gani 476 and the differentation history of the martian meteorites inferred from their radiogenic isotopic systematics. *Geochimica et Cosmochimica Acta*, 67(18), pp.3519–3536.

Bridges, J.C., and Warren, P.H. (2006). The SNC meteorites: basaltic igneous processes on Mars *Journal of the Geological Society of London*. Vol. 163 p.229-251.

Cartwright, J.A. Ott, U., Hermann, S., and Agee, C.B. (2014). Modern atmospheric signatures in 4.4 Ga Martian meteorite NWA 7034. *Earth and Planetary Science Letters*, 400(March), pp.77–87.

Christensen P.R., Bandfield, J.L., Hamilton, V.E., Ruff, S.W., Kieffer, H.H., Titus, T.N., Malin, M.C., Morris, R.V., Lane, M.D., Clark, R.L., Jakosky, B.M., Mellon, M.T., Pearl, J.C., Conrath, B.J., Smith, M.D., Clancy, R.T., Kuzmin, R.O., Roush, T., Mehall, G.L., Gorelick, N., Bender, K., Murray, K., Dason, S., Greene, E., Silversam, S. and Greenfield, M. (2001). Mars Global Surveyor Thermal Emission Spectrometer experiment: Investigation description and surface science results. *Jouranl of Geophysical Research*, 106(E10), pp.23,823-23,871.

Franchi, I.A., Wright, I.P., Sexton, A.S. and Pillinger, C.T. (1999). The oxygen-isotope composition of Earth and Mars. *Meteocritics and Planetary Science*, 34, pp.657-661.

Frey, H. and Schultz, R.A. (1988). Large impact basins and the mega-impact origin for the crustal dichotomy on Mars. *Geophysical Research Letters*, 15(3), pp.229-232.

Gendrin, A., Mangold, N., Bibring, J-P., Langevin, Y., Gondet, B., Poulet, F., Bonello, G., Quantin, C., Mustard, J., Arvidson, R. and LeMouelic, S. (2005). Sulfates in Martian Layered Terrains: The OMEGA/Mars Express View. *Science*, 307 pp.1587-1591.

Gierasch, P.J. (1974). Martian Dust Storms. *Reviews of Geophysics and Space Physics*, 12(4) pp.730-734.

Golabek, G.J., Keller, T., Gerya, T.V., Zhu, G., Tackley, P.J. and Connolly, J.A.D. (2011). Origin of the martian dichotomy and Tharsis from a giant impact causing massive magmatism. *Icarus*, 215 pp.346-357.

Goins, N.R., and Lazarewicz, A.R. (1979). Martian seismicity *Geophysical Research Letters*, 6(4) pp.368-370.

Hartmann, W.K. and Neukum, G. (2001). Cratering chronology and the evolution of Mars. *Space Science Reviews*, 96(1–4), pp.165–194.

Humayun, M. (2004). Geochemical Evidence for Excess Iron in the Mantle Beneath Hawaii. *Science*, 306(5693), pp.91–94.

Jugo, P.J., Luth, R.W., and Richards, P. (2005). An Experimental Study of the Sulfur Content in Basaltic Melts Saturated with Immiscible Sulfide or Sulfate Liquids at 1300 C and 1.0 GPa. *Journal of Petrology*, 46(4), pp.783–798.

Jugo, P.J., Wilke, M. and Botcharnikov, R.E. (2010). Sulfur K-edge XANES analysis of natural and synthetic basaltic glasses: implications for S speciation and S content as a function of oxygen fugacity. *Geochimica et Cosmochimica Acta*, 74, pp.5926-5938.

King, P.L. and McLennan, S.M. (2010). Sulfur on Mars. *Elements*, 6, pp.107-112.

Klimm, K., Kohn, S.C., O'Dell, L.A., Botcharnikov, R.E. and Smith, M.E. (2012b). The dissolution mechanism of sulphur in hydrous silicate melts. II: Solubility and speciation of sulphur in hydrous silicate melts as a function of fO2. *Chemical Geology*, 322–323, pp.250–267.

McLennan, S.M., Boynton, W.V., Karunatillake, S., Hahn, B.C., Taylor, G.J and The Mars Odyssey GRS Team. (2010). Distribution of sulfur on the surface of Mars determined by the 2001 Mars Odyssey Gamma Ray Spectrometer. *Lunar and Planetary Science Conference*, 41:2174.

McSween, H.Y. (1984). The SNC meteorites: Are they Martian rocks? *Geological Society of America*, 12, pp.3-6.

McSween, H.Y. (1994). What we have learned about Mars from the SNC meteorites. *Meteocritics,* 29, pp.757-779.

McSween, H.Y., Arvidson, R.E., Bell, J.F., Blaney, D., Cabol, N.A., Christiensen, P.R., Clark, B.C., Crisp, J.A., Crumpler, L.S., Des Marais, D.J., Farmer, J.D., Gellert, R., Ghosh, A., Gorevan, S., Graff, T., Grant, J., Haskin, L.A., Herkenhoff, K.E., Johnson, J.R., Jolliff, B.L., Klingelhoefer, G., Knudson, A.T., McLennan, S., Milam, K.A., Moersch, J.E., Morris, R.V., Rieder, R., Ruff, S.W., Souze Jr, P.A., Squyres, S.W., Wanke, H., Wang, A., Wyatt, M.B., Yen, A., and Zipfel, J. (2004). Basaltic Rocks Analyzed by the Spirit Rover in Gusev Crater. *Science*, 305(5685), pp.842–845.

McSween, H.Y., Grove, T.L. and Wyatt, M.B. (2003). Constraints on the composition and petrogenesis of the Martian crust. *Journal of Geophysical Research,* 108(E12), 5135.

McSween, H.Y., Taylor, G.J. and Wyatt, M.B. (2009). Elemental composition of the Martian crust. *Science* 324(5928), pp.736–9.

MetBase: Meteorite information Database, *Birkbeck Library, University of London*, April 2015.

Nimmo, F., and Stevenson, D.J. (2001). Estimates of Martian crustal thickness from viscous relaxation of topography. *Journal of Geophysical Research*. Vol. 106(E3) pp.5085-5098.

Nyquist, l.e., Bogard, D.D., Shih, C-Y., Greshake, A., Stoffler, and D. Eugster, O. (2001). Ages and Geologic histories of Martian Meteorites *Chronology and Evolution of Mars*. Vol.96 pp.105-164.

Laul, J.C., Wakita, H., Showalter, D.L., Boynton, W.V., and Schmitt, R.A. (1972). Bulk, rare earth and other trace elements in Apollo 14 and 15 and Luna 16 samples. *Lunar Science Conference, 3rd, January* 10-13, Houston TX.

Levy, J.S., Fassett, C.I., Head, J.H., Schwartz, C., and Watters, J.L. (2014). Sequestered glacial ice contribution to the Martian water budget: Geometric constraints on the volume of remnant,

midlatitude and debris-covered glaciers. *Journal of Geophysical Research: Planets*, 119(10) pp.2188-2196.

Lodders, K., Fegley, B. (1997). An Oxygen Isotope Model for the Composition of Mars. *Icarus*, 126 pp.373–394.

Lowell, P. (1911). Mars and its canals. *The Macmillan Company Ltd.*

Murchie, S.L., Mustard, J.F., Ehlmann, B.L., Milliken, R.E., Bishop, J.L., McKeown, N.K., Noe Dobrea, E.Z., Seelos, F.P., Buczkowski, D.L., Wiseman, S.M., Arvidson, R.E., Wray, J.J., Swayze, G., Clark, R.N., Des Marais, D.J., McEwan, A.S. and Bibring, J-P. (2009). A synthesis of Martian aqueous mineralogy after 1 Mars year of observations from the Mars Reconnaissance Orbiter. *Journal of Geophysical Research*, 114, E00D06. DOI:10.1029/2009je003342.

Palme, H. and Jones, A. (2003). Solar System Abundance of the elements. *Treatise on Geochemistry*, Vol 1, pp.41-61.

Palme, H. and O'Neill, H.S.T. (2003). Solar System Abundance of the elements. *Treatise on Geochemistry*, Vol 1, pp.41-61.

Pepin, R.O. (1985). Evidence of Martian Origins. *Nature*, 317 pp.473–475.

Sleep, N.H. (1994). Martian plate tectonics. *Journal of Geophysical Research,* 99(E3), pp.5639-5655.

Spagnuolo, M.G., Rossi, A.P., Hauber, E. and van Gasselt, S. (2011). Recent tectonics and subsidence on Mars: Hints from Aureum Chaos. *Earth and Planetary Science Letters,* 312(1) pp.13-21.

Stewart,A.J., Schmidt, M.W., Westrene, W. and Liebske, C. (2007). Mars: A New Core-Crystallization Regime. *Science,* 316(5829) pp.1323-1325.

Taylor, G.J., Boynton, W., Bruckner, J., Wanke, H., Dreibus, G., Kerry, K., Keller, J., Reedy, R., Evans, L., Starr, R., Squyres, S., Karunatillake, S., Gasnault, O., Maurice, S., d'Uston, C., Englert, P., Dohm, J., Baker, V., Hamara, D., James, D., Sprague, A., Kim, K. and Drake, D. (2006). Bulk composition and early differentiation of Mars. *Journal of Geophysical Research,* 111 E03S10.

Treiman, A.H., Gleason, J.D. and Bogard, D.D. (2000). The SNC meteorites are from Mars. *Planetary and Space Science,* 48(12–14), pp.1213–1230.

Tuff, J., Wade, J., and Wood, B.J. (2013). Volcanism on Mars controlled by early oxidation of the upper mantle. *Nature*, 498(7454), pp.342–5.

Wadhwa, M. (2001). Redox State of Mars' Upper Mantle and Crust from Eu Anomalies in Shergottite Pyroxenes. Science, 291(5508), pp.1527–1530.

Wanke, H. and Dreibus, G. (1988). Chemical Composition and Accretion History of Terrestrial Planets. Philosophical Transactions of the Royal Society A: *Mathematical, Physical and Engineering Sciences*, 325(1587), pp.545–557.

Wanke, H., Dreibus, G. and Wright, I.P. (1994). Chemistry and Accretion History of Mars *Transactions of the Royal Society A: Mathematical, Physical and Engineering Sciences*, 349(1690), pp.285–293.

Yoder, C.F., Konopliv, A.S., Yuan, D.N., Standish, E.M. and Folkner, W.M. (2003). Fluid Core Size of Mars from Detection of the Solar Tide. *Science,* 300 pp.299-303.

Zhong, S. and Zuber, M.T. (2001). Degree-1 mantle convection and the crustal dichotomy on Mars. *Earth and Planetary Science Letters,* 189 pp.75-84.

Chapter 2

Manufacture of synthetic olivine capsules for use in experiments

A more concise version of this chapter as been published as:

Nash, W., Smythe, D.J., Wood, B.J., 2016 Synthetic olivine capsules for use in experiments *American Mineralogist* Vol. 101(10) pp. 2260-2263

2.1 – ABSTRACT

A method for manufacturing polycrystalline olivine capsules has been developed. These capsules are suitable as containers for olivine-saturated melts in near-liquidus experiments. The objective was to avoid some of the problems found in 1-atmosphere gas-mixing experiments, notably Fe loss from silicate melts to Pt wire loops and reaction between noble metal loops and sulfide liquids. Use of olivine capsules of fixed Mg/Fe enables the Mg# of the coexisting melt to be controlled and doping of the capsule with minor elements of interest enables partition coefficients to be determined at measureable concentrations.

Development of a suitable manufacture process largely consisted in suppressing capsule porosity, which proved to be the largest obstacle to retention of melt for extended periods, and which is enhanced by the considerable wetting of olivine by Fe-rich silicate melts. Capsules with olivine compositions ranging from Fo_{70} to Fo_{90} have now been manufactured and found to remain impermeable to basaltic melts for 24 hours. In the case of magnesian compositions (~Fo_{90}), several cycles of heating and cooling (from 1250°C to 1550°C) are required to enhance grain growth and reduce permeability to an acceptable level. In contrast, a more iron-rich composition (Fo_{70}) functions well after a single cycle of heating from 800°C to 1350°C.

2.2 - INTRODUCTION AND MOTIVATION

Experimental studies of Martian magmatism commonly involve charges that are more Fe-rich than their terrestrial analogues, reflecting the greater assumed Fe content of the Martian mantle. This presents a problem for studies conducted in olivine capsules within one-atmosphere gas mixing furnaces, because the olivine crystals available typically have inappropriate Mg numbers.

Olivine capsules are typically used in response to problems such as charges reacting with their containers or supporting loops, the classic example being Fe-loss from silicates into platinum capsules or wire loops (e.g. Donaldson, 1979). Such unwanted loss of Fe was encountered during the sulfur speciation campaign described in Chapter 3. Although this issue may be largely overcome by pre-conditioning the Pt wire with Fe-bearing silicate melt at the appropriate oxygen fugacity (as was done in Chapter 3, with mixed results), this rarely prevents Fe loss entirely. The use of metals that dissolve Fe less readily, such as Au, Ag or Re, is occasionally possible. A further potential hazard is dissolution of the container or suspension wire by the charge itself, a problem also encountered in this project when using sulfide melts and Re suspension wires. This has led previous experimenters to use machined single crystals of natural San Carlos (Fo_{90}) olivine as their capsule material in multi-anvil (Brey *et al.* 2008) and piston-cylinder experiments (Ballhaus *et al.* 1991, Berry *et al.* 2005). A further advantage of using olivine as a capsule material is its capacity for containing experiments equilibrated at fO_2 conditions close to the Fayalite-Magnetite-Quartz (FMQ) buffer; graphite and metal capsules being limited to values that are higher or lower. Ballhaus *et al.* (1991) successfully used bored singe-crystal San Carlos olivines to contain a series of spinel harzburgites and lherzolites equilibrated at the Ni-NiO (NNO) buffer (~FMQ+1). The use of natural olivine as a capsule material – as demonstrated by these studies – is nonetheless restrictive, since ideally the experimenter would have the freedom to employ a capsule having any desired composition, both with respect to the olivines' Mg number and to its concentrations of trace elements. This requirement is especially pertinent to studies of olivine-melt trace element partitioning, since diffusion of many species of interest through olivine is extremely slow, and olivines with the desired initial trace element concentration are not always readily available.

To expand the possible applications of olivine as a capsule material, a process for manufacturing polycrystalline olivine capsules from synthetic starting materials of Fo_{90} and Fo_{70} composition has been explored. An important requirement was that the process be achievable using equipment that is readily available in most experimental laboratories; such as gas mixing furnaces and simple

tools made from hardened steel. As an example of the capsule's potential applications, we doped some olivine starting materials with moderate levels of NiO and MnO and investigated the equilibration of capsule with a melt of approximately basaltic (although fairly Fe-rich) composition at 1-atmosphere pressure. The key to manufacture turned out to be the development of a heat treatment procedure which renders the polycrystalline capsule impermeable to the melt over reasonable time scales, overcoming the largest obstacle to melt retention: absorption by the capsule into the spaces between the grains.

2.3 - THE MANUFACTURE METHOD

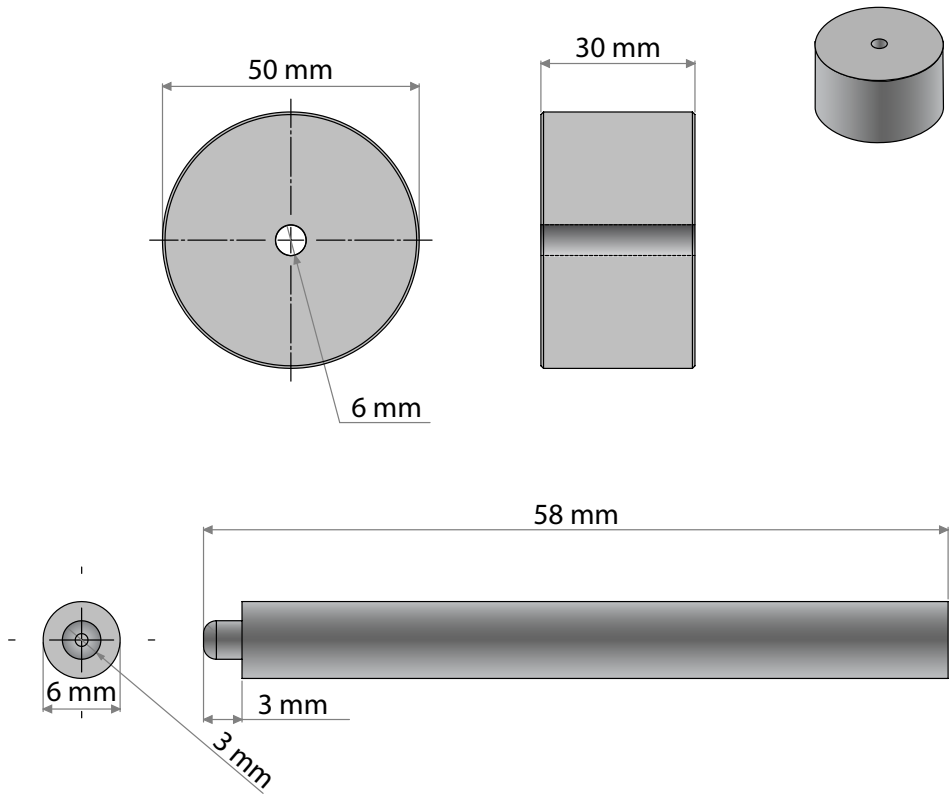
The capsule manufacture is essentially a two-stage process. In this case the desired olivine composition was first prepared from a mixture of analytical grade MgO, SiO_2 and Fe_2O_3. Small amounts (1-2 wt%) of NiO and MnO were added together with the stoichiometric amount of SiO_2 to make olivine, as required. Because of the non-stoichiometry of "FeO" powder, and the difficulty of obtaining complete reaction between Fe metal and Fe_2O_3, the initial heat treatment involves substantial reduction in addition to olivine synthesis.

The powdered starting material was ground under ethanol until fine and homogeneous. The mixture was then pressed into pellets of 12.7 mm diameter and approximately 5 mm thickness using PVA binder, and reduced and recrystallized into olivine in a one-atmosphere gas-mixing furnace for >2 hours at 1300°C and an oxygen fugacity of 1 log unit below the FMQ buffer. After breaking the pellet open to confirm that the product was uniformly green and reduced the sample was pulverized using a percussion mortar and re-ground under acetone.

The second stage employs a die made of hardened tool steel (Fig 2.3). The ones used in this study are made from high chromium (~12%) D2 steel which can be hardened in air and undergoes little distortion. They were machined leaving the bore slightly undersize, hardened to R_c 56 and the bores honed to the desired dimensions. The pistons (Fig 2.3) were fabricated from standard drill "blanks" with a nipple machined and then polished at one end to produce the sample space in the interior of the olivine capsule. It was found that a rounded and highly polished end to the nipple (as shown) helps release the capsule from the piston. For capsules destined for use in 1-atm experiments, dimensions of 6 mm O.D., 3 mm I.D. and 6 mm height, are appropriate, and represent the main focus of this study. However, smaller capsules with 3mm O.D. and 1mm I.D.

have also ben successfully produced, which would be suitable for high-pressure experiments. In order to make 6mm O.D. capsules 0.37g was found to be the optimum mass of reacted starting materials. These were placed in a mortar and moistened with an aqueous solution of PVA (50 g/l), which was worked into the mixture (initially stiff), until a "flaky" consistency was obtained. This material was then transferred to the die and compressed to a pressure not exceeding 1 GPa. Liberal application of PTFE spray to the die bore and piston was found to be necessary for a smooth removal of the capsules after pressing. Finally, the pressed capsules were suspended in the gas-mixing furnace and subjected, initially, to a single anneal at 1550°C, in a 67% CO_2 : 33% CO gas mixture. For Fo_{90} compositions however, this annealing temperature profile turned out to be inappropriate as the resulting capsules were too porous, and absorbed basaltic melt into their walls as discussed below.

Figure 2.3: Technical specifications of the die and piston used for capsule manufacture. Drawing courtesy of Jamie Long, (Earth Science workshop).



2.4 - METHOD DEVELOPMENT

The intention with the two-stage manufacturing process was to minimize pore space, by separating the recrystallization of the starting powder into olivine (together with its disruptive volume change) from the process of annealing the olivine grains into a capsule. Nevertheless, basaltic melts showed a strong tendency to infiltrate the pore spaces in our prototype capsules, due to their low wetting angles[1] with olivine (fig 2.4a). Interconnected networks of pore spaces therefore made these capsules permeable, and incapable of retaining large pools of melt for extended periods. In order to reduce interconnectivity, the annealing process was modified to incorporate cycles of heating and cooling. Various temperature profiles were trialled unsuccessfully, before it emerged that for the Fo_{90} capsules, the saw-tooth cycling shown in fig 2.4b generated capsules of low permeability after 12 hours of heat-treatment. One explanation for this is that the cooling cycles "unlock" grain boundaries, enhancing grain-growth during the succeeding heating cycle and isolating the pore space. Fig 2.4a shows a BSE-image of a Fo_{90} capsule treated in this way. As can be seen, there is no evidence of infiltration by the melt into the capsule wall, especially since the large vesicles left behind by the PVA binder remain empty.

[1] The wetting angle (or contact angle) is the dihedral angle between a planar solid substrate and the surface of a liquid making contact with ('wetting') that substrate.

Figure 2.4a: Backscattered Electron Images of some capsules and their melts. Fig A shows the melt-capsule boundary that resulted from an unsuccessful test. The melt in this case was olivine-saturated, but nonetheless infiltrated the spaces between the grains in the capsule wall. Fig B shows the voluminous melt-pool that may be retained by an impermeable capsule. The discontinuity between the melt and surrounding walls is relatively sharp. The holes inside the capsule are a mixture of olivine grains plucked out by the grinding process, and vesicles formed by volatilization of the PVA binder.

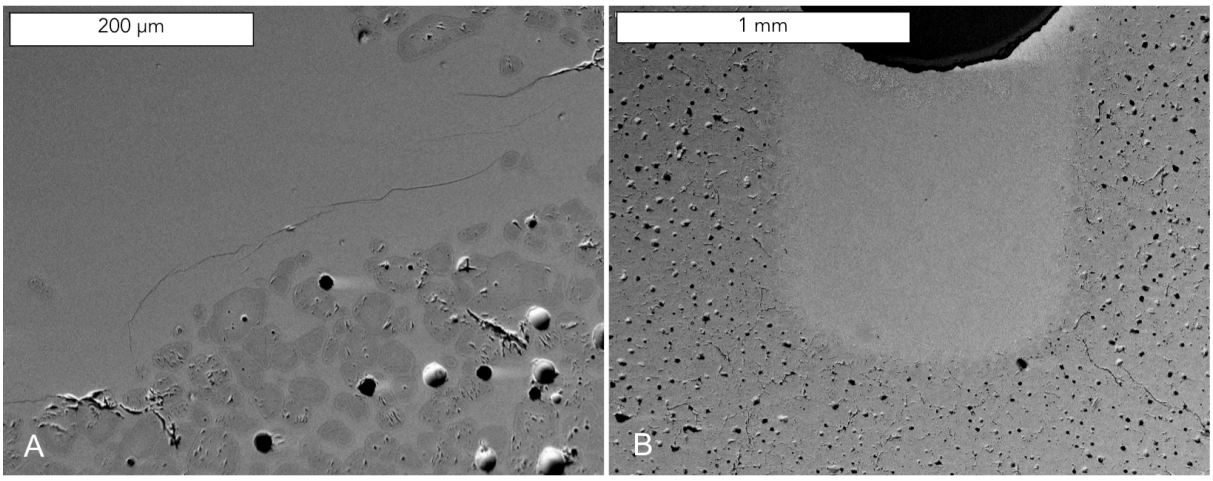
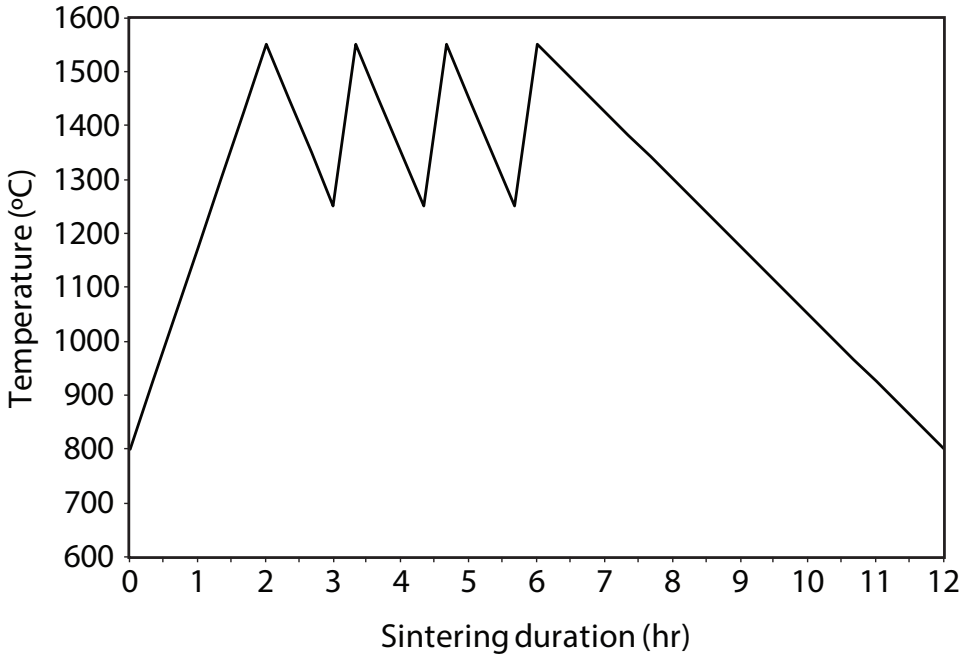


Figure 2.4b: The temperature profile found to be necessary for annealing of Fo_{90} capsules. A single CO:CO2 mixing ratio of 65:135 may be used for the whole sintering process (giving rise to cycles of fO_2 about QFM-1).



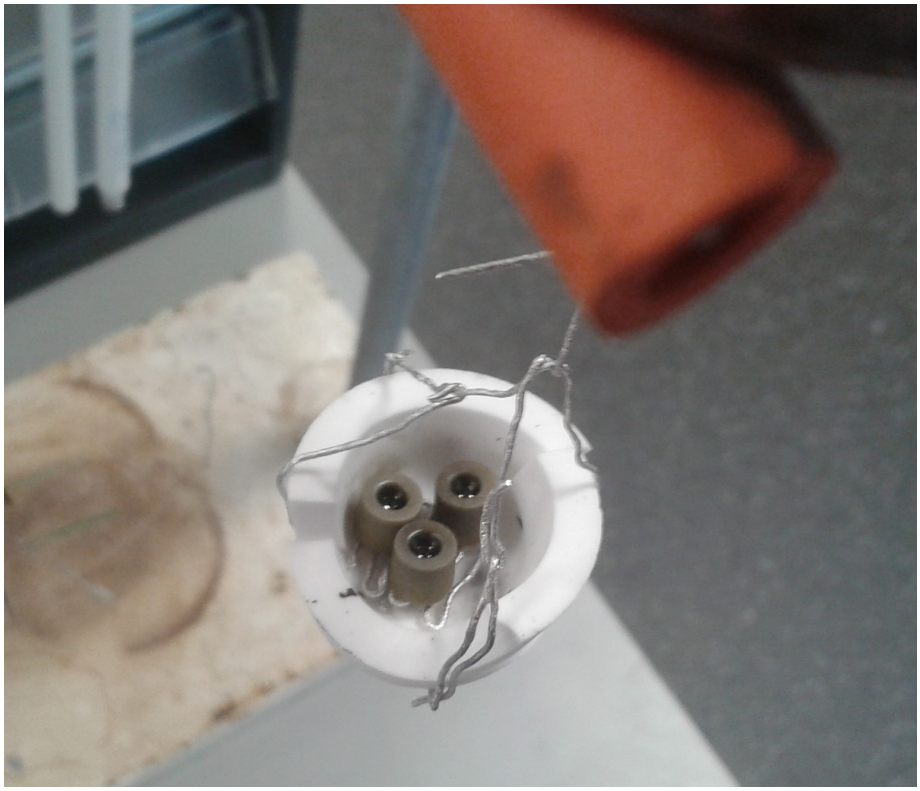
Interestingly, the Fo_{70} composition capsules manufactured in the more straightforward way did not require a complex heat-treatment to become impermeable. A single cycle of heating from 800° to 1250°C in 1 hour followed by a 3 hour temperature ramp from 1250 to 1350°C and a 30 minute anneal at the latter temperature in a gas mixture of 67% CO_2 and 33% CO was sufficient to reduce permeability to acceptable levels. Quenched capsules resulting from this simpler heat treatment are shown in Fig 2.4c.

Cracks that formed during removal of the pressed capsules from the die represented an important source of unwanted porosity. To suppress their formation, trials were undertaken using a variety of non-contaminating binding agents, which were mixed into the recrystallized mixture before being pressed, with the aim of holding the capsule together during removal from the die. Water, ethanol, ammonia solution, tetraethyl orthosilicate and polyvinyl alcohol solution (PVA 50g/l) were tried, and PVA was found to be the only suitable binder. Use of PVA does leave pores (gas bubbles) within the sintered capsules, but these are not problematic because they generally do not form an interconnected network (fig 2.4a).

One approach that wasn't ultimately successful (but which was hoped would permit capsules to be annealed at a lower temperature) was the use of two olivines with complementary forsterite numbers, mixed in proportions yielding the desired composition. The logic behind this approach was that the more Fe-rich of these olivines would melt at the annealing temperature, and therefore fill any pore spaces between the more Mg-rich grains, before being absorbed by them. Although the capsules resulting from this procedure were regularly shaped[2], testing with basaltic melts showed them to be highly permeable, and therefore unsuitable as containers for melt-bearing experiments.

2 Capsules that absorb their melts typically deform, becoming wider at their base as the matrix of olivine crystals sags under its own weight.

Figure 2.4c: Three Fo70 capsules following their removal from the furnace. Note the highly reflective surfaces of the melts within their interiors.



2.5 – CAPSULE EVALUATION

2.5.1 Time Series Experiments

A time-series of experiments was performed (2, 4, 8, and 24 hours) at 1200°C and an fO_2 of FMQ-1 log units to test whether the capsules could retain silicate melts for extended periods, and to investigate their potential for studying equilibrium partitioning. Four Fo_{70} capsules containing 1% Mn_2SiO_4 and 2% Ni_2SiO_4 were packed with powdered oxides constituting an iron-rich basaltic composition. The composition chosen (limited to the CFMAS system) was a putative Martian basalt (Bertka and Holloway, 1994b), with its Mg# modified such that it would be in equilibrium with Fo_{70} olivine. Each experiment was quenched rapidly by emersion into water.

The capsules were sectioned, ground and polished, before being analyzed by WDS using a JEOL JXA-8600 electron-microprobe. A traverse from the outer wall to the centre of the melt pool was taken for each experiment (Fig 2.5). Olivine analysis spots were positioned on grain centres in order to properly evaluate the approach to equilibrium.

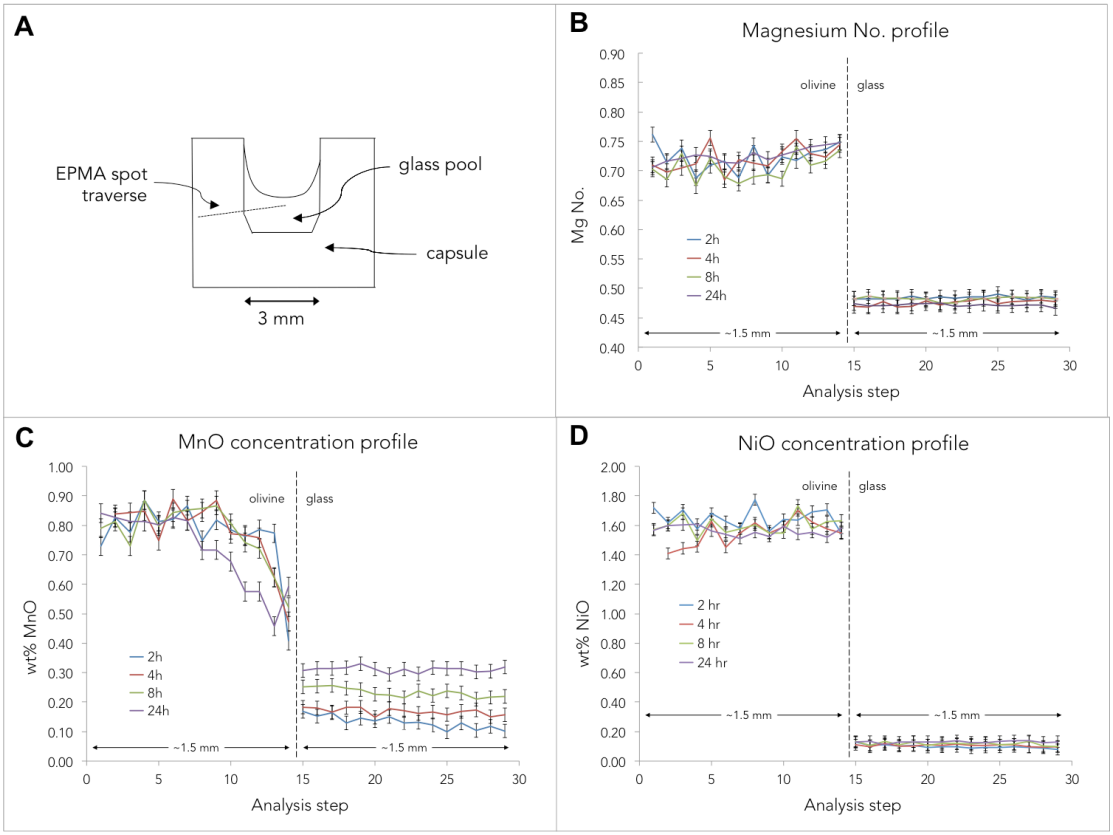
Each capsule retained a large pool of melt, indicating that absorption into pore spaces was negligible even after 24 hours. Mn and Ni, initially present exclusively in the olivine, diffused into the melt pools during the experiment. Mg and Fe also show some re-equilibration, indicating that the starting materials were not exactly in equilibrium with one another with respect to their Mg ad Fe concentrations.

2.5.2 Diffusion Profiles and Approach to Equilibrium

As expected, because the Ni and Mn contents of the melt were initially zero, a diffusional approach to equilibrium is observed in experiments of increasing duration (Fig 2.5). As experiment duration increased, zoning of Ni in the olivine capsule wall diminished progressively, and the compositions of individual olivine grains became more uniform as the Ni content of the product glass increased. With increasing experiment duration, apparent Ni olivine-liquid partition coefficients ($D_{Ni}^{ol\text{-}liq}$) exhibited successively closer approximations to a value of 12.2, which can be considered a close approach to equilibrium. Although the $D_{Ni}^{ol\text{-}liq} = (124/MgO)-0.9$ relation of Hart and Davis (1978) predicts a value of 14.4 for this coefficient, we expect slightly lower values, as observed in earlier Fe-bearing experiments (Kinzler *et al.*, 1990). As the variation among olivine analyses reduces with increased runtime, the calculated Mg-Fe exchange K_D

(=$(Fe/Mg)_{ol}/(Fe/Mg)_{melt}$) settles to the 0.35 (± 0.01) value reported for Fe-rich basalts by Filiberto and Dasgupta (2011).

Figure 2.5: Results of the 1200°C time-series experiments performed with Ni and Mn-doped Fo_{70} capsules. A shows the melt-capsule geometry, including a typical EPMA spot traverse. Figures B, C and D are concentration profiles for Mg number, MnO and NiO, after 2, 4, 8 and 24 hours. Note that Fe-Mg and Ni equilibrium are achieved relatively quickly, exhibiting no variation among their liquid's profiles for the various durations. MnO didn't reach equilibrium even after 24 hours, probably due to the greater mass transfer required to achieve its equilibrium concentration in the melt.



Unlike Ni contents and Mg/Fe ratios, the Mn concentrations in the olivines and melts do not approach constant values even in 24 hour experiments. This is almost certainly because, with $D_{Mn}^{ol\text{-}liq}$ close to 1.0 (Watson 1977), the mass of Mn required to be transported to approach equilibrium is much greater than in the case of Ni ($D_{Ni}^{ol\text{-}liq}$=12.2). Thus, a NiO concentration in the melt of

1300ppm indicates an approach to equilibrium, while for MnO in this case, equilibrium values of ~8000ppm would be required. After 24 hours we actually reach a concentration of only 3100ppm MnO in the quenched glass. Despite the failure of Mn to reach equilibrium, the capsule's impermeability after even 24 hours implies that longer runtimes may be used than those explored here.

Experimentation with different melt compositions showed that only those that are olivine–saturated can be retained by the synthetic capsules. Olivine-under-saturated melts are rapidly absorbed by the capsule, presumably because they preferentially dissolve olivine from the grain surfaces, connecting and widening pore spaces and undermining the capsule's impermeability. However, addition of sacrificial fine-grained olivine to such melts saturates them in olivine rapidly during the experiment and, as expected, avoids the problem of capsule impregnation.

2.5.3 An Attempt to measure Cr-isotope fractionation

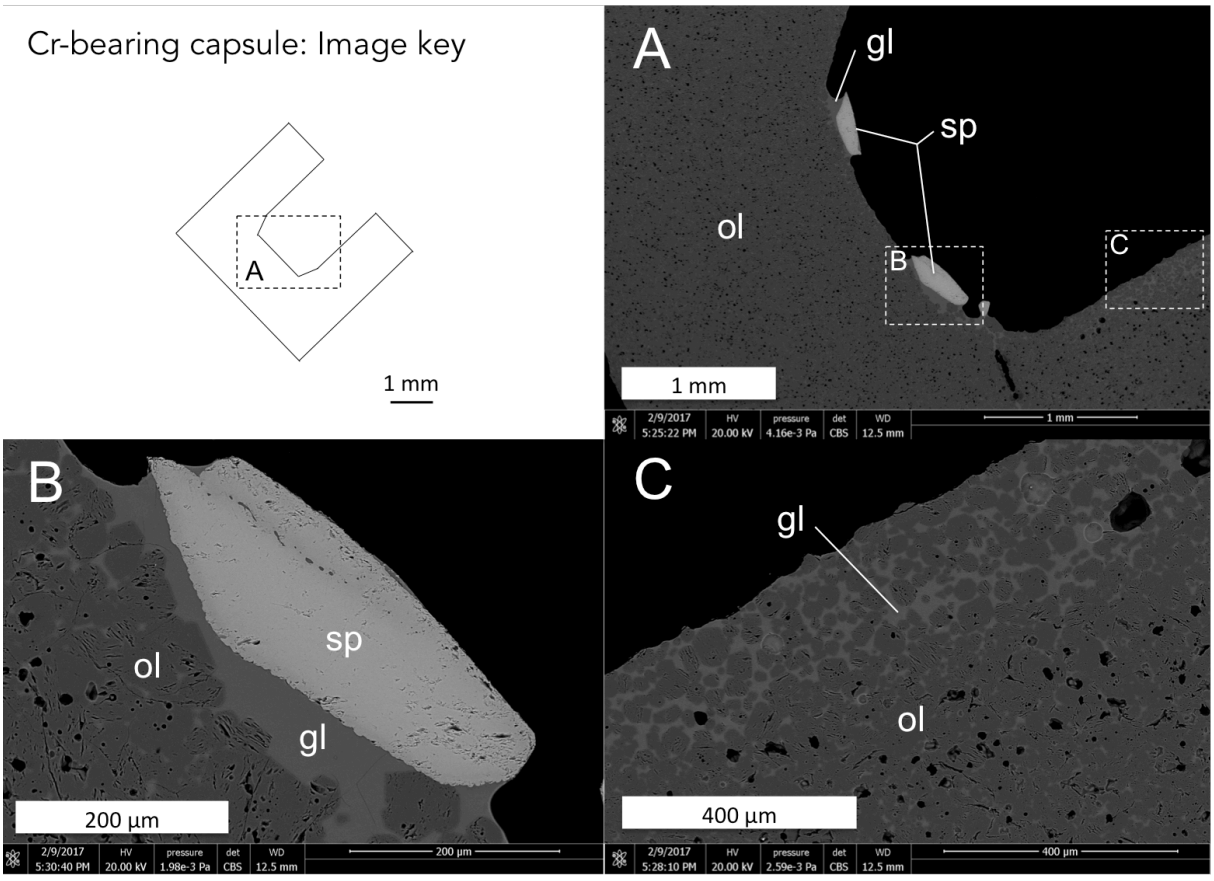
As a more ambitious test of the capsules' survivability, a 1 week duration experiment was performed with Fo_{70} capsules containing chromite spinels and Cr-free basaltic melt. If successful, this experiment would serve to demonstrate a further use for the capsules as tools for experimentally measuring isotope fractionation.

In the case of this attempt, the Cr-isotope ratio of the chromites was known, and the isotopic fractionation of Cr between the basaltic melt and olivine was the desired objective. The requirement for capsules in this case arose from the need to keep the olivines and the melt separate from one another, since the most widely available method for measuring chromium isotopes requires relatively large and uncontaminated volumes of each phase of interest. The long duration of the experiment was necessary because the diffusion of chromium through olivine is extremely slow. For this reason the experiment was performed at the highest temperature permitted by the oxygen-fugacity constraints, which at FMQ+1 was 1300°C. Capsules containing identical contents were run together (supported by an alumina crucible): one manufactured with temperature cycling and the other without; so that the relative merits of these procedures could be compared.

Regrettably, neither capsule retained a sufficiently large pool of melt for mass spectrometry. Furthermore, no difference was observed between the melt-retention of the two capsules. The capsule manufactured without temperature cycling is shown in figure 2.5.3. As in previous

attempts, the melt was absorbed by the capsule walls, both into the olivines and into the space between them. These results indicate that rather than removing pore spaces completely, the manufacture process developed in this study reduces permeability to such an extent that melt absorption is significantly slowed, but not prevented entirely.

Figure 2.5.3: Backscattered electron images of the spinel-bearing experiment, following 7 days of equilibration in the one-atmosphere furnace at 1300°C. Panel A is an overview of the interior space of the capsule, showing that no melt pool was retained. Panels B and C reveal that small quantities of melt did survive, clinging to the underside of spinel crystals (B) and occupying the spaces between olivine grains just inside the capsule wall (C). Label meanings are as follows: gl, glass; ol, olivine; sp; spinel.



2.5.4 Capsules at high pressure

A second type of capsule was trialled, with smaller dimensions than the original: 3mm tall, 3mm in outer diameter, and 1mm inner diameter. These were manufactured by exactly the same procedure as the larger capsules, although with the addition of a lid, comprising an olivine disc of the same outer diameter as the capsule. Duane Smythe (a co-author on the paper in which this work is described) successfully used one of these capsules (composition Fo_{72}) to equilibrate a basaltic melt at 1300°C and 1.5GPa in a piston-cylinder apparatus. Following the experiment, a large pool of melt remained in the capsule, with no breach of the walls visible under examination with reflected light. The duration of this run was 4 hours. Clearly, the imposition of a large hydrostatic pressure doesn't accelerate infiltration of the capsule walls by this basaltic melt. This run confirms the usefulness of these capsules for high-pressure experiments, although more trials with longer run durations and melt compositions are needed.

2.6 - CONCLUSIONS AND IMPLICATIONS

A method is described for the fabrication of synthetic polycrystalline olivine capsules suitable for the performance of experiments with olivine-saturated melts at high temperature. It has been shown that specific olivine compositions require specific heat treatments in order to render them impermeable to infiltration by basaltic melts with which they are in equilibrium. Several cycles of heating to 1550°C and cooling to 800°C are required for Fo_{90} capsules to become impermeable. In this case, experiments of 24 hours duration, hosting pools of basaltic melt at temperatures of 1400°C indicated no infiltration by the melt. A simpler single-stage heat treatment to 1350°C was found to be adequate for capsules of Fo_{70} composition.

The principal implication of this study is that for olivine-saturated experiments for which noble metal capsules or wire loops are inappropriate, researchers will no longer be restricted to the use of natural olivine single crystals as capsules. It is relatively straightforward to extend the range of available capsule compositions from Fo_{90}, similar to single crystals from San Carlos (AZ), to Fo_{70} enabling more iron-rich melts to be studied. Furthermore, the development of synthetic polycrystalline capsules enables control of trace and minor element concentrations in the olivine, meaning that crystal-liquid partitioning studies can be performed at desired and appropriate concentrations.

2.7 - REFERENCES

Ballhaus, C., Berry, R.F. and Green, D.H. (1991). High pressure experimental calibration of the olivine-orthopyroxene-spinel oxygen geobarometer: implications for the oxidation state of the upper mantle. *Contributions to Mineralogy and Petrology*, 107, 27-40.

Berry, A. J., Hermann, J., O'Neill, H. S. C., and Foran, G. J. (2005). Fingerprinting the water site in mantle olivine. *Geology*, 33, 869-872.

Bertka, C., and Holloway, J. (1994b). Anhydrous partial melting of an iron-rich mantle II: primary melt compositions at 15 kbar. *Contributions to Mineralogy and Petrology*, 115(3), 323-338.

Brey, G. P., Bulatov, V. K., Girnis, A. V., and Lahaye, Y. (2008). Experimental Melting of Carbonated Peridotite at 6-10 GPa. *Journal of Petrology*, 49(4), 797-821.

Filiberto, J., and Dasgupta, R. (2011). Fe^{2+}-Mg partitioning between olivine and basaltic melts: Applications to genesis of olivine-phyric shergottites and conditions of melting in the Martian interior. *Earth and planetary science letters*, 304, 527-537.

Gale, A., Dalton, C. A., Langmuir, C. H., Su, Y. and Schilling, J-G. (2013). The mean composition of ocean ridge basalts. *Geochemistry Geophysics Geosystems*, 14(3), 489-518.

Grove, T.L. (1981). Use of FePt alloys to eliminate the iron loss problem in 1 atmosphere gas mixing experiments: Theoretical and practical considerations. *Contributions to Mineralogy and Petrology* 78, 298-304

Hart, S. R., and Davis, K. E. (1978). Nickel partitioning between olivine and silicate melt. *Earth and planetary science letters*, 40, 203-219.

Kinzler R. J., Grove, T. L., and Recca, S. I. (1990). An experimental study on the effect of temperature and melt composition on the partitioning of nickel between olivine and silicate melt. *Geochimica et Cosmochimica Acta*, 54(5), 1255-1265.

Watson, E.B. (1977). Partitioning of manganese between forsterite and silicate liquid. *Geochimica et Cosmochimica Acta* 41, 1363-1374

Woodland, A.B. and O'Neill, H.S.C. (1997). Thermodynamic data for Fe-bearing phases obtained using noble metal alloys as redox sensors. *Geochimica et Cosmochimica Acta*, 61(20), pp.4359–4366.

Chapter 3

Control of sulfur capacity and speciation by silicate melt chemistry

3.1 - ABSTRACT

To investigate the influence of silicate melt chemistry on sulfur speciation, six common magma compositions have been brought to equilibrium with a range of CO-CO_2-SO_2 gas mixtures, representing a range of oxygen fugacity (fO_2) conditions spanning QFM-1.67 to QFM+1.6. Quenched melts from these experiments were analyzed using XANES to determine their sulfur speciation as a function of fO_2. Measurements of absolute sulfur concentration were also made using SIMS, so that the sulfide and sulfate capacities of the melts could be investigated. All experiments were conducted at one-atmosphere pressure within a gas-mixing furnace, at a constant temperature of 1300°C. The magma compositions investigated are diverse: a pair of terrestrial MORBs (one primitive, one enriched), a pair of putative Martian basalts (both primary mantle melts representing differing melt fractions), and a pair of more differentiated terrestrial magmas (a typical andesite, and a typical dacite).

The quenched glasses' XANES spectra confirm that sulfide and sulfate are the only stable species, and that a transition from the former to the latter occurs with increasing fO_2 as indicated by previous studies on related materials. In addition, comparisons between the spectra of glasses equilibrated under the same fO_2 conditions demonstrate clear differences in their speciation, confirming that silicate melt chemistry influences the fO_2 position of the sulfide-sulfate equilibrium. Sulfate mole fractions ($S^{6+}/\Sigma S$) determined using XANES spectra are consistently lower for Fe-rich melts, suggesting that Fe exerts the dominant control over speciation by shifting the sulfide-sulfate crossover towards more oxidizing conditions. Trends in overall sulfur concentration obtained using SIMS confirm the changes in speciation, but are unable to provide quantitative data on their dependence on fO_2. A relation is presented linking the ratios $S^{6+}/\Sigma S$ and $Fe_2O_3/(FeO^2)$, which explains the dependence on Fe concentration, and potentially offers a means to determine $S^{6+}/\Sigma S$ ratios without synchrotron data. Finally, sulfate concentrations measured under the most oxidizing conditions exhibit a good inverse correlation with the abundance of tetrahedrally co-ordinated cations (Si and Ti) in each melt.

3.2 - INTRODUCTION AND MOTIVATION

Sulfur is exceptional among the elements for its broad range of chemical species, and their prevalence in natural materials, both terrestrial and Martian. This diversity is especially significant because sulfur's geochemical character strongly depends on its chemical speciation (typically expressed by its oxidation state). On Earth, the sulfide (S^{2-}) ion is commonly associated with igneous rocks and ores (Mandeville 2010), while the sulfate (S^{6+}) ion is ubiquitous in sediments, chiefly evaporate deposits (Deer *et al.* 1992). Elemental sulfur (S^0) occurs around volcanic vents and as a by-product of anaerobic respiration in salt domes (Mandeville 2010). Finally, the sulfite ion (S^{4+}) occurs in gaseous form as SO_2, which is expelled from silicic volcanoes, occasionally in very large quantities (Self 2006). Both the sulfide and sulfate species have been observed in Martian rocks, the former in basalts (King *et al.* 2010) and the latter in sediments (Gendrin *et al.* 2005).

All of Earth's crustal and atmospheric sulfur is ultimately derived from the mantle, through partial melting and surface-ward migration of sulfur-bearing magma. The solubility of the various sulfur species in these magmas exhibits an order-of-magnitude range (Jugo *et al.* 2005), so their relative stability under different conditions is essential for estimating the flux of sulfur between these major reservoirs of the Earth. The largest flux of sulfur out of the mantle probably occurs at mid-ocean ridges. Mid ocean ridge basalts (MORBs) have been known since the 1960s' to contain trace quantities of sulfur, typically present both as both a trace element dissolved in the glass, and as sulfide blebs (Mathez 1976). The occurrence of these blebs suggests that MORBs are frequently sulfide-saturated upon eruption. Volcanic outgassing at convergent tectonic margins represents another route out of the mantle. SO_2 is among the most common volcanic gases, and more recently, anhydrite has also been detected in silicic magmas (Luhr 2008).

As a result of sampling difficulties, much less is known about the Martian sulfur cycle. Nevertheless, the scarce information that is available indicates that sulfur is more prevalent in sedimentary rocks on Mars than it is on Earth. Gamma Ray Spectroscopic (GRS) data from the Mars Odyssey mission indicate a planet-wide concentration of ~1.76wt% (McLennan *et al.* 2010). This is consistent with the apparent absence of plate recycling on Mars, which on Earth operates to return sulfur to the mantle via subducted oceanic crust.

The purpose of this study was to determine the fO_2 conditions of the sulfide-sulfate crossover for a range of common silicate melts, to search for any influence over sulfur's speciation by major element composition. Although the fO_2 conditions of the sulfide-sulfate crossover have been

identified before (Carroll and Rutherford 1988, Jugo *et al.* 2010, Klimm *et al.* 2011), this study broadens the range of melts investigated, and directly compares different melt compositions equilibrated under the same conditions of oxygen and sulfur fugacity. For each of the conditions studied, sulfur speciation was investigated in each melt type using two independent methods: directly by XANES, and indirectly by applying a sulfide-capacity model to SIMS data on total sulfur concentration. The range of melts investigated includes a pair of putative Martian basalts, allowing constraints to be placed on the oxidation state of the ancient Martian mantle (the probable source for the Gusev crater basalts; see Chapter 1). In addition to speciation, the equilibrium sulfate and sulfide concentrations of the different magmas are explored, since these form the basis for most models of the solubility of these species in silicate melts.

3.3 – PREVIOUS WORK

3.3.1 Sulfur dissolution in molten silicates: A brief and broadly chronological review

3.3.1.1 Early determination of speciation by indirect methods

The study of sulfur dissolution in molten silicates was initiated by Fincham and Richardson (1954), who measured the sulfur concentrations of a range of synthetic melts after their equilibration with various sulfur and oxygen bearing gases. They investigated simple 2 and 3 component systems (CaO-SiO_2, MgO-SiO_2, FeO-SiO_2, CaO-Al_2O_3 and CaO-SiO_2-Al_2O_3) at a range of superliquidus temperatures (1350-1650°C) at one-atmosphere pressure. Oxygen and sulfur fugacity (the parameters of particular interest to them) were varied independently for each melt composition, using an H_2-CO_2-SO_2 gas mixture.

Fincham and Richardson were primarily concerned with the dissolution process (the chemical speciation and bonding site) for sulfur in silicate melts. For every melt composition they studied, they observed the same relationship between log fO_2 and the resulting sulfur concentration (expressed as a log): a V-shaped profile with a minimum centred at -5 log units fO_2 (0.4 log units above the FMQ buffer at 1500°C). This is shown in the upper plot of figure 3.3.1.1, which graphs the log S against log fO_2 for four suites of melts (represented by the crosses, dots, filled and unfilled circles), all equilibrated at a single fS_2, but various fO_2s. On such a chart, the existence of an equilibrium involving dissolved sulfur and gaseous oxygen ought to manifest itself as a linear relationship between these two variables, since the data points of each suite are essentially just different instances (or positions) of the same equilibrium. The presence of two separate trends, as exhibited by figure 3.3.1.1, implies that two separate equilibria govern sulfur dissolution, which dominate at opposite ends of the fO_2 range explored (either side of the observed minimum). Therefore, on the basis of this inflection in sulfur concentration, Fincham and Richardson (1954) proposed that sulfur can dissolve in molten silicate as either S^{2-} (sulfide) or SO_4^{2+} (sulfate), and that the concentrations of these species are determined by the following chemical equilibria:

$$\frac{1}{2}S_{2\,gas} + O^{2-}_{melt} = \frac{1}{2}O_{2\,gas} + S^{2-}_{melt} \quad (3.1)$$

$$\frac{1}{2}S_{2\,gas} + \frac{3}{2}O_{2\,gas} + O^{2-}_{melt} = SO^{2-}_{4\,melt} \quad (3.2)$$

To corroborate their suggestion, Fincham and Richardson used their experimental data to calculate equilibrium constants (slightly modified) for these reactions, and showed that these remained constant for each melt composition studied, as even as the fO_2 and fS_2 were varied (see figure 3.3.1.1, bottom). They termed these pseudo-equilibrium constants sulfide and sulfate *capacities*, (*Cs* and *Cs'*) defining them as:

$$log\,\mathrm{Cs} \;=\; log[\mathrm{S^{2-}}] \;+\; \tfrac{1}{2} log \frac{f\mathrm{O}_2}{f\mathrm{S}_2} \tag{3.3}$$

$$log\,\mathrm{Cs'} \;=\; log[\mathrm{SO_4^{2-}}] \;-\; \tfrac{3}{2} log\, f\mathrm{O}_2 \;-\; \tfrac{1}{2} log\, f\mathrm{S}_2 \tag{3.4}$$

Figure 3.3.1.1: The major findings from Fincham and Richardson's (1954) study. Note the V-shaped relationship between sulfur concentration and fO_2 in their figure 2a, and the constancy of the sulfide and sulfate capacities in their figure 2b. Their original captions are included to aid interpretation of the figures.

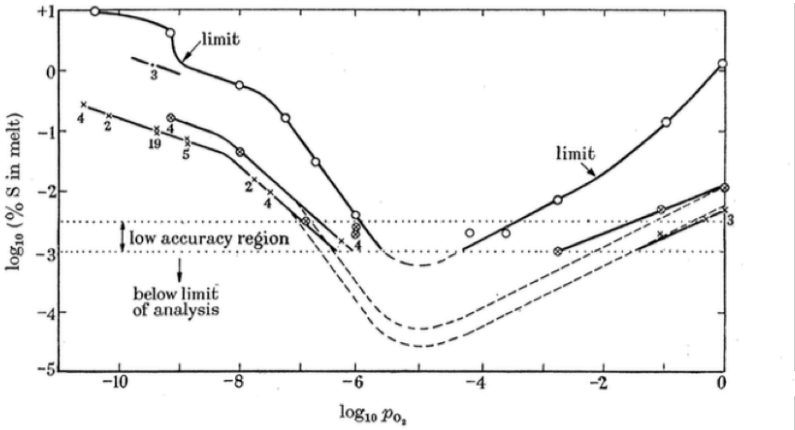


FIGURE 2*a*. Sulphur equilibria at 1500° C. The experimental points are joined by full lines. The dashed lines are extrapolations on the basis of the sulphur equilibrium constants. ×, *S*1, 1 % SO_2; ⊗, *S*1, 2 % SO_2; •, *S*5, 1 % SO_2; ○, *S*5, 2 % SO_2.

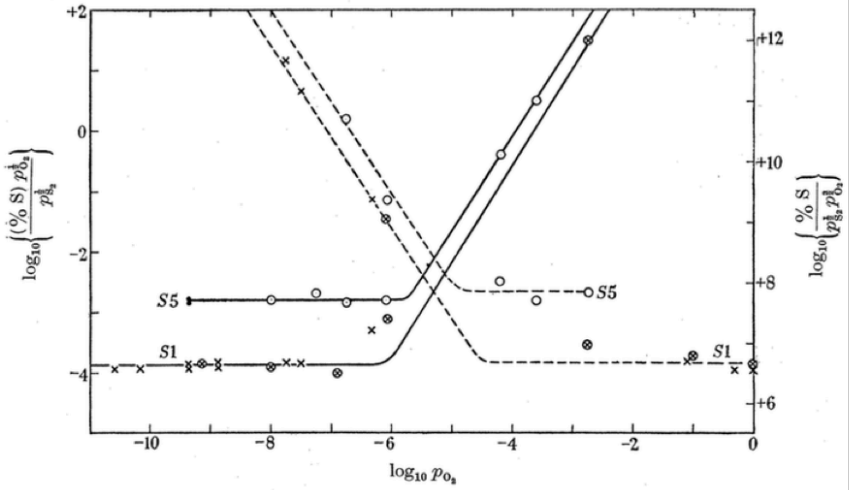


FIGURE 2*b*. The sulphide and sulphate equilibrium constants and the ranges of oxygen pressures over which they hold. All the sulphur is counted as sulphide for the full lines and as sulphate for the broken lines.

The useful feature of sulfide and sulfate capacities is that they remain constant for a particular silicate melt composition, provided that two assumptions are made; that the activity of oxygen in the silicate melt is unaffected by addition of sulfur, and that sulfur forms a solution in the melt whose activity coefficients are invariant (so called *Henrian* behaviour). These parameters therefore provide a way to empirically relate a melt's sulfur concentration to its major-element chemistry, and have formed the basis for all subsequent work on sulfur dissolution in silicate melts.

Fincham and Richardson also performed a more direct test of their assertion that distinct equilibria (involving distinct sulfur species) govern sulfur dissolution at opposite ends of the fO_2 range. They equilibrated two glasses of the same composition with S-bearing gases yielding contrasting fO_2s (-8 and -3 log units), and measured the resulting sulfur contents in both using two contrasting methods, one of which was insensitive to SO_4^{2-}. As expected, both methods reported the same value for the reduced glass, but different values (zero for the sulfate-insensitive method) for the oxidized glass. For this composition they were therefore able to confirm directly that more than one sulfur species is soluble in silicate melts.

3.3.1.2 Spectroscopic observations of speciation, and its dependence on fO_2

Fincham and Richardson's dissolution model predicts that silicate melts equilibrated at successively higher fO_2 conditions should experience a crossover between the dominance of reduced and oxidized sulfur. This prediction was decisively confirmed by Carroll and Rutherford (1985, 1987, 1988) who used the valence-dependent shift in the wavelength of sulfur's characteristic X-rays to directly measure the S^{6+}/S^{2-} ratio in natural and experimental glasses. This energy shift arises because oxidized sulfur's greater nuclear charge (and consequently inferior electron shielding) confers more energy to its orbitals than does reduced sulfur. This is expressed through the energy of its characteristic X-rays as a ~10eV positive shift in the Kα peak position. Carroll and Rutherford (1988) used an electron-microprobe to measure the position of the Kα peak in their glasses, and by assuming a linear relationship between peak position and species mole fraction, estimated the proportions of the reduced and oxidized species in their samples. The peak positions defining the fully reduced and fully oxidized end-members were obtained from synthetic iron sulfide and anhydrite standards.

Since fO_2 and melt composition were not co-varied in their study, Carroll and Rutherford were unable to locate the fO_2 conditions of the sulfide-sulfate crossover for each of their melt compositions individually (they studied a basalt, two andesites and a dacite). However, their aggregated results revealed a clear and sharp transition between sulfide- and sulfate-dominated sulfur (fig 3.3.1.2a), located between the fayalite-magnetite-quartz buffer (FMQ) and FMQ+2 log units of fO_2, confirming that fO_2 plays the dominant role in determining sulfur speciation. This role may be quantitatively expressed by the equilibrium reaction between sulfide and sulfate in silicate melts:

$$S^{2-}_{melt} + 2O_{2\,gas} = SO^{2-}_{4\,melt} \tag{3.5}$$

By defining an equilibrium constant for this relationship, and rearranging the associated terms, the sulfate/sulfide ratio can be expressed as a function of fO_2.

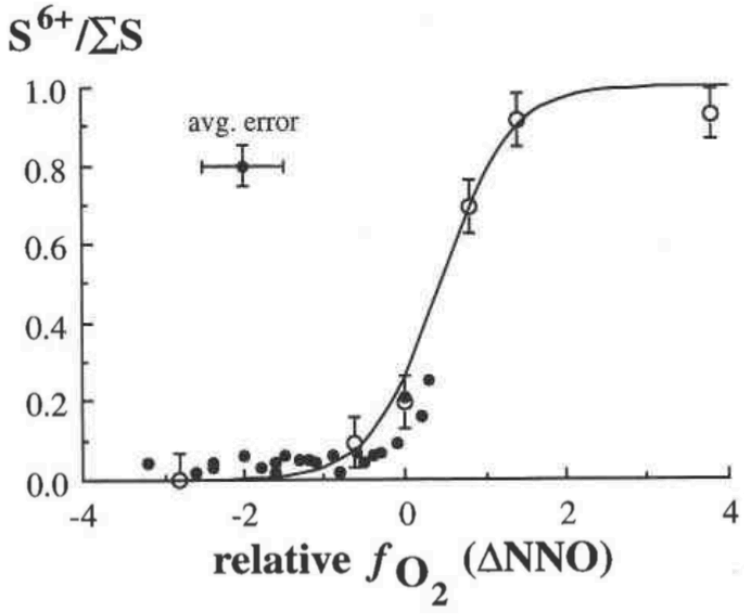
$$K = \frac{a\,SO_4^{2-}}{a\,S^{2-}\ fO_2^{\,2}} \tag{3.6}$$

$$log\frac{[SO_4^{2-}]}{[S^{2-}]} = log\,K + 2log fO_2 \tag{3.7}$$

Equation 3.7 assumes that sulfide and sulfate dissolve ideally in silicate melts, since the ratio on the left hand side is, strictly speaking, an activity ratio.

When the sulfate/sulfide ratio in equation 3.7 (rather then its log) is expressed as a sulfate mole fraction, and plotted against log fO_2, a sigmoidal shape emerges, consistent with the replacement of one species by the other. This relationship is clear from figure 3.3.1.2a (solid black line), which shows Carroll and Rutherford's original data and that of a later study.

Figure 3.3.1.2a: The replacement of sulfide by sulfate with increasing fO_2, illustrated by the EPMA peak-shift measurements of Carroll and Rutherford 1988 (open circles) and Wallace and Carmichael 1994 (filled circles). Although the general form of the relationship between the two species is clear, the steepness of the transition is inconsistent with the stoichiometry of reaction 3.5 (explained later). Figure taken from Wallace and Carmichael (1994).



Subsequent applications of the EPMA "peak-shift" technique to various natural and experimental compositions have confirmed the existence of this crossover between reduced and oxidized sulfur in many molten silicates (Wallace and Carmichael 1994, Metrich and Clocchiatti 1996, Jugo *et al.* 2005). Studies of this kind have further shed light on the identity of the sulfur species involved, generally shoring up the Carroll and Rutherford's original assumption (based on standard matching) that S^{2-} and S^{6+} dominate. Wallace and Carmichael (1994) ruled out the presence of significant S^{-} within reduced basalts, by showing that their sulfur Kα wavelengths lie closer to the value expected for S^{2-}, despite the very minor contamination by sulfate (indicated by vacuum distillation of similar materials). By demonstrating that hydrated basalts exhibit the same peak shifts as anhydrous ones, they also ruled out the presence of H_2S and HS^{-}.

Despite its success in confirming the existence of the reduced-oxidized crossover, the EPMA peak-shift approach suffers from severe limitations. The electron probe's energy resolution is inadequate to tell S^{6+} apart from S^{4+} for example, and at concentrations below around 500ppm the peak position cannot be measured at all. Most importantly however, evidence obtained more

recently (Jugo *et al.* 2010) indicates that the electron beam alters the sulfur oxidation state during analysis. These limitations have precluded use of the technique to confirm the identity of sulfur species beyond doubt, or to precisely determine the position of the crossover in fO_2 space.

Fortunately, with the dawn of the new millennium, a more sensitive approach to measuring sulfur speciation was demonstrated. Paris *et al.* (2001) used X-ray absorption spectroscopy to show that the energy of the sulfur K-edge[1] depends on sulfur's oxidation state, and that the ~12eV difference in edge-energy between sulfide and sulfate is easily resolvable with synchrotron radiation. This special case of X-ray absorption spectroscopy is called XANES (X-ray absorption Near-Edge Spectroscopy), and is explained in detail in section 3.5.4.2. In addition to precisely measuring the energy of sulfur K-edges (and thus providing a clear distinction between sulfide and sulfate) the shapes of the edges are recoverable by XANES, and these are also characteristic of the chemical species present (detailed examples are given later, in section 3.5.4.3). Correspondence between spectral features and chemical species can be established empirically through the use of standards, whose chemistry has been established by independent methods.

Paris *et al.'s* original (2001) XANES study examined a range of silicate glasses including those analyzed by Carroll and Rutherford (1985, 1988), and reported sulfide and sulfate to be the only species present. Additionally, they found good agreement with earlier S^{6+}/S^{2-} measurements made using EPMA. Metrich *et al.* (2002) applied K-edge sulfur XANES to olivine-hosted melt inclusions in hydrous basalts, and reported evidence for S^{4+} (sulfite) in addition to sulfate within their more oxidized samples. However, this was subsequently shown by Metrich *et al.* (2009) to be an analytical artefact, arising from photo-reduction by the X-ray beam[2].

The most comprehensive application of XANES to understanding the dependence of sulfur speciation on fO_2 specifically, was undertaken by Jugo *et al.* (2010), who obtained S^{6+}/S^{2-} ratios for natural and synthetic basalts equilibrated at closely spaced fO_2 conditions straddling the sulfide-sulfate crossover position. As in previous studies, they used standards of known speciation to assign chemical species to the features observed in their spectra. They obtained S^{6+}/S^{2-} ratios by treating their spectra as approximately linear combinations of those collected from their most reduced and oxidized samples (assumed to contain only sulfide or sulfate respectively).[3]

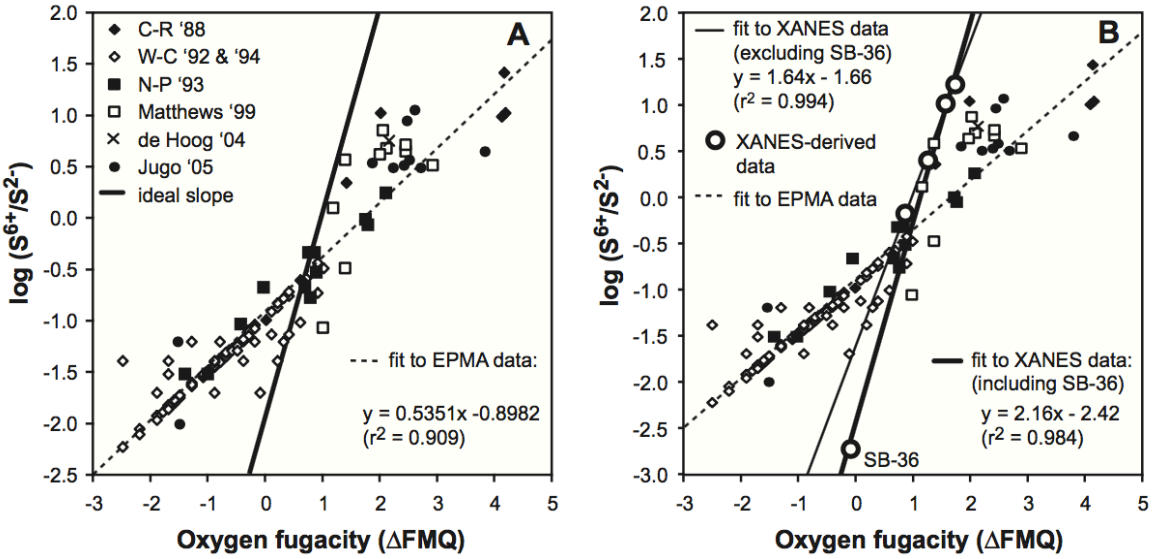
---

[1] This is the energy at which K-shell electrons may be ejected from an atom, causing a sharp rise in its X- ray fluorescence.

[2] This effect was also observed during this study, and measures for its suppression are described later.

[3] It is important to recognize that the errors associated with the ratio S^{6+}/S^{2-} are extremely large at very high and very low fO_2s. This did not preclude Jugo *et al.* (2010) from characterizing the sulfide-sulfate

Figure 3.3.1.2b: Compilation of EPMA and XANES-derived sulfate/sulfide ratios, graphed against log fO_2. To better illustrate the discrepancy between the measured and predicted rates of change, the log of the ratio is plotted. Panel A (left) shows EPMA data only, and Panel B (right) has the XANES data overlain. The dashed line is a linear regression to all data. The bold line is the 'ideal' slope which has the gradient of 2 predicted by the stoichiometry of equilibrium 3.5. Notice the closeness of the XANES data to this 'ideal' slope, in contrast to the data collected by EPMA. Figure taken from Jugo *et al.* (2010).



The most important finding by Jugo *et al.* (2010) concerns the rate of change of the S^{6+}/S^{2-} ratio with fO_2. This rate is governed by the stoichiometry of the sulfide-sulfate equilibrium relation (equation 3.5), specifically the co-efficient of O_2 in this equilibrium. This coefficient determines the constant of proportionality in the linear relationship between log S^{6+}/S^{2-} and log fO_2 (the gradient of the line in figure 3.3.1.2b). The reaction's stoichiometry requires a gradient of 2, whereas the gradient implied by data collected using EPMA is considerably shallower (approximately 0.5). By contrast, Jugo *et al.*'s (2010) XANES data define a slope with the predicted gradient, confirming that equilibrium 3.5 is indeed realized in silicate melts, and that the S^{6+}/S^{2-} ratios determined using EPMA are in error. Leading candidates for the source of this error are photo-reduction to form S^{4+} at high fO_2, and electron-exchange with iron at low fO_2, both promoted by the high intensity of the electron beam.

The most comprehensive study of sulfur speciation in silicates to date was undertaken by Klimm *et al.* (2012a, 2012b), who obtained XANES spectra for 4 different hydrous glasses: Soda lime

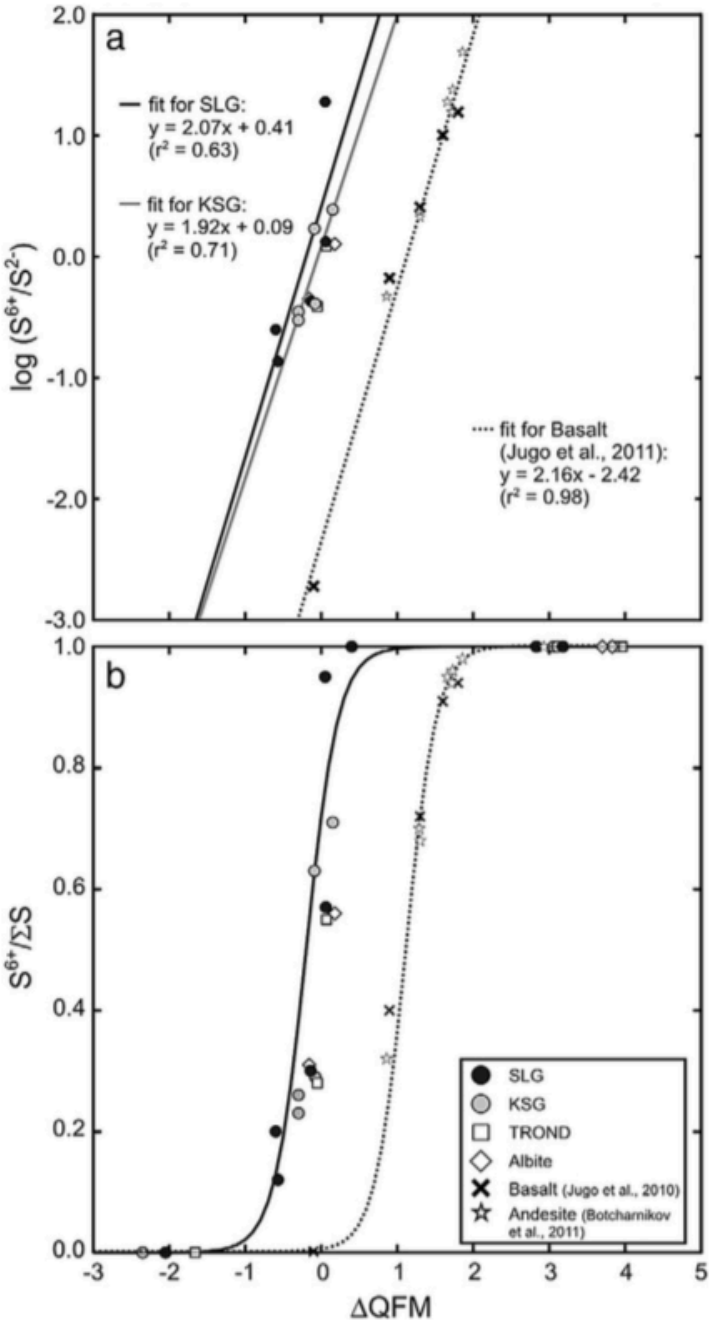
---

crossover near the fO_2 where it occurs, since it is only in this intermediate region that its exact value is important.

glass (CaO-SiO_2-Na_2O, abbreviated to SLG), $K_2Si_4O_9$ (KSG), albitic glass and trondhjemite glass. These were brought to equilibrium in cold-seal and internally heated pressure vessels at 200MPa at superliquidus or near-superliquidus temperatures. Sulfur was added to the experimental charges (in elemental form), and Fe_2O_3 was also added to some runs to investigate the effect of Fe. To corroborate the assumptions made by earlier studies about the correspondence between features at the sulfur K-edge and chemical species within their samples, Klimm *et al.* (2012a) obtained NMR and Raman spectra of their experimental products, in addition to their XANES spectra. For oxidized glasses they were able to correlate the sharp 2482eV "sulfate" feature in silicate glasses with a 990cm^{-1} Raman peak, associated with S-O bonding in silicates. The wavenumber of this Raman peak confirms that the sulfate ion is present in oxidized silicate melts as SO_4^{2-}. They further reported that under reducing conditions S occurs as S^{2-} if the melt is Fe-bearing, but as HS^- or H_2S if it is Fe-free.

In addition to their verification of the stable species in silicate melts, Klimm *et al.* (2012b) reported the first strong evidence for a dependence of sulfur speciation on melt chemistry; specifically, the stabilization of the S^{2-} ion by Fe. To test their suggestion, they compared the crossover fO_2s for their Fe-free glasses with those of the Fe-bearing basalts of Jugo *et al.* (2010). Their comparison (displayed in fig 3.3.1.2c) shows a ~1.5 log unit difference in crossover position; consistent with Fe playing a controlling role in sulfur speciation. Since the materials being compared here vary in ways other than Fe content, this shift in crossover position cannot be conclusively attributed to the presence of Fe (or indeed any aspect in the glasses' composition). Nonetheless, these observations are strongly suggestive of a major-element control over sulfur speciation, and clearly justify further study in this direction.

Figure 3.3.1.2c: The difference in fO_2 of the sulfide-sulfate crossover for Klimm *et al.* (2012b) and Jugo *et al.'s* (2010) glasses. Although the data are suggestive of Fe as the controlling element, the influence of other differences between these materials cannot be ruled out. The glasses studied by Kilmm *et al.* (12012b) were hydrous, and were brought to equilibrium under lower pressure and temperature than those of Jugo *et al.* (2010). Figure taken from Jugo *et al.* (2010).



3.3.1.3 Summary

Prior to this research effort, the following facts about sulfur speciation had been established. The stable species in silicate melts (both chemically simple melts and more complex natural ones) are the sulfide and sulfate ions. The mole fractions of these species in the melt are very likely governed by equilibrium 3.5, and consequently follow a sigmoidal relationship with oxygen fugacity (figure 3.3.1.2a). The inflection in this relationship (the sulfide-sulfate "crossover") is around 1.5 log units in width for all melts yet studied, implying approximately ideal mixing of sulfur in molten silicate. Circumstantial evidence exists that the fO_2 position of the crossover has some dependence on silicate melt composition. Although the identity of the controlling element(s) are not known conclusively, Fe is the leading candidate, apparently acting to stabilize sulfide in the melt, and thereby shifting the sulfide-sulfate crossover to more oxidizing conditions.

Motivated by these latter observations, this study explores compositional controls over sulfur speciation in more detail, considering a broader range of natural compositions, prepared in such a way as to isolate the effects of melt chemistry specifically. Since Fe has been identified as a being potentially influential, melts exhibiting a four-fold range in Fe concentration have been chosen. If Fe does play a dominating role in relocating the sulfide-sulfate equilibrium, this has clear implications for Martian magmatism, since Martian basalts are considerably more Fe-rich than their terrestrial counterparts. For this reason, two putative Martian basalts are included as part of this study.

3.4 EXPERIMENTAL METHODS

3.4.1 Choice of Melt Compositions

Silicate melt compositions were chosen so as to represent a broad range of terrestrial and Martian igneous rocks, with a particular emphasis on mantle melting. The Martian basalts were taken from the comprehensive experimental study of Bertka and Holloway (1994a, 1994b), and represent primary melts of the most widely accepted model for the composition of Mars' mantle. "JFR-4" represents a ~10% melt fraction, and "DWF-37" an approximately ~50% melt fraction. These experimentally derived compositions were used in preference to meteorite compositions since their genetic relation to the putative Martian mantle is known exactly – by contrast, none of the Shergottite meteorites, even the most apparently primitive, are uncontroversial primary mantle melts. The terrestrial basalts represent typical primitive and evolved melts of Earth's mantle. These were supplied by Andrew Matzen (personal communication). The primitive MORB (henceforth "PRI") was calculated by addition of olivine to an average MORB (from Gale *et al.* 2013) until equilibrium with Forsterite 90.5 was achieved at FMQ and 1 bar pressure. The evolved MORB (henceforth "EVO") was calculated by fractional crystallization of PRI until saturation with Fe-Ti oxides. The andesitic and dacitic melts ("AND" and "DAC") were taken from Carmichael *et al.* (1974), and were included so that comparisons could later be drawn with terrestrial arc magmas.

3.4.2 Experimental Procedure

The starting compositions for the six magmas studied are shown in table 3.4.2. Each was prepared from powdered oxides or carbonates (in the case of sodium and potassium) and mixed under ethanol in an agate mortar until fine and homogeneous. All of the component powders were dehydrated (oxides at 800°C, carbonates at 110°C) before weighing and combining them, to minimize weighing errors arising from unwanted water. Each mixture was also de-carbonated overnight (~12h) in air at 1000°C. An excess quantity of each mixture (6g) was prepared to further minimize weighing errors.

Experiments were conducted in a GERO 1-atmosphere furnace (figure 3.4.2a). Each experimental charge was suspended within the furnace on a loop of thin (0.25mm) wire. The charges were attached to the wire loops by mixing them with paraffin to form a thick fluid paste, which clung readily to the loop, courtesy of its surface tension. Once the charges were lowered into the

furnace the paraffin burned off, but remained long enough for the charges to melt so that their surface tension kept them adhered to the wire. For experiments run at fO_2s below FMQ, the loops were made out of rhenium wire, since rhenium absorbs very little iron under these relatively reducing conditions. For more oxidizing conditions (fO_2 greater than FMQ), rhenium's volatility made it unsuitable, and therefore platinum wire was used instead. Iron is significantly soluble in platinum so each loop had to be pre-saturated with iron. This was done by equilibrating each of loop with their silicate melt in a sulfur-free gas mixture of the appropriate fO_2, and then carefully removing the silicate melt with a razor blade before using them in their intended (sulfur-bearing) run.

An important requirement of this study was the exposure of each melt composition to the same conditions of temperature and fO_2, so that composition-dependent variations in sulfur redox state could be investigated. To achieve this, a chandelier was made from which all six charges could be suspended in the furnace simultaneously (figure. 3.4.2b). The chandelier was constructed from platinum wire and 2-bore alumina tubing, and suspended beneath the primary platinum hooks with a thin (0.12mm) platinum wire. All six charges were quenched simultaneously by passing a large current through this wire and melting it, causing the whole chandelier to fall into a beaker of cold water. Quench rates were in excess of 500°C/second (quench duration being approximately equal to the time taken for the chandelier to fall ~1m; from the furnace hot-spot to the beaker of cold water beneath).

The run conditions for the successful experiments are displayed in table 3.4.2b. In addition to those shown, many trials were carried out to optimize the bead sizes, choice of binding agent and loop and chandelier designs. In addition to these, many failures resulted from the use of inappropriate gas mixtures, which principally caused precipitation of elemental sulfur within the furnace tube, preventing a rapid exit of the chandelier into the water beaker (thus increasing cooling time).

Figure 3.4.2a: A GERO 1-atmosphere gas-mixing furnace of the type used for this study. The only feature not shown is the Sulfur-scrubber, which was attached between the bottom collar and the gas-out line.

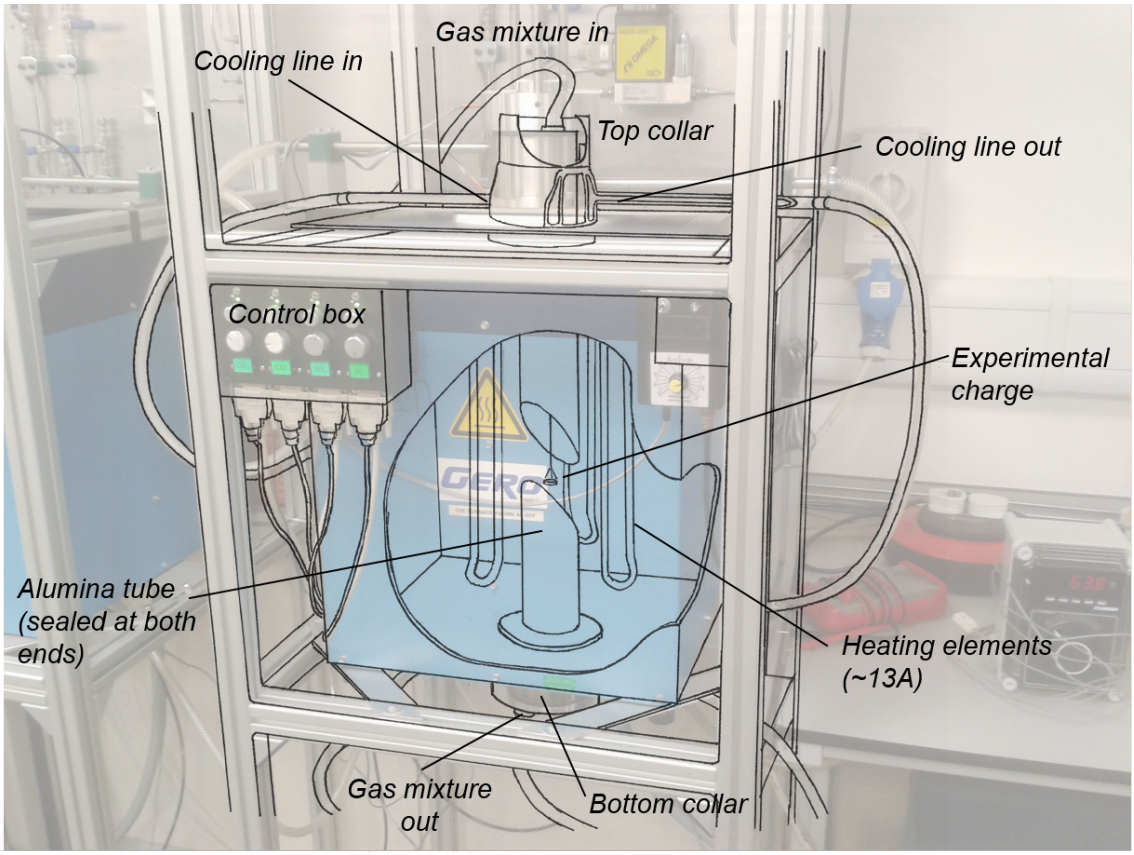


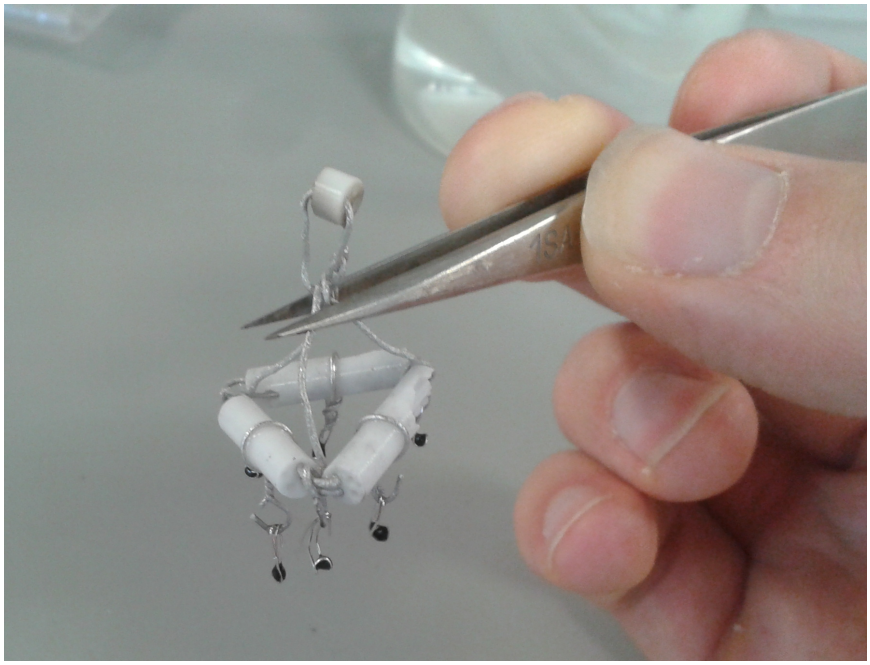
Table 3.4.2a: The six melt compositions prepared and equilibrated with sulfur in this study.

	wt % oxides										
Melt name	SiO2	TiO2	Al2O3	Cr2O3	FeO	MnO	MgO	CaO	Na2O	K2O	TOTAL
JFR-4	45.13	1.50	13.07	0.14	17.39	0.38	8.94	9.62	3.84	0.00	100
DWF-37	51.38	0.42	8.11	0.36	19.77	0.56	12.68	6.30	0.44	0.00	100
PRI	49.96	1.26	12.50	0.00	10.52	0.18	16.14	9.43	0.00	0.00	100
EVO	53.66	3.81	10.59	0.00	18.64	0.39	4.68	8.22	0.00	0.00	100
AND	55.02	1.33	17.43	0.00	8.75	0.15	4.43	8.04	3.73	1.13	100
DAC	64.19	0.65	16.83	0.00	5.07	0.11	2.14	5.58	4.02	1.41	100

Table 3.4.2b: Experimental conditions for the successful experiments (approximately the same number again were discarded either as trials or because they retained too few beads of melt). The sulfur and oxygen fugacities shown are those calculated for the gas mixtures used. For each run, all six melts were simultaneously subjected to the conditions listed, using the chandelier shown in fig 3.4.2b.

	Experimental conditions				gas mixtures			fugacities		
Experiment name	T (°C)	P (atm)	duration (h)	loop material	CO	CO2	SO2	*f*S2	*f*O2	*f*O2 (Δ FMQ)
SPE-1.67	1300	1	24	Re	152	99	48	-1.20	-8.97	-1.67
SPE-0.94	1300	1	12	Re	52	165	33	-1.80	-8.24	-0.94
SPE-0.7	1300	1	28	Re	50	188	62	-1.80	-8.00	-0.70
SPE-0.41	1300	1	16.5	Re	23	95	62	-1.81	-7.71	-0.41
SPE-0.19	1300	1	13	Re	25	85	153	-1.80	-7.49	-0.19
SPE-0.13	1300	1	16	Re	16	136	200	-2.30	-7.17	0.13
SPE+0.62	1300	1	12	Re	10	167	200	-2.85	-6.68	0.62
SPE+0.62pt	1300	1	12	Pt	10	167	200	-2.85	-6.68	0.62
SPE+1.04	1300	1	12	Pt	9	239	200	-3.50	-6.26	1.04
SPE+1.21	1300	1	12	Pt	10	355	200	-4.10	-6.09	1.21
SPE+1.6	1300	1	12	Pt	0	200	200	-5.00	-5.70	1.60

Figure 3.4.2b: The chandelier used to hang all 6 melts in the gas mixture simultaneously, shown just after its removal from the furnace. My thumb provides a convenient scale.



Every glass recovered from the furnace was mounted in epoxy, and the resulting solid mounts were ground with emery paper until their surfaces exposed a cross-section through each glass. The mount surfaces were polished with (1μm) microdiamonds on a lap, to flatten the surface as much as possible. The quality of each polish was assessed by reflected-light microscopy (pits and scratches appear as dark specks or lines when viewed under this illumination). Once sufficiently smooth, each mount was cleaned thoroughly with ethanol-wipes and compressed air.

3.4.3 Control of temperature and fugacity

Temperature was continuously measured using a Pt-Rh thermocouple, and controlled by setting the current through the furnace elements with Eurotherm 3204 controller.

The oxygen and sulfur fugacities (fO_2 and fS_2) were controlled by continuously fluxing appropriate mixtures of CO, CO_2 and SO_2 gas through the furnace. During each experiment, mixtures of these gases were flushed through the furnace in proportions that gave rise to equilibria with the desired fO_2 and fS_2 at 1300°C. The appropriate gas mixing ratios were calculated iteratively using the method of White *et al.* (1958), using a MATLAB script with thermodynamic data for the various species comprising oxygen, carbon and sulfur.

The flux of each gas through the furnace was set with a mass flow controller (MFC): an electronically controlled valve whose aperture is continuously adjusted in response to the flux reported by a built-in flow sensor. The operation of the MFCs is described in more detail in appendix 1. For each run, the desired mixing ratios of the different gases were set by adjusting their respective fluxes using their MFCs. Gas leaving the furnace was routed through a purpose-built scrubber that precipitated sulfur onto a matrix of wire-wool. This measure was taken to avoid blockage of the narrow gas lines with precipitating sulfur, and prevent back-pressure forming inside the furnace tube, which might interfere with the performance of the MFCs.

3.4.4 Choice of gas flux

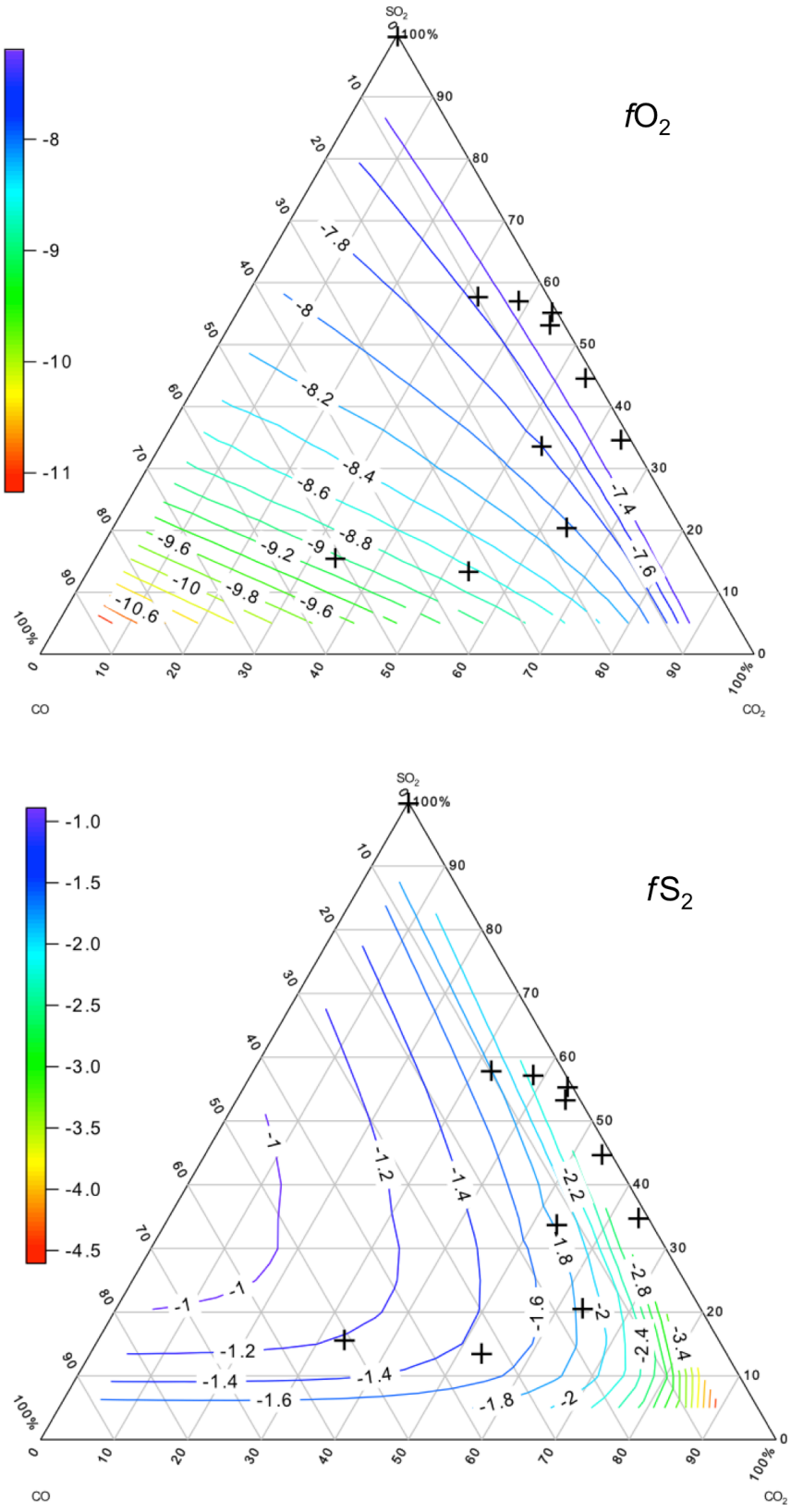
To obtain XANES spectra with the largest possible signal/noise ratios it was necessary to maximize the absolute sulfur concentrations in each of the glasses. Equilibrium relations (3.3) and (3.4) indicate that the concentration of dissolved sulfur increases with increasing fS_2, so we required gas mixtures which maintained the highest possible fS_2 at each fO_2 of interest. Unfortunately, the equilibrium relations for the CO-CO_2-SO_2 system are such that at fixed temperature and pressure, fS_2 and fO_2 cannot be arbitrarily or independently chosen by simply adjusting the gas mixture. In particular, the restriction that the furnace's total pressure cannot exceed one-atmosphere severely constrains the range of attainable fugacities, since any increase in one must be balanced by a decrease in the other. On top of this, an upper limit in fS_2 was imposed by the platinum holding the chandelier, which decomposed to form platinum sulfide if the ambient fS_2 reached the platinum-platinum sulfide buffer. At the conditions prevailing inside our furnace (1300°C, 1bar), this upper limit was -1.2 log units fS_2[4].

To assist in the selection of gas mixtures, fO_2 and fS_2 were contoured against the molar proportions of CO, CO_2 and SO_2 (see figure 3.4.4) at the desired 1300°C temperature. The fugacities shown were calculated from the equilibrium constants relating all of the possible gas species which could be formed from carbon, oxygen and sulfur at the required conditions. These calculations were performed and plotted using the MATLAB software package.

Our initial selection of gas mixtures was intended to give the same fO_2/fS_2 ratio, so that irrespective of the quality of the XANES spectra, the fO_2 position of the sulfide-sulfate crossover could be identified by any change in sulfur concentration with fO_2. However, most of the fS_2 conditions required by this strategy were higher than the aforementioned Pt-PtS limit. Therefore, this approach was abandoned in favour of maintaining the highest reasonable fS_2 for each melt.

[4] Use of H_2 gas to expand the range of achievable fO_2 and fS_2 conditions was not possible with the available laboratory configuration, and would have required modifications beyond the scope of this project.

Figure 3.4.4: Ternary diagrams showing the fO_2 and fS_2 for gas mixtures in the CO-CO_2-SO_2 system. The mixtures used in this study are indicated by the black crosses. Note the proximity of mixtures with the highest fO_2 to the CO_2-SO_2 join. The low CO concentrations required for these make them extremely challenging to produce with the MFCs available to this study.



It is clear from the contrasting geometries for fO_2 and fS_2 in CO-CO_2-SO_2 space that the required gas mixtures are somewhat squashed together, and pressed right up against the SO_2-CO_2 join. This is unfortunate because gas mixtures located closer to the edges of the ternary involve larger uncertainties, not only because small variations here translate into large variations in fugacity, but also because the performance of the MFCs deteriorate at low flow rates. The gas mixtures used in each experiment are displayed by the black crosses in figures 3.4.4a and b, illustrating the circuitous path taken across the mixture-space to achieve the desired fugacities.

During each experimental run, deposits of elemental sulfur precipitated near the top and bottom ends of the inside of the furnace tube. This necessitated regular cleaning of the extremities of the furnace tube and the wire wool inside the scrubber. As a safety measure, argon gas was pumped through the furnace after every experiment to prevent diffusion of SO_2 gas into the laboratory.

3.4.5 Experimental uncertainties

Errors in temperature, determined by the use of a second thermocouple lowered into the hotspot, were ± 3°C. The wire loops supporting each experiment were cut to a standard length to ensure that every melt experienced the same temperature, including melts equilibrated during different experimental runs.

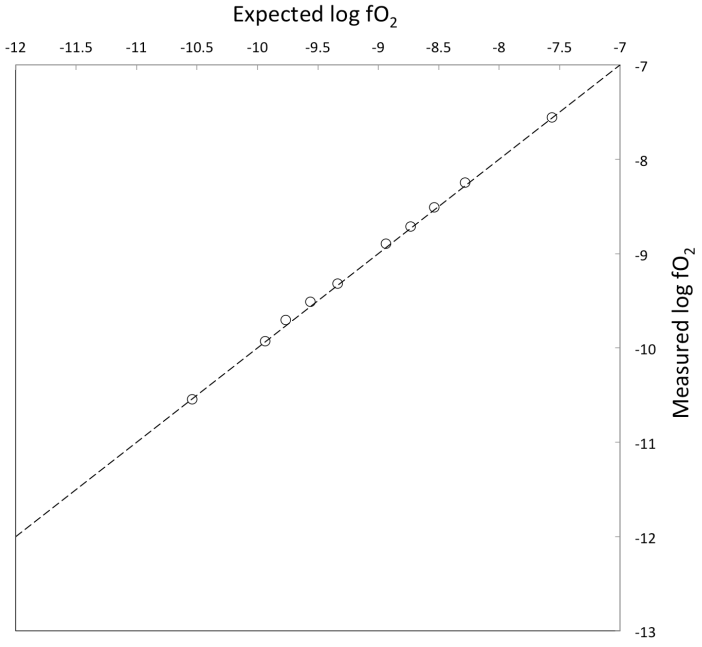
The uncertainty in fO_2 and fS_2 arises overwhelmingly from the uncertainty in the gas fluxes reported by the MFCs. Their accuracy is reported by their manufacturer's specifications as ± 1.5% for fluxes greater than 20mL/min, and ± 3% for fluxes lower than this value. The reproducibility is ± 0.5% of the maximum flow, so this comprises the largest contribution to the uncertainty for experiments performed using low fluxes. Critically, the gas flux reported by the MFCs becomes essentially unknown below around 5mL/min, because under these circumstances the gas flux through the capillary sensor (see appendix 1) is not laminar, and the feedback between the sensor and the valve becomes erratic.

To explore the potential for unobserved variation in fugacity, the specifications above were used to calculate the maximum and minimum possible fO_2s and fS_2s from each gas mixture, by computing the fugacities corresponding to every combination of erroneously high and low gas flow rates (max CO: max CO_2: max SO_2 through to min CO: min CO_2: min SO_2): essentially a calculation of worst-case scenarios. The variation about the expected fugacity never exceeded the 0.1 log units reported by the empirical test described below, except for one experiment, for

which a flow of 3ml(CO)/min was used. Since the errors associated with this experiment are so large (several log units) it has been excluded from the results presented later on (although it has been retained as a useable record of the differences in speciation between melts, since all of them were brought to equilibrium at the same fO_2, whatever it is!).

In addition to uncertainty in the gas flux, a further potential source of error is the quality of the furnace seal, since any leaks would introduce contaminants (most crucially oxygen) into the furnace tube. To search for leaks, and to experimentally verify the performance of the MFCs, a series of direct fO_2 measurements were made using a Y-Zr electrochemical sensor. Various gas mixtures were set using the MFCs, and the expected fO_2 compared with that reported by the sensor. Ideally, sulfur fugacity could also have been measured directly in this way, but since SO_2 gas in known to damage the Y-Zr sensor, only measurements of fO_2 were possible. The performance of the SO_2 MFC was assumed to be the same as those controlling CO and CO_2. This series of test measurements indicated no leaks, and confirmed that the fO_2 reported by the gas mixtures was never grater than 0.1 log units from the "real" measured value: the average error being 0.03 log units. Therefore, 0.1 log units is the error in fO_2 and fS_2 adopted for the presentation and interpretation of the results later on.

Figure 3.4.5: Mass Flow Controller calibration. This is a comparison between the expected fO_2 (the value implied by the mass flow controller readings) and the actual fO_2, measured in-situ using a Y-Zr sensor. The dashed line indicates the ideal 1:1 relationship.



3.4.6 Attainment of Equilibrium

To determine the time required for the melts to reach equilibrium with their gas mixtures, several "time-series" of experiments were performed. The time-series melts were left to equilibrate for 2, 8, 12 and 24 hours in the same gas mixture, and their sulfur concentrations measured after their quenching in water. These experiments were performed using exactly the same methodology as the main experiments, but on beads of significantly larger size so as to ensure that the durations obtained were conservative. Two separate time series were performed, one with the JFR (basaltic) melt and the other on the dacitic glasses, to ensure that the equilibration times obtained were valid for the full range of melt compositions.

The sulfur concentrations in the glasses were determined by SIMS (described later). Five analysis spots were positioned in a line from core to rim to evaluate the homogeneity of each bead of glass. The averages of these are displayed in the figures below. The sulfur concentrations for both time-series are shown in figures 3.4.6a and 3.4.6b. The 8-hour experiment for the JFR melt was not recovered from the furnace and is therefore missing from the figure.

Figure 3.4.6a: Time-series for the JFR melt composition. The glass from the 4 hour duration experiments was not recovered from the furnace, having presumably dropped off the chandelier.

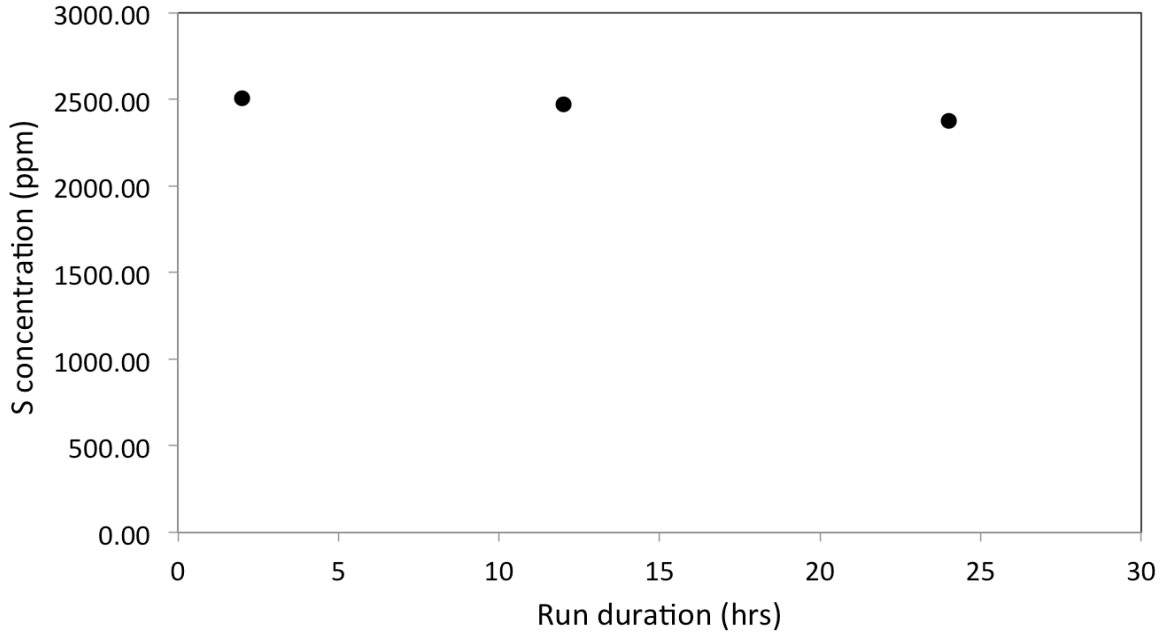
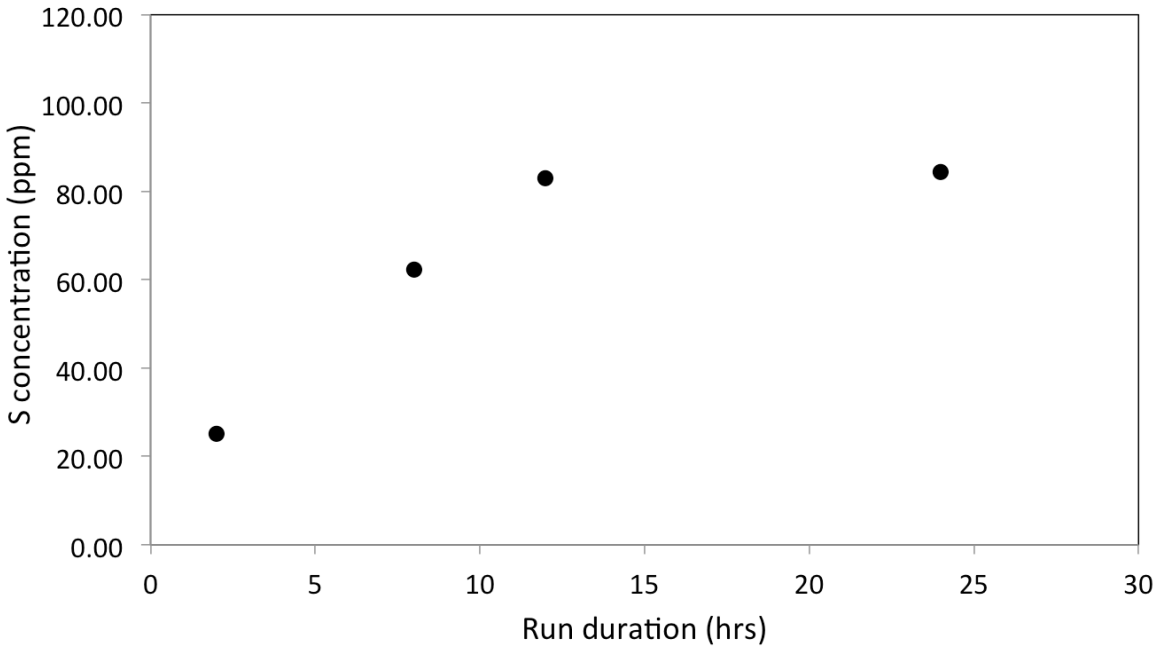


Figure 3.4.6b: Time-series for the DAC melt composition. Diffusion of sulfur through this melt is clearly slower than it is through the more basaltic melts studied.



Comparison between these two figures indicates that the basaltic glasses reached equilibrium significantly faster than the dacitic glasses (within 2 hours, rather than 12). Nonetheless, the minimum duration of the main experiments was 12 hours (see table 3.4.2.b), so all can be considered to have reached equilibrium. This view is further supported by the minimal variation observed in the sulfur concentrations measured for the individual glasses.

3.5 ANALYTICAL METHODS

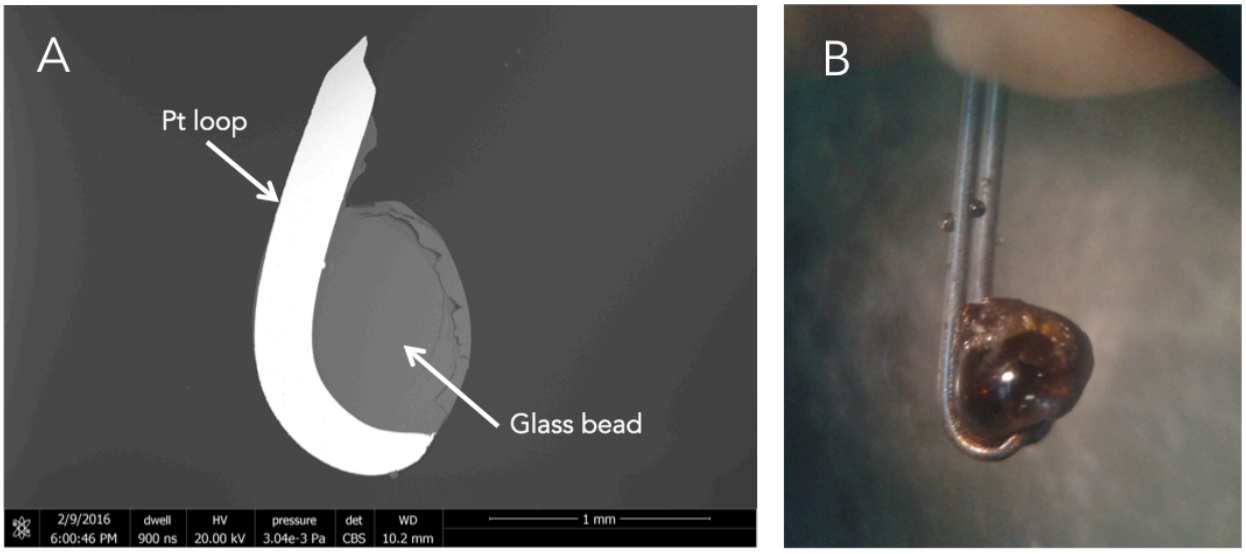
3.5.1 Overview

The major-element composition of each glass was determined by wavelength-dispersive X-ray spectroscopy (WDS) using an electron-microprobe. Sulfur speciation was investigated using X-ray absorption spectroscopy (XAS), as well as results derived from absolute sulfur concentrations determined by secondary-ion mass spectrometry (SIMS), which are explained in detail later. A scanning electron microscope was used to image each of the glasses to search for phases other than the expected quenched silicate phase. These images also served as maps for navigation when performing SIMS analyses.

3.5.2 Imaging of glasses by SEM

Backscattered Electron and Secondary Electron images were obtained for every glass using an FEI Quanta FEG 650, scanning electron microscope at the Oxford University Earth Sciences Department. A typical glass is shown in figure 3.5.2.

Figure 3.5.2: Quenched melts, imaged using BSE (fig A) and with an optical microscope (B).



BSE images of a sulfur-free pilot experiment (comprising simple melting and quenching of each composition at 1300°C) indicated that the high melt-fraction Martian basalt "DWF-37" had crystallized olivine. The co-existing melt was analyzed by electron microprobe and its composition used in preference to the initial DWF-37 composition during subsequent experiments. The composition shown in table 3.4.2 is this new composition, which is molten or nearly molten at 1300°C.

Images of the sulfur-bearing glasses confirmed that very few contained additional phases besides glass. The only contaminants observed were minor crystals of olivine in a few of the DWF-37 glasses (which exerted a negligible effect on melt chemistry), and sparse blebs of sulfide in some of the Primitive MORB glasses. These are puzzling because at the conditions studied, these melts are not expected to have reached sulfide saturation. Of the four basalts they are the most FeO poor, and (as discussed later), FeO is known to increase the solubility of sulfur in basaltic melts. However, sulfide blebs were not observed in the andesitic or Dacitic glasses, which contain even less FeO. Since these blebs are small and sparse – and therefore do not interfere with analysis of the glass – they do not adversely affect the foregoing study into speciation.

3.5.3 Major element analysis by WDS

Glasses were analyzed using the JEOL 8600 Electron Microprobe at Oxford University's Research Laboratory for Archaeology and the History of Art. All analysis was conducted with an accelerating voltage of 15kV and a beam current of 20-60nA. A defocused beam (5μm in diameter) was used to reduce the X-ray intensity and thereby minimize beam damage. Primary standards were provided by wollastonite for Si and Ca, periclase for Mg, hematite for Fe, jadeite for Al and Na, fowlerite for Mn, chromium metal for Cr and rutile for Ti. A well-characterized almandine served as a secondary standard.

In addition to determining the major element compositions of the glasses, an attempt was made to determine their sulfur concentrations with EPMA. However, only the group brought to equilibrium under the most reducing conditions contained sufficient sulfur to be detectable in all six glasses, the detection limit of the instrument being 30ppm. Sulfur concentrations for the rest of the glasses were investigated using SIMS, and these analyses are described in the next section. Galena and Barite were used as primary standards for calibration, and a sulfide-bearing glass of basaltic composition (L17) was used as a secondary standard.

3.5.4 Analysis of sulfur by XANES

3.5.4.1 Overview

XANES was used to determine the speciation of sulfur within every glass recovered from the furnace. XANES is a variant of X-ray absorption spectroscopy (XAS). Since it is relatively new to the geological sciences, and since a thorough understanding is necessary to interpret the spectra presented later on, it is explained in detail in the succeeding section.

3.5.4.2 Introduction to X-ray absorption spectroscopy (XAS)

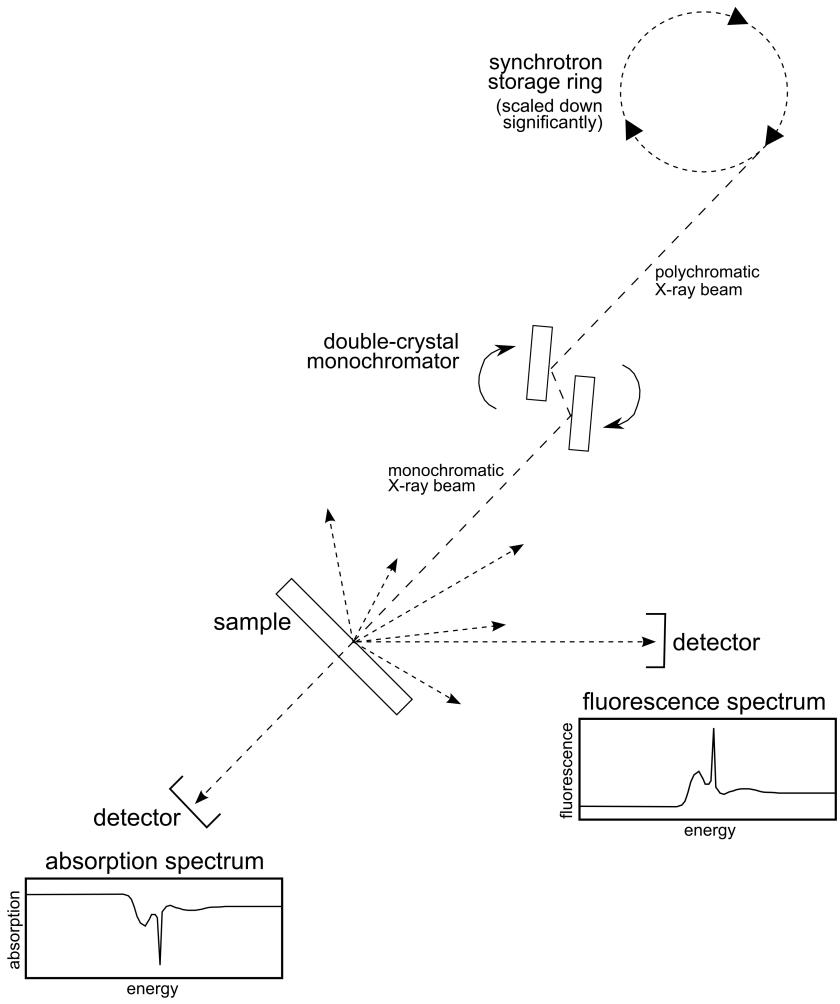
X-ray absorption spectroscopy (XAS) is a non-destructive analytical technique sensitive to chemical speciation. The following description begins by drawing parallels with WDS since both techniques rely on the same physical processes (electron-X-ray interactions), and since comparing the two clarifies the need for XAS.

As with WDS, XAS exploits the correspondence between characteristic X-rays and specific electronic transitions within a material. Both techniques use these characteristic X-rays as monitors for the presence of particular electronic orbitals (or pairs of atomic orbitals) within a sample. Since orbital energies are element-specific, an element's abundance can be determined by simply counting the appropriate characteristic X-rays, and comparing the number of counts obtained with that acquired for some standard material. This counting and comparing procedure is the basis for WDS, which disperses X-rays emitted by an excited sample through a crystal so that only those with the characteristic energy of interest reach a detector. The energy resolution attainable with WDS is limited by the thermal stability, purity, and defect-density of the crystal used for dispersion, and is typically around 5eV, which is more than adequate for locating peaks on which to carry out this counting procedure. But it is insufficient for precisely measuring peak energies or characterising their shape.

XAS however is far more discriminating, and its superior energy resolution yields information about the electronic structure surrounding the elements in a sample; in particular their valence state and bonding geometry. This information is available because the character and geometry of bonding marginally alter the energies of any electronic orbitals involved. The most informative transitions in this regard are electrical excitations between shells and the unbound state, (rather than those between shells) and therefore these are the transitions typically monitored by XAS.

The analytical procedure for XAS is as follows. A monochromatic X-ray beam illuminates the sample, which absorbs and re-emits some of the X-rays at a new wavelength. The wavelength of the beam is incrementally shortened, and the sample's response (absorption or fluorescence) recorded for each successive wavelength. Two configurations are possible: one in which the detector is placed behind the sample, and used to monitor its absorption of the beam (absorption mode); and another in which the detector faces the illuminated surface of the sample and monitors its fluorescence (fluorescence mode). These alternative configurations are shown in fig 3.5.4.2a. Since fluorescent X-rays ultimately result from absorbed X-rays, both approaches monitor the same process, and the spectra they generate are the inverse of each other. That the technique is referred to as XAS rather than XFS merely reflects a bias in popularity of the two approaches, rather than any difference in their principles of operation.

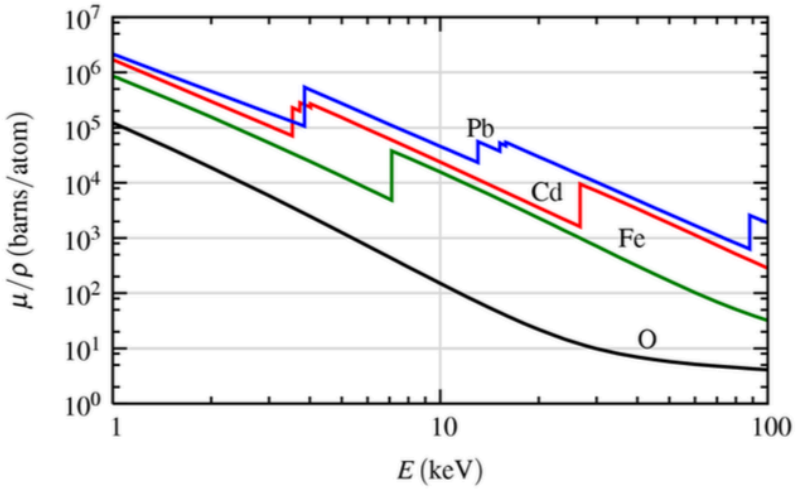
Figure 3.5.4.2a: The configuration for analysis by XAS.



The X-ray absorption by a given material is a smooth function of the incident X-ray energy (across most of energy range – see fig 3.5.4.2b). This smooth drop in absorption with increasing energy follows an inverse cube law, but is punctuated by sharp steps called "absorption edges". Edges occur when the incident X-rays have precisely enough energy required to remove electrons from a particular shell, and in doing so they are strongly absorbed (this is referred to as an *excitation*). Excitations leave vacancies in the shell from which the electron originated, which are promptly filled by electrons decaying from elsewhere - either higher shells or the unbound state. These decays are accompanied by the emission of fluorescent X-rays. Since the energies of atomic shells element specific, so too are edge energies. Edges characteristic of a given element are named after the shell from which the electrons are excited, so for example the Fe K-edge refers to the energy difference between an iron atom's core (K) shell and the unbound state. Edge energies for elements heavier than sodium are very high (e.g. 2.4kV for the Sulfur K-edge), necessitating the use of synchrotron radiation as an X-ray source.

The extremely fine energy resolution required for monitoring variations in edge energy is achieved by diffracting the X-ray beam through a monochromator: a pair of extremely pure silicon crystals, whose apparent lattice-spacing is finely adjusted by changing their orientation to select the appropriate Bragg angle. Although continuous, the range of energies collected by the X-ray detector is bounded. This is called "windowing", and is necessary to ensure that features in the spectrum arise exclusively from electronic transitions originating from a particular element within the sample. Windowing is important because in addition to fluorescent X-rays, scattered X-rays can make a substantial contribution to the measured intensity, and interfere with the absorption spectrum.

Figure 3.5.4.2b: X-ray absorption spectra for a selection of elements. Incident X-ray energy is plotted on the x-axis, and spans an enormous range (hundreds of times that of a typical XANES spectrum). The y-axis is a normalized absorption coefficient, which quantifies to the proportion of X-rays absorbed by the material (higher values correspond to greater absorption). Note the discontinuous absorption edges. XANES entails making very high resolution scans across these, to measure very subtle changes in their energy and shape. Figure taken from Newville (2004).



3.5.4.3 Interpretation of X-ray absorption spectra

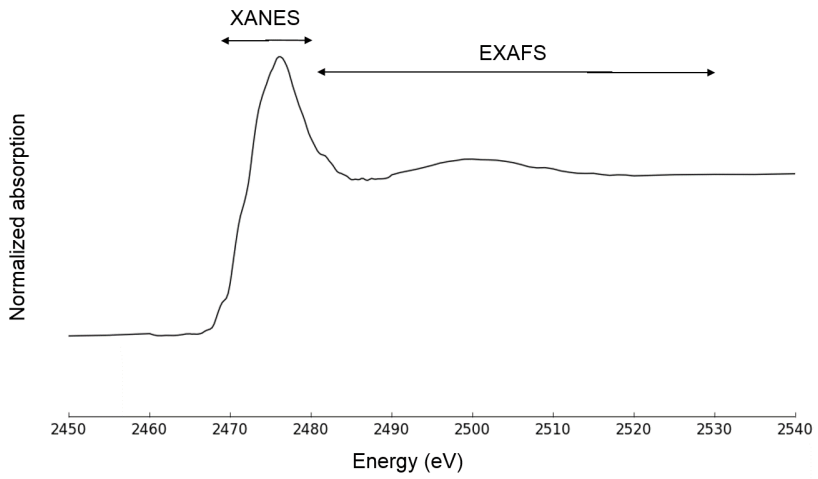
A XAS spectrum is essentially a time-series, showing the first appearance of an excitation as the energy of the incident X-ray beam is incrementally increased. Each point in the spectrum represents the sample's overall response (its absorption or fluorescence) to excitation by a specific energy, and the spectrum as a whole displays the relative sizes of many such responses. In other words, a XAS spectrum represents the correspondence between incident X-ray energy (the abscissa) and the number of allowed electronic transitions within the sample (the ordinate).

The spectrum may be divided into three regions: the *background*, the near-edge or XANES ("X-ray Absorption Near Edge Structure") region, and the post-edge or EXAFS ("Extended X-ray Absorption Fine Structure") region. These are shown for a typical spectrum in fig 3.5.4.3.

At any given energy, many types of photon-electron interactions take place. At energies lower than the edge, there is a "background" level of fluorescence, comprising thermal noise, braking radiation, scattered X-rays, and fluorescent X-rays induced by relatively low energy transitions (between the outermost atomic orbitals). When the incident X-ray beam energy reaches the edge, a series of more energetic transitions are permitted.

The edge energy is determined by the strength of the attraction between the nucleus and its orbiting electrons. More oxidized species (possessing greater effective nuclear charge) attract their K-shell electrons more strongly, shifting their K-edges to higher energy. The magnitude of this edge-energy shift scales with the difference in nuclear charge. The 8 electron contrast between S^{2-} and S^{6+} gives it an unusually large shift, making sulfur an ideal candidate for this technique.

Figure 3.5.4.3: A typical XAS spectrum, illustrating the XANES and EXAFS regions.



The object of XANES is to measure small variations in absorption arising from incremental changes in input energy near to the edge. Rather than taking the form of a simple step, edges often have a more complicated structure – typically a peak in absorption located at the edge, with "oscillations" in absorption occurring at higher energies (the so-called "Extended X-ray Absorption Fine Structure", or "EXAFS" region). EXAFS typically contains information about the identities of neighbouring elements, and is complex to interpret.

Without an exhaustive knowledge of every electronic transition happening inside each sample (there are rather a lot of these!), some useful conclusions can nevertheless be drawn. The strategy adopted in this study is to assume a correspondence between specific features of the edges and the chemical properties of the samples (the presence of particular ionic species). This approach is

essentially empirical, and relies on comparisons with standards of known composition and structure (outlined later).

3.5.4.4 XANES Analytical Procedure for the sulfur-bearing glasses

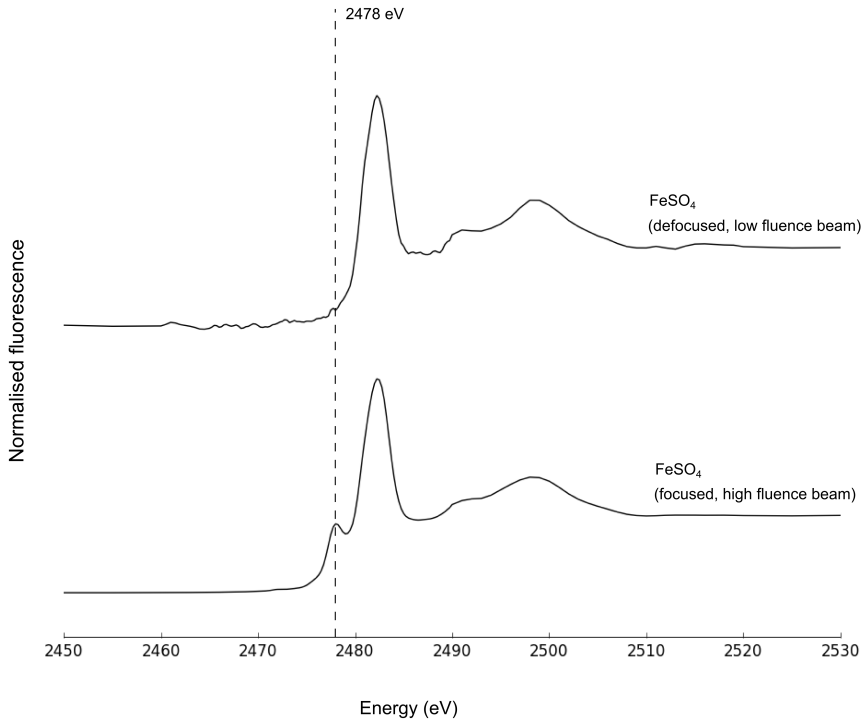
The glasses recovered from each experiment were analyzed by XANES at beamline I18 of the Diamond Synchrotron (UK). Spectra were obtained across the sulfur K-edge using the Si121 monochromator, with the instrument in fluorescence mode. The take-off angle was 40°. The energy step-size across the region of interest (the XANES region) was 0.25eV, although this was broadened to 5 eV at the extremities of each spectrum to minimize acquisition time while collecting sufficient data for good spectrum normalization. Time constraints prevented the collection of more than one spectrum per glass, although repeat analyses were collected on a few glasses to verify the instrument's reproducibility (the possibility of sample-heterogeneity having been eliminated previously by EPMA).

Previous experience with synchrotron radiation has shown that an intense X-ray beam can modify solid materials. In particular, the presence of a peak representing sulfite (S^{4+}) is clearly visible in a spectrum collected from our standards (fig 3.5.4.4), as well as those of previous authors (Jugo *et al.* 2010). A comprehensive investigation into the effects of beam damage was undertaken by Wilke *et al.* (2008), who concluded that both photo-reduction and photo-oxidation can result from irradiation with an excessively intense beam. By comparing spectra obtained using different beam conditions, (as well as spectra recorded for successive analyses of the same position) they showed the sulfite species to be a product of sample damage, rather an intrinsic feature of geological materials. This is in contradiction to earlier suggestions by Metrich *et al.* (2002) that sulfite might be an intermediate product of sulfur redox reactions. Wilke *et al.* (2008) eliminated these effects by continuously moving their samples beneath the beam.

The configuration of beamline I18 didn't permit movement of samples during analysis, so damage was suppressed instead by employing a defocused beam (a 50x50μm square) with the lowest possible fluence, and by positioning the detector as close as possible to the sample. Acceptable signal/noise ratios were achieved for these low intensities by enclosing the incident beam, sample and detector within a helium-filled bag, which minimized X-ray absorption by the ambient atmosphere. The effects of sample damage can be seen in figure 3.5.4.4, which presents two analyses of the same $FeSO_4$ standard, before and after the above damage mitigations had been made. Note the S^{4+} peak in the initial spectrum, indicative of photo-reduction of the $FeSO_4$.

Repeat analyses of a selection of other glasses confirmed the absence of any beam-induced damage.

Figure 3.5.4.4: Normalized XANES spectra collected under contrasting beam conditions. Note the absence of a peak at 2478eV in the spectrum collected using a low fluence, defocused beam. Note also the greater roughness in the "undamaged" spectrum, indicating that the overall signal/noise ratio was significantly reduced by the use of this softer beam.



3.5.4.5 Spectrum normalization

Variations in the glasses' sulfur concentration lead to greatly different amplitudes for their spectra. These variations in amplitude are not relevant to chemical speciation, which depends exclusively on the energies and relative intensities of the features at the sulfur edge. To assist inter-spectra comparisons, all have been normalized to their average post-edge intensity so that the differences in the amplitudes of their various peaks represent true variations in sulfur speciation. This practice of spectrum normalization is well established in the literature (Newville, 2004), and described in more detail in the following paragraphs.

Spectrum normalization comprises subtraction of the background, identification of the edge, and division of the whole spectrum by the intensity at the edge position. This has the effect of removing the slope, and rescaling each spectrum such that the post-edge region approximates a flat line of intensity 1. This procedure eliminates irrelevant differences between spectra, so that comparisons can be made concerning the two features of interest: the edge-step energy and the variations in edge shape that arise from variations in bonding geometry.

Normalization was performed using the software *Athena* (Ravel and Newville 2005). To remove the background, a polynomial function was fitted to the pre-edge region and subtracted from the spectrum. Maxima in the first-derivatives of the spectra were used to select an edge-step energy (E_0) for each spectrum. Two clusters of almost identical values resulted, consistent with the difference in sulfur oxidation state anticipated for the glasses. For consistency the same value of either 2471.5eV (dominantly reduced) or 2481.5eV (dominantly oxidized) was applied to every spectrum depending on its predominant oxidation state. A second polynomial was then fitted to the post-edge region, and the whole spectrum divided by the value of this polynomial at the edge energy (E_0), forcing the edge-step height of every spectrum to be one. The pre- and post-edge fitting parameters were defined individually for each spectrum, but followed specific criteria to ensure consistent feature matching.

3.5.5 Determination of total sulfur concentration by SIMS

3.5.5.1 Overview

Electron-microprobe analysis revealed the sulfur concentrations in almost all of the glasses to be lower than the instrument's detection limit (30ppm), necessitating analysis with a more sensitive technique. The Oxford University Earth Sciences department's in-house La-ICP quadrupole Mass Spectrometer was inappropriate because its mass resolution is inadequate to distinguish ^{32}S from $^{32}O_2$ (mass difference ~0.01 a.m.u.). This O_2-on-S interference is clearly a showstopper for samples which, like those collected here, contain more oxygen than anything else. Furthermore, the ICP's sampling laser ablates volumes of material typically more than 50μm in diameter, which is inappropriate for samples that occasionally contain small olivines or minor blebs of sulfide.

Therefore analyses were performed with Secondary Ion Mass Spectrometry (SIMS), a technique that combines the high mass resolution of a double-focusing magnetic sector spectrometer, with the high spatial resolution of a focused ion beam.

Previous attempts to measure sulfur by SIMS have largely focused on obtaining isotope ratios rather than absolute concentrations, but the analytical procedure is the same in both cases. The most important findings of these previous investigations have been the need for matrix-matched standards, to mitigate the uncertainty. The importance of sample structure in determining ion yield was elegantly demonstrated by Kozdon *et al.* (2010), who obtained different $^{34}S/^{32}S$ ratios for analyses made of the same isotopically homogeneous sphalerite crystal under different orientations with respect to the primary Cs^+ beam. This underscores the need to use standards as similar as possible to unknowns. The application of SIMS to analysis of sulfur in silicate glasses was demonstrated by Hauri *et al.* (2002), who used independently characterized standards to construct a calibration curve for S from the $^{32}S/^{60}Si$ ratio measured with SIMS. Hauri *et al.* (2002) reported detection limits for S routinely below <1ppm. An updated version of this calibration curve may be found in the brief but informative review by Ripley *et al.* (2011).

3.5.5.2 Analytical routine

Sulfur concentrations were obtained for each glass using the Cameca 1270 Mass Spectrometer at the Edinburgh Materials and Micro Analysis Centre (EMMAC) at Edinburgh University. A glass with a relatively high sulfur concentration (JFR-2, 2208ppm) was used as a primary standard, its sulfur concentration having been determined by WDS. (Viewed from this perspective, SIMS was essentially being used to lever down the detection limits of the electron-microprobe.)

A primary ion beam of Cs^+ was used to ablate the glasses, and secondary ions of ^{32}S, ^{18}O, ^{30}Si, ^{19}F and ^{12}C were detected by the spectrometer. Each analysis was preceded by a 30 second ablation with the primary ion beam, to locally remove the gold coat and expose the sample beneath. Each analysis comprised 20 separate 4-second cycles on each element. The count-rates recorded during these cycles were averaged and combined with an appropriate ion yield to calculate a concentration (details outlined below).

A sulfur blank was not measured since even the very lowest count rates measured greatly exceeded the background count rate of the electron photomultipliers. This is 1 count per minute according to the manufacturers' specifications, corresponding to a detection limit of 4 ppb.

3.5.5.3 Sample preparation

The ion probe's vacuum requirements are more demanding than those for the electron probe. Therefore the glasses were removed from their acrylic rounds (by bathing in acetone) and remounted in epoxy, which has a lower propensity to degas under high vacuum. After grinding and polishing with 1-micron diamond paste, a 30nm coat of gold was added to the surface of each sample.

3.5.5.4 Standardization

A well-established empirical approach was used to calculate sulfur concentrations from the count-rates obtained from the spectrometer. Accordingly, a linear relationship was assumed between the concentration of sulfur ([*s*]) and its count-rate (cps_S):

$$[s] \ \alpha \ cps_s \tag{3.8}$$

The proportionality constant for any such relation is element-specific (different elements are ablated with varying efficiency for a given ion beam), and is referred to as that particular element's *ion yield* (IY).

$$IY_i \ = \ \frac{cps_i}{[i]} \tag{3.9}$$

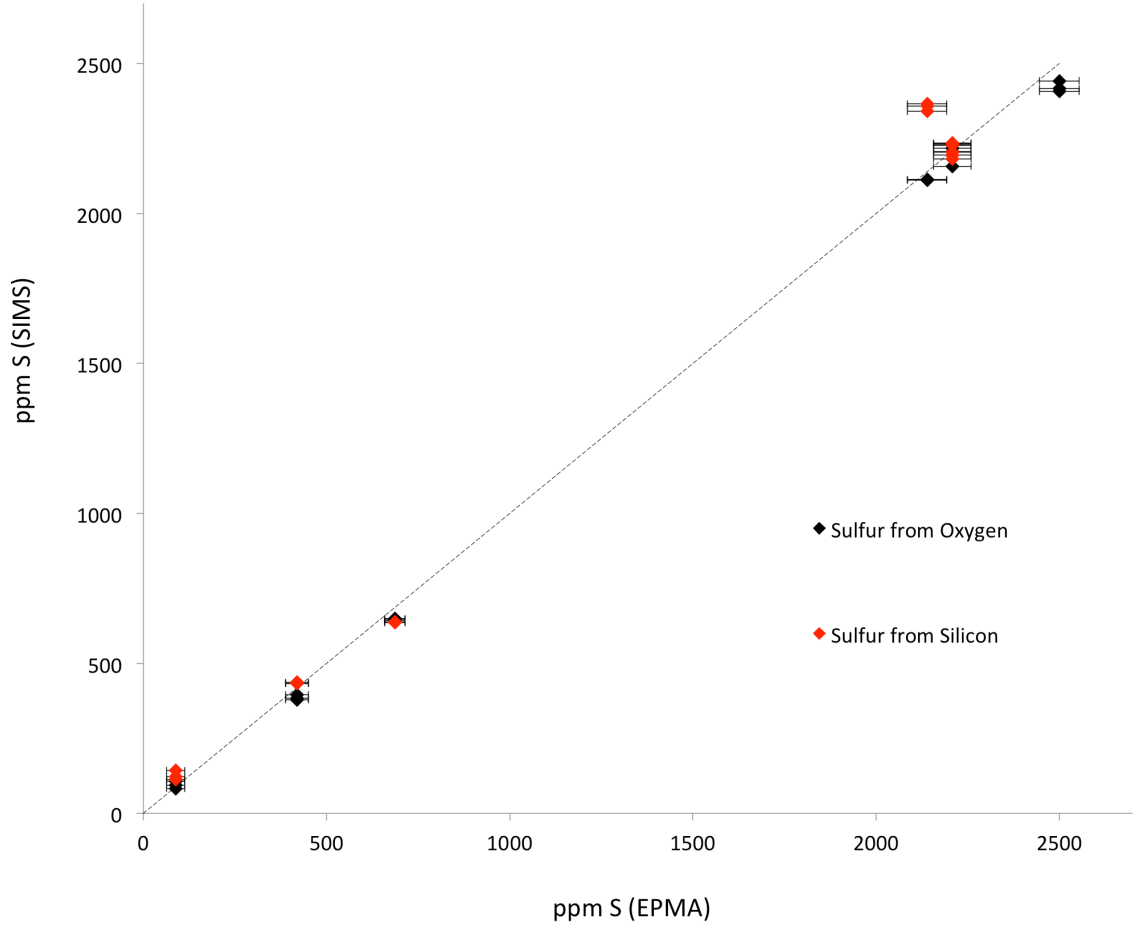
Ion yields are considered constant for a given material, but are known to be sensitive to atomic structure, since bonding type and geometry affect the efficiency with which material is disrupted by the primary ion beam. However, these effects are broadly systematic for pairs of elements, such that for many materials, ion yield ratios remain constant. Such ratios are called *relative ion yields* (*RIY*), and may be defined for any pair of elements, such as sulfur and oxygen for example:

$$RIY_{\frac{S}{O}} \ = \ \frac{IY_S}{IY_O} \tag{3.10}$$

To minimize analytical uncertainties, it is necessary to choose a "denominator" element whose concentration is relatively high and well known, in both the standard and the unknowns. Both oxygen and silicon were trialled as denominator elements, yielding relative ion yields calculated with respect to oxygen and silicon ($RIY_{S/O}$ and $RIY_{Si/O}$). These relative ion yields were then used to calculate the sulfur concentration in five additional secondary standards, whose sulfur concentration had been determined independently by WDS. The values obtained by SIMS using the oxygen and silicon relative ion yields are graphed against these "actual" values in fig 3.5.5.4, and the quality of each *RIY* as a measure of sulfur concentration are indicated by the proximity of

the sulfur concentrations obtained to the ideal (1:1) line. Both yields produce close fits, although oxygen is significantly superior to silicon. For this reason, all subsequent sulfur concentrations were obtained by combining the sulfur and oxygen count-rates with $RIY_{S/O}$.

Figure 3.5.5.4: Comparison between the sulfur concentrations measured by SIMS using relative ion yields (RIYs) based on silicon and oxygen. The sulfur-oxygen RIY offers a closer match across the whole range. Error-bars for sulfur determined by SIMS are smaller than the markers.



Since analysis of oxygen by EPMA is not straightforward, the oxygen concentrations used to calculate the relative ion yield were calculated by stoichiometry. This calculation is complicated by the need to determine the Fe^{3+}/Fe^{2+} ratio for each glass. This was done by applying the fO_2s recorded for each experiment to the model of Jayasuriya *et al.* (2004).

Since ion yields vary with atomic structure it is imperative to use standards that are structurally as similar as possible to the unknowns. The JFR melt composition equilibrated at the lowest fO_2

conditions ("JFR-2") was used as a primary standard, and the other five glasses equilibrated at the same fO_2 were used as the secondary standards against which the RIY was checked (fig 3.5.5.4). Since our primary standard (from which the ion yields were derived) shares its composition and structure with our unknowns closely or exactly, our standards fulfil the matrix-matching requirement satisfactorily, and this is further demonstrated by the relative invariance of the RIY for each of the six glasses analyzed.

3.5.5.5 Errors in Sulfur Concentration

The errors associated with an individual SIMS analysis derive from three sources: uncertainty in the count-rate reported by the instrument, uncertainty regarding the composition of the standard used to calculate the ion yield (the "primary" standard), and uncertainty arising from the different ablation propensities of the different glass types. This third source of error is referred to as the "matrix" uncertainty, since differences in ablation propensity derive from variations in material's atomic structure (or matrix). These three sources of error are combined in equation 3.11:

$$err\ (\mathrm{SIMS}) = conc\ \sqrt{err(countrate)^{\,2} + err(standard)^2 + err(matrix)^2} \qquad (3.11)$$

Each term inside the square-root is a value expressed as a fraction of the total, and each is described individually in the following text. Since their sizes vary from one glass to another, they were calculated and combined individually for each analysis.

Uncertainty in countrate

Uncertainties in count-rate obtained by SIMS are expressed using Poisson counting statistics, since the arrival times for ions at the detector are distributed randomly and uniformly over the duration of each analysis (thereby meeting the criteria for a *Poisson process*). The standard error on each measurement therefore closely approximates the square root of the number of counts collected. This varied from ~1.5 million to ~200, yielding errors between 0.5% and 5% relative (glasses with the lowest sulfur concentration exhibiting the largest errors).

Uncertainty in primary standard composition

The sulfur concentration of the primary standard was determined by EPMA to be 2208 ppm (by mass). Consistent with its importance as the standard for all of the SIMS data, 30 analyses were made on this standard, each with long counting times (4 minutes) on the sulfur Kα peak. To improve the counting statistics further, each analysis was acquired at 40nA (comparison with analyses acquired at lower beam currents having indicated no sample damage). The count-rate

obtained yielded a standard error of 3%. To assess the heterogeneity of the glass, analysis spots were widely distributed across its surface. The standard deviation among the analyses was 51ppm, equal to approximately 3% of the measured concentration. Since this value is no larger than the error arising from counting statistics, the glass can be considered homogeneous based on the resolution attained here. The error applied to the sulfur concentration of the primary standard is therefore 3% relative.

Matrix effects

The influence of a glasses' matrix on its ablation potential is expressed by its ion yield. Variations in glass matrix are therefore represented by variations in ion yield or relative ion yield. To assess the importance of matrix effects on the sulfur-oxygen *RIY*, the other five glass types were analyzed as secondary standards, and their sulfur concentrations were calculated using the RIY derived from the primary standard. The sulfur concentrations obtained are graphed against the "actual" sulfur concentration (measured by EPMA) in fig 3.5.5.4. Here, real deviations (outside the range of measurement uncertainty) from the "ideal" 1:1 slope indicate measureable matrix effects.

It is clear from figure 3.5.5.4 that for every melt type, the ideal slope lies inside the scatter among the sulfur concentrations determined by EPMA. This indicates that the influence of inter-glass matrix variations are too small to resolve by the techniques employed here, and that the matrix uncertainties cannot be larger than the uncertainty in the secondary standard's compositions, as determined by WDS. The RIY calculated for the primary standard is therefore appropriate for the other five glass types being analyzed, but the matrix term is set equal to the WDS uncertainty in each case.

3.6 ANALYTICAL RESULTS

3.6.1 Major-Element chemistry by WDS

The glasses' major-element compositions are presented in table 3.6.1a. Of this rather lengthy index of numbers, two observations are especially relevant. Firstly, repeat analyses of all glasses show them to be chemically homogeneous, indicating that each reached equilibrium with respect to their major-element chemistry. Secondly, the desired aim of producing glasses whose composition remains invariant across the whole fO_2 range was not achieved. Experiments conducted with platinum wire exhibit depletion in Fe, due to absorption by the wire, in spite of the efforts to precondition them beforehand. This depletion is most severe just above the FMQ buffer, and is less pronounced under more oxidizing conditions (consistent with Fe's lower solubility in platinum at higher fO_2).

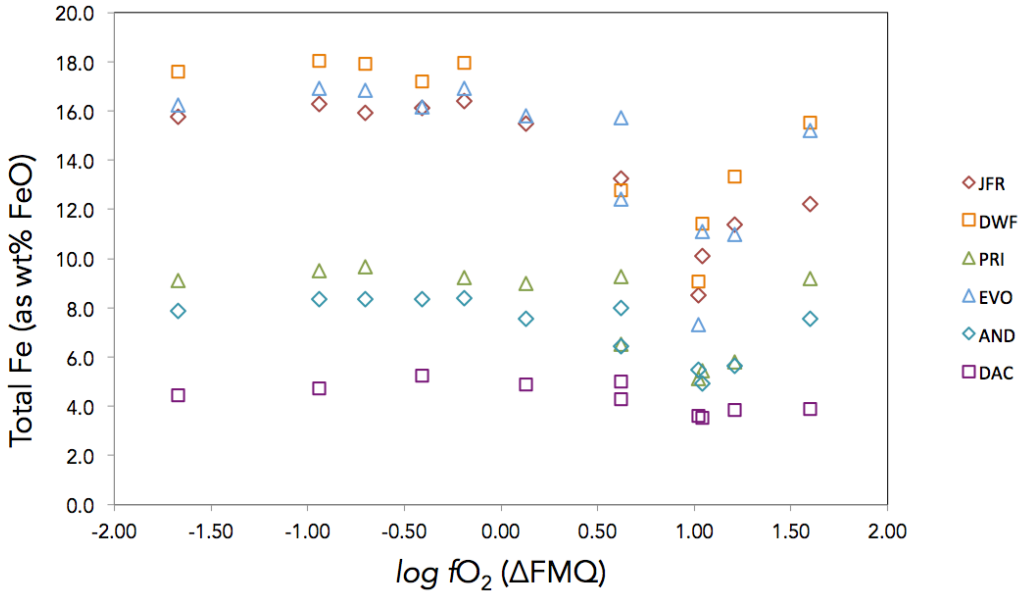
In some cases, totals for probe analyses are below the generally accepted minimum acceptable value (98%), and this is attributed to volatilization of Na by the electron beam or variations in carbon-coat thickness. These low totals could not be remedied by changing the beam conditions (even for very low beam currents), but in any case are not considered problematic, since they are not catastrophically low and only affect a minority of the samples.

Table 3.6.1a: Major-element analyses of sulfur-bearing glasses, determine by electron-microprobe WDS). Fe was measured initially as FeO, and the of FeO and Fe_2O_3 were determined using the Fe^{3+}/Fe^{2+} ratio, calculated from the model of Sack *et al.* (1980). This figure continues onto the succeeding page.

		wt% oxides										
*f*O2	Glass name	SiO2	TiO2	Al2O3	Cr2O3	Fe2O3	FeO	MnO	MgO	CaO	Na2O	TOTAL
-1.67	JFR	46.16	1.39	13.56	0.12	1.12	15.76	0.38	9.47	9.77	0.34	98.23
-1.67	DWF	51.44	0.38	7.96	0.31	1.18	17.60	0.53	13.09	6.40	0.43	99.52
-1.67	PRI	49.79	1.24	13.17	0.01	0.65	9.10	0.17	14.46	10.00	0.30	98.95
-1.67	EVO	52.99	3.47	10.71	0.01	1.14	16.24	0.38	4.80	8.16	0.50	98.56
-1.67	AND	56.31	1.25	17.86	0.01	0.53	7.89	0.14	4.64	8.12	1.55	98.32
-1.67	DAC	65.77	0.64	17.40	0.00	0.29	4.45	0.11	2.27	5.65	2.29	98.89
-0.94	JFR	46.51	1.53	13.32	0.14	1.59	16.27	0.38	8.86	9.95	0.05	98.61
-0.94	DWF	50.76	0.44	8.10	0.27	1.63	18.02	0.56	12.26	6.44	0.04	98.51
-0.94	PRI	50.00	1.27	13.30	0.01	0.92	9.50	0.18	13.79	9.87	0.02	98.88
-0.94	EVO	52.24	3.67	10.36	0.01	1.61	16.90	0.39	4.45	8.25	0.04	97.94
-0.94	AND	56.29	1.35	17.64	0.01	0.77	8.37	0.15	4.46	8.35	1.12	98.54
-0.94	DAC	66.13	0.66	17.05	0.01	0.42	4.74	0.10	2.10	5.73	1.98	99.08
-0.70	JFR	45.91	1.46	13.25	0.13	1.68	15.93	0.38	8.66	9.51	1.45	98.37
-0.70	DWF	51.24	0.41	8.24	0.26	1.61	17.90	0.56	12.17	6.39	0.01	98.79
-0.70	PRI	49.94	1.28	13.07	0.01	0.94	9.67	0.18	13.78	9.97	0.01	98.87
-0.70	EVO	52.29	3.64	10.34	0.01	1.60	16.83	0.39	4.44	8.23	0.02	97.79
-0.70	AND	57.64	1.34	18.02	0.01	0.71	8.35	0.14	4.38	8.27	0.04	98.91
-0.70	DAC	-	-	-	-	-	-	-	-	-	-	-

		wt% oxides										
*f*O2	Glass name	SiO2	TiO2	Al2O3	Cr2O3	Fe2O3	FeO	MnO	MgO	CaO	Na2O	TOTAL
-0.41	JFR	46.02	1.49	13.15	0.12	1.97	16.13	0.39	8.91	9.71	0.01	97.92
-0.41	DWF	51.25	0.41	7.78	0.25	1.96	17.21	0.56	12.40	6.39	0.01	98.23
-0.41	PRI	-	-	-	-	-	-	-	-	-	-	-
-0.41	EVO	52.55	3.64	10.27	0.01	1.95	16.18	0.39	4.47	8.19	0.01	97.67
-0.41	AND	56.69	1.37	17.79	0.01	0.90	8.35	0.15	4.45	8.26	0.01	97.98
-0.41	DAC	64.81	0.70	18.05	0.01	0.52	5.25	0.14	2.35	6.09	0.46	98.40
-0.19	JFR	45.39	1.49	13.29	0.10	2.24	16.42	0.41	8.81	9.58	0.00	97.74
-0.19	DWF	49.97	0.40	8.39	0.15	2.27	17.94	0.51	11.76	6.24	0.00	97.63
-0.19	PRI	48.82	1.30	12.82	0.00	1.27	9.21	0.16	13.95	9.75	0.01	97.31
-0.19	EVO	51.23	3.80	10.34	0.01	2.27	16.92	0.36	4.45	8.06	0.01	97.45
-0.19	AND	56.17	1.32	17.34	0.00	1.02	8.38	0.15	4.40	8.26	0.01	97.06
-0.19	DAC	-	-	-	-	-	-	-	-	-	-	-
0.13	JFR	45.90	1.46	13.17	0.14	2.40	15.48	0.37	8.85	9.68	0.01	97.46
0.13	DWF	-	-	-	-	-	-	-	-	-	-	-
0.13	PRI	49.21	1.28	12.96	0.01	1.39	8.97	0.18	14.03	9.80	0.02	97.85
0.13	EVO	52.48	3.60	10.22	0.01	2.38	15.79	0.38	4.45	7.97	0.01	97.30
0.13	AND	53.73	1.27	17.39	0.01	1.28	7.57	0.14	4.46	8.12	2.86	97.36
0.13	DAC	65.58	0.68	17.82	0.01	0.60	4.87	0.12	2.27	5.96	0.18	98.12
0.62	JFR	-	-	-	-	-	-	-	-	-	-	-
0.62	DWF	-	-	-	-	-	-	-	-	-	-	-
0.62	PRI	48.47	1.30	12.39	0.01	1.64	9.27	0.17	14.12	10.02	0.01	97.40
0.62	EVO	51.13	3.66	10.31	0.01	2.70	15.73	0.39	4.46	8.16	0.00	96.56
0.62	AND	56.18	1.38	17.62	0.01	1.23	8.01	0.15	4.51	8.37	0.01	97.47
0.62	DAC	64.10	0.67	16.74	0.01	0.76	5.02	0.12	2.30	6.02	1.09	96.85
0.62	JFR	45.87	1.49	13.48	0.11	2.47	13.25	0.41	9.07	9.82	0.96	96.95
0.62	DWF	53.95	0.43	8.42	0.20	2.10	12.79	0.60	12.91	6.83	0.02	98.26
0.62	PRI	50.00	1.27	13.42	0.01	1.14	6.51	0.19	14.60	9.98	0.01	97.15
0.62	EVO	54.03	3.72	10.97	0.01	2.14	12.42	0.39	4.66	8.47	0.02	96.83
0.62	AND	56.11	1.32	17.42	0.00	1.17	6.42	0.15	4.57	8.33	2.37	98.13
0.62	DAC	64.44	0.67	17.11	0.01	0.75	4.30	0.12	2.20	5.76	3.02	99.06
1.04	JFR	48.36	1.60	14.12	0.08	2.26	10.11	0.40	9.24	10.38	1.74	98.31
1.04	DWF	54.98	0.50	9.25	0.12	2.11	11.40	0.64	12.14	7.20	0.02	98.37
1.04	PRI	51.51	1.39	13.19	0.01	1.10	5.43	0.21	14.69	10.64	0.01	98.18
1.04	EVO	55.25	4.03	11.37	0.01	2.18	11.11	0.41	4.85	8.98	0.02	98.22
1.04	AND	57.12	1.39	18.06	0.01	1.06	4.92	0.15	4.32	8.25	3.10	98.83
1.04	DAC	65.19	0.68	17.32	0.00	0.69	3.53	0.12	2.20	5.95	3.02	99.31
1.21	JFR	46.89	1.56	13.53	0.07	2.95	11.38	0.43	8.85	9.95	2.37	98.00
1.21	DWF	53.52	0.46	8.71	0.10	2.75	13.33	0.60	12.57	6.61	0.12	98.79
1.21	PRI	51.63	1.37	13.26	0.01	1.31	5.79	0.22	14.28	10.39	0.01	98.28
1.21	EVO	55.61	3.88	11.33	0.03	2.41	10.97	0.41	4.66	8.74	0.03	98.07
1.21	AND	56.44	1.34	17.80	0.00	1.39	5.63	0.16	4.22	8.05	3.25	98.92
1.21	DAC	63.25	0.65	16.31	0.01	0.91	3.86	0.10	2.18	5.95	3.37	97.42
1.60	JFR	45.66	1.42	12.81	0.02	4.84	12.20	0.37	8.16	9.77	2.34	97.65
1.60	DWF	50.36	0.39	8.09	0.03	4.84	15.54	0.54	11.56	6.25	0.18	97.79
1.60	PRI	48.06	1.18	12.21	0.01	3.03	9.20	0.16	14.76	9.27	0.05	97.93
1.60	EVO	50.60	3.63	10.22	0.01	4.99	15.20	0.38	4.42	8.03	0.09	97.58
1.60	AND	53.63	1.27	17.07	0.01	2.81	7.56	0.14	4.16	7.80	3.18	98.30
1.60	DAC	63.76	0.65	16.98	0.01	1.36	3.88	0.11	2.11	5.78	3.44	99.06

Figure 3.6.1: Fe loss for the six melt compositions, plotted against their fO_2 of equilibration. Total Fe is expressed here as wt% FeO (no corrections have been made to the probe data). The precipitous drop in Fe concentration at FMQ+0.13 is evident, caused by the switch to Pt rather than Rh loops. This was in spite of efforts to pre-saturate the loops. This effect becomes less severe as conditions become more oxidizing, and the equilibrium concentration of Fe in the Pt is reduced.



Absolute sulfur concentrations were obtained by WDS for the most reduced group of glasses only, and are displayed in table 3.6.3.1b (SIMS section), since they are used for calibration of the ion-probe. As with the major elements, repeat analyses of each sample indicated no heterogeneity.

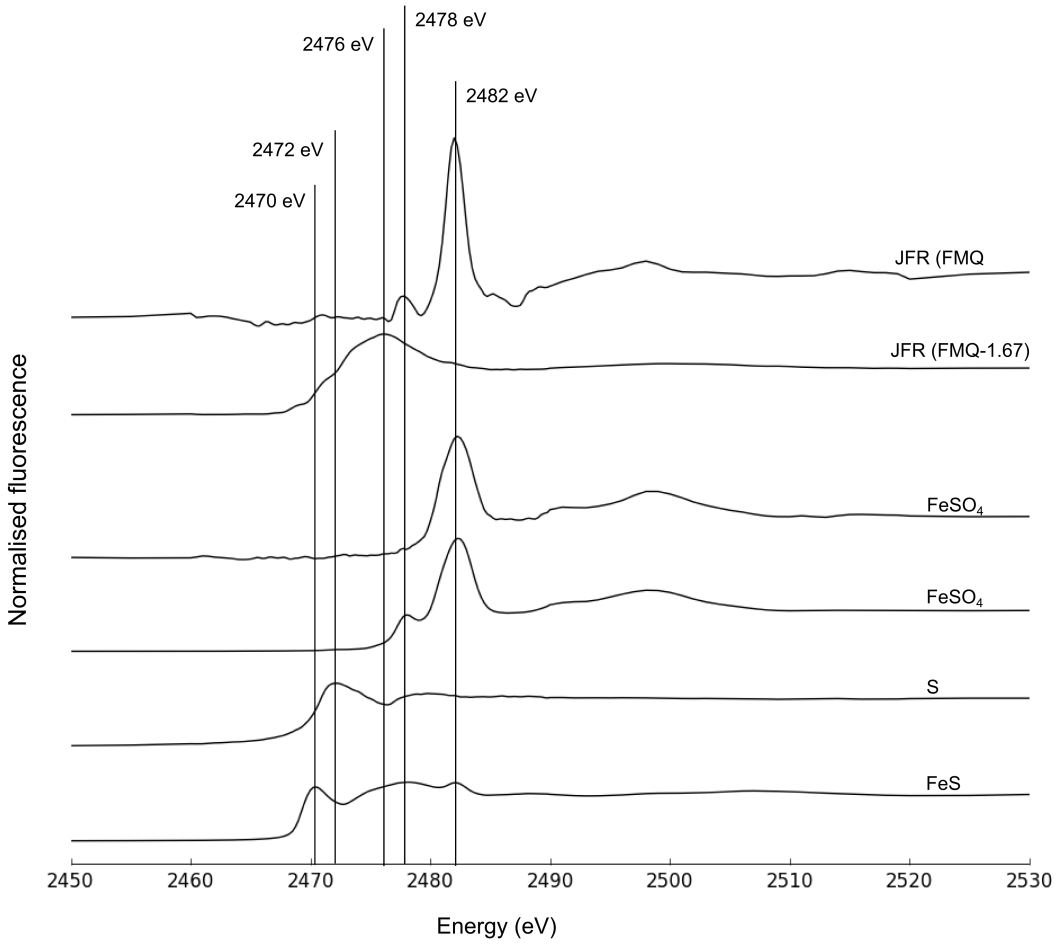
3.6.2 Sulfur Speciation from XANES

3.6.2.1 Reference Materials and Peak Interpretation

Following the methodology of previous researchers (e.g. Jugo *et al.* 2010) we have adopted an empirical approach to determining speciation, whereby we assume a correspondence between specific features of the spectra and the particular ionic species in the glasses. This correspondence is established through the use of our own standard materials (FeS, S and $FeSO_4$) and those of previous studies, in particular those of Wilke *et al.* (2011) and Klimm *et al.* (2011). The relevant standards are shown in figure 3.6.2.1, and their spectral features are described in the succeeding text.

The iron sulfide spectrum exhibits three distinct peaks: a fairly sharp one at 2470.4eV, a much broader one at around 2478eV, and a smaller peak at 2482eV. The 2470.4eV peak corresponds to 1s to 3p and 3d electron transitions (Wilke *et al.* 2011), and its amplitude in sulfides has been shown to depend on the cation that S^{2-} is bonded to; transition metal sulfides exhibit a large peak at this energy, and metals such as Mg and Ca exhibit none at all (Fleet 2005). The broader feature centred around 2478eV represents a combination of 1s to 3p transitions and multiple scattering resonances, and is always observed in metal sulfide spectra (Wilke *et al.* 2011). This is the feature that is considered diagnostic of S^{2-} within glasses (Jugo *et al.* 2010), although its structure can be complicated because it depends on the local bonding environment. The small peak at 2482eV shares its position with the 1s to 3p signature for sulfate, suggesting that our iron sulfide powder had undergone some minor oxidation.

Figure 3.6.2.1: Normalized spectra of standard materials. Peaks correlated with particular species are labelled, and described in detail in the text. Two glass spectra are included to illustrate the imperfect match between the FeS standard and S^{2-} peak (see section 3.6.2.2).



The iron sulfate spectrum has a sharp peak at 2482.3eV, which is characteristic of excitations from the sulfur 1s to the sulfur 3p and oxygen 2p orbitals of the SO_4^{2-} ion (Wilke *et al.* 2011). Spectra for sulfates analyzed by all previous workers have showed this feature, and its association with the sulfate anion is now well established in the literature. Furthermore, comparisons between XANES and Raman spectra of similar materials by Klimm *et al.* (2012) have correlated this feature with the 1000cm^{-1} Raman peak, which is considered characteristic of the tetrahedrally co-ordinated sulfate ion's $\nu 1$ stretching vibration. Two iron sulfate spectra are displayed in figure 3.6.2.1, illustrating the difference between analysis under a high and low fluence X-ray beam (the former resulting in partial photo-reduction of the glass, as evidenced by the nascent peak at 2478eV).

3.6.2.2 Qualitative Interpretation of XANES Spectra

All of the spectra collected are shown in figures 3.6.2.2a-f, grouped by glass composition; and again in figs 3.6.2.2g-l, grouped by fO_2. Figures a-f illustrate the progression in speciation from most reduced to most oxidized, and figures g-l permit comparisons between the glasses at each of the fO_2 conditions. An unfortunate outcome of the equilibria governing sulfur dissolution is that the glasses' sulfur abundances drastically decrease as their gas mixtures become more oxidizing[5]. Therefore, the spectra of glasses equilibrated at higher fO_2 are generally noisier, and their interpretation considerably less certain. In extreme cases no peak is detectable, and such spectra have been omitted from figures 3.6.2.2a-l. Nonetheless, useful inferences can be made from the spectra which are useable.

Two major spectral features are common to all six glasses at some point in their fO_2 range: a broad peak centred at 2476eV, and a sharper peak at 2482eV. The broad feature is attributable to dissolved S^{2-}, although it is displaced slightly from the peak in the iron sulfide standard. This is consistent with previous studies (Lennie and Vaughan 1996, Alonso Mori *et al.* 2009, Farrell *et al.* 2002, Fleet *et al.* 2005 Jugo *et al.* 2010), which have shown the shape and position of the sulfide edge to depend strongly on glass composition and sulfide bonding geometry. These variations are likely responsible for the two subtle shoulders at 2469eV and 2471eV. The sharper feature at

[5] As explained in the section 3.4.4, this is because gas mixture limitations prevented the use of arbitrarily high fS_2

2482eV is indicative of S^{6+}, coinciding exactly with the single sharp peak in the sulfate standard. Hence *S^{2-} and S^{6+} are the dominant species within the silicate melts*, as expected.

Furthermore, it is clear from figures a-f that as conditions become progressively more oxidizing, *each of the glasses undergo the expected transition between S^{2-} and S^{6+}*, indicated by the progressive growth of the "sulfate" peak at expense of the "sulfide" peak. This interpretation presumes a correlation between peak amplitude and abundance within the glass, which as well as being physically reasonable, has formed the basis for many previous applications of XANES to chemical speciation (e.g. Werner and Prietzel 2015, Jugo *et al.* 2010).

The spectra representing the most oxidized glasses (FMQ+1.6) exhibit a small peak at 2478eV indicative of the presence of minor quantities of sulfite. It is most likely that this is an analytical artefact resulting from partial photo-reduction by the X-ray beam. Damage tests performed prior to our analyses showed that this process does take place if the beam fluence is sufficiently high. Curiously however, the sulfite peak is not present in all of the sulfate-dominated spectra (FMQ+1 for example). This is inconsistent with the damage hypothesis unless the glasses susceptibility to damage is somehow dependent on their degree of oxidation.

In addition to their shared features, important differences exist between the glasses' spectra. Of most relevance to the relationship between glass chemistry and sulfur speciation is the observation that glasses equilibrated at the same fO_2 often exhibit different relative proportions of sulfide and sulfate. This is most clear in fig 3.6.2.2g, for which the JFR-4, DWF-37 and EVO basalts' spectra are dominated by the large "sulfide" feature at 2476eV, and have only very minor or absent "sulfate" features at 2482eV, indicating $S^{6+}/\Sigma S$ ratios of zero or near-zero. The basaltic and andesitic melts (PRI and AND) exhibit more prominent sulfate peaks, indicating low but positive $S^{6+}/\Sigma S$ ratios. But the dacitic melt (DAC) represents the largest contrast of all, with prominent sulfide and sulfate features, implying a much higher $S^{6+}/\Sigma S$ ratio of around 0.2 (this calculation is explained in the next section). Although often obscured by the noisiness of the spectra, differences in redox ratio such as these can be observed for many of the fO_2 conditions explored, confirming that silicate melt composition exerts some influence over the position of the sulfide-sulfate equilibrium (eqn. 3.7). Importantly, this conclusion is unaffected by the iron-loss suffered by the platinum-supported melts, since it is these sample's spectra that were too noisy to interpret and which were therefore excluded from figures 3.6.2.2a-f and 3.6.2.2g-l.

Figure 3.6.2.2a: Normalized spectra from the JFR composition (~10% Martian primary melt), equilibrated under various conditions of oxygen fugacity. Spectra nearer to the top of the figure represent successively higher fO_2 conditions. The 2476eV and 2482eV peak positions (considered characteristic of sulfide and sulfate) are labelled. The progressive replacement of sulfide by sulfate with increasing fO_2 is evident.

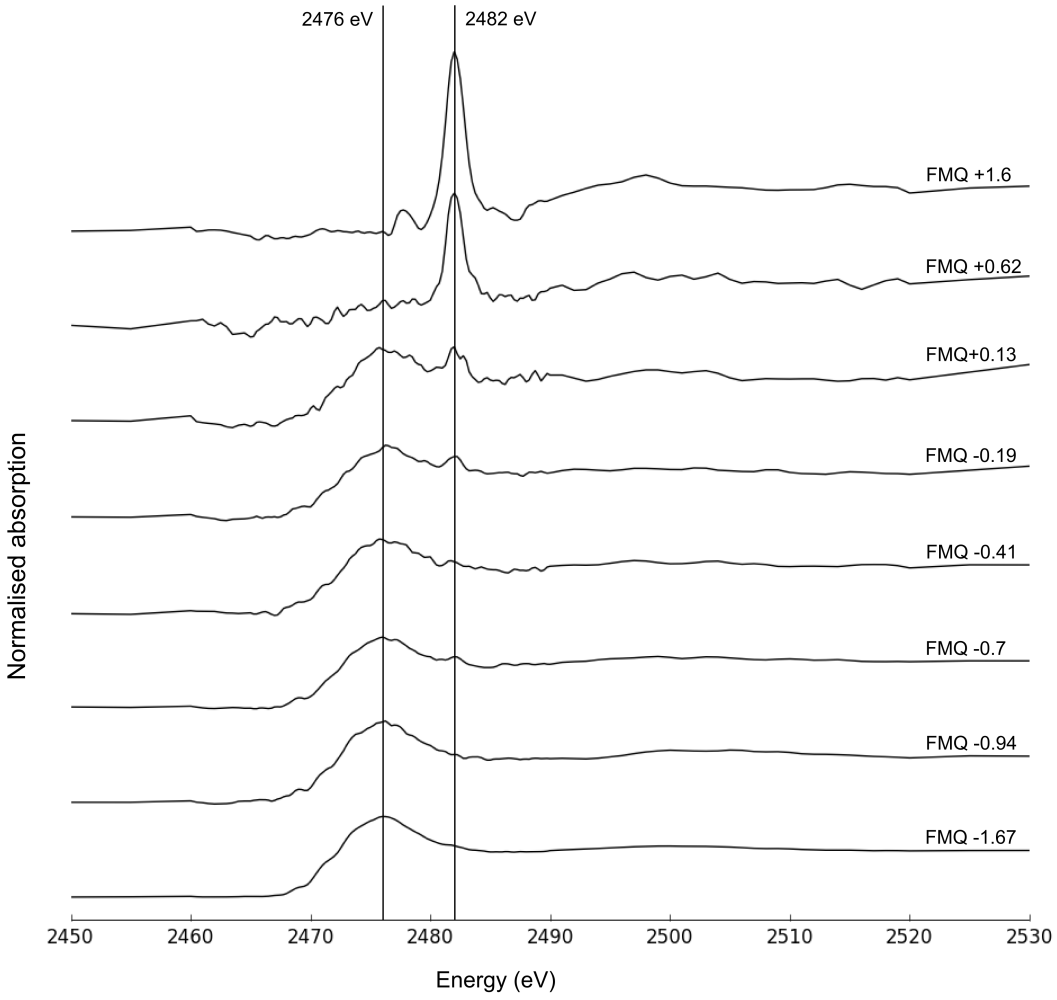


Figure 3.6.2.2b: Normalized spectra from the DWF composition (~50% Martian primary melt), equilibrated under various conditions of oxygen fugacity. Spectra nearer to the top of the figure represent successively higher fO_2 conditions. The 2476eV and 2482eV peak positions (considered characteristic of sulfide and sulfate) are labelled. The progressive replacement of sulfide by sulfate with increasing fO_2 is evident.

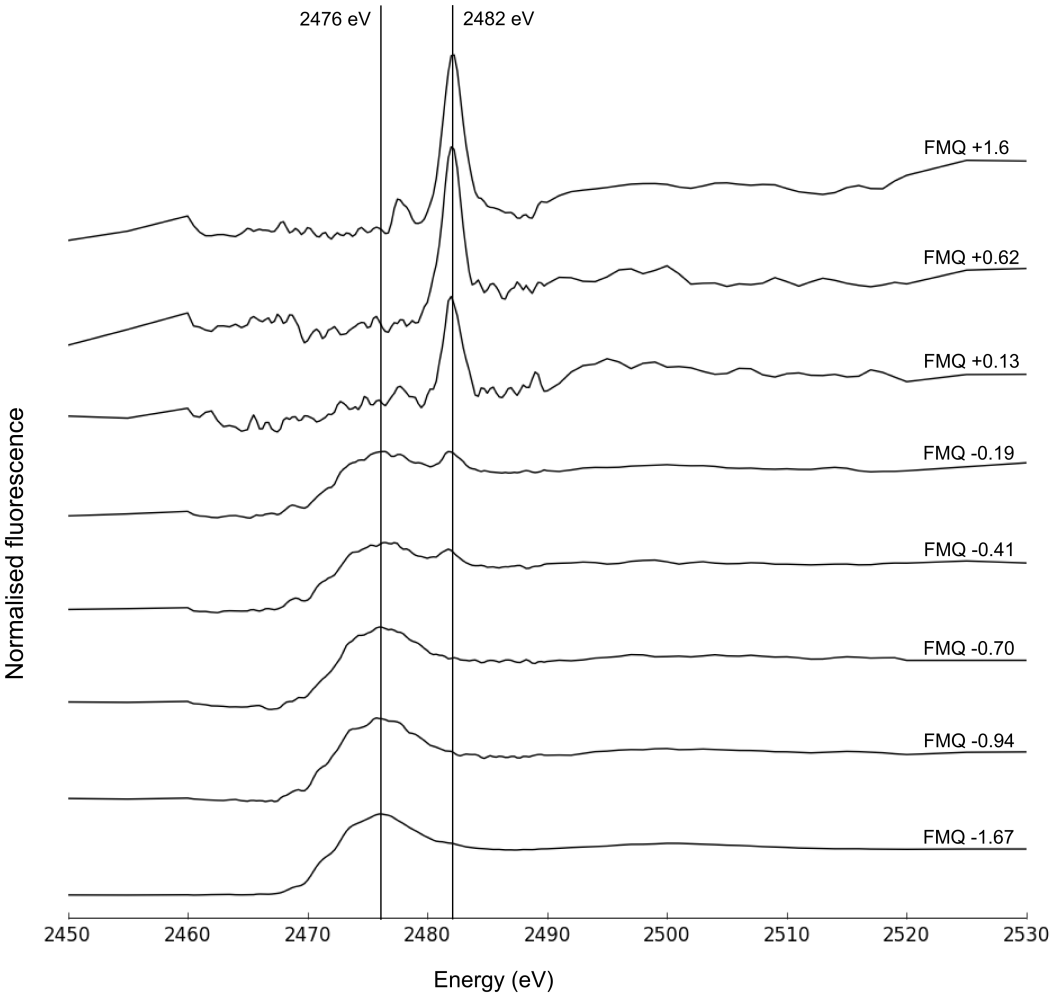


Figure 3.6.2.2c: Normalized spectra from the PRI composition (primitive terrestrial MORB), equilibrated under various conditions of oxygen fugacity. Spectra nearer to the top of the figure represent successively higher fO_2 conditions. The 2476eV and 2482eV peak positions (considered characteristic of sulfide and sulfate) are labelled. The progressive replacement of sulfide by sulfate with increasing fO_2 is evident. The presence of a peak at 2472eV in one of the glasses is suggestive of saturation by FeS.

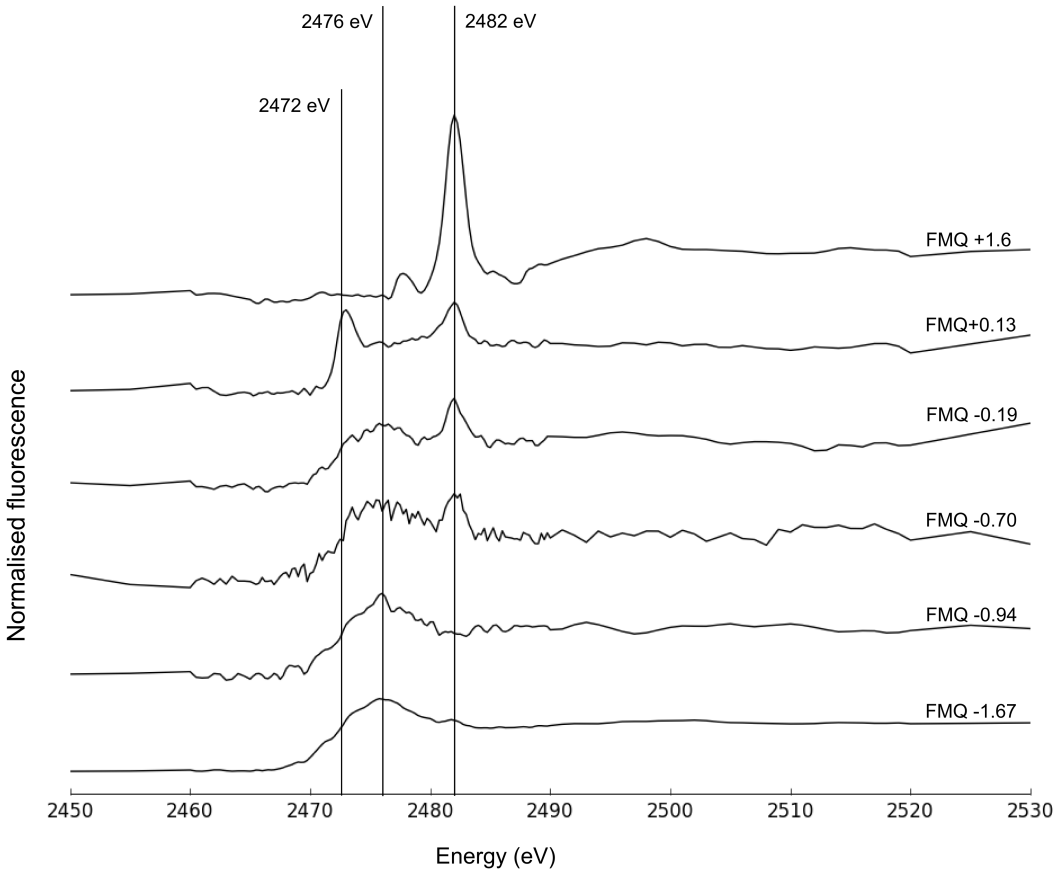


Figure 3.6.2.2d: Normalized spectra from the EVO composition (evolved terrestrial MORB), equilibrated under various conditions of oxygen fugacity. Spectra nearer to the top of the figure represent successively higher fO_2 conditions. The 2476eV and 2482eV peak positions (considered characteristic of sulfide and sulfate) are labelled. The progressive replacement of sulfide by sulfate with increasing fO_2 is evident.

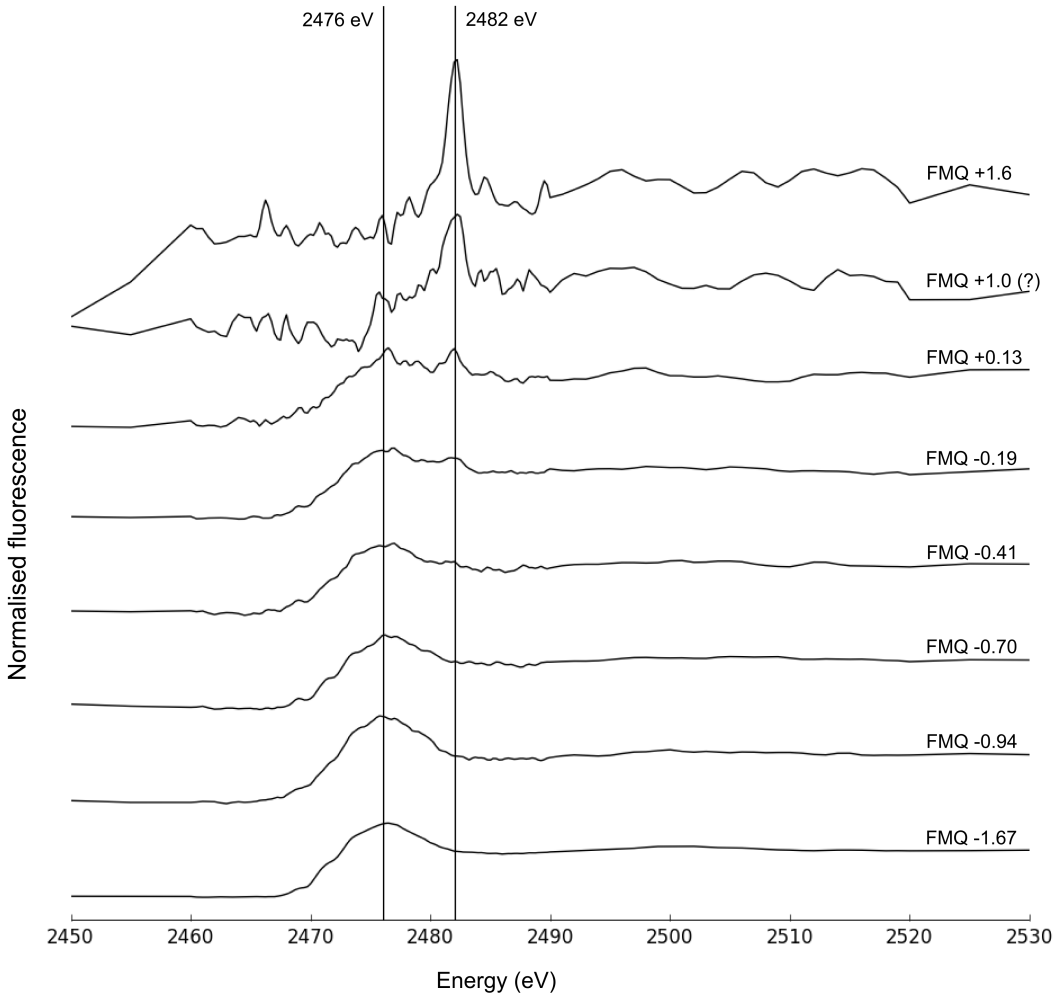


Figure 3.6.2.2e: Normalized spectra from the AND composition (terrestrial andesite), equilibrated under various conditions of oxygen fugacity. Spectra nearer to the top of the figure represent successively higher fO_2 conditions. The 2476eV and 2482eV peak positions (considered characteristic of sulfide and sulfate) are labelled. Although generally noisy, the progressive replacement of sulfide by sulfate with increasing fO_2 is discernible.

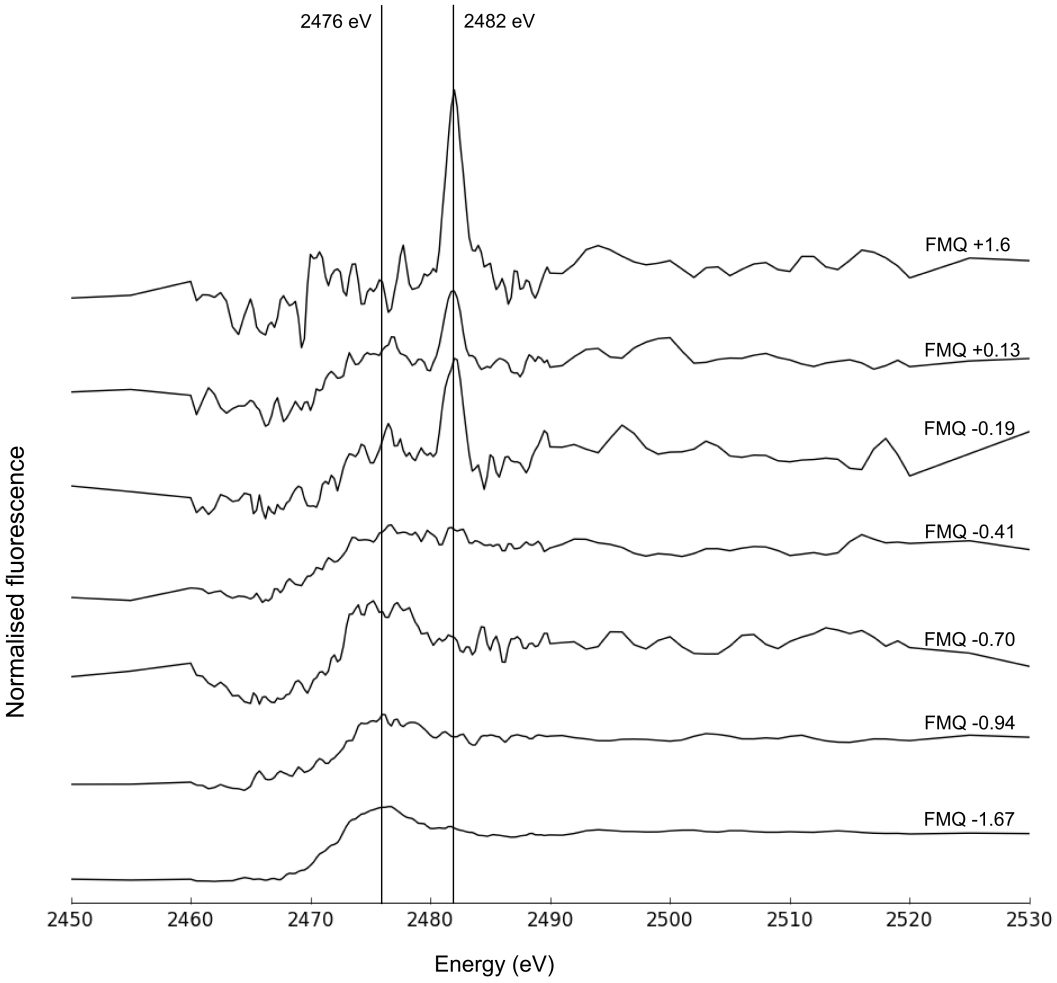


Figure 3.6.2.2f: Normalized spectra from the DAC composition (terrestrial dacite), equilibrated under various conditions of oxygen fugacity. Spectra nearer to the top of the figure represent successively higher fO_2 conditions. The 2476eV and 2482eV peak positions (considered characteristic of sulfide and sulfate) are labelled. These spectra are extremely noisy, even at the lowest fO2 conditions. The only glass that definitely exhibits both peaks is the glass equilibrated at FMQ-1.67, under which conditions the other five glasses are dominated by sulfide. In aggregate, these spectra are consistent with the sulfide-sulfate crossover taking place under more reducing conditions than it does in the other melts.

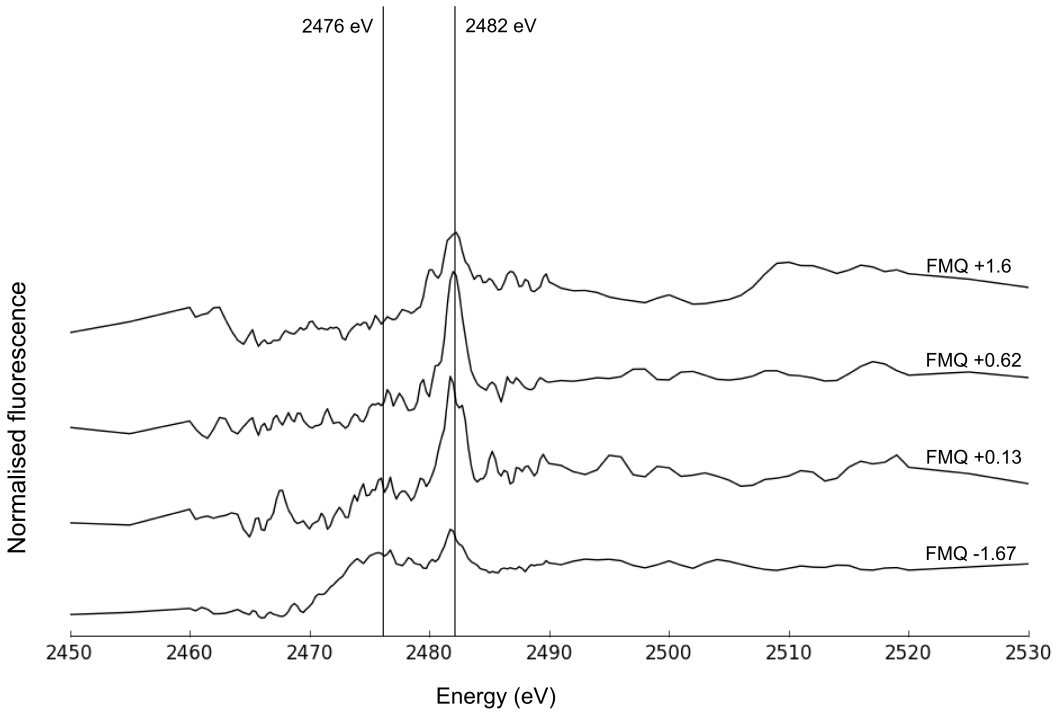


Figure 3.6.2.2g: Normalized spectra for the six melts equilibrated at FMQ-1.67. Note the contrast in the amplitude of the peak at 2482eV, characteristic of the sulfate ion. This peak is smallest (or even absent) for those melts that contain the greatest FeO concentration. These were the melts with the highest sulfur abundances, and therefore exhibit the least noisy spectra.

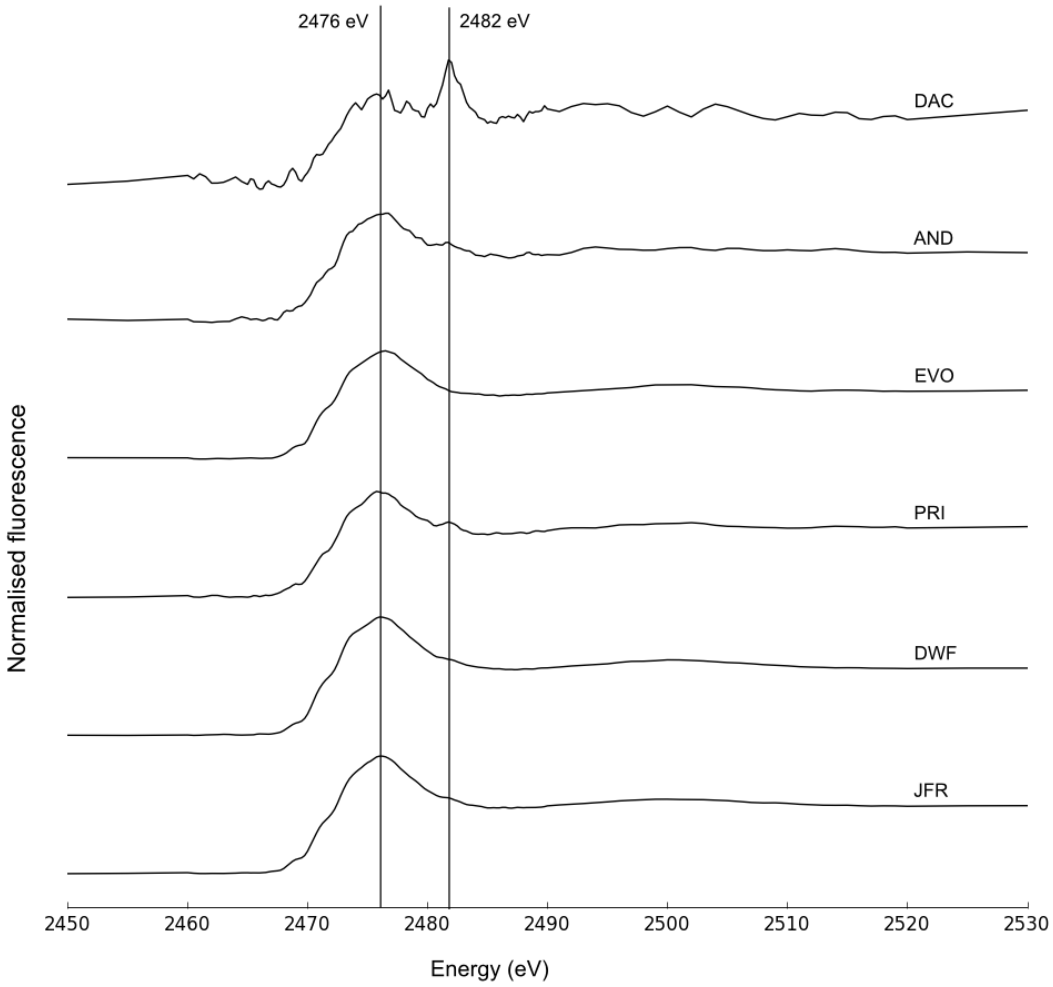


Figure 3.6.2.2h: Normalized spectra for the melts equilibrated at FMQ-0.94. The sulfur concentrations in these glasses are lower than in those equilibrated at FMQ-1.67, and consequently these spectra are more noisy. This explains the absence of the sulfate peaks observed in the previous figure, which presumably have smaller amplitudes than the noise. Note the absence of the Dacitic melt, which was not recovered from the furnace.

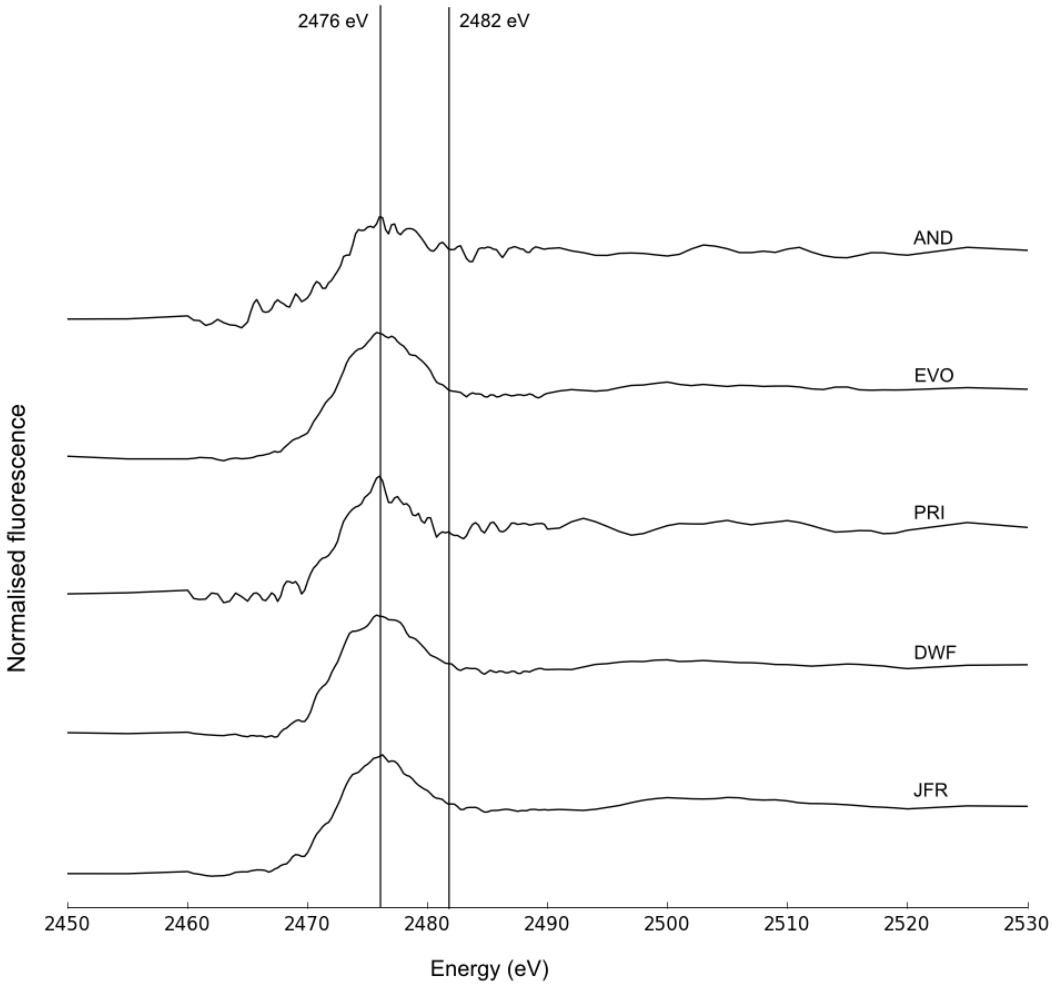


Figure 3.6.2.2i: Normalized spectra for the six melts equilibrated at FMQ-0.70. The contrast in overall sulfur concentration is evident from the contrasting noise between the PRI and AND melts and the other three basalts. Provided that the absence of a peak at 2482eV in AND is a result of noise, the inverse relationship between sulfate mole fraction and wt% FeO continues to hold.

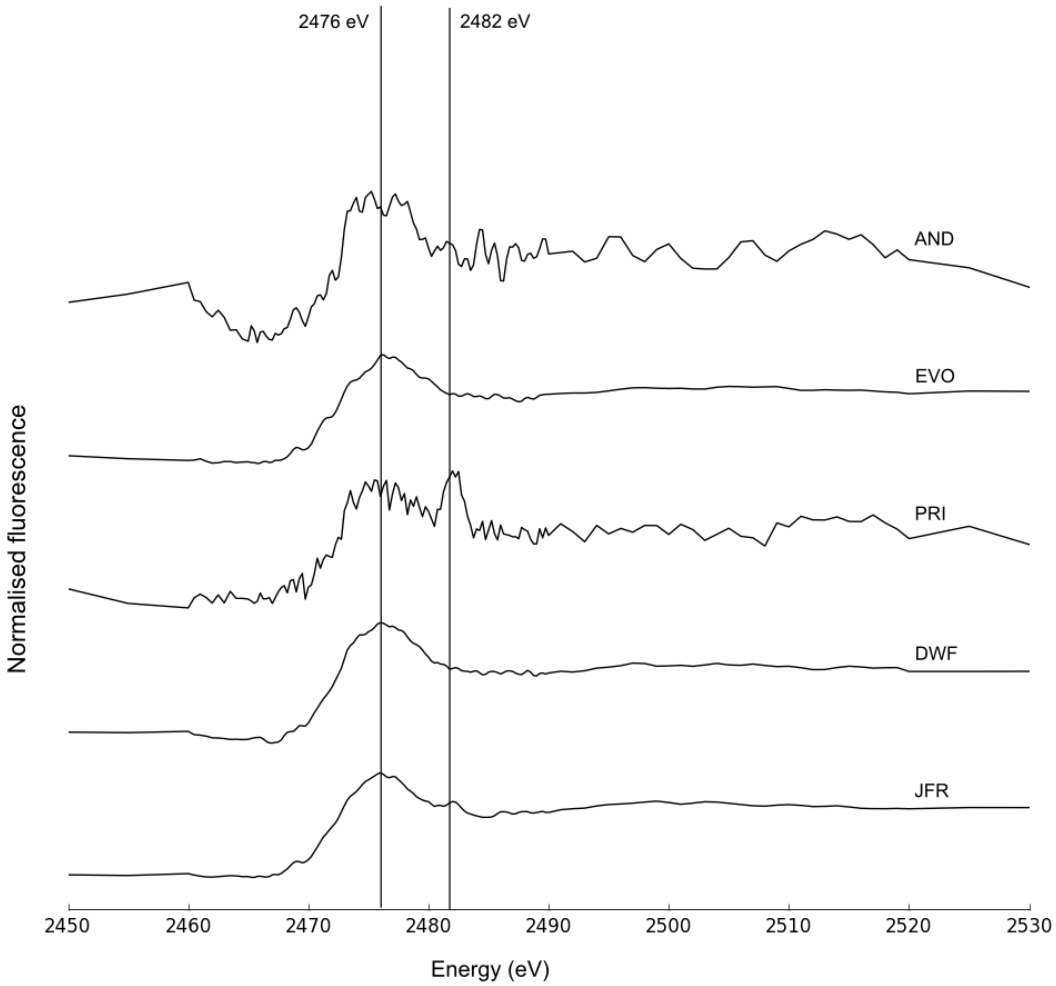


Figure 3.6.2.2j: Normalized spectra for the six melts equilibrated at FMQ-0.41. The spectra for the basalts shown here do not conform to the established pattern: the only glass unambiguously exhibiting a sulfate peak is DWF, which has the largest FeO concentration of the three (although only by ~1%, all three basalts have approximately 19 wt% FeO). This anomaly might be due to differential noise among these spectra, although this is puzzling too because SIMS analyses (described later) indicate concentrations of around 190ppm for all three of them. This is suggestive of an additional control besides FeO.

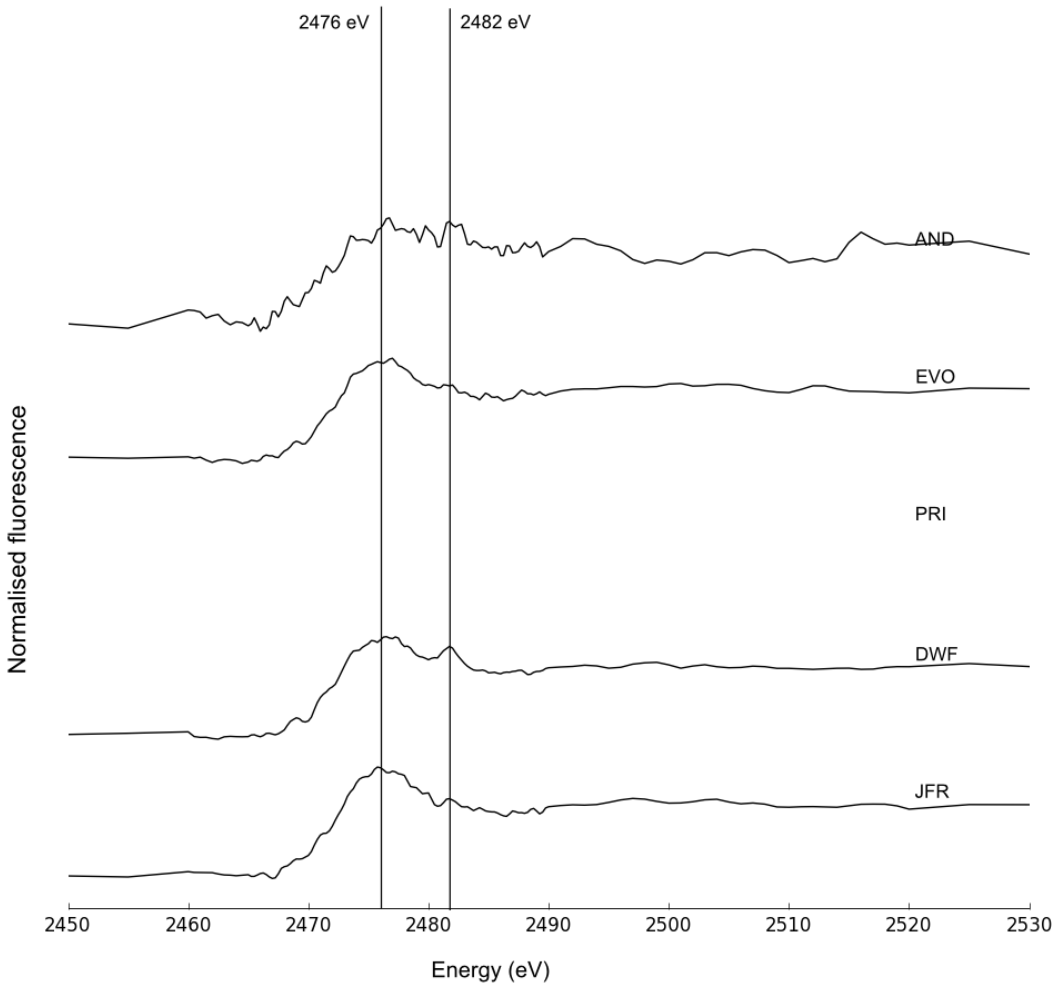


Figure 3.6.2.2k: Normalized spectra for the six melts equilibrated at FMQ-0.19. Every melt exhibits peaks characteristic of both sulfur species in proportions consistent with the inverse relationship with wt% FeO. (~9wt% in AND and PRI, and ~17wt% in the remaining three basalts).

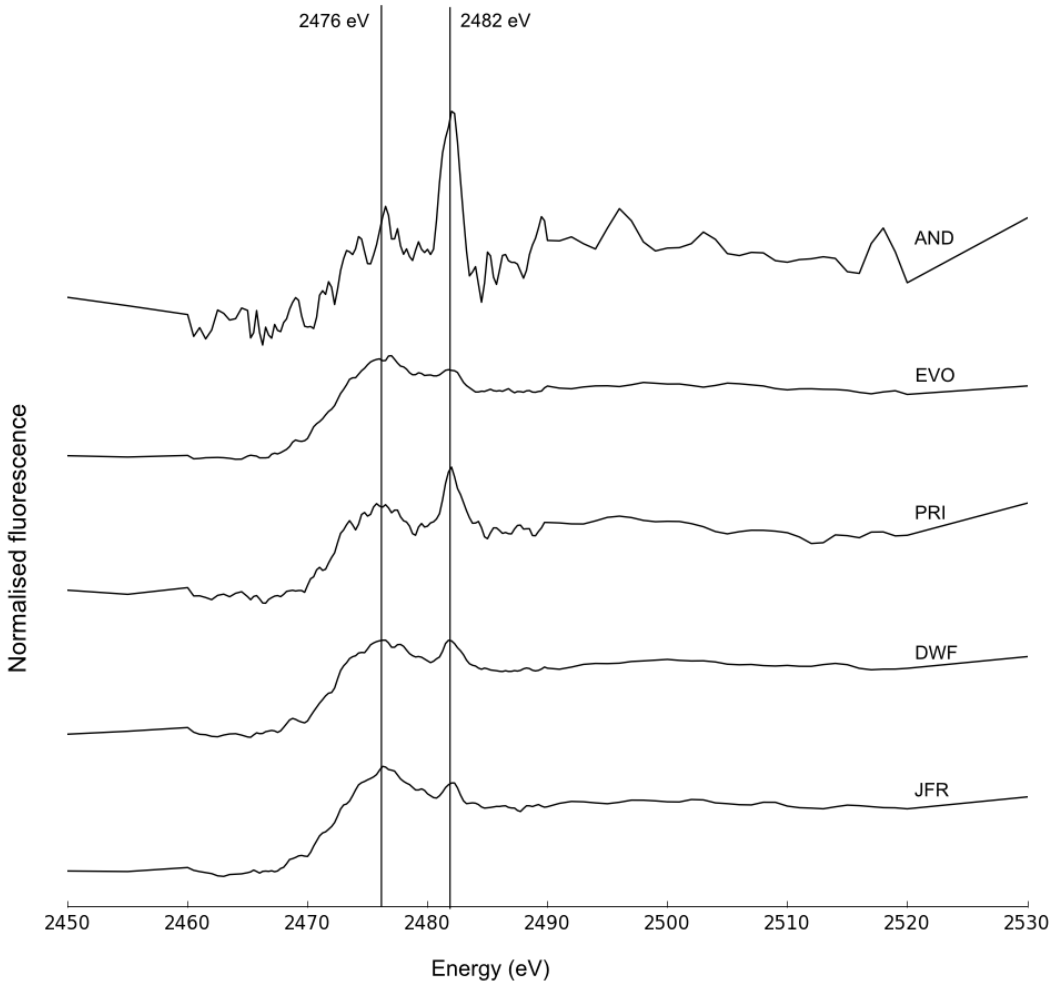
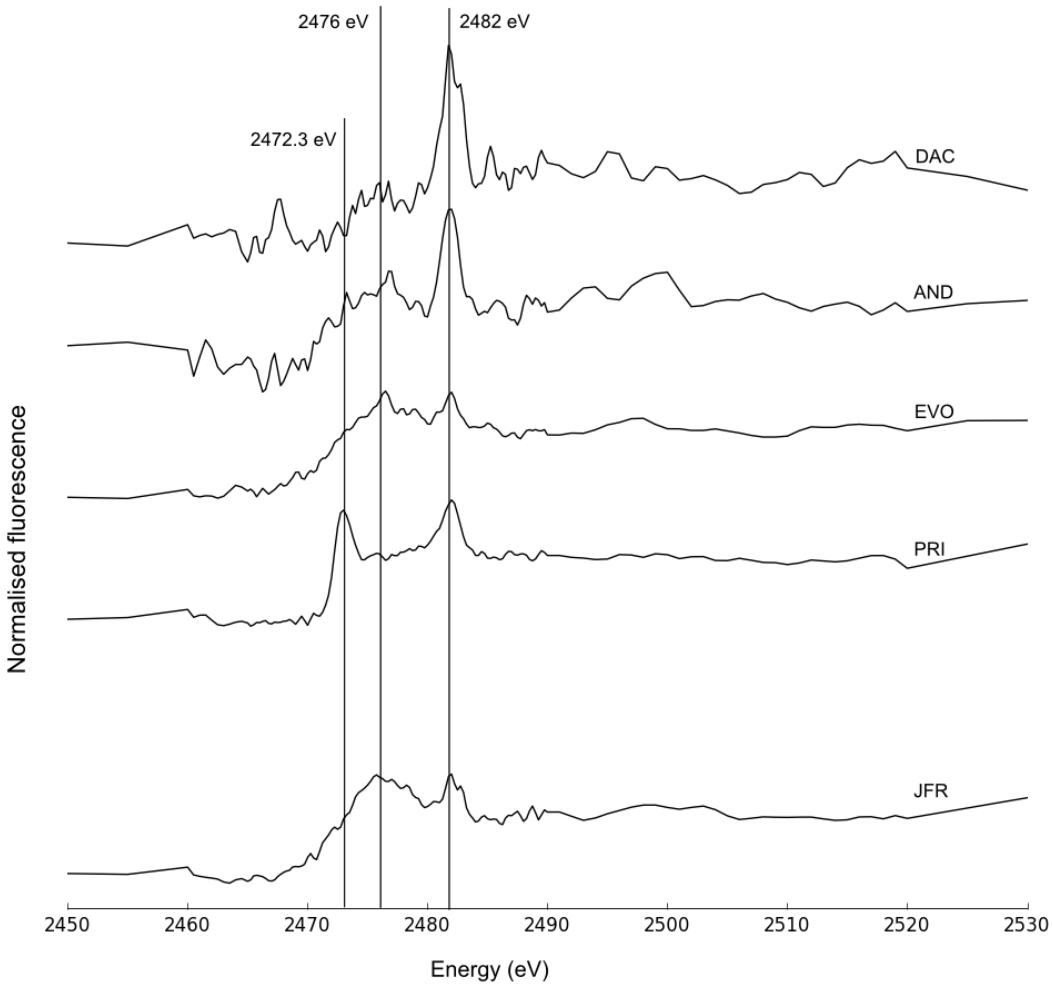


Figure 3.6.2.2l: Normalized spectra for the six melts equilibrated at FMQ+0.13. Besides the presence of the sulfate ion, nothing can be concluded about the DAC melt since its spectrum is so noisy. Both species are resolvable in the remaining melts, and in proportions consistent with the established pattern. The primitive MORB (PRI) also exhibits a prominent feature at 2482eV, characteristic of FeS specifically. The most likely explanation for this is that FeS precipitated from this melt, although it is unclear why this would happen since this melt is not expected to be saturated under the conditions of the experiment.



The element most consistently correlated with speciation appears to be Fe, which exhibits a four-fold range among the melts studied (greater than any other element). At every fO_2 studied, the relative dominance of the sulfide peak is consistently greater for more FeO-rich melts. Examining figure 3.6.2.2g again, the most FeO rich basalts (~20wt%) display little or no sulfate, whereas the more Fe-poor primitive basalt and the andesite, both containing ~10wt% FeO, have a more prominent sulfate peak. The dacite, with 5wt% FeO, has the most prominent sulfate peak of all. Inspection of figures 3.6.2.2g-l reveal that this trend is consistent throughout the whole series of experiments. This is further demonstrated in the next section, which attempts to quantitatively determine $S^{6+}/\Sigma S$ ratios for those glasses with sufficiently clean spectra.

Given the marked contrast in speciation between the dacite and the other five melts, it is worthwhile to consider whether the large proportion of sulfate implied by the XANES spectra might be an artefact of the analysis. Beam-induced changes in speciation have been documented by Wilke *et al.* (2008) (see the previous discussion of beam damage in section 3.5.4.4), who investigated the origin of sulfite in silicate glasses. In the case of this study specifically, the process under consideration is a net transfer of electrons from sulfide, so as to yield a greater quantity of oxidized sulfur. The plausibility of this process depends on two questions: where is the sink for these lost electrons (it is unlikely that the sample becomes charged during the analysis), and can they reasonably travel to this sink with the kinetic energy imparted to them by the X-ray beam? A very reasonable answer to the first question is Fe, which is present in quantities so much larger than sulfur (even in the dacite) that it can easily absorb any electrons liberated from sulfide. The question of electron mobility is more difficult to answer, since the point-to-point migration of electrons through glasses is not well studied, and therefore remains an uncertain possibility. However, the plausibility of charge-transfer notwithstanding, the consistency of the variations in speciation with FeO implies that it is unlikely to have exerted an influence on the results larger than that arising from variations in melt chemistry.

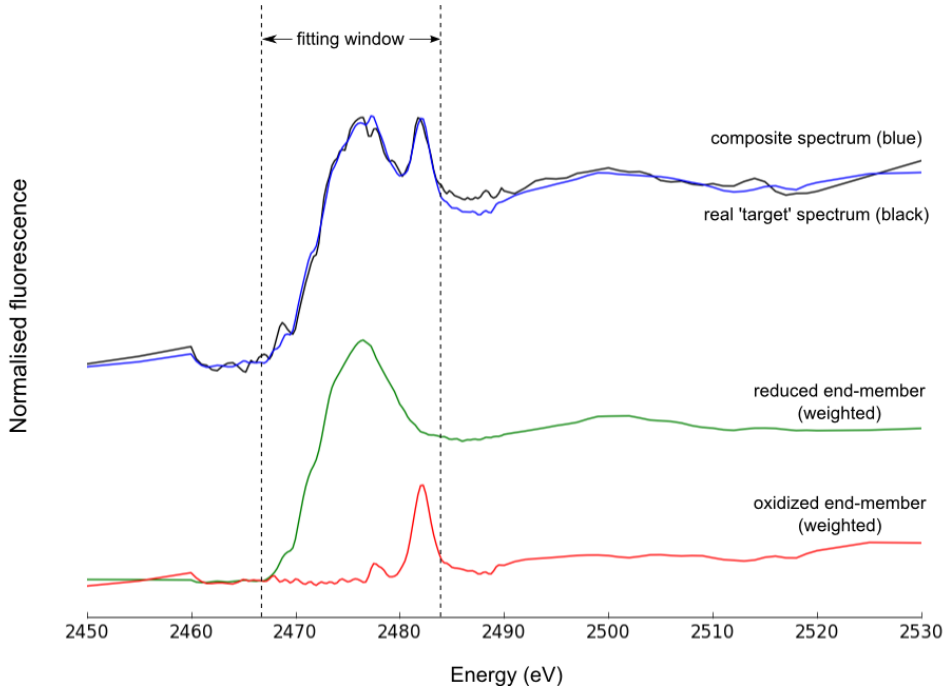
If beam-induced charge transfer of the kind described does occur, it is difficult to see how it could be mitigated, except by determining the sulfur speciation with some other method (wet chemical analysis for example). In addition to confirming (or invalidating) the measures of speciation reported here, this would definitively show whether beam-induced oxidation is real, and worthy of mitigation by future studies.

3.6.2.3 Estimating Redox Ratios by Linear Combination Fitting

In addition to the qualitative finding that sulfur speciation in silicate melts varies with their major-element chemistry, redox ratios can be estimated quantitatively for glasses yielding sufficiently clean (noise-free) spectra. Comparisons between melts equilibrated under the same fO_2 can then be made quantitatively, and the influence of particular elements established more concretely. Furthermore, where possible, the sequence of $S^{6+}/\Sigma S$ ratios for a particular melt composition may be graphed against fO_2 so that the shape and location of the sulfide-sulfate transition can be evaluated.

Broadly following the approach of previous researchers (Jugo *et al*. 2010, Klimm *et al*. 2012b), $S^{6+}/\Sigma S$ ratios were estimated by linear combination fitting (LCF) of spectra representing glasses containing pure sulfide or sulfate (so-called "end-member" spectra), to generate composites that most closely matched the spectra of glasses equilibrated at intermediate fO_2 conditions. This treatment assumes a linear relationship between the sulfide and sulfate peak integrals and their relative proportions in the glass. Both species are therefore assumed to have identical or (nearly identical) fluorescence yields. This assumption has been tested for synthetic mixtures of phosphorus compounds by Werner and Prietzel (2015) who performed LCF on spectra obtained from compounds with known mixing ratios. A similar check has yet to be performed with sulfur, but the assumption is physically reasonable. This procedure is illustrated by figure 3.6.2.3, which shows the weighted end-members, and composite spectra for a typical glass with mixed sulfur speciation.

Figure 3.6.2.3: The linear combination fitting procedure for a typical melt exhibiting mixed-speciation (the DWF composition at -0.19 log units fO_2). The real (or 'target') spectrum is shown in black, above the reduced and oxidized end-members (the green and red curves respectively). These end-members are glasses whose spectra are indicative of pure sulfide or sulfate. The end-members are weighted such that their linear sum most closely approximated the target spectrum in the fitting region (enclosing the two peaks of interest – dashed line in the figure). In the example shown, the weighting factors are 0.857 and 0.143 for the reduced and oxidized end-members respectively, and a close match is achieved to the target spectrum. The $S^{6+}/\Sigma S$ ratio is therefore considered to be 0.143.



End-member spectra were selected from glasses believed to host sulfide or sulfate exclusively. For each melt composition, the most oxidized spectrum served as the pure sulfate end-member. The spectrum representing the most reduced EVO-type melt was used as the pure-sulfide end-member for all of the other glasses, since it was the only spectrum exhibiting no peak at 2482eV (and therefore no sulfate) under the most reducing conditions. Since the shapes and energies of the peaks representing sulfide and sulfate are invariant from one melt composition to the next, this use of one melt composition's spectrum to fit another's is not considered problematic. For each "unknown" spectrum, the end-members were iteratively superposed with different weights applied to them, so that the weights offering the closest match to each intermediate unknown spectrum could be identified. Since both the end-member and the unknown spectra have been normalized,

these weights represent the relative proportions of sulfide and sulfate in the unknown. Although this contrasts with the procedure followed by Jugo *et al.* (2010), the governing assumptions about peak amplitude and mole fraction are the same.[1]

LCF was carried out using the software Athena (Ravel and Newville 2005). Rather than attempting to superpose the spectra across their entire energy range, the fitting process was confined to an energy window enclosing the peaks indicative of sulfide and sulfate. This window extended 13eV above and 5eV below the edge-energy for each spectrum being fitted. This was necessary because the spectra's EXAFS regions are sensitive to factors other than sulfur speciation, so the spectra representing mixed speciation may not approximate a linear superposition of end-members across this region. The LCF procedure was performed twice, before and after a three-point smoothing filter was applied to the spectra. Differences between the $S^{6+}/\Sigma S$ ratios obtained in each case were negligible compared with the uncertainty arising from end-member non-uniqueness (described below), so the smoothed data were discarded from further analysis.

Uncertainties in redox ratios obtained by LCF are dominated by non-uniqueness in the normalization parameters applied to the end-member spectra. Since every spectrum exhibits a very similar pre-edge, the variation in pre-edge fitting parameters from one spectrum to the next is extremely minor, and results in negligible uncertainty in the normalized peak amplitude of any given spectrum. In contrast, the normalized peak amplitudes are strongly influenced by the post-edge curve shape, because a broader range of fitting parameters can reasonably be fitted to the post-edge region (recall that the edge-step height, and by extension the amplitude of any peaks, is determined by the value of the post-edge curve at E_0). This non-uniqueness is especially significant for the most oxidized spectra, for which the 2482eV "sulfate" peak is small in comparison to the noise in the background. To account for all of the peak height variation permitted by variation in post-edge normalization, the LCF procedure was applied to each spectrum twice, with two separate normalization procedures applied to the end-member spectra. These normalization procedures for the first pair of end-members was intended to generate the largest and smallest reasonable reduced and oxidized peaks, while the opposite was the case for the second pair. In

[1] Jugo *et al.* (2010) generated a series of synthetic composite spectra from their end-members, and calculated integrals across the sulfide and sulfate peaks of each composite. The relative size of these integrals was then expressed as the ratio $I(S^{6+})/(I(S^{6+}) + I(S^{2-}))$ (the implied sulfate mole fraction) which was graphed against the "actual" sulfate mole fractions of each composite. The resulting calibration curve expressed a near-linear relationship between the sulfate mole fractions and those measured by peak integrals. The value in this approach presumably derives from the simplicity of taking integrals rather than iteratively combining the spectra of end-members.

this manner, the maximum and minimum redox ratios interpretable by the variation in normalization parameters were obtained. The $S^{6+}/\Sigma S$ ratio assigned to each spectrum was the midpoint between these two extremes.

3.6.2.4 The sulfide-sulfate crossover position

The $S^{6+}/\Sigma S$ ratios obtained by linear combination fitting are plotted against log fO_2 for five of the six glasses in figures 3.6.2.4a-e. The lowest-fO_2 value for the Dacitic melt is shown on each for comparison (none of the other dacite spectra were amenable to LCF). Also shown in figures a-e is a compilation of data from two previous studies by Jugo *et al.* (2010) and Klimm *et al.* (2012b). The curves shown are best-fit models for the data, with their first derivatives forced to the value of ½ expected from equation. 3.5.

For the basaltic and andesitic melts studied, the progression in $S^{6+}/\Sigma S$ with fO_2 is consistent with the expected behaviour: a sharp transition between sulfide and sulfate-domination takes place, relatively close to the FMQ buffer. For reasons related to the gas mixtures (explained in section 3.4.4), the sulfur concentration in each melt diminishes with increasing fO_2, before making a resurgence under the most oxidizing conditions (FMQ+1.6 log units). Consequently, the noise in the spectra overwhelms any peaks at conditions above FMQ, so there is a gap between FMQ and FMQ+1.6. The initial rise in sulfate mole fraction is therefore well resolved for each of these five melts, but the "shoulder" further up is hidden. The crossover midpoint (the region of maximum rate of change) is resolved only for the Martian basalts and the andesitic melt, although the upper boundary of the crossover is well constrained in every case by the most oxidized glasses (by FMQ+1.6, all glasses were sulfate-dominated).

With the precision achieved here (limited by the uncertainty in fO_2), no difference can be detected between the crossover position of the two Martian basalts and the Evolved terrestrial MORB: the centre-point for each is close to FMQ+0.5 log units. Note that these are the melts with the highest Fe concentration (between 17 and 19 wt%). The Primitive MORB appears to share its crossover position with the andesitic melt, although it is relatively poorly constrained (only the rising-edge is resolved). This is because the spectrum at FMQ+0.13 contains a sharp feature at 2472eV, which is unseen in any of the other basalts, and which precludes the possibility of accurate LCF. This feature is characteristic of FeS, and is observed in the spectra obtained for natural basalts from the Galapagos Spreading centre and the Juan de Fuca ridge by Jugo *et al.* (2010). These basalts are

known to be sulfide-saturated, so the possibility of contamination by immiscible blebs of iron-sulfide is likely. BSE images of PRI at FMQ+0.13 do reveal very sparse fragments of some high-density phase, possibly tiny blebs of sulfide, which is not observed in any of the other melts.

The only Dacitic melt spectrum amenable to LCF was that which represented the most reducing conditions, subsequent spectra being too noisy for any meaningful quantitative treatment. Nonetheless, visual inspection of these spectra indicates domination by sulfate at all fO_2 conditions above the FMQ buffer. Therefore, it is reasonable to fit a model to this single data point similar to those applied to the other five melts. The model shown presumes that the crossover width is identical to those used previously, which is also a reasonable assumption given that the crossover width is primarily controlled by the stoichiometry of equation 3.5, and is likely insensitive to the activities of the components involved. The large difference in crossover position between the dacite and the more Fe-rich melts in particular is strongly suggestive of a major-element control on sulfur speciation, for these differences are certainly larger than the uncertainties in the data.

Figure 3.6.2.4a: The sulfide-sulfate crossover for the JFR and DAC melts, determined by LCF of XANES spectra. A compilation of previous researchers data is shown for comparison. The crossover position for JFR is well constrained by the data, and lies more than 2 log units of fO_2 higher than the assumed dacite position.

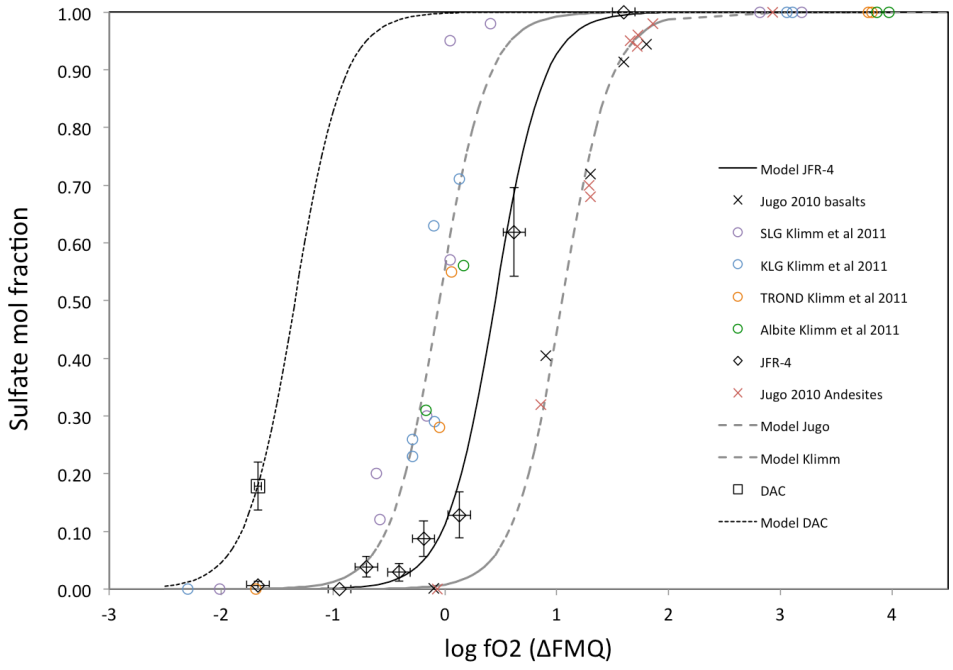


Figure 3.6.2.4b: The sulfide-sulfate crossover for the DWF and DAC melts, determined by LCF of XANES spectra. A compilation of previous researchers data is shown for comparison. Within error, this melt shares its position with the other Martian melt; both have very similar FeO contents (~19 wt%).

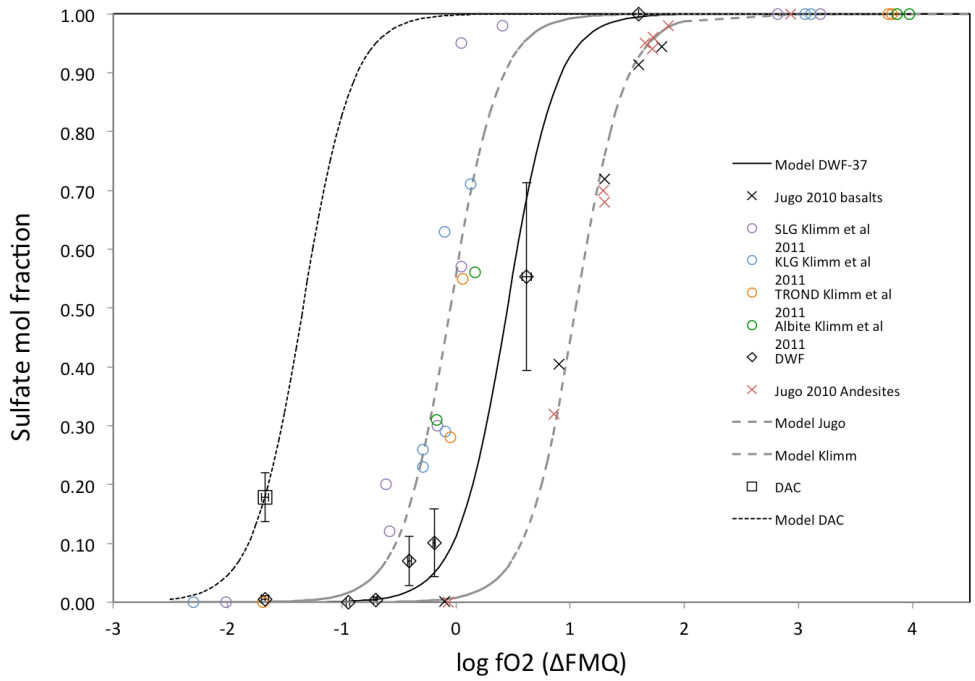


Figure 3.6.2.4c: The sulfide-sulfate crossover for the PRI and DAC melts, determined by LCF of XANES spectra. A compilation of previous researchers data is shown for comparison. The crossover position for this melt is poorly constrained by the data, but appears to be shifted marginally to lower fO_2.

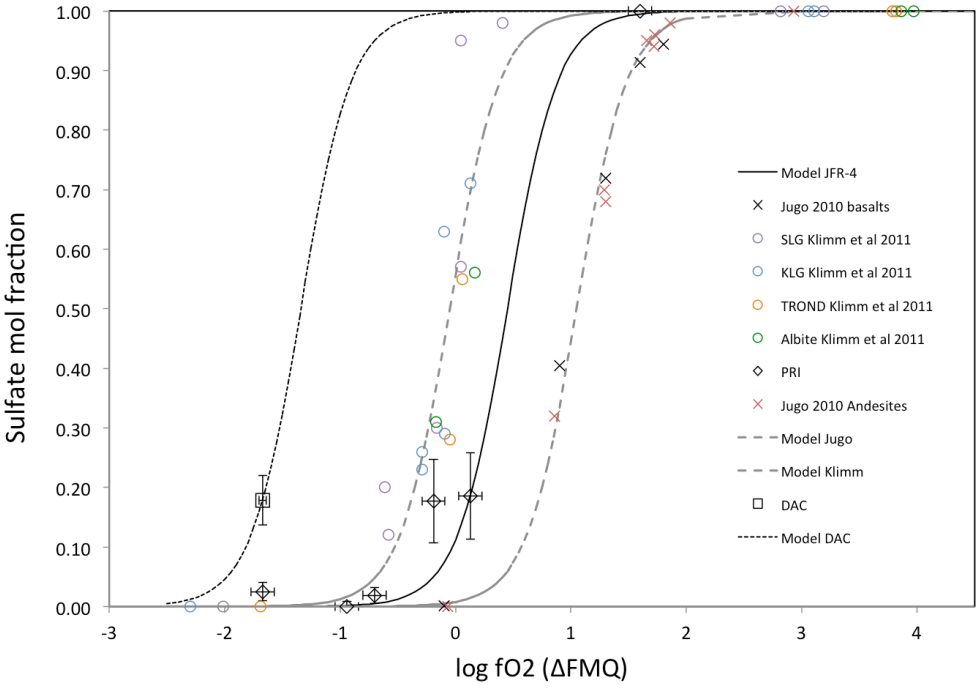


Figure 3.6.2.4d: The sulfide-sulfate crossover for the EVO and DAC melts, determined by LCF of XANES spectra. A compilation of previous researchers data is shown for comparison. Though poorly constrained, the crossover position implied for EVO is similar to those of the Martian basalts (centered close to FMQ+0.5).

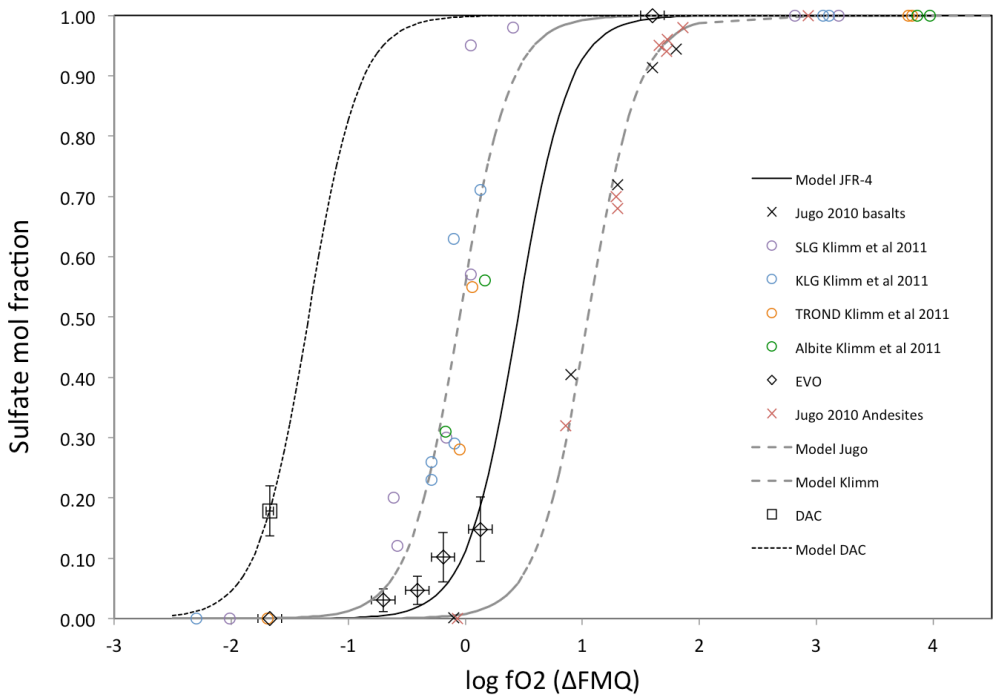
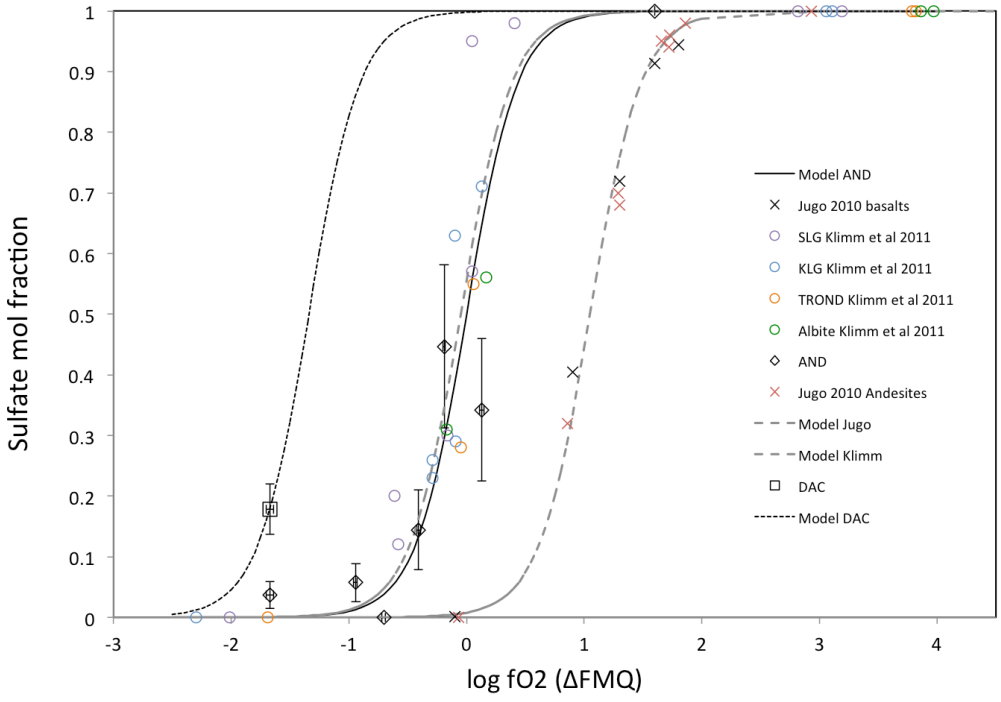


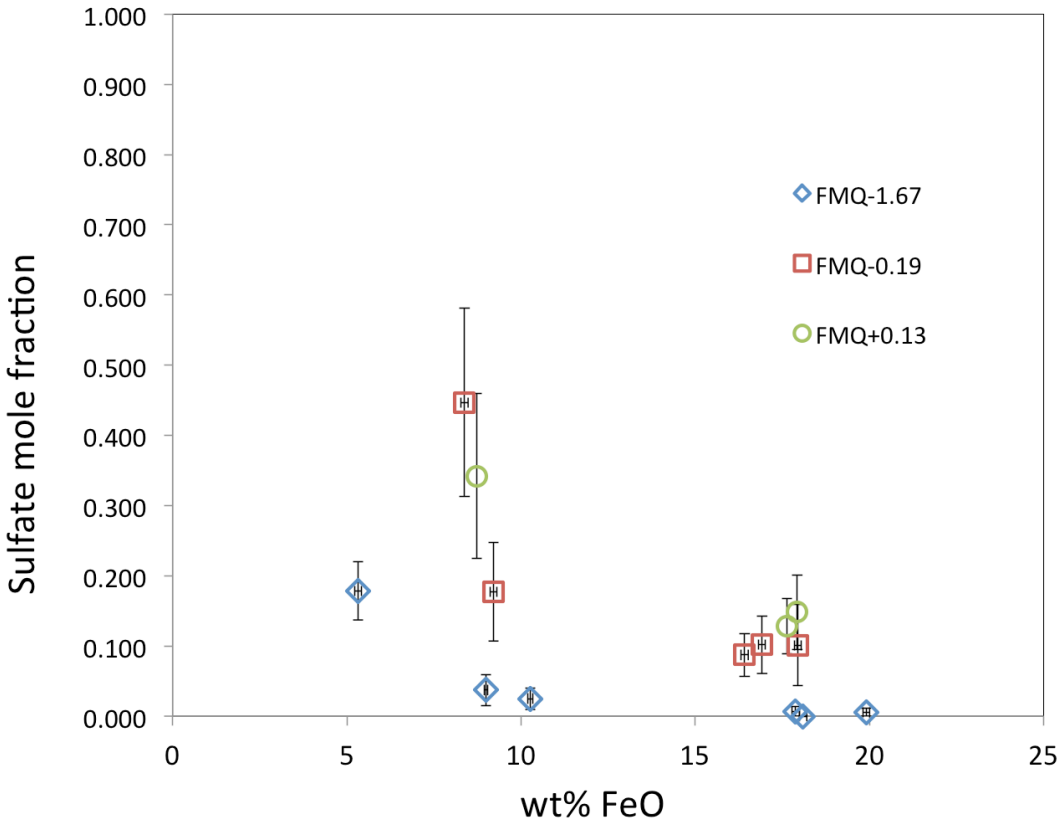
Figure 3.6.2.4d: The sulfide-sulfate crossover for the AND and DAC melts, determined by LCF of XANES spectra. A compilation of previous researchers data is shown for comparison. The crossover position falls among Kilmm et al's (2011) Fe-free melts, half a log unit lower in fO_2 than the basalts of this study.



3.6.2.5 Differences in speciation at constant fO_2

Sulfate mole fractions determined by LCF for the various melts are graphed against wt% FeO in figure 3.6.2.5. Melts equilibrated under three fO_2 conditions are shown: those yielding the highest quality spectra. It is clear from this figure that sulfate mole fraction consistently correlates negatively with iron concentration.

Figure 3.6.2.5: The relationship between melt wt% FeO and sulfate mole fraction. Points of the same colour represent melts brought to equilibrium under the same conditions of oxygen fugacity. Note that melts that are richer in FeO consistently exhibit lower sulfate mole fractions.



3.6.2.6 Comparisons with previous researchers' results

The crossover position indicated by the Fe-rich basalts (JFR, DWF and EVO) is intermediate in fO_2 between those indicated by previous studies. The melts studied by Jugo *et al.* (2010) were hydrous basalts and andesites brought to equilibrium at 200MPa and 1050°C. These define a crossover centred very close to FMQ+1, half a log unit higher than the anhydrous rocks of this study. These melts display no perceptible variation in crossover position. However this is consistent with the hypothesis that Fe is the dominant speciation controller, since they differ in wt% FeO by only 2% on average (their concentrations being 9.2% and 7.2% respectively). At an fO_2 slightly less than half a log unit lower than these is the crossover implied by the experiments of Klimm *et al.* (2012b), which comprise a mixture of various compositions, including soda-lime, potassic, trondjhemitic and albitic glasses. These were brought to equilibrium at 800-1000°C, and 200MPa. All are hydrous and Fe-free. They exhibit slightly more scatter than Jugo *et al.* (2010)'s melts, but nonetheless also imply a sharp transition with the expected sigmoidal shape.

The melts of Klimm *et al.* (2011) undergo the expected speciation change at a higher fO_2 than the dacitic melt of this study. This is potentially problematic for the hypothesis that Fe exerts the dominant chemical control over speciation, since their melts were Fe free, whereas the dacite contains 5.1 wt% FeO. However, because the conditions of temperature and pressure investigated in this study are so different from those of Kilmm *et al.* (2011), direct comparisons between the sulfide-sulfate transitions cannot be used to rule out the effects of chemistry, since these might simply be compensated for by differences in some other controlling variable (such as T, P, aH_2O). The intensive parameters of Jugo *et al.* (2010) and Kilmm *et al.'s* (2011) experiments are reasonably similar to each other, and therefore permit a tentative comparison based on their chemistry. As with the data presented here, the Fe-free melts undergo the transition between sulfide and sulfate at more reducing conditions.

3.6.3 Sulfur concentrations determined by SIMS

3.6.3.1 Speciation implied by the relationship with log fS_2/fO_2

Sulfur concentrations obtained by SIMS are given in table 3.6.3.1. All concentrations are reported in ppm (by mass), consistent with the literature convention. The sulfur concentrations of the glasses used to calibrate the SIMS are displayed in table 3.6.3.1b. These were determined by electron-probe WDS.

The sulfur concentrations for each of the six melts are graphed against their fS_2/fO_2 ratio in figures 3.6.3.1a-f. Both parameters are plotted as logs, so the proportionality relation derived from the sulfide dissolution equilibrium reaction (equation 3.1) should emerge as a straight line in the data. Although the abscissa in these plots is a fugacity ratio, the fugacities used for each experiment were such that points lying further towards the left consistently represent more oxidizing conditions.

Table 3.6.3.1a: The concentration of sulfur in each of the six glasses for every fO_2 studied. These measurements were made with SIMS, calibrated using electron-probe data for the six most reduced glasses.

	Sulfur concentration (ppm)										
log fO2 (ΔFMQ)	-1.67	-0.94	-0.70	-0.41	-0.19	0.13	0.62	0.62	1.04	1.21	1.60
JFR	2208	740	692	278	245	105	-	35	7	4	88
DWF	2421	805	563	268	258	-	-	21	4	2	43
PRI	647	230	180	-	72	32	16	9	3	1	93
EVO	2112	725	533	254	236	95	46	22	4	2	17
AND	386	102	164	73	29	32	9	8	4	2	20
DAC	95	17	-	11	-	2	3	3	2	2	4

Table 3.6.3.1b: Sulfur concentrations for the six glasses, equilibrated under the most reducing conditions. These values were determined by EPMA, using galena as a standard (see analytical methods: section 3.5.3).

log fO_2	Glass name	S (ppm)	S (stdev)	S (det limit)
-1.67	JFR	2208	51	64
-1.67	DWF	2500	54	63
-1.67	PRI	686	28	63
-1.67	EVO	2139	54	64
-1.67	AND	420	31	60
-1.67	DAC	88	25	59

The errors included in figures 3.6.3.1a-f have been calculated individually for each point, based on propagation of gas mixture uncertainties for the fS_2/fO_2 ratio, and both counting statistics and primary standard uncertainties for the sulfur concentration (these procedures are explained in the sections 3.4.5 and 3.5.5.5 respectively). Beneath each plot is shown the FeO concentration (in wt. %) for each experiment, plotted on the same abscissa to aid comparison with the chart above. The depletion in FeO for experiments more oxidizing than the FMQ buffer is readily apparent.

At oxygen fugacities lower than the FMQ buffer it is clear that each of the six compositions exhibit a linear relationship between log S and log (fS_2/fO_2), consistent with the presence of the sulfide ion, according to equilibrium 3.1. The lines on each plot are best fits to the data at low fO_2,[2] but with gradients forced to the value of ½ expected from equation 3.3. These "pure sulfide" lines represent the theoretical trend in sulfur concentration arising in the absence of any sulfate. Note that where conditions are sufficiently reducing, and the equilibrium concentration of sulfate is vanishingly low, the actual trend in sulfur concentration closely approximates this linear trend. Large deviations from this trend indicate the presence of sulfur species other than sulfide, provided that the melt's major element compositions are invariant from one experiment to another. However, as is clear from the FeO plots, this condition is not met for melts equilibrated under conditions more oxidizing than around FMQ, due to the Fe loss that resulted from insufficient pre-saturation of their platinum loops. Although these variations in FeO wt% preclude the most straightforward interpretation of the data, the dependence of sulfide concentration on FeO concentration is well studied, and corrections can be made to compensate for this variation in melt chemistry. This is attempted in the succeeding sections.

[2] These were obtained by taking averages of the sulfide capacities for the most reduced glasses, and using this to fix the position of the line in the y-direction.

Figure 3.6.3.1a: Sulfur concentrations determined for the putative ~10% Martian primary melt ("JFR") by SIMS. FeO concentrations are shown below so that the region for which constant melt composition was maintained can be readily located. Melts equilibrated under progressively higher fO_2 conditions occur towards the left of the diagram.

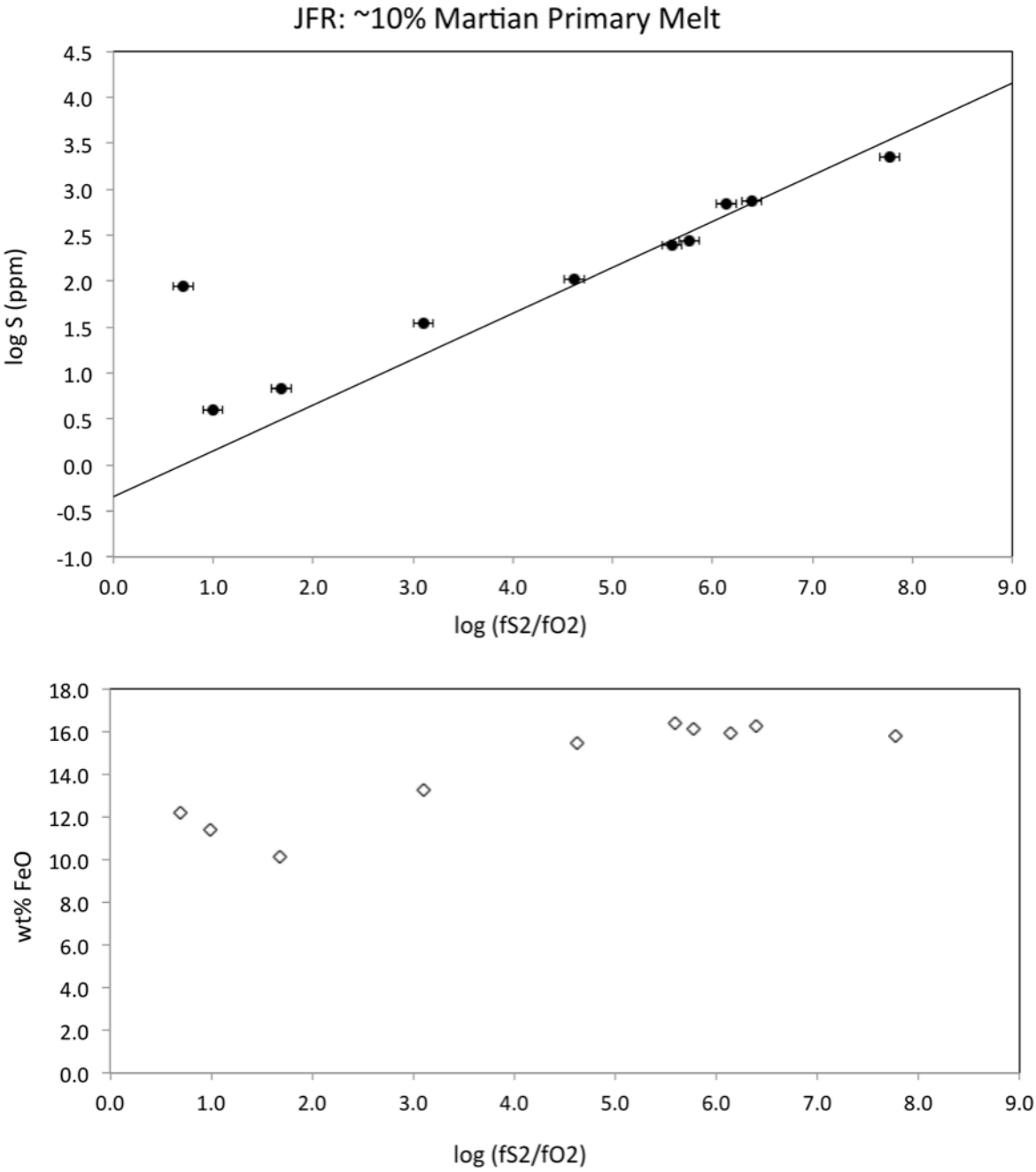


Figure 3.6.3.1b: Sulfur concentrations determined for the putative 50% Martian primary melt ("DWF") by SIMS. FeO concentrations are shown below so that the region for which constant melt composition was maintained can be readily located. Melts equilibrated under progressively higher fO_2 conditions occur towards the left of the diagram.

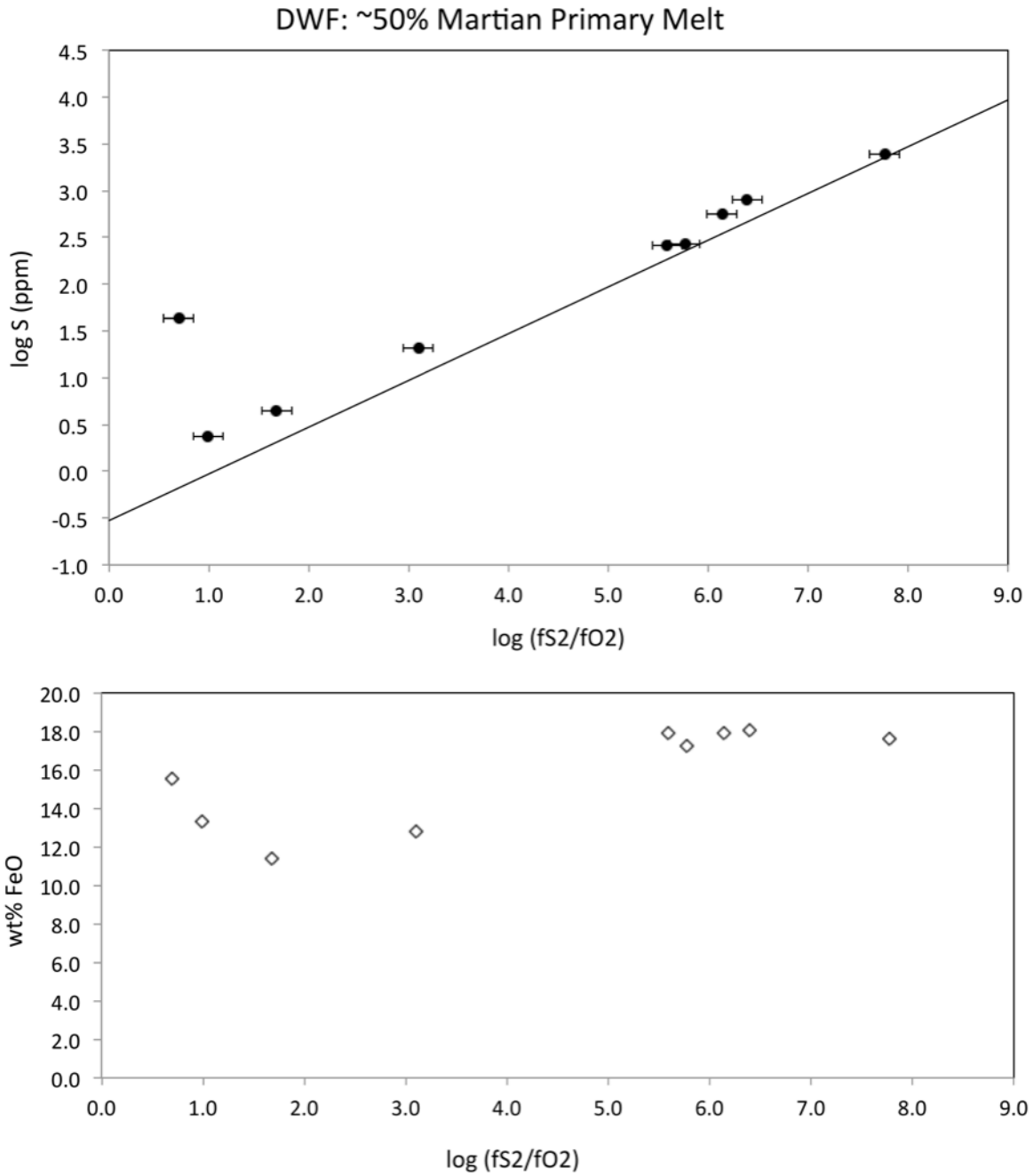


Figure 3.6.3.1c: Sulfur concentrations determined for the primitive terrestrial MORB ("PRI") melt by SIMS. FeO concentrations are shown below so that the region for which constant melt composition was maintained can be readily located. Melts equilibrated under progressively higher fO_2 conditions occur towards the left of the diagram.

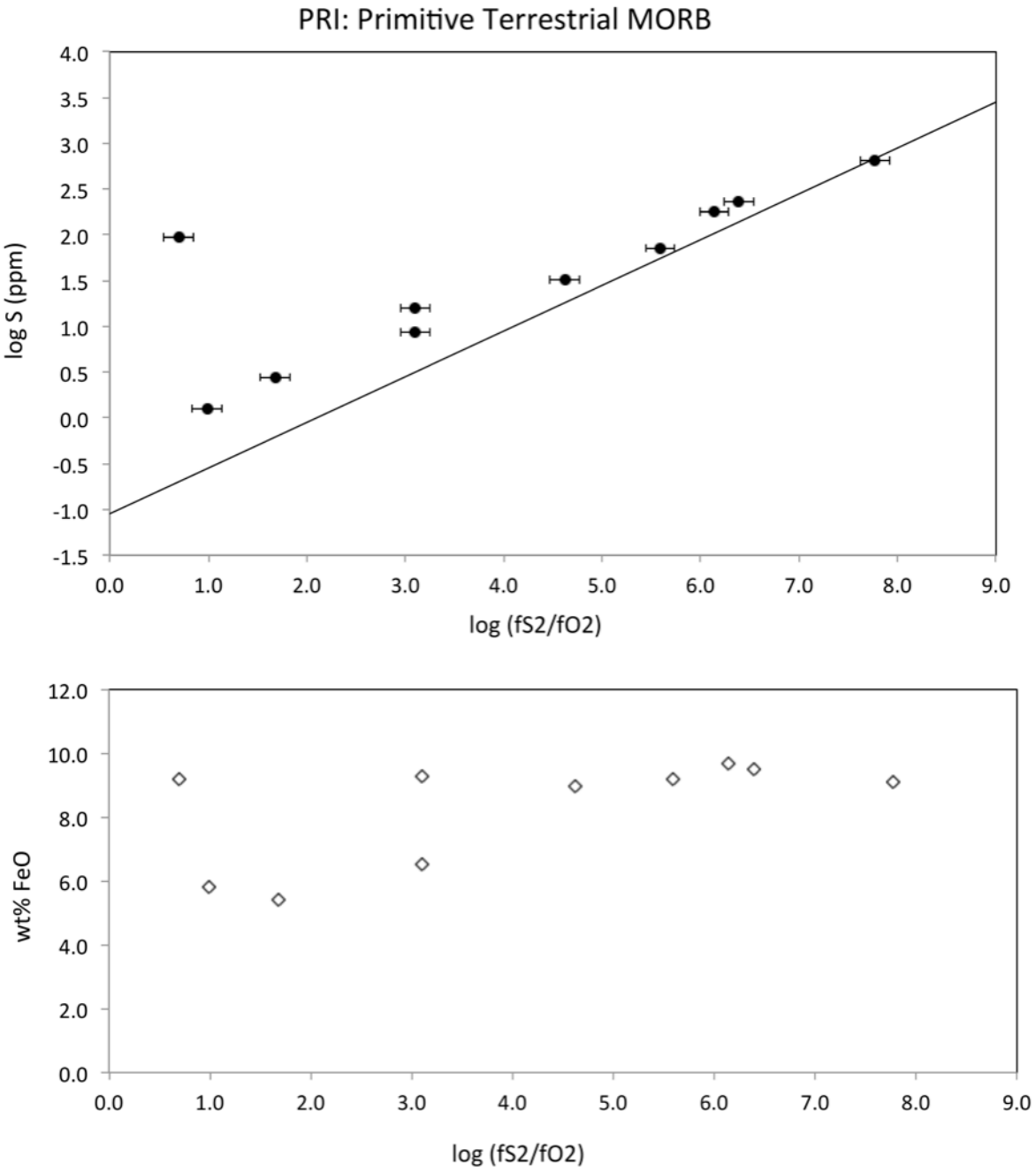


Figure 3.6.3.1d: Sulfur concentrations determined for the evolved terrestrial MORB ("EVO") by SIMS. FeO concentrations are shown below so that the region for which constant melt composition was maintained can be readily located. Melts equilibrated under progressively higher fO_2 conditions occur towards the left of the diagram.

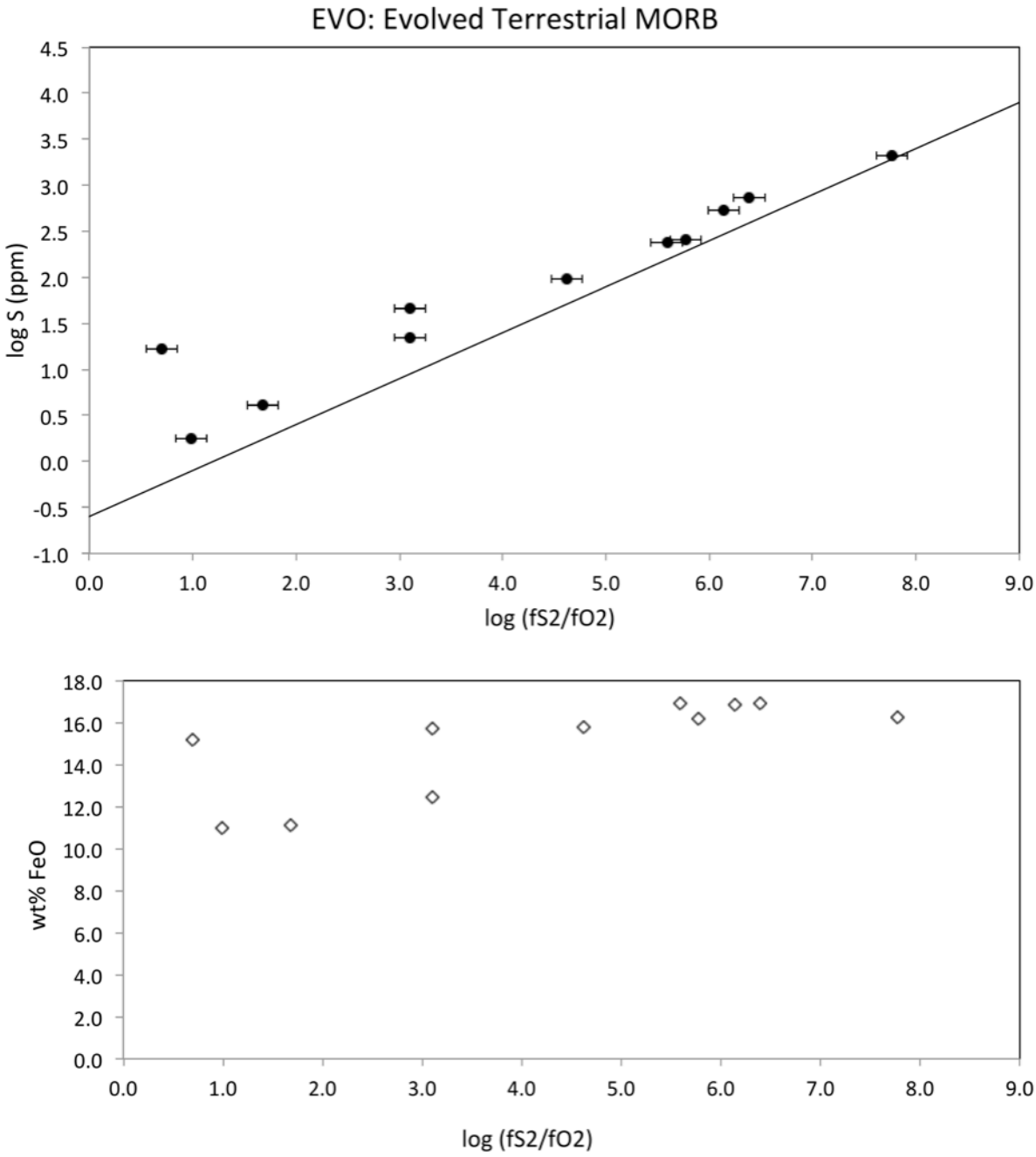


Figure 3.6.3.1e: Sulfur concentrations determined for the terrestrial andesite ("AND") by SIMS. FeO concentrations are shown below so that the region for which constant melt composition was maintained can be readily located. Melts equilibrated under progressively higher fO_2 conditions occur towards the left of the diagram.

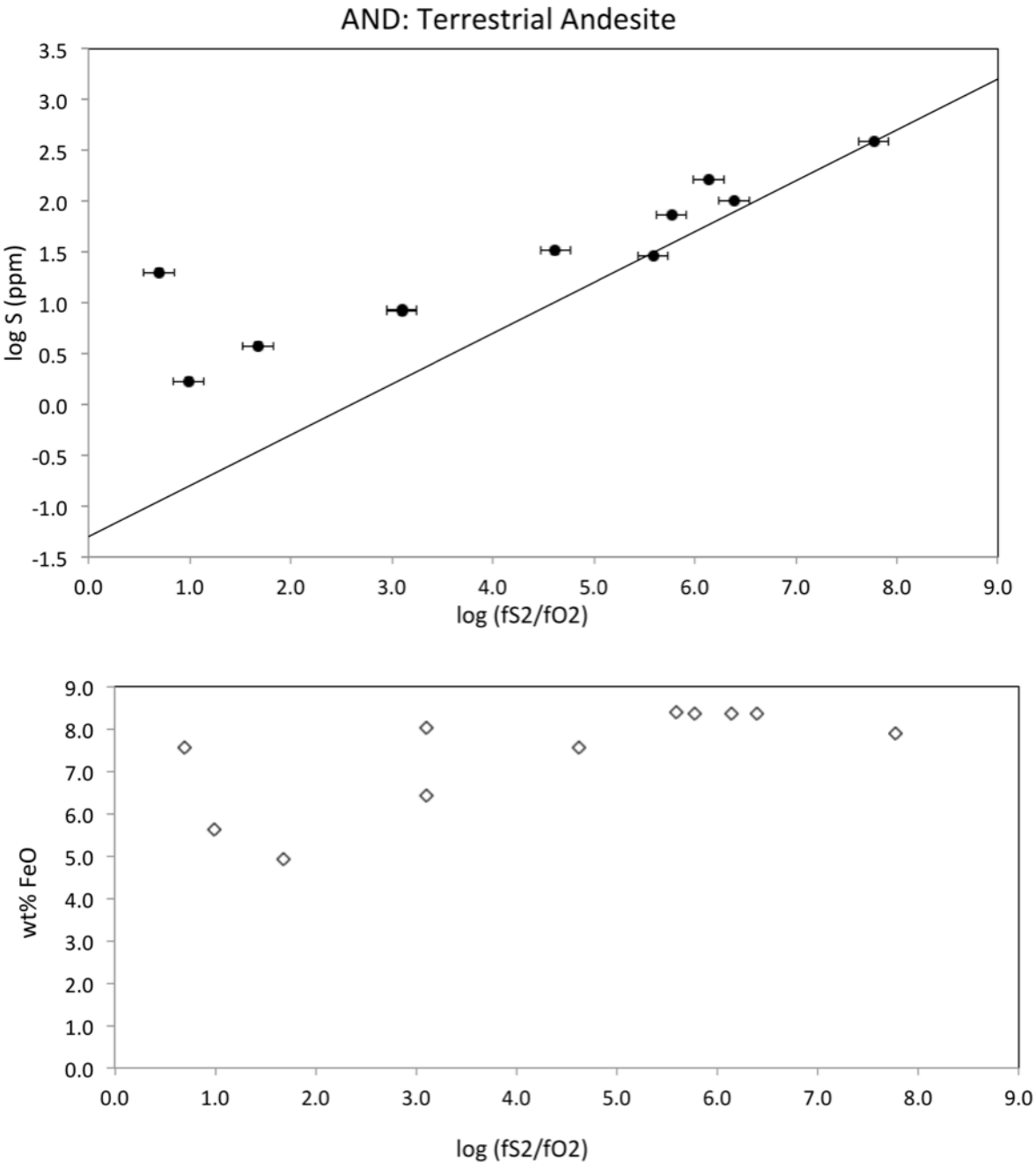
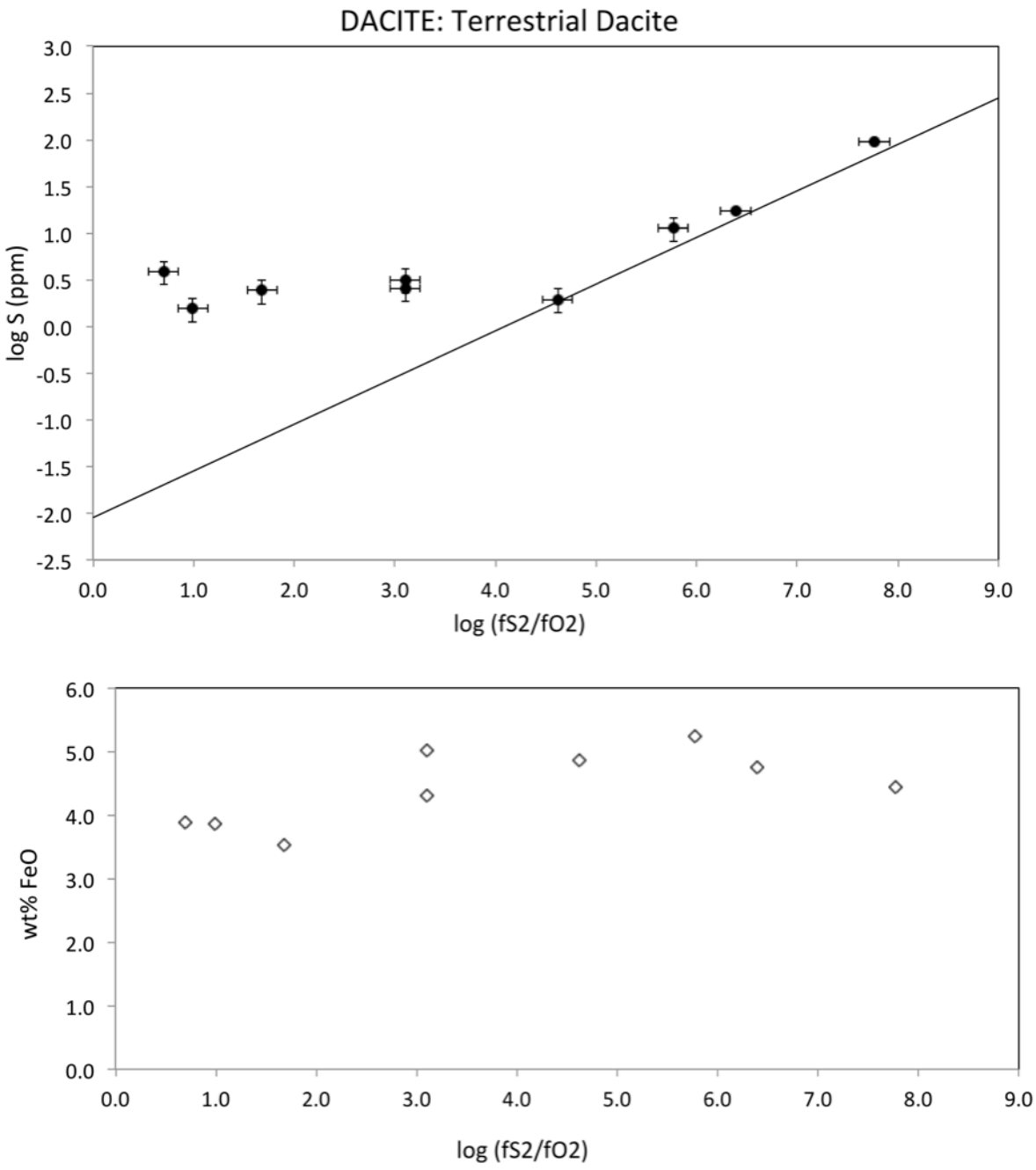


Figure 3.6.3.1f: Sulfur concentrations determined for the terrestrial dacite ("DAC") by SIMS. FeO concentrations are shown below so that the region for which constant melt composition was maintained can be readily located. Melts equilibrated under progressively higher fO_2 conditions occur towards the left of the diagram.



3.6.3.2 Estimating sulfur speciation from concentration data

Consider first, the most basic and qualitative interpretation of the data. Since the departures from the sulfide-dissolution trend are always positive (the glasses contain sulfur in excess of that expected from dissolution of pure sulfide) the presence of a species other than S^{2-} at high fO_2 is irrefutable, for depletions in Fe can only have reduced the sulfide concentration. The identity of this additional species is most likely to be the sulfate ion according to the XANES spectra presented in section 3.6.2.2, and other findings by previous researchers (Fleet *et al.* 2005, Klimm *et al.* 2012).

Were the FeO concentrations of each glass invariant across the fO_2 range, the sulfide concentration in each could simply be read off from the "pure sulfide line" fitted to the data, and the abundance of the additional species could be calculated from the height of each point above this line (representing the difference between ΣS and S^{2-}). Since in reality the data display a range of FeO concentrations, a correction has to be made for each. In general, the effect of Fe-loss is to depress this sulfide-line below its present position on each chart. The extent of this depression is point specific, since it depends on the magnitude of Fe-loss in each experiment.

Quantitative models relating the sulfur concentration at sulfide saturation (SCSS) with wt% FeO are available (Mavrogenes and O'Neill 2002, Li and Ripley 2005, Smythe *et al.* (2017), and have been shown to reliably reproduce experimental data for mafic to rhyolitic melts. These models essentially express a near-linear relationship between sulfide concentration and wt% FeO (with some minor effects exerted by the other elements present). We used the solubility model of Smythe *at al.* (2017) to calculate the sulfide concentrations for each experimental silicate glass, as well as for their intended compositions (assuming the full, initial complement of FeO). The former was divided by the latter to yield a scaling factor for each experiment, which could be multiplied by the "intended" sulfur concentration implied by the sulfide-line. This method rests upon the assumption that the linear relationship between wt% FeO and log(SCSS) also holds for wt% FeO and log(Cs) (Mavrogenes and O'Neill 2002). Corrections were applied in this manner to every glass equilibrated at or above the FMQ buffer, so as to estimate their true sulfide concentration. This is described in further detail in appendix 4.

The "pure sulfide line" was itself fitted by taking an average of sulfide capacities calculated for all experiments performed below FMQ (recall sulfide capacity's definition as $[S]^*(fS_2/fO_2)^{1/2}$. These values are discussed later on. Although desirable, it is not possible to display theoretical sulfate concentrations on the axes shown in figures 3.6.3.1a-e because the sulfate dissolution equilibrium

(equation 3.4) cannot be rearranged to express sulfate concentration as a function of the same variables.

Sulfate mole fractions calculated for the Fe-depleted experiments are plotted against fO_2 in figures 3.6.3.2a-e. The errors associated with these values are calculated using the maximum variation in sulfide capacity permitted by the scatter among the most reduced experiments. Differently stated, on each plot, the "pure sulfide" line (from which the sulfate mole fractions are calculated) was shifted up and down so as to lie on the uppermost and lowermost points – thus encompassing the total variation in position contained in the data. This procedure is perhaps unduly conservative, giving rise to the very large error-bars in plots 3.6.3.2a-e. On the other hand, these represent a very honest representation of the data. It is important to note that the data on each plot do not represent instances of a single melt composition, since they have suffered differing degrees of Fe-depletion. Therefore they do not usefully characterize the sulfide-sulfate transition for any particular melt. Nonetheless, they do permit inter-glass comparisons at each fO_2, allowing a further test of the hypothesis that sulfur speciation is a function of melt chemistry. As with the XANES-derived data, the data for the Dacitic melt (DAC) is presented alongside each of the other five melt compositions.

Despite the large errors associated with these modelled sulfate mole fractions, a clear difference can be observed between individual basaltic/andesitic and dacitic melts[3]. Independent of any the spectroscopic information from XANES, this confirms the presence of a major-element composition on sulfur speciation, and further supports the notion that Fe is the controlling element. Of course, this conclusion rests on the reliability of the models used to calculate the sulfide capacities.

[3] It is important to note that these comparisons are insensitive to the oxygen fugacity of equilibration, since the melts were equilibrated in the same gas mixture. The sources of error pertinent to these comparisons are those arising from the respective analytical techniques, and (most importantly) the modelling used to compensate for Fe-loss to the platinum loops.

Figure 3.6.3.2a: The sulfide-sulfate crossover for JFR-like and DAC-like melts, estimated using SIMS data and models for each melt's sulfide concentration.

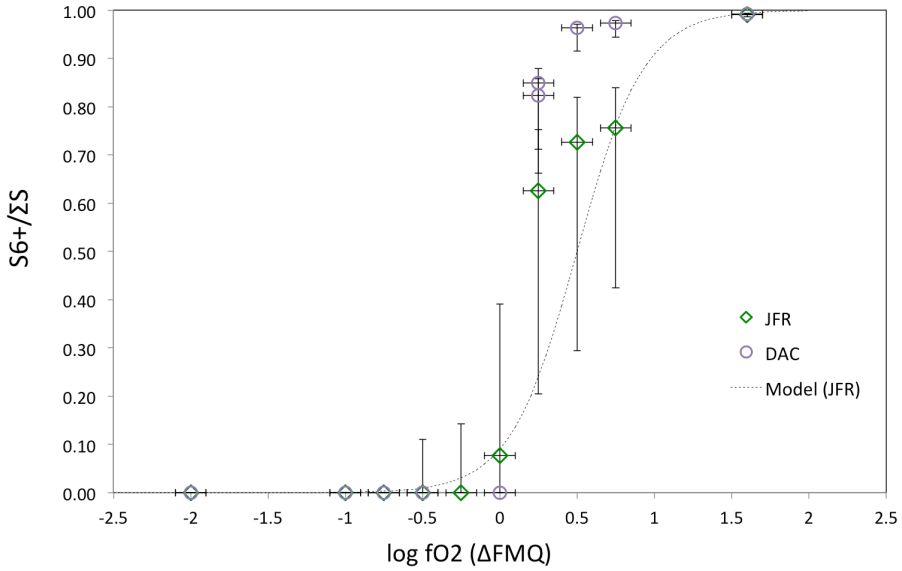


Figure 3.6.3.2b: The sulfide-sulfate crossover for DWF-like and DAC-like melts, estimated using SIMS data and models for each melt's sulfide concentration.

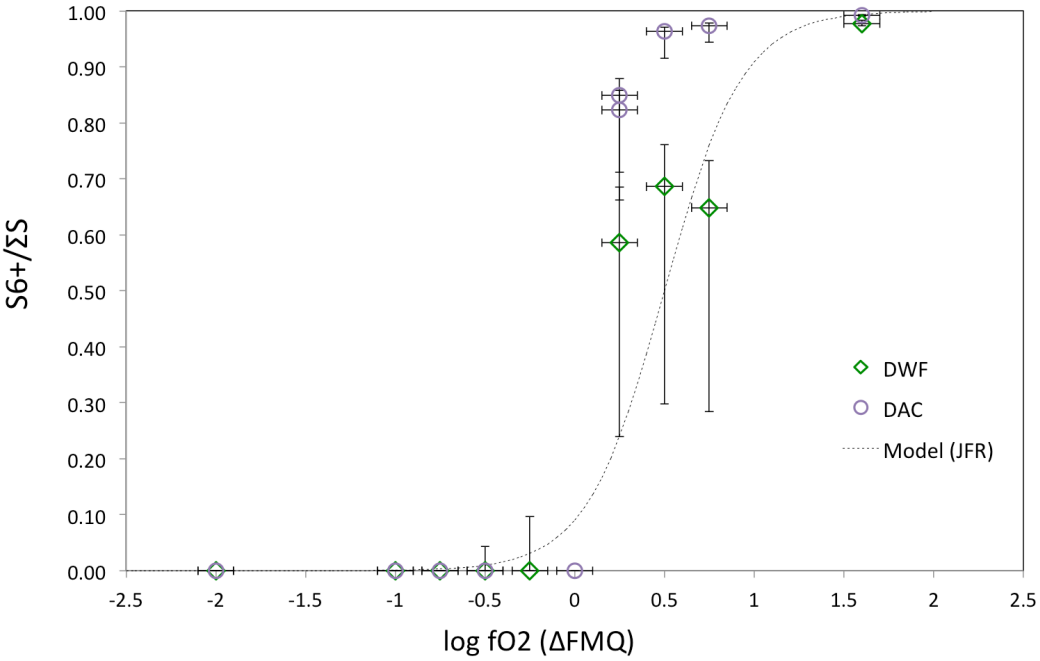


Figure 3.6.3.2c: The sulfide-sulfate crossover for PRI-like and DAC-like melts, estimated using SIMS data and models for each melt's sulfide concentration.

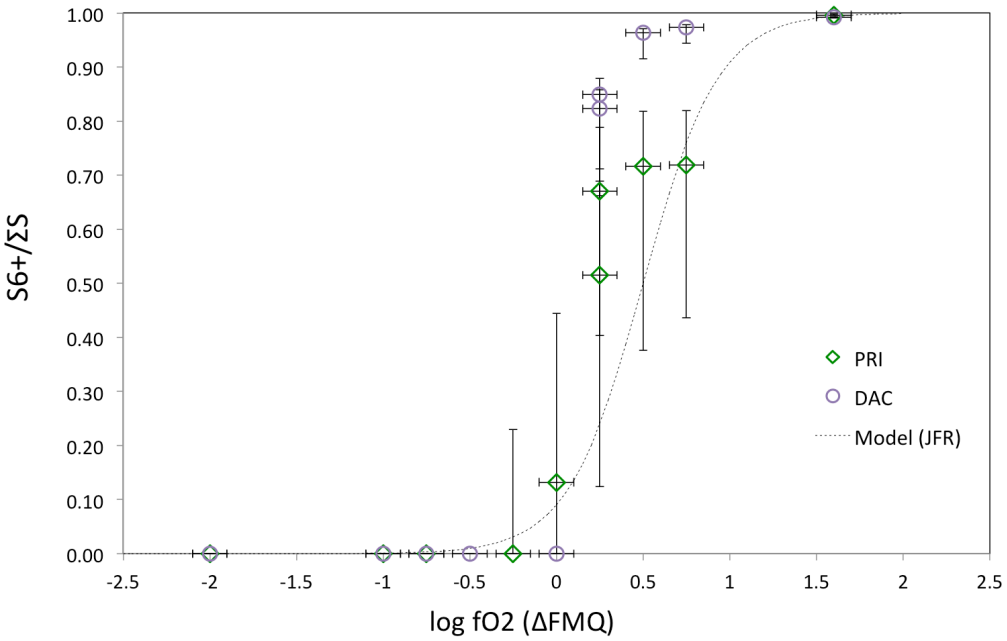


Figure 3.6.3.2d: The sulfide-sulfate crossover for EVO-like and DAC-like melts, estimated using SIMS data and models for each melt's sulfide concentration.

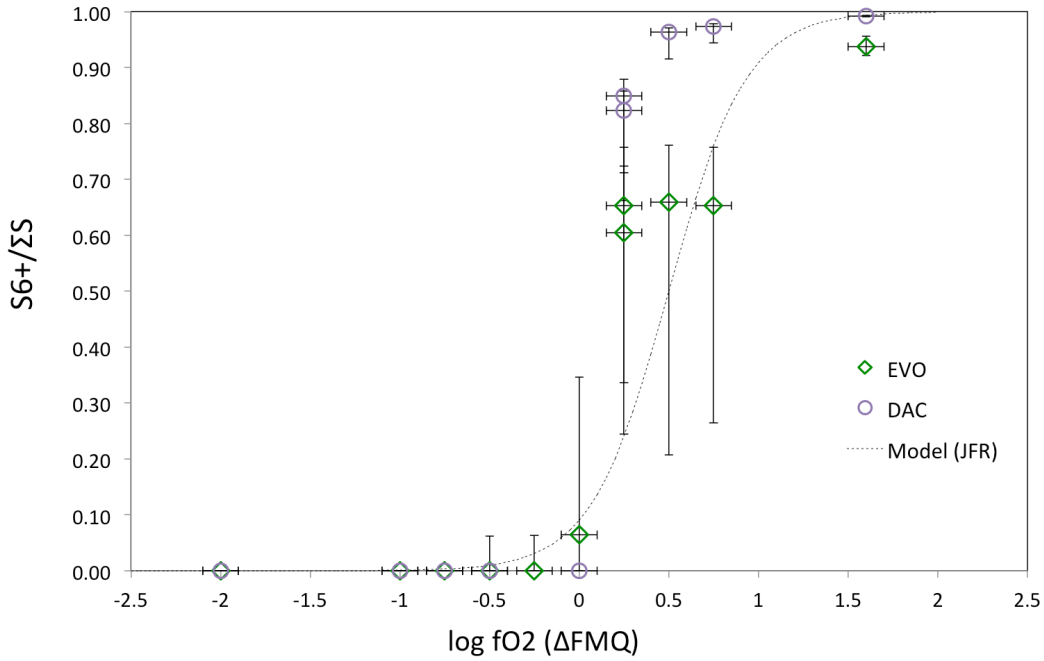
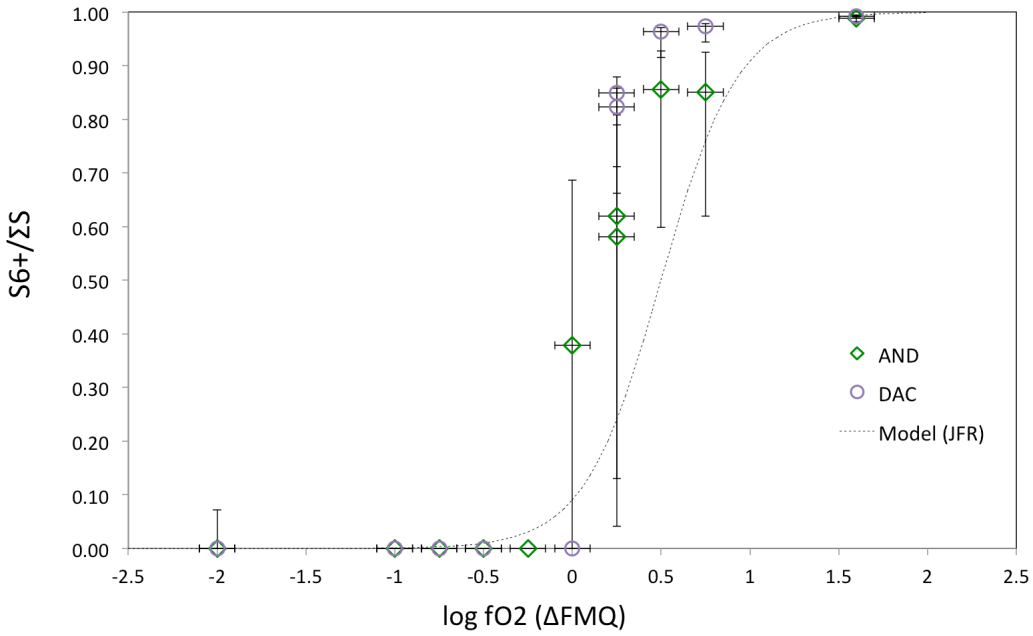


Figure 3.6.3.2e: The sulfide-sulfate crossover for AND-like and DAC-like melts, estimated using SIMS data and models for each melt's sulfide concentration. The implied difference in crossover position shown here is smaller than for the basaltic melts.

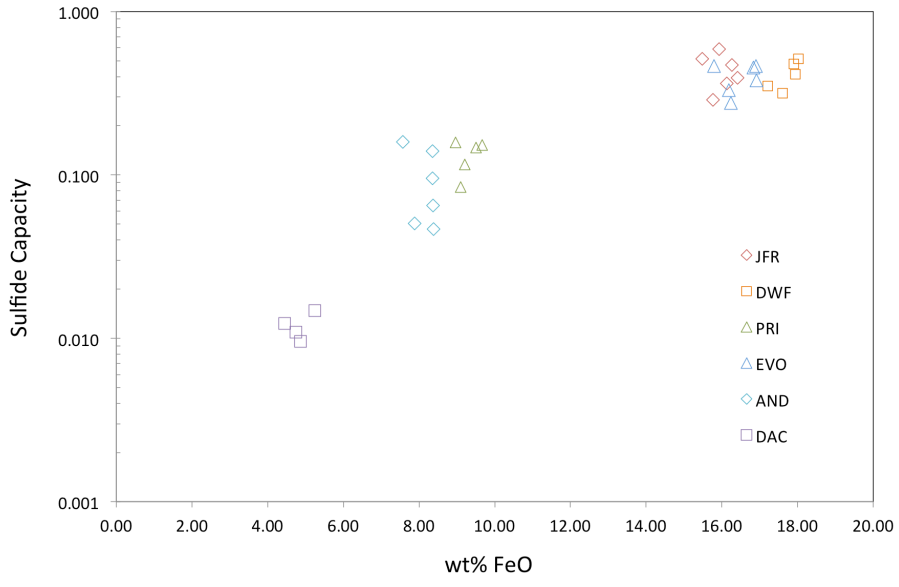


An obvious mechanism by which Fe could influence the sulfate/sulfide ratio, is by simply raising or lowering the sulfide capacity of a silicate melt. Melts with higher Cs would be expected to contain more sulfide (and thus a greater fraction of sulfide) than others when equilibrated at the same fO_2 and fS_2 - all else being equal – giving the appearance of a shift in crossover position. The dominance of FeO in determining sulfide capacities is well documented in the literature (e.g. Haughton *et al.* 1974, Li and Ripley 2005, O'Neill and Mavrogenes 2002), and the results of this study permit an additional test of this dependence for very Fe-rich compositions. Direct comparison with the models proposed by these studies is complicated by their contrasting experimental conditions, and the manner in which their expressions for the sulfide capacity have been formulated (in particular, the absence of terms accounting for temperature). However, the direction in which these models predict Cs to change with changes in FeO concentration may be assessed. Accordingly, sulfide capacities have been calculated for all melts here equilibrated under conditions more reducing than FMQ+0.13, and are shown in figure 3.6.3.2f. For all except the dacitic types, these glasses are believed to contain sulfide exclusively, judging by their redox ratios obtained from XANES. Cs has been shown to increase exponentially with the FeO concentration of basalts (O'Neill and Mavrogenes 2002), and this prediction is entirely consistent with the arrangement of the data in figure 3.6.3.2f: more FeO rich melts do exhibit higher values for Cs. The

location of the dacitic values below the hypothetical trend passing through the rest of the data is consistent with their mixed oxidation, since these data do not represent true sulfide capacities. However, whether the variations in Cs are alone responsible for the differences in speciation is impossible to deduce from these measurements on their own.

An alternative mechanism by which which Fe might influence sulfur speciation is by changing the activity coefficients of the sulfide and sulfate species in the silicate melts. The most direct way to test this is to saturate the melts with sulfide and sulfate, so that the chemical potentials of S^{2-} and S^{6+} can be fixed, and their concentrations in the melts measured. However, this method obviously requires the melts to be at saturation, and their behaviour at lower concentrations may not reflect that at saturation. A further phenomenon that also cannot be ruled out by the data collected here, is broadening (or compression) of the fO_2 range over which sulfur transitions from sulfide to sulfate. Theoretically, the width of this transition is determined exclusively by the coefficient of oxygen in the sulfide-sulfate equilibrium (eqn. 3.5). However, the *appearance* of a broader transition might be given by appropriate changes in either species' activity coefficients with concentration. It is especially important to remember that changes in fO_2 bring about changes in the speciation of Fe, which might in turn influence the activity coefficients of sulfide or sulfate. This possibility is discussed in more detail later. It is sufficient to say here that the possibility of a broader transition for the dacitic melts cannot verified by the data collected here, due to the sparseness of useable XANES spectra (sulfur concentrations in the Dacitic melts being prohibitively low).

Figure 3.6.3.2f: The sulfide capacities for reduced glasses calculated from SIMS data. The dependence on FeO content offers a possible explanation for the differing crossover conditions of the various melts.



3.6.4 Evaluation of SIMS results, and comparison with XANES

The XANES spectra presented in the previous sections indicate that for each melt studied, a change in speciation occurs, with sulfate ions replacing sulfide ions over a narrow fO_2 interval (approximately 1 log unit in width). This finding is confirmed by the SIMS data, which show that as conditions become more oxidizing, a positive deviation occurs from the line representing the sulfide concentration of each glass. As concerns the nature of the changes taking place, the two methods agree. They are disagree however over the positions of the crossover for the dacite.

In theory, the data's deviation from the "sulfide lines" in figures 3.6.3.1a-f mark the sulfide-sulfate crossover position in fO_2 space. For the basaltic and andesitic melts, the position implied by XANES does coincide with this divergence from sulfide line in the SIMS data. Importantly however, this is not the case for the Dacitic melt. The linear trend exhibited for the dacite between FMQ-2 and FMQ implies that the sulfide ion is present exclusively across this range. This contradicts the XANES spectra, which imply a crossover to sulfate domination at more reducing conditions. A likely resolution to this conundrum is that SIMS is insufficiently sensitive for measuring the differences in sulfur concentration taking place across this range. The discrepancy certainly calls into question the usefulness of SIMS as a tool for quantitatively monitoring sulfur speciation at such low concentrations (ppm).

The second major conclusion from XANES was that sulfate-sulfide crossover position is a function of silicate melt composition, in particular FeO concentration; positive differences in $S^{6+}/\Sigma S$ corresponding to lower FeO concentrations at the same fO_2. The uncertainties in $S^{6+}/\Sigma S$ from SIMS data are too large to usefully compare the basalts and andesite with one another, and in any case, their Fe-depletion means that they no longer represent instances of a single melt composition[4]. However, comparisons between individual basalts/andesites and dacitic melts, as presented in figures 3.6.3.2a-e, do indicate variation in $S^{6+}/\Sigma S$ larger than experimental uncertainties. Furthermore, the direction of this variation is consistent with the pattern establish previously, for which FeO reduces the $S^{6+}/\Sigma S$ at a given fO_2. It is important to bear in mind that this conclusion is somewhat uncertain, given the reservations expressed previously concerning the usefulness of SIMS as a tool for sensing speciation.

[4] It is for this reason that only relative differences in speciation between pairs of melts can be discussed.

3.7 DISCUSSION

3.7.1 A possible explanation for the observations: Fe-S coupling

Besides sulfur, iron is the only multivalent element present in the glasses in significant quantities[5]. Therefore it is not especially surprising that iron and sulfur speciation might be interdependent. However, what has been observed here is a dependence on the absolute concentration of iron, rather than simply its speciation.

This being the case, the relationship between FeO concentration and sulfur speciation might be an outcome of both element's sensitivity to fO_2. The fO_2 conditions of the transition from Fe^{2+} to Fe^{3+}, and S^{2-} to S^{6+}, are determined by the equilibrium constants for their respective electron-exchange reactions:

$$S^{2-}_{melt} + 2O_{2\,gas} = SO^{2-}_{4\,melt} \quad (3.12)$$

$$2\,FeO_{melt} + \tfrac{1}{2}O_{2\,gas} = Fe_2O_{3\,melt} \quad (3.13)$$

In both cases, the position of the crossover between the reduced and oxidized species depends on the value of the equilibrium constants for the two reactions, which are themselves determined by the activities of the various components in the silicate melt (at constant temperature). It is to be expected that the reactants and products of these equilibria might be coupled, such that the following equilibrium is realized in the silicate melt:

$$S^{2-} + 4\,Fe_2O_3 = SO^{2-}_4 + 8\,FeO \quad (3.14)$$

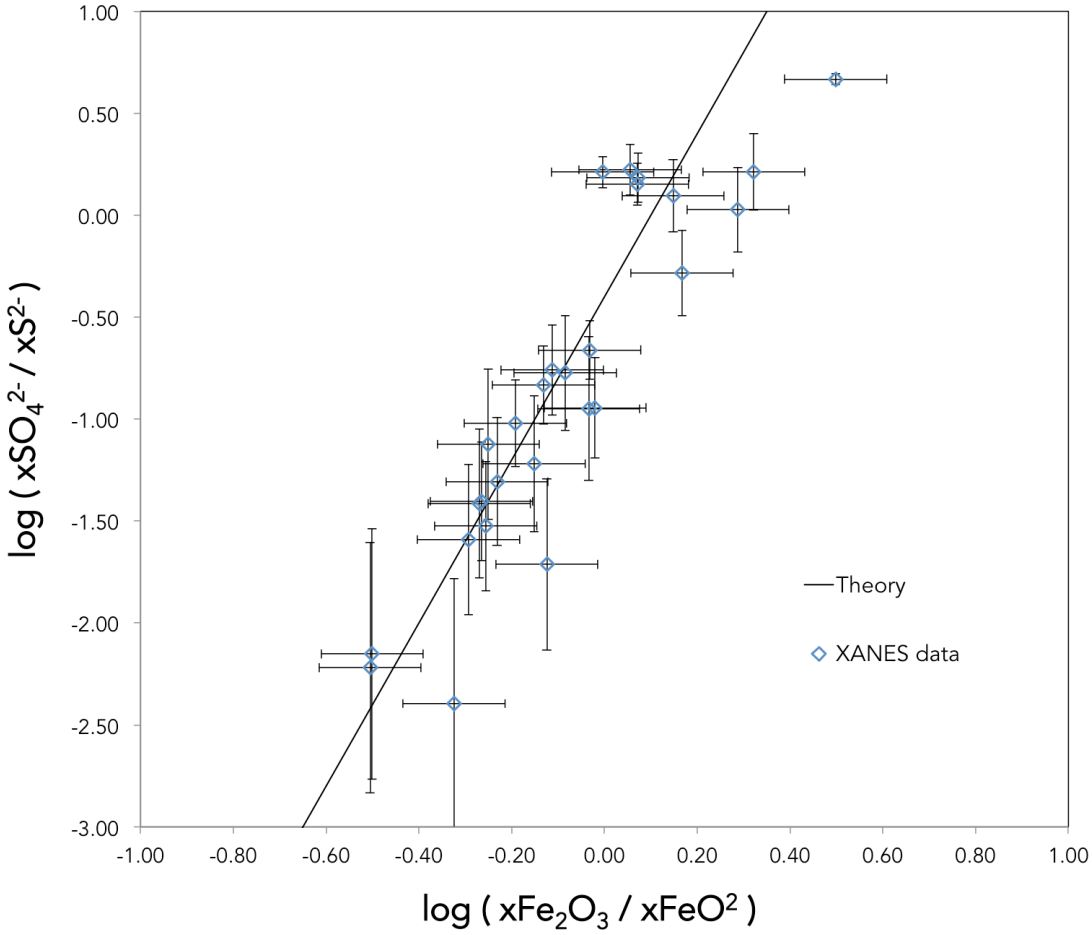
…for which the following relationship is implied:

$$log\frac{a\,SO^{2-}_4}{a\,S^{2-}} = 4\,log\frac{a\,Fe_2O_3}{a\,FeO^{\,2}} + log\,K \quad (3.15)$$

Note that there is no fO_2 term in this expression: the activities of both of the iron and sulfur species are completely determined by one another. Assuming ideal mixing of all components, the data in this study enable a test of this relationship, which is illustrated in figure 3.7.1. Note that S^{6+} is assumed here to reside in the silicate melt as SO_4^{2-}.

[5] Although manganese occurs at concentrations approaching 0.5 wt%, and also exhibits concentration changes consistent with sulfate mole fraction, the oxidation of MnO to MnO_2 occurs at far higher oxygen fugacities than those explored here (O'Neill and Pownceby 1993), so it can be considered exclusively divalent in the context of this study.

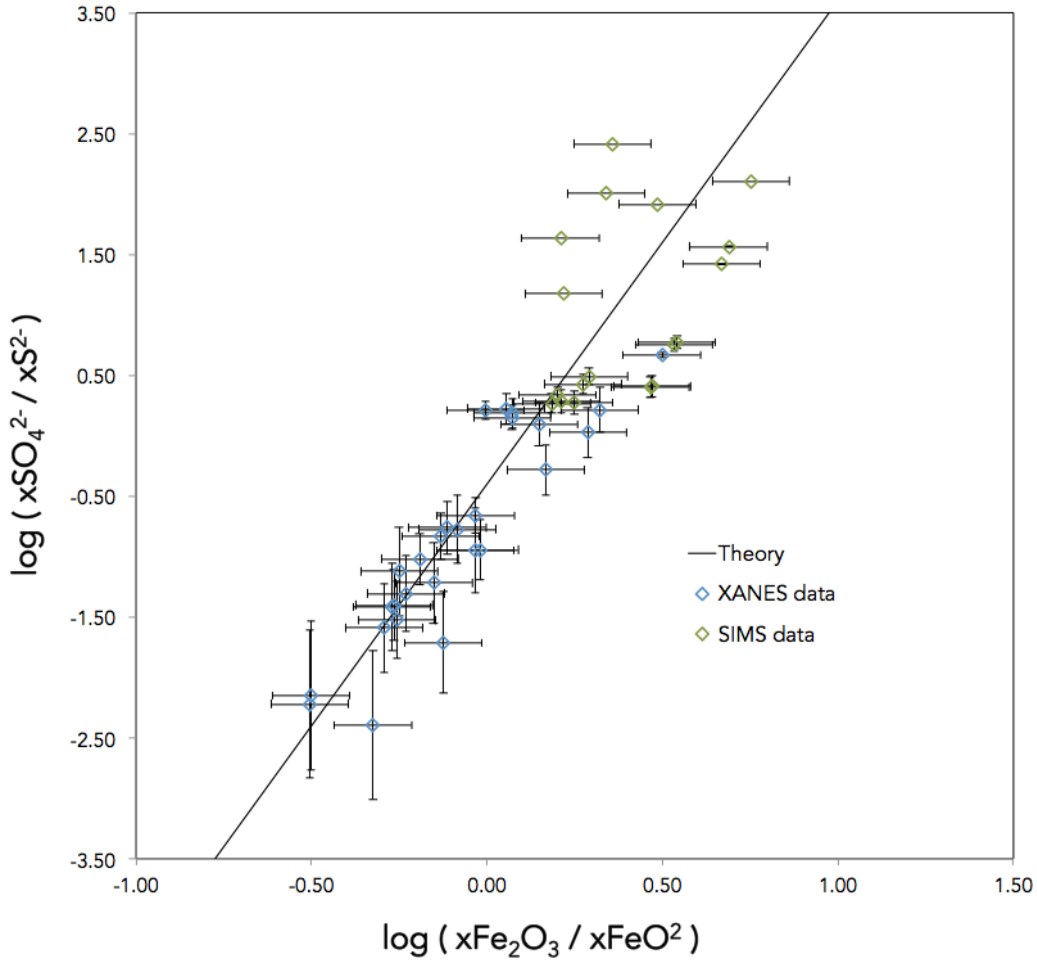
Figure 3.7.1a: The ratio Fe_2O_3/FeO^2 graphed against SO_4^{2-}/S^{2-} for the experimental glasses of this study. The solid line is the theoretical relationship predicted by equation 3.15, with an intercept calculated from the standard state Gibbs energies of reaction 3.14.



Since the procedure for calculating S^{6+}/S^{2-} ratios from XANES data is more straightforward than that using SIMS (no modelling is necessary), the XANES data are shown alone in figure 3.7.1a, and then together with the SIMS data in figure 3.7.1b. Errors in S^{6+}/S^{2-} are those displayed in the previous sections. The model of Sack *et al.* (1980) was used to calculate Fe^{2+}/Fe^{3+} ratios of each of the melts from their major-element chemistry and fO_2 of equilibration. From these, FeO and Fe_2O_3 were calculated. Errors in log (Fe_2O_3/FeO^2) comprise two components: the uncertainty in total FeO reported by the electron probe, and the uncertainty associated with the model used to calculate the Fe^{2+}/Fe^{3+} ratio for each glass.

The solid line in both figures is the theoretical trend, (explained in more detail presently) against which the XANES data exhibit an R-squared value of 0.75.

Figure 3.7.1b: Both XANES and SIMS data for the experimental glasses of this study. The solid line is the same theoretical relationship shown in the previous figure. Note the scatter introduced by the inclusion of the SIMS data.



As predicted, the data in figure 3.7.1a describe a linear trend, with the gradient required by the stoichiometry of the reaction in eqn. 3.14. The blue and green diamonds in figure 3.7.1b represent the XANES- and SIMS-derived data respectively. Despite plotting in the expected region of the chart, the SIMS-derived ratios introduce a considerable amount of scatter to the data, although, crucially, their inclusion does not weaken the coefficient of determination. It is important to note that this scatter is most severe for melts equilibrated under the most oxidizing conditions (where the logarithm of S^{6+}/S^{2-} is most sensitive to small uncertainties in this ratio), while those melts equilibrated under more reducing conditions fall inside the XANES-defined trend.

This broad agreement between these two complimentary datasets is encouraging, because they conform not only to the anticipated gradient, but also the expected intercept of the proposed

relationship. This intercept is equal to the *log K* term in equation 3.15. This value may be calculated from thermodynamic data, since it is related to the Gibbs energy of the reaction by:

$$\Delta G^\circ = -RT \log K \tag{3.16}$$

…and to the individual components' Gibbs energies of formation by:

$$\Delta G^\circ = G^\circ_{f\,FeSO4} + 8\,G^\circ_{f\,FeO} - G^\circ_{f\,FeS} - 4\,G^\circ_{f\,Fe2O3} \tag{3.17}$$

Gibbs energies of formation for each component at 1300°C and 1-atmosphere pressure (as pure phases) are available from Barin (1995), and were used to calculate *log K* for reaction 3.15. In the case of $FeSO_4$, data had to be extrapolated beyond the experimentally calibrated temperature range (which terminated at 727°C). A value of -0.4 was obtained for *log K*, which coincides nicely with the trend described by the XANES data (see the solid line in figures 3.7.1a and b).

Of the four components involved in expression 3.15, activity models are available only for FeO. The model of Wood and Wade (2013) was used to calculate activity coefficients for FeO for each of the silicate melts using the expression:

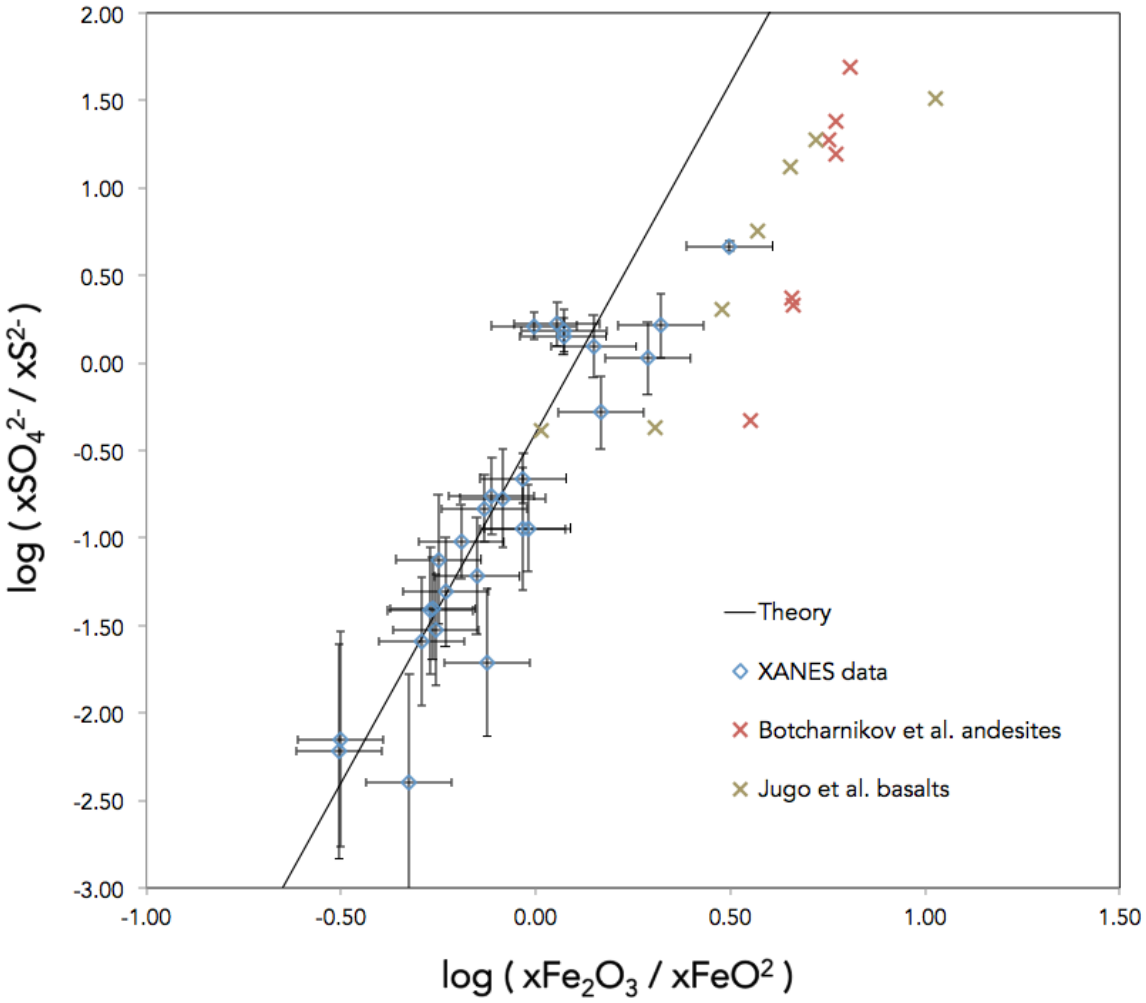
$$RT\,ln\,\gamma_{FeO} = -18994 + 99579X_{Na} + 192553X_{Al}X_{Si} + 282789X_{Ca}X_{Mg} + 79492X_{Ca}^2 + 120972X_{Fe}^2 \tag{3.18}$$

The values obtained were consistently around 1.3. The application of these values to the data (replacing FeO mole fractions) shifts the array of points horizontally by approximately one log unit in the positive direction, adjusting the implied *log K* value by around 4. In addition, it introduces more scatter to the data, weakening the R^2 value considerably. It is clear then that if equation 3.15 does describe a really existing relationship, the activities of FeO and Fe_2O_3 must vary together sympathetically, such that the trend in figure 2.7.1a is preserved. Application of the FeO activity coefficients to Fe_2O_3 does indeed have this effect, although this clearly is not a serious proposition at this point.

To test the generality of this relationship further, data from two additional experimental studies is included on figure 3.7.1c. These are the studies of Jugo *et al.* (2010) and Botcharnikov *et al.* (2011), who performed experiments on synthetic basalts and andesites in pressure vessels. The sulfate mole fractions in their materials were, like those here, determine by XANES. Although hydrous, and equilibrated at much lower temperatures and pressures (1050°C and 200MPa), these glasses define a similar trend with a similar orientation to that formed by the glasses of this study. The Jugo *et al.* (2010) basalts in particular, with a single exception, lie approximately parallel to the theoretical slope in figure 3.7.1c. The displacement from this theoretical slope might indicate that

the thermodynamic data used to define the equilibrium constant for equation 3.14 require adjustment (a shift by less than one log unit in SO_4^{2-}/S^{2-} would unite the two data sets), or alternatively it might reflect the differing run conditions of these experiments. Finally, it could reflect differing activity coefficients for the various species in these melts, as suggested in section 3.6.3.2. At the very least, the pattern described by the data demonstrates that both iron and sulfur undergo complimentary changes in valence between FMQ-2 and FMQ+2.

Figure 3.7.1c: Comparison between redox trends defined by XANES-derived ratios from this study and those of Jugo *et al.* (2010) and Botcharnikov *et al.* (2011). The solid line is the same theoretical relationship shown in the previous figures. The SIMS-derived data are excluded for consistency.

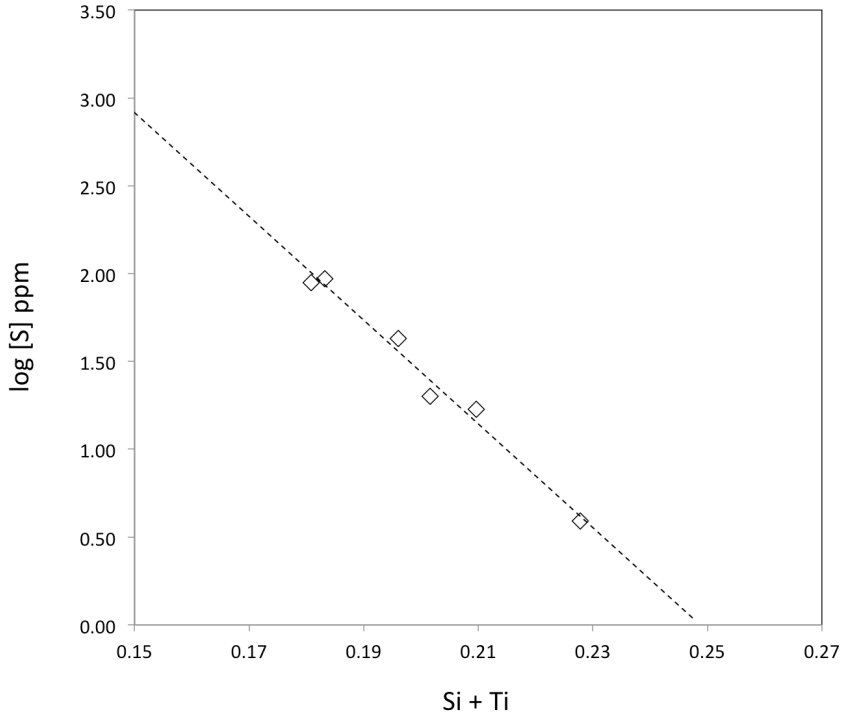


In summary, the closeness of fit of the XANES data to the trend implied by the iron and sulfur coupling relationship in equation 3.14 is reasonably strong, and certainly warrants further investigation. The agreement with other researcher's data is also encouraging. Direct measurement of the Fe^{3+}/Fe^{2+} ratio would reduce the uncertainty, as would measurements made on glasses with higher sulfur concentrations. If sufficiently robust, equation 3.15 might offer a convenient alternative to measuring sulfur speciation by spectroscopic methods.

3.7.2 A compositional control over sulfate capacity

The glasses prepared under the most oxidizing conditions (FMQ+1.6) exhibit a factor of 20 range in sulfur concentration. The XANES data indicate that under these conditions, virtually all of this sulfur exists in sulfate form. This range therefore demonstrates a major dependence of sulfate capacity on silicate melt composition. An exhaustive search revealed that the only aspect of melt chemistry reliably correlated with these sulfate concentrations is the abundance of the tetrahedrally-co-ordinated cations silicon and titanium, which display a strong inverse relationship with sulfate concentration. This relationship is displayed in figure 3.7.2a. The dashed line is a best-fit to the data, yielding an R-squared value of 0.98.

Figure 3.7.2a: Sulfate concentration plotted against the mole fractions of Si and Ti. The dashed line is a best fit to the data. These concentrations were obtained from the six glasses equilibrated at FMQ+1.6.

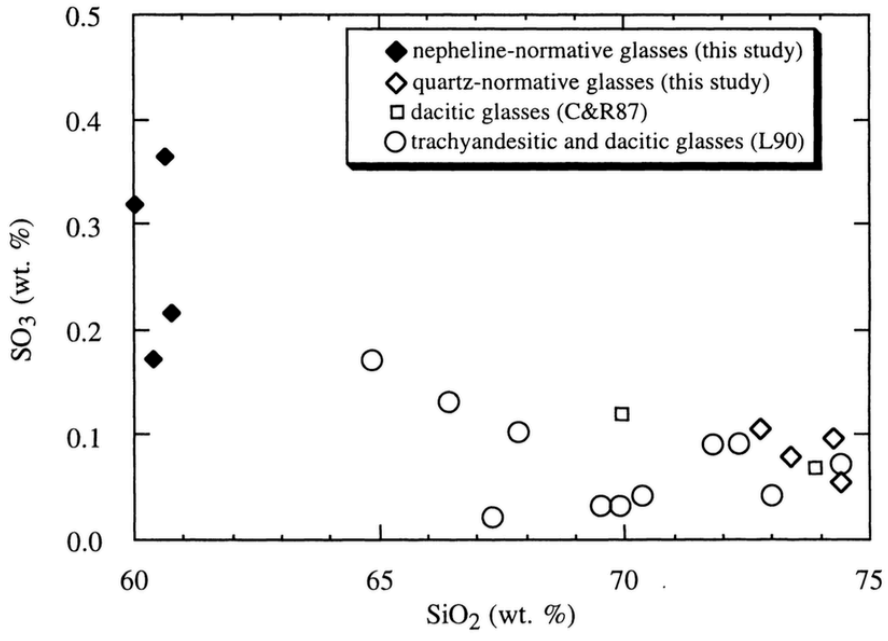


This relationship may be interpreted as an outcome of competition for the tetrahedrally co-ordinated sites within the silicate melt. Assuming that silicon and titanium preferentially occupy these sites within the melt's structure, melts that are richer in these elements might be expected to accept a smaller concentration of sulfate. This hypothesis is consistent with the structural information obtained about the sulfate species in similar materials by Klimm *et al.* (2012a), who observed a 1000^{-1} peak in the Ramen spectra of sulfate-bearing silicate melts, a feature that is characteristic of the ν1 stretching vibration associated with tetrahedrally co-ordinated sulfur.

Correlations with more explicit measures of melt structure such as NBO/T and optical basicity are very weak, suggesting that the mechanism for dissolution is the simple substitution of sulfur for silicon or titanium.

The question of whether a similar relationship holds for anhydrite solubility (rather than simply concentration, as shown in figure 3.7.2a) cannot be addressed by the data presented in this study. However, a compilation of experimental results published by Ducea *et al.* (1999) clearly shows an inverse relationship between the sulfate solubility and the silica concentration of hydrous rhyolitic melts (figure 3.7.2b). Assuming that this finding is robust, it supports the structural control over sulfate dissolution proposed here, and further suggests fractional crystallization as a mechanism for generating the large volumes of SO_2 gas expelled from arc volcanoes.

Figure 3.7.2b: Sulfate concentration plotted against the mole fractions of Si and Ti. The dashed line is a best fit to the data. These concentrations were obtained from the six glasses equilibrated at FMQ+1.6.



3.7.3 The importance of quench effects

A pertinent question is whether the species identified using XANES are those present within these silicates when molten, or whether appreciable electron exchange takes place during the quench. This consideration is especially relevant because Fe is also multivalent, and is present in much larger quantities than sulfur, permitting electron exchange between these two elements. The likelihood of this depends on how the position of equilibrium for equilibria 3.12 and 3.13 change with temperature. If lower temperature promotes the reduction of sulfur and oxidation of iron (for example), the rate of electron transfer between the various iron and sulfur species is then crucial. These parameters are extremely difficult to investigate experimentally, and while the overall electrical conductivity of silicate melts has been studied extensively (e.g. Ni *et al.* 2011, Guo *et al.* 2016), most investigations have concerned the transfer of large currents over macroscopic distances, rather than the transfer of individual electrons between neighbouring atoms.

The consistency of the results presented here (in particular the agreement between the observed and theoretical shape of the sulfide-sulfate crossovers) suggests that either electron transfer during the quench is negligible, or that its influence of the final speciation is systematic. Nonetheless, this remains a realistic possibility, and a sensible direction for further work.

3.8 CONCLUSIONS

3.8.1 Summary of findings

The most important finding of this study is the unambiguous identification of a major-element control over sulfur speciation in molten silicates. Although suggested by previous work, the series of experiments presented here, through their systematic fixing of the intensive parameters of T, P, oxygen and sulfur fugacity, provide the strongest evidence yet for a dependence of the $S^{6+}/\Sigma S$ ratio on the composition of its host silicate melt. As expected, sulfide and sulfate were the only species observed in all of the experimental materials, and their relative concentrations change places as the conditions of equilibration become more oxidizing. The data indicate that the position of this crossover in fO_2-space is around FMQ+0.5 for the most Fe-rich melts, FMQ for those with intermediate Fe-enrichment, and FMQ-1.5 for the most Fe-depleted melt studied. While the shape of the crossover for this latter composition could not be characterized by the methods employed here, the data available are consistent with the assumption that its shape is similar to those of the other five melts.

The explanation for this shift in redox crossover fO_2 that is most consistent with other information about sulfide dissolution, is that the activity of S^{2-} is dependent on a silicate melt's Fe concentration. Such a dependence suggests coupling between these two species in silicate melts. Consistent with this suggestion, the glass compositions measured by XANES exhibit a simple linear relationship between their S^{6+}/S^{2-} and $Fe_2O_3/(FeO)^2$ ratios. The general agreement between the XANES- and SIMS-derived data is particularly encouraging, since these represent entirely independent methods for measuring the S^{6+}/S^{2-} ratio. If sufficiently general and robust, this relationship might provide a useful way to characterize sulfur speciation in the future without measuring it directly, by instead making the much simpler measurements of total Fe concentration and Fe^{3+}/Fe^{2+} ratio.

A final conclusion is that under oxidizing conditions, a strong inverse correlation exists between sulfate concentration (measured by SIMS) and the abundance of the tetrahedrally co-ordinated cations SiO_2 and TiO_2 in each silicate melt. An explanation for this that invokes activity-composition relationships is likely to be complex, because there is no correlation between sulfate concentration any particular component in the melts. Alternatively, an explanation involving considerations about melt structure seems more plausible, given the tetrahedral co-ordination implied for the sulfate ion by other spectroscopic methods (Raman spectroscopy).

3.9 – REFERENCES

Alonso Mori, R., Paris, E., Giuli, G., Eeckhout, S.G., Kavcic, M., Bucar, K., Petterson, L.G.M. and Glatzel, P. (2009). Electronic structure of sulfur studied by X-ray absorption and emission spectroscopy. *Anal. Chem*, 81, pp.6516-6525

Barin, I. (1995). Thermochemical Data of Pure Substances *VCH Verlagsgesellschaft mbH*

Bertka, C.M. and Holloway, J.R. (1994a). Anhydrous partial melting of an iron-rich mantle I: subsolidus phase assemblages and partial melting phase relations at 10 to 30 kbar. *Contributions to Mineralogy and Petrology*, 115(3), pp.313–322.

Bertka, C.M. and Holloway, J.R. (1994b). Anhydrous partial melting of an iron-rich mantle II: primary melt compositions at 15 kbar. *Contributions to Mineralogy and Petrology*, 115(3), pp.323–338.

Botcharnikov, R.E., Linnin, R.L., Wilke, M., Holtz, F., Jugo, P.J. and Berndt, J. (2011). High gold concentrations in sulphide-bearing magma under oxidizing conditions. *Nature Geoscience*, 4, pp.112-115.

Carmichael, I.S.E, Turner, F.J. and Verhoogen, J. (1974). Igneous Petrology. *McGraw-Hill*.

Carroll, M.R. and Rutherford, M.J. (1985). Sulfide and sulfate saturation in hydrous silicate melts. *Journal of Geophysical Research*, 90(S02), pp.C601–C612.

Carroll, M.R. and Rutherford, M.J. (1987). The stability of igneous anhydrite: Experimental results and implications for sulfur behavior in the 1982 El Chichon trachyandesite and other evolved magmas. *Journal of Petrology*, 28(5), pp.781–801.

Carroll, M.R. and Rutherford, M.J. (1988). Sulfur speciation in hydrous experimental glasses of varying oxydation states: Results from measured wavelength shifts of sulfur X-rays. *American mineralogist*, 73(February 2016), pp.845–849.

Deer, W.A., Howie, R.A. and Zussman, J. (1992). An introduction to the Rock-forming minerals. *Pearson Education Limited*, 2nd edition.

Ducea, M.N., McInnes, B.I.A. and Wyllie, P.J. (1999). Experimental determination of compositional dependence of hydrous silicate melts on sulfate solubility. *European Journal of mineralogy*, 11, pp.33-43.

Farrell, S.P., Fleet, M., Stekhin, I., Kravtsova, A., Soldatov, A.V. and Liu, X. (2002). Evolution of local electronic structure in alabandite and niningerite solid solutions [(Mn,Fe)S, (Mg,Mn)S,

(Mg,Fe)S] using sulfur K- and L-edge XANES spectroscopy. *American Mineralogist*, 87(10), pp.1321–1332.

Fincham, C.J.B. and Richardson, F.D. (1954). The Behaviour of Sulphur in Silicate and Aluminate Melts. *Proceedings of the Royal Society A: Mathematical, Physical and Engineering Sciences*, 223(1152), pp.40–62.

Fleet, M.E., Liu, X., Harmer, S.L. and King, P.L. (2005). Sulfur K-Edge XANES Spectroscopy: Chemical State and Content of Sulfur in Silicate Glasses. *The Canadian Mineralogist*, 43(5), pp.1605–1618.

Gale, A., Dalton, C.A., Langmuir, C.H., Su, Y. and Schilling, J-G. (2013). The mean composition of ocean ridge basalts. *Geochemistry, Geophysics, Geosystems*, 14(3), pp.489–518.

Gendrin, A., Mangold, N., Bibring, J-P., Langevin, Y., Gondet, B., Poulet, F., Bonello, G., Quantin, C., Mustard, J., Arvidson, R. and LeMouelic, S. (2005). Sulfates in Martian layered terrains: the OMEGA/Mars Express view. *Science (New York, N.Y.)*, 307(5715), pp.1587–91.

Guo, X., Chen, Q. and Ni, H.W. (2016). Electrical conductivity of hydrous silicate melts and aqueous fluids: Measurement and applications. *Science China Earth Sciences*, 59(5), pp.889–900.

Haughton, D.R., Roeder, P.L. and Skinner, B.J. (1974). Solubility of sulfur in mafic magmas. *Economic Geology*, 69(4), pp.451–467.

Hauri, E., Wanh, J., Dixon, J.E., King, P.L., Mandeville, C. and Newman, S. (2002). SIMS analysis of volatiles in silicate glasses 1. Calibration, matrix effects and comparisons with FTIR. *Chemical Geology*, 183, pp.99-114.

Jayasuriya, K.D., O'Neill, H.S.T., Berry, A.J and Campbell, S.J. (2004). A Mossbauer study of the oxidation state of Fe in silicate melts. *American Mineralogist*, 89, pp.1597-1609.

Jugo, P.J., Luth, R.W., Richards, P. (2005). An Experimental Study of the Sulfur Content in Basaltic Melts Saturated with Immiscible Sulfide or Sulfate Liquids at 1300 C and 1.0 GPa. *Journal of Petrology*, 46(4), pp.783–798.

Jugo, P.J., Wilke, M. and Botcharnikov, R.E. (2010). Sulfur K-edge XANES analysis of natural and synthetic basaltic glasses: Implications for S speciation and S content as function of oxygen fugacity. *Geochimica et Cosmochimica Acta*, 74(20), pp.5926–5938.

King, P.L., and McLennan, S.M. (2010). Sulfur on Mars. *Elements*, 6, pp.107-112.

Klimm, K., Kohn, S.C., O'Dell, L.A., Botcharnikov, R.E. and Smith, M.E., (2012a). The dissolution mechanism of sulphur in hydrous silicate melts. I: Assessment of analytical techniques in determining the sulphur speciation in iron-free to iron-poor glasses. *Chemical Geology*, 322–323, pp.237–249.

Klimm, K., Kohn, S.C., O'Dell, L.A., Botcharnikov, R.E. and Smith, M.E. (2012b). The dissolution mechanism of sulphur in hydrous silicate melts. II: Solubility and speciation of sulphur in hydrous silicate melts as a function of fO2. *Chemical Geology*, 322–323, pp.250–267.

Kozdon, R., Kita, N.T., Huberty, J.M., Fournelle, J.H., Johnson, C.A and Valley, J.W. (2010). In situ sulfur isotope analysis of sulfide minerals by SIMS: Precision and accuracy, with application to thermometry of ~3.5 Ga Pilbara cherts. *Chemical Geology*, 275, pp.243-253.

Lennie, A R. and Vaughan, D.J. (1996). Spectroscopic studies of iron sulfide formation and phase relations at low temperatures. *Mineral Spectroscopy: a Tribute to Roger G. Burns*, (5), pp.117–131.

Li, C. and Ripley, E.M. (2005). Empirical equations to predict the sulfur content of mafic magmas at sulfide saturation and applications to magmatic sulfide deposits. *Mineralium Deposita*, 40(2), pp.218–230.

Luhr, J.F. (2008). Primary igneous anhydrite: Progress since its recognition in the 1982 El Chichón trachyandesite. *Journal of Volcanology and Geothermal Research*, 175(4), pp.394–407.

Mandeville, C.W. (2010). Sulfur: A Ubiquitous and Useful Tracer in Earth and Planetary Sciences. *Elements*, 6(2), pp.75–80.

Mathez, E.A. (1976). Sulfur solubility and magmatic sulfides in submarine basalt glass. *Journal of Geophysical Research*, 81(23), pp.4269–4276.

McLennan, S.M., Boynton, W.V., Karunatillake, S., Hahn B.C. and Taylor, G.J. (2010). Distribution of sulfur on the surface of Mars determined by the 2001 Mars Odyssey Gamma Ray Spectrometer. *40th Annual Lunar and Planetary Science Conference*, 41, pp.2174.

Metrich, N. and Clocchiatti, R. (1996). Sulfur abundances and its speciation in oxidized melts. *Geochemica et Cosmochemica Acta*, 60(21), pp.4151–4160.

Métrich, N. (2002). Presence of sulfite (S IV) in arc magmas: Implications for volcanic sulfur emissions. *Geophysical Research Letters*, 29(11), pp.1538.

Métrich, N., Susini, J., Foy, E., Farges, F., Massare, D., Sylla, L., Lequien, S. and Bonnin-Mosbah, M. (2006). Redox state of iron in peralkaline rhyolitic glass/melt: X-ray absorption micro-spectroscopy experiments at high temperature. *Chemical Geology*, 231(4), pp.350–363.

Newville, M. (2004). Fundamentals of XAFS, *Consortium for Advanced Radiation Sources, University of Chicago, IL*.

Ni, H., Keppler, H., Manthilake, M.A.G.M. and Katsura, T. (2011). Electrical conductivity of dry and hydrous $NaAlSi_3O_8$ glasses and liquids at high pressures. *Contributions to Mineralogy and Petrology*, 162(3), pp.501–513.

O'Neill, H.S.C. and Pownceby, M.I. (1993). Thermodynamic data from redox reactions at high temperatures. II. The MnO-Mn_30_4 oxygen buffer, and implications for the thermodynamic properties of MnO and Mn_30_4. *Contributions to Mineralogy and Petrology*, 114, pp.315–320.

O'Neill, H.S.C. and Mavrogenes, J.A. (2002). The Sulfide Capacity and the Sulfur Content at Sulfide Saturation of Silicate Melts at 1400°C and 1 bar. *Journal of Petrology*, 43(6), pp.1049–1087.

Paris, E. Giuli, G., Carroll M.R. (2001). The valence and speciation of sulfur in glasses by X-ray absorption spectroscopy. *The Canadian Mineralogist*, 39, pp.331–339.

Ravel, B. (2005). A practical introduction to multiple scattering theory. *Journal of Alloys and Compounds*, 401(1–2), pp.118–126.

Ravel, B., and Newville, M. (2005). ATHENA, ARTEMIS, HEPHAESTUS: data analysis for X-ray absorption spectroscopy using IFEFFIT, Journal of Synchrotron Radiation 12, pp.537–541.

Ripley, E.M., Li, C., Moore, C.H., Elswick, E.R., Maynard, J.B., Paul, R.L., Sylvester, P., Seo, J.H. and Shimizu, N. (2011). Analytical Methods for Sulfur Determination in Glasses, Rocks, Minerals and Fluid Inclusions, *Reviews in Mineralogy and Geochemistry* 73, pp.9-39.

Sack, R.O., Carmichael, I.S.E., Rivers, M., Ghiorso, M.S., 1980. Ferric-ferrous equilibria in natural silicate liquids at 1 bar. *Contributions to Mineralogy and Petrology*, 75(4), pp.369–376.

Self, S. (2006). The effects and consequences of very large explosive volcanic eruptions. *Philosophical transactions. Series A, Mathematical, physical, and engineering sciences*, 364(1845), pp.2073–2097.

Smythe, D.J., Wood, B.J. and Kiseeva, E. (2017). The S content of silicate melts at sulfide saturation: new experiments and a model incorporating the effects of sulfide composition. *American Mineralogist*. DOI: 10.2138/am-2017-5800CCBY.

Wallace, P.J. and Carmichael, I.S.E. (1994). S speciation in submarine basaltic glasses as determined by measurements of S Kα X-ray wavelength shifts. *American Mineralogist*, 79(1–2), pp.161–167.

Werner, F. and Prietzel, J. (2015). Standard Protocol and Quality Assessment of Soil Phosphorus Speciation by P K-Edge XANES Spectroscopy. *Environmental Science and Technology*, 49(17), pp.10521–10528.

Wilke, M. Jugo, P.J., Klimm, K., Susini, J., Botcharnikov, R., Kohn, S.C. and Janousch, M. (2008). The origin of S^{4+} detected in silicate glasses by XANES. *American Mineralogist*, 93(1), pp.235–240.

Wilke, M., Klimm, K. and Kohn, S.C. (2011). Spectroscopic Studies on Sulfur Speciation in Synthetic and Natural Glasses. *Reviews in Mineralogy and Geochemistry*, 73(1), pp.41–78.

White, W.B., Johnson, S.M and Dantzig, G.B. (1958). Chemical Equilibrium in Complex Mixtures. *Journal of Chemical Physics*, 28(5), pp.751-755.

Wood, B.J. and Wade, J. (2013). Activities and volatilities of trace components in silicate melts: A novel use of metal-silicate partitioning data. *Contributions to Mineralogy and Petrology*, 166(3), pp.911–921.

Chapter 4

High Pressure experiments related to partial melting of the Martian mantle

4.1 - ABSTRACT

Experiments have been performed at high pressure (1.5GPa) to measure the sulfur concentration at sulfide saturation (SCSS) for a ~10% partial melt of the putative Martian mantle. The value obtained compares favourably (±20%) with recent models for this parameter, which assume a positive dependence on FeO concentration, and a negative dependence on pressure. Additional experiments exploring sulfur dissolution under more oxidizing conditions are also presented, and the valence of sulfur in their quenched glasses determined using XANES. No evidence for mixed oxidation states was observed under the conditions of fO_2 explored, constraining the position of the sulfide-sulfate crossover at 1.5GPa to between +0.8 and –2 log units relative to the fayalite-magnetite-quartz (FMQ) buffer. Attempts to more precisely locate the fO_2 of this transition by varying the ratios of reduced and oxidized starting materials (FeS and $FeSO_4$) were unsuccessful.

Comparisons between the SCSS reported here and measured sulfur concentrations in Martian meteorites imply either significant sulfur loss prior to their crystallization, or mantle concentrations of sulfur lower than those presently accepted. There is no way to conclusively distinguish between these alternatives, but the extraordinary abundance of sulfur in the sedimentary rocks of Mars' surface suggests that sulfur has been lost from the basalts that originally transported it from the mantle, and potentially represent the sink for this loss.

In addition, Rare Earth Element (REE) partitioning experiments have been performed for Martian primary phases in equilibrium with a 10% partial melt similar to that described above. These experiments confirm the validity of the elastic strain model for pyroxene and olivine in equilibrium with Fe-rich melts, confirming that partitioning in these systems is insensitive to melt composition. The partition coefficients obtained enable modelling of a simple end-member case of partial melting process in Mars, and confirm that for both the slightly depleted (SD) and heavily depleted (HD) shergottites, melt-solid equilibria involving a phase in addition to pyroxene are necessary to explain their chondrite normalized REE profiles. This conclusion is consistent with the presently accepted view that Mars' mantle is partitioned into chemically separate reservoirs.

4.2 – INTRODUCTION AND MOTIVATION

4.2.1 Sulfur in Martian meteorites

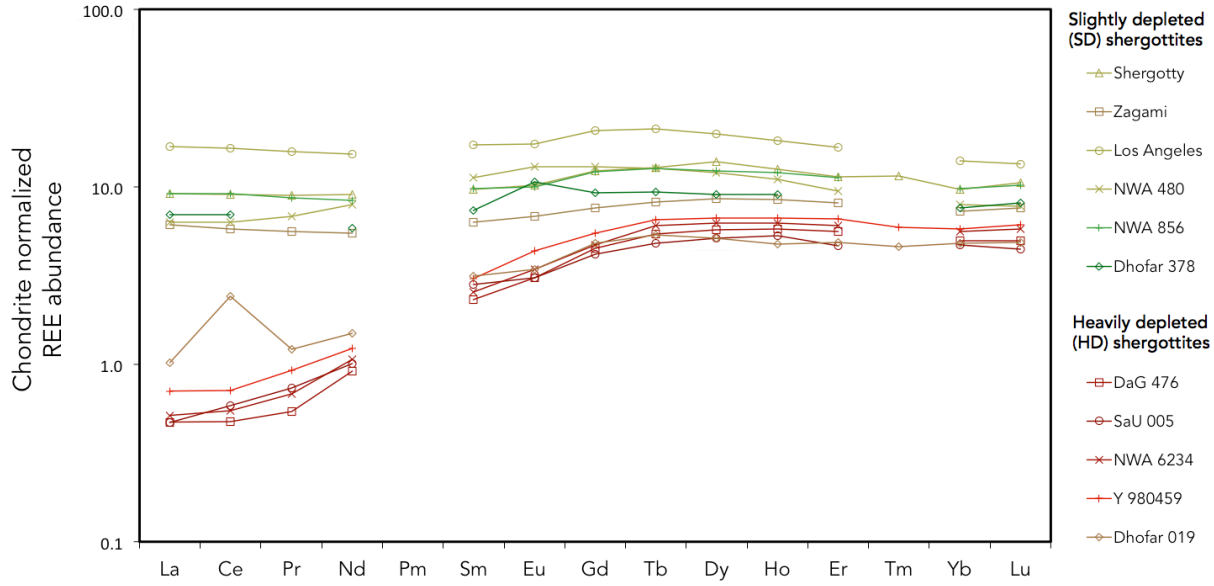
Martian basaltic meteorites contain widely varying quantities of sulfur, mostly in the form of sulfide minerals. Measured concentrations range from below 100 to almost 3000ppm, averaging 1067ppm, with a standard deviation of 739 (Ding *et al.* 2015). Since many of these meteorites do not represent true primary melts (frequently containing cumulus minerals, principally olivine), it is unclear whether they were sulfide-saturated during their separation from the Martian mantle (McSween 1994). As explained in the introduction, this question of saturation (or not) is critical for understanding both the bulk concentration of sulfur on Mars, and its distribution between the Martian core, mantle and crust, because reverse-modelling the genesis of these basalts is the most direct way of constraining these parameters.

Consistent with its importance, prediction of sulfur concentration at sulfide saturation (SCSS) for basaltic melts has been attempted by many researchers, and successful models have been developed (most notably Li and Ripley 2005, Jugo *et al.* 2009, Smythe *et al.* 2017). However, the applicability of these models to basalts with the super-terrestrial FeO contents characterized by Martian samples has not been comprehensively investigated. Furthermore, the fO_2 at which sulfur changes its valence to sulfate, thereby undergoing a marked change in solubility, is similarly uncertain. Experiments were therefore attempted to determine SCSS and sulfur concentration at anhydrite saturation (SCAS), and the fO_2 conditions over which they are stable in FeO-rich basalts, under pressures representative of Martian mantle melting.

4.2.2 REE elements in Martian meteorites

Martian basaltic meteorites may be classified into three distinct geochemical groups on the basis of their REE concentrations (Bridges and Warren 2006). In particular, their relative depletion in Light Rare Earth Elements (LREEs, lanthanum to gadolinium) relative to Heavy Rare Earth Elements (HREEs, terbium to lutetium). The "slightly depleted" (SD) group exhibit almost flat REE profiles, with a very subtle "lazy-S" shape, and La/Lu ratios around 1.0. The "heavily depleted" (HD) group have abruptly stepped profiles, steepest between Cerium and Samarium, and La/Lu ratios closer to 0.1. A third group (moderately depleted, MD) display intermediate degrees of LREE depletion. A section of these are shown in figure 4.2.2.

Figure 4.2.2: A compilation of REE profiles for shergottite meteorites. Shown in green are members of the slightly depleted group, with their high La/Lu ratios and "lazy-S" shape; shown in red are members of the heavily depleted group, with much smaller La/Lu ratios and a characteristic "step" between gadolinium and praseodymium. Meteorites exhibiting intermediate degrees of LREE/HREE enrichment are omitted for clarity.



As with terrestrial rocks, REE profiles in Martian samples have been interpreted as evidence for chemically separate reservoirs in Mars' mantle. The difficulty with making such inferences lies in distinguishing between the effects of late-stage melting/crystallization, and characteristics that are truly inherited from their source regions. Models that appeal to the first scenario (Assimilation of crustal material and Fractional Crystallization; often referred to as AFC) derive their support from the complex and often disequilibrium mineralogy of the Shergottites, which demonstrate mixing must have played some role in their formation (McSween *et al.* 1994). Evidence for the second scenario comes from the poor correlation between these mineralogical indices of differentiation, and the meteorites' trace element signatures (Borg and Draper 2003). A independent source of support for an early stage (or "inherited") origin is provided by Sm-Nd and Rb-Sr isotopic ratios, which argue strongly for at least two separate Martian mantle reservoirs, which separated early in the planet's history, ~4.49Ga (Borg *et al.* 2003). The most comprehensive model invoking separate mantle reservoirs is that of Borg and Draper (2003), who suggested protracted crystallization of a magma ocean as the most plausible segregation process. Their model envisages the

geochemically depleted and enriched Shergottites as products of melting of this magma ocean's cumulates and late-stage liquids respectively. However, while it predicts the broadest features of the REE profiles (whether they are enriched or depleted in incompatible elements), none of the specific characteristics are reproduced – in particular the lazy-S shape of the SD Shergottites, or the inflections observed in the HD Shergottites. This is unsurprising since such an objective depends on accurate knowledge of the partition coefficients for the REEs. This is the primary motivation for this study.

4.3 – PREVIOUS WORK

4.3.1 A brief introduction to trace element partitioning

The equilibrium concentrations of trace elements in coexisting solid and liquid phases are known to assume predictable ratios, making their measured abundances in natural rocks useful for studying igneous processes such as partial melting. These concentration ratios are referred to as partition coefficients (D). A model for predicting these was first provided by Brice (1975), and was comprehensively tested and appropriately modified by Blundy and Wood (1994, 1997). This model predicts D_i (the partitioning coefficient for an element *i*) using the properties of the crystallographic site hosting the element concerned: specifically its radius (r_o) and elasticity (expressed as its Young's modulus, E). For a given crystallographic site, D_i follows a parabolic dependence on ionic radius (figure 4.3.1). Larger values of E ('stiffer' sites) give rise to parabolas with steeper limbs. This relationship may be expressed explicitly:

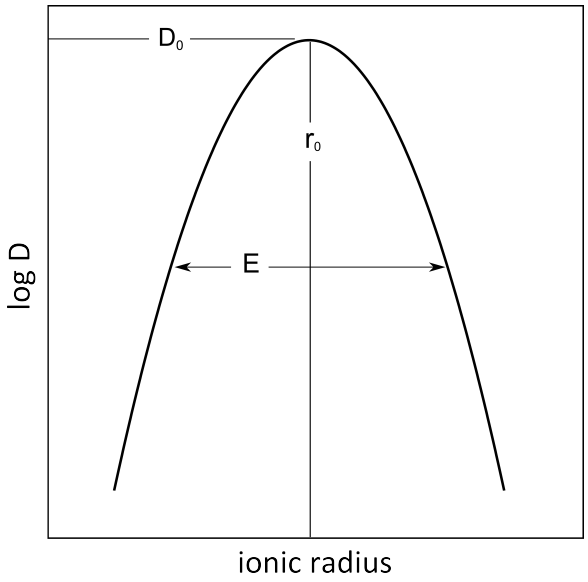
$$\mathrm{D}_i \;=\; \mathrm{D}_0 \; exp\left(\frac{4\,\pi\, E N_A(\frac{r}{2}(r_i - r_0)^2 \;+\; \frac{1}{3}(r_i - r_0)^3)}{\mathrm{RT}}\right) \tag{4.1}$$

Where D_i and r_i are the partition coefficient and radius of an element of interest, D_0 is the ideal or "strain-compensated" partition co-efficient, E is the site's Young's modulus, r_0 is the site radius, and T is the temperature in kelvin. R and N_A are the gas constant and Avogadro constants respectively.

Partitioning coefficients provided by the elastic strain model have been invaluable in the calculation of equilibrium trace element concentrations in various situations from partial melting of the mantle to crustal interactions with hydrothermal fluids. However, controversy surrounds the role played by the melt co-existing with the mineral in question (Mysen 2004), since melt-compositional effects on partitioning have been reported for some systems (e.g. Toplis and Corgne 2002). Application of the elastic-strain model to the more Fe-rich and Al-poor melts represented by the Martian meteorites requires a search for any similar melt-induced effects on partitioning which might necessitate modifying the model. One such study to do this was McKay *et al.* (1986), who performed REE partitioning experiments between various pyroxenes and liquids approximating the composition of the intercumulus melt of the Shergotty meteorite. They reported no melt effects, but a strong positive correlation between the Ca-concentration of the pyroxenes and the mineral-melt partition coefficients for the REEs. This is predicted by the lattice strain model (Blundy and Wood 1997) since Ca^{2+}, being a larger ion than Mg^{2+} or Fe^{2+}, is expected to increase the ideal radius of the M1 crystallographic site so that it more readily accommodates REEs. McKay *et al.* (1986) also confirmed that the melt and pyroxene Mg/Fe ratios have negligible effects on partitioning; an observation that is obviously relevant to studies of Mars' Fe-rich mantle. The effect of pressure was not studied, since all of these experiments were performed at 1-atmosphere. More recently, a study has been undertaken at higher pressure by Blinova and Herd (2009), who investigated partitioning between the highly depleted shergottite Y980459 and its liquidus phases between 1350-1650°C and 1-2 GPa. Although they reported no anomalies in partitioning behaviour, the minerals they investigated differ from those here, being crystallization products of an assumed primary melt, rather than subsolidus phases of the putative Martian mantle.

A potential application of REE partition coefficients for Martian compositions has been demonstrated by Wadhwa (2001), who exploited the multivalent nature of Eu to monitor the fO_2 at which Shergottite pyroxenes were last in equilibrium with their mantle source. This method implies a mantle fO_2 close to the Iron-Wustite (IW) buffer, overlain by a more oxidized crust. Studies such as this clearly depend on accurate REE partitioning data (for Martian systems specifically), in addition to knowledge of the Eu^{3+}/Eu^{2+} ratio and it's variation with fO_2.

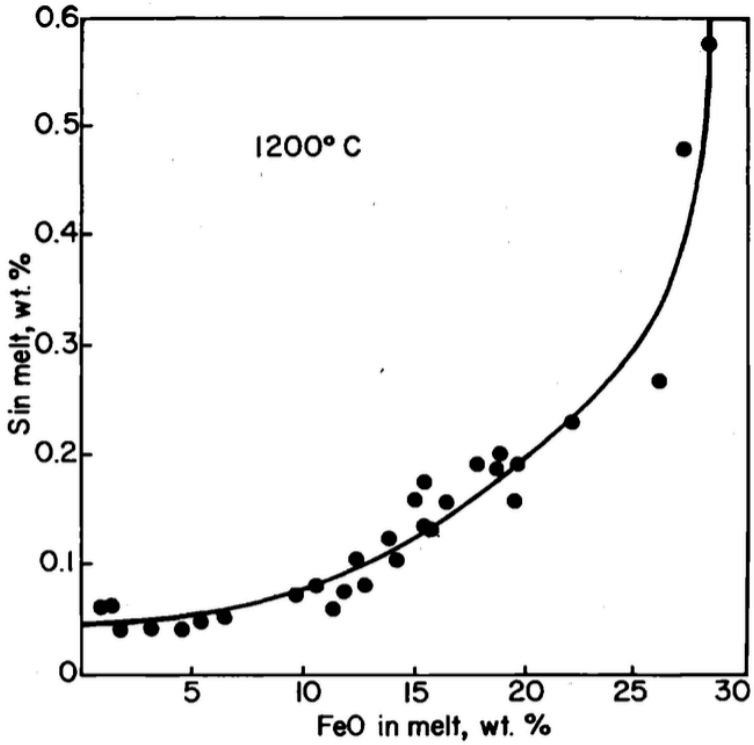
Figure 4.3.1: The parabolic relationship between the log of element partitioning coefficients and their ionic radii. The particular form of the relationship for a specific crystallographic site is determined by the three parameters shown; the ideal radius (r_0), and site elasticity (E), and the ideal partition coefficient (D_0). Note that larger values of E give rise to shorter distances between the parabola limbs (the distance indicated by the arrow labelled 'E'). Partition coefficients are typically obtained by measuring concentrations in experiments or natural samples, but this relationship permits the calculation of theoretical coefficients from knowledge of a particular mineral's chemistry.



4.3.2 Sulfide solubility in magmas

Experimental studies into the sulfur concentration at sulfide saturation (SCSS) of basaltic melts began with Haughton *et al.* (1974), who explored the influence of melt composition at one atmosphere pressure. They identified Fe as the major controlling element, and reported an exponential dependence of SCSS on FeO content that has been confirmed by subsequent studies (e.g. Buchanan and Nolan 1979, Wallace and Carmichael 1992). The influence of temperature and pressure on SCSS have been studied independently by various researchers (Wendlandt 1982, Mavrogenes and O'Neill 1999, Li and Ripley 2005), and found to have positive and negative effects respectively. Although models incorporating all of these parameters are now available, the conditions of interest to this study lie on the margins of their calibrated range.

Figure 4.3.2a: The exponential dependence of SCSS on the FeO concentration of various basaltic melts, reported by Haughton *et al.* (1974). The data shown represent experiments performed at 1200°C and one-atmosphere pressure, for a range of oxygen and sulfur fugacities. Each basalt was in equilibrium with varying Fe-S-O liquids. Log fO_2 ranged from -8.9 to -12.04, and log fS_2 from -0.82 to -2.64.



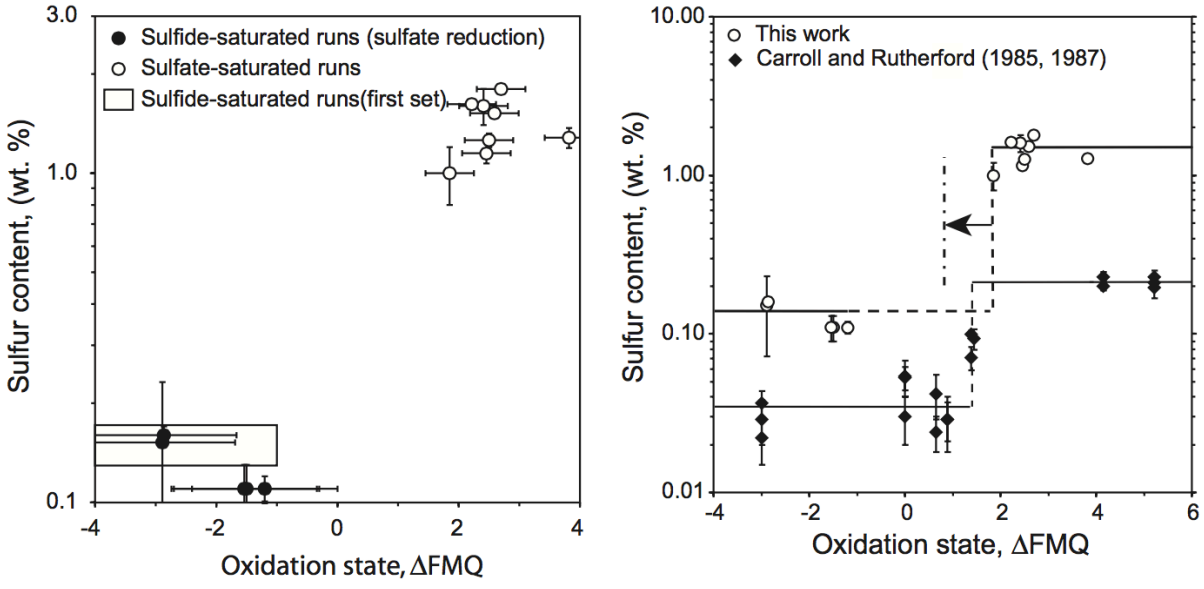
Two recent studies are of particular relevance to the transport of sulfur by Martian magmatism. Jugo *et al.* (2005) measured SCSS and SCAS for basaltic melts under 1GPa pressure, and reported an order-of-magnitude contrast in solubility between sulfide (~1500ppm) and sulfate (~1.5wt%). They further constrained the fO_2 of this transition to between -1 and +2 log units relative to the FMQ buffer. Since their interest was in terrestrial magmatism, the basalts they studied had FeO concentrations unrepresentative of Martian compositions. Nonetheless, their determination of the fO_2 conditions, and the magnitude of the solubility contrast between oxidized and reduced sulfur is potentially very relevant to the Martian sulfur cycle. Figure 4.3.2b shows the abrupt change in solubility reported by Jugo *et al.* (2005). It is important to note that here, sulfur concentrations have been measured at sulfide or sulfate saturation, and that structural considerations about the availability of sites for hosting these species in the melts now govern their concentration. The exchange reactions described in the previous chapter (equations 3.3 and 3.4) therefore no longer

apply, and the fugacity ratios in these expressions no longer determine abundance of dissolved sulfur. For this reason the V-shaped profile of Fincham and Richardson (1954) is now absent, and there is no sulfur concentration minimum near the FMQ buffer.

The second study of particular interest is that of Righter *et al.* (2009), who investigated SCSS for four SNC meteorites at 0.8GPa pressure. Their objective was to investigate the applicability of previous models for sulfur solubility (chiefly those described above) to Martian compositions, which are Fe-rich and Al-poor. Their findings confirmed the strong impact of FeO on SCSS, demonstrating that the Fe-rich melts that typify Mars' mantle are capable of dissolving 2400ppm sulfur at sulfide saturation. Their study did not experimentally explore the effect of fO_2 on solubility as all of their experiments were performed at either FMQ-1.3 or FMQ-1.7. As a result, they did not address the question of sulfur speciation at pressure, or of anhydrite solubility (indeed, sulfate was not observed in any of their run products).

The purpose of the present study therefore, is to bridge the gap between these latter investigations, and investigate the solubility of both sulfur species in Martian basalts, at pressures relevant to melting of the Martian mantle.

Figure 4.3.2b: SCSS and SCAS measured at 1GPa pressure by Jugo *et al.* (2005). The contrasting solubility of sulfide and sulfate are evident from the figure, although the exact position of the crossover from one to the other is not systematically constrained. The melts represented here are terrestrial basalts, with FeO concentrations never exceeding 9wt%; approximately half the typical value for Martian basalts.



4.4 – EXPERIMENTAL METHODS

4.4.1 Choice of Melt Compositions

REE partitioning experiments were performed on three mineral-melt pairs, including a higher-calcium pyroxene, a lower-calcium pyroxene, and an olivine (see table 4.4.1). The solid minerals chosen are likely close approximations to those present in the Martian mantle. These were obtained from Part I of Bertka and Holloway's (1994a) comprehensive study into the expected mineralogy of the "DW" model for Mars' mantle (see introduction). Although the pyroxenes are distinguished from one another by the names "higher-Ca" and "lower-Ca" in this study, both are decidedly Ca-poor by terrestrial standards, as stated in the introduction. The melt composition JFR-2 is a putative ~10% partial melt of this "DW" composition, and was sourced from Part II of the same study (Bertka and Holoway 1994b).

The sulfur-bearing experiments involved two starting compositions: a melt very similar to that described above (termed JFR-4, an alternative from the same paper representing a similar melt fraction), and a Fo_{72} olivine composition found to be in equilibrium with it at 1300°C, 1.5GPa. This was included to prevent aggregation of the Ir blebs that were added to each experiment as an fO_2 sensor, since this would have impeded their absorption of Fe from the melt.

Prior to the main experimental campaign, a pilot experiment was performed to verify the composition of the JFR-4 mixture. A small quantity was raised to 1500°C (well above its inferred liquidus) in a graphite capsule using the piston-cylinder apparatus, and the quenched product of this run was analyzed by wavelength dispersive spectroscopy (WDS).

The REEs lanthanum, praseodymium, neodymium, samarium, gadolinium, dysprosium and ytterbium were added to the high- and low- calcium pyroxenes and the olivine, along with the transition metals scandium and yttrium. These were chosen because they are nominally trivalent under the fO_2 conditions of mantle melting.

Table 4.4.1: Starting compositions for the REE-partitioning experiments (top four) and sulfur-bearing experiments (bottom two). All compositions except for the Fo72 olivine were taken from Bertka and Holloway (1994a, 1994b). Note that the two 'JFR' melts are very similar in composition.

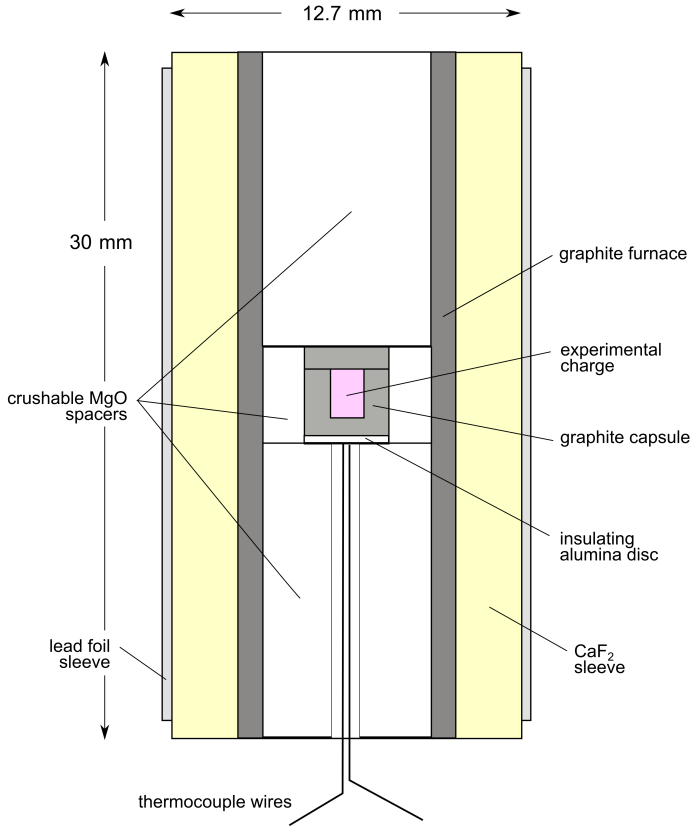
	wt % oxides										
Mixture name	SiO2	TiO2	Al2O3	Cr2O3	FeO	MnO	MgO	CaO	Na2O	K2O	TOTAL
JFR-2	45.60	1.28	12.30	0.32	18.80	0.31	9.12	10.10	2.07	0.00	99.9
high-Ca pyx	51.50	0.20	5.33	1.63	12.80	0.33	19.40	8.28	0.56	0.00	100.03
low-Ca pyx	52.10	0.13	4.54	1.14	13.30	0.41	25.90	2.08	0.34	0.00	99.94
Fo76 olivine	37.80	0.00	0.13	0.13	22.90	0.46	38.30	0.27	0.00	0.00	99.99
JFR-4	45.13	1.50	13.07	0.14	17.39	0.38	8.94	9.62	3.84	0.00	100
Fo72 olivine	38.00	0.00	0.00	0.00	25.12	0.00	36.88	0.00	0.00	0.00	100.00

4.4.2 Experimental Procedure

Starting materials were prepared from powdered oxides and carbonates, using a four-decimal place balance. Each mixture was de-carbonated overnight at 1000°C in air. Iron was added as hematite (since wustite is generally non-stochiometric) and each mixture was reduced in a one-atmosphere gas-mixing furnace to achieve the correct $Fe^{3+}/\Sigma Fe$ ratio. 1000ppm equivalent of each trace element was added (in 1µm/l solution form) and incorporated into each mixture with a mortar and pestle. Small (<50µm) beads of metallic Iridium were added to the sulfur-bearing experiments to monitor their fO_2.

All experiments were performed at 1.5GPa in a 1/2' Boyd-England type end-loaded piston-cylinder apparatus. Oxygen fugacity was controlled either by buffering with the capsule material, or varying the composition of the experimental charges. For the partitioning experiments and the reduced sulfur-bearing experiments, graphite capsules buffered the fO_2 at the carbon-carbon dioxide (CCO) buffer. For the more oxidized sulfur-bearing experiments, capsules made from gold-palladium alloy ($Au_{80}Pd_{20}$) were used, and control of fO_2 was attempted by varying the composition of the starting materials. Experimental capsules were encased in crushable MgO to impose a hydrostatic pressure. A graphite furnace permitted electrical heating of the charges, and CaF_2 sleeves were used to prevent contact between these and the surrounding steel bomb. A single layer of lead foil encased each assembly to minimize gouging of the bomb cavity during removal after each experiment. A typical experimental assembly is shown in figure 4.4.2a. A cutaway through the piston-cylinder apparatus is shown in figure 4.4.2b.

Figure 4.4.2a: The assembly used for piston-cylinder experiments at 1.5GPa. The assembly as shown is inverted and compressed by a hydraulic ram to the desired pressure, while being heated using a large current applied to the graphite furnace.

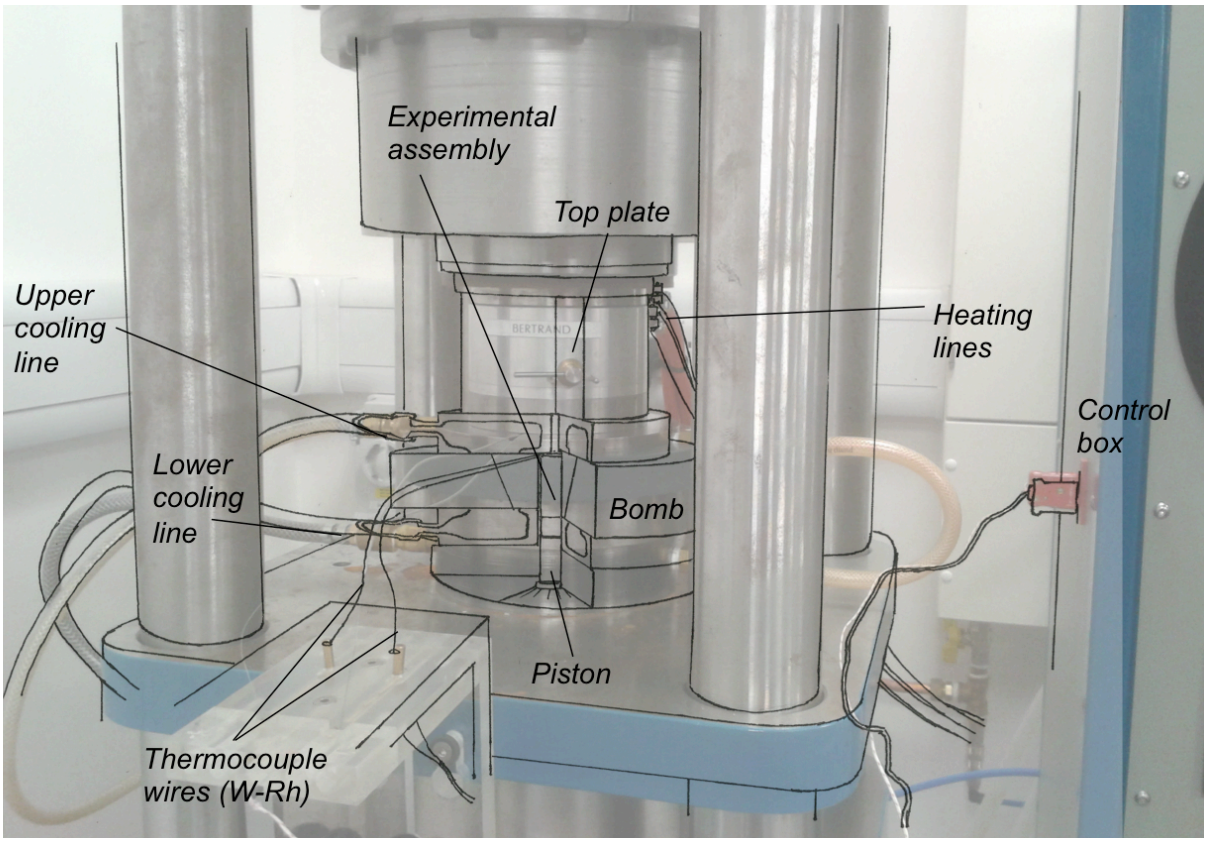


Graphite capsules were manufactured from graphite rod, and sealed passively during each experiment by the pressure imposed on their lids by the piston-cylinder ram. In contrast, Au-Pd capsules were sealed before each experiment using an arc-welder. These Au-Pd capsules were constructed from tubes 12mm in length, which were annealed in air at 1000°C to make them malleable, and shaped into capsules by deforming their extremities into a "three-way crimp" geometry.

Experimental charges were heated by passing a large (~13A) current through their surrounding graphite furnaces. Temperature was continuously measured using a $W_{95}Re_5$-$W_{74}Re_{26}$ thermocouple, and controlled by a Eurotherm 2404 PID controller, which

continuously adjusted the current in response to changes in temperature reported by the thermocouple.

Figure 4.4.2b: A cutaway through the piston-cylinder apparatus, shown while in operation. The experimental assembly is confined laterally by the bomb (a thick disc of hardened steel), and compressed vertically by the piston, driven by a hydraulic ram. The bomb and piston are cooled by a continuous flow of water, and the sample temperature is monitored using a thermocouple.



Each experiment was terminated by stopping the current supplied to the graphite furnace. This yielded quench rates in excess of 100°C/s, and consequent cooling through the glass transition temperature around 5 seconds after the quench was initiated. The quench rate was estimated by Ashley Norris (personal communication) who filmed quenching temperature profiles on similar experiments with a high frame-rate digital camera.

Following quench, the experimental charges were carefully removed from their assemblies with a razor blade and mounted in 1' acrylic rounds. These were then ground so as to expose the experimental charge, and polished on a lap using 3 and 1 μm microdiamond paste.

Sulfur-bearing experiments were polished under paraffin rather than water to prevent dissolution of any sulfate phases present.

4.4.3 Measurement of oxygen fugacity

Small beads of Iridium metal were added to each of the sulfur-bearing experiments to serve as an fO_2 sensor. The fO_2 was calculated retrospectively for each of these experiments by measuring the concentrations of Fe in these beads, and of FeO in the silicate melt. These parameters are related to fO_2 by the following equilibrium:

$$\mathrm{Fe}_{metal} + \frac{1}{2}\mathrm{O}_{2\,gas} = \mathrm{FeO}_{silicate} \quad (4.2)$$

Which implies the following relation among the activities of oxygen, Fe and FeO:

$$2\,log\,K = 2\,log\,a_{FeO}^{silicate} - 2\,log\,a_{Fe}^{metal} - log\,f\mathrm{O}_2 \quad (4.3)$$

Setting *log K* equal to zero (the equilibrium condition for this reaction), and defining standard conditions as the temperature and pressure of interest, this expression may be rearranged to yield fO_2 relative to the iron-wustite (IW) buffer (the reaction in equation 4.2). This relative fO_2 is denoted here by ΔfO_2.

$$\Delta\,log\,f\mathrm{O}_2 = 2\,log\,a_{FeO}^{silicate} - 2\,log\,a_{Fe}^{metal} \quad (4.4)$$

The activity co-efficient for FeO (γFeO) in the silicate melt was provided by Woodland and O'Neill (1997). The activity co-efficient for Fe in the Ir-Fe alloy (γFe) was taken from Rohrbach and Schmidt (2011), who obtained Margules[1] parameters for this system through least squares fitting of a binary asymmetric regular solution model to crystallographic data for face-centred cubic Ir-Fe alloy. Their expression for the γFe in the alloy is:

$$\mathrm{RT}\,ln\,\gamma_{Fe} = 2X_{Fe}X_{Ir}W_{G\,Ir-Fe} + 2X_{Ir}^2W_{G\,Fe-Ir} - 2G^{XS} \quad (4.5)$$

Where X_{Fe} and X_{Ir} are the mole fractions of Fe and Ir in the alloy, $W_{G\,Ir\text{-}Fe}$ and $W_{G\,Fe\text{-}Ir}$ are the Margules parameters for Fe and Ir, and G^{XS} is the excess Gibbs free energy of mixing.

Errors in fO_2 were calculated by propagation of the uncertainties associated with probe analyses of XFe and XFeO in the metal and silicate respectively.

[1] Margules parameters are used to express deviations from thermodynamic ideality, and comprise simple relationships between a component's concentration and its thermodynamic activity.

The REE-partitioning experiments simply were assumed to have reached the CCO buffer, since all were conducted in graphite capsules. Knowledge of their fO_2 was considered less important since REE partitioning is not expected to depend strongly of fO_2; the only redox sensitive REEs – Ce and Eu – were not added, and the Fe^{3+}/Fe^{2+} ratio in the melts is known to vary gradually with fO_2 (Jayasuriya *et al.* 2004). The impact on partitioning of ferric iron in pyroxenes is potentially more significant, but since the impact of fO_2 on partitioning was not the main aim of this study, it was deemed sufficient to assume that each charge reached equilibrium with its graphite capsule (functionally equivalent to the CCO buffer), and therefore redox sensors were not included in these experiments.

4.4.4 Run conditions and objectives of Sulfur-bearing experiments

To investigate the fO_2 at which dissolved sulfur changes its valence from sulfide and sulfate, it was necessary to control the fO_2 in the capsules. This was attempted by varying the capsule material and composition of the starting composition. Ultimately, the desired series of evenly spaced fO_2 conditions were not achieved (see results section).

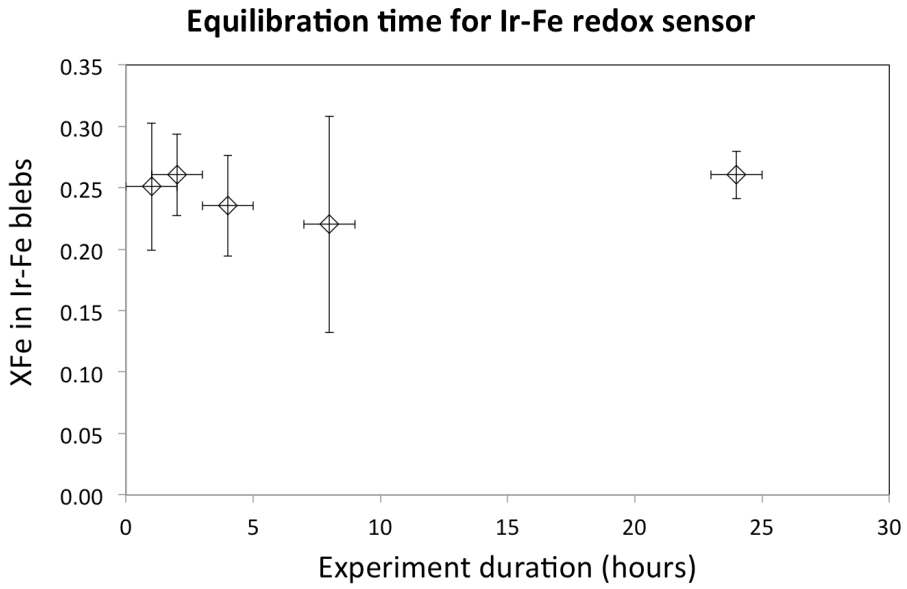
First, experiments were performed with pure FeS and $FeSO_4$ in graphite and Au-Pd capsules (respectively), to define the extremes of the fO_2 space under investigation. Subsequent to these, equilibration under intermediate fO_2 conditions was attempted by adding varying ratios of FeS and $FeSO_4$ to the starting materials. FeS:$FeSO_4$ ratios of 1:3 and 2:3 were attempted initially, and both yielded high fO_2s. On the basis that these sulfide/sulfate ratios might have been too low, further experiments were performed with ratios of 0.6:0.4, 0.7:0.3, 0.8:0.2 and 0.9:0.1. These "mixed ratio" experiments were all carried out in Au-Pd capsules, since these are expected to be non-buffering. In addition, a further experiment was conducted containing hematite to further raise the fO_2.

Experiments conducted in graphite capsules were heated to 1400°C, while those performed in Au-Pd capsules were undertaken at 1300°C, to avoid melting the capsule.

4.4.5 Attainment of equilibrium

A time-series of experiments was performed to ensure that the contents of every capsule reached equilibrium. As the rate-limiting step towards complete equilibrium, the diffusion of Fe through Ir metal was carefully measured at the lower of the two temperatures studied. The mole fraction of Fe measured within the beads by WDS is shown in fig 4.4.5. Within error, no upward or downward trends can be seen in the data, indicating that equilibrium between these blebs and the silicate melt was reached quickly: within the first 2-4 hours. Homogeneity among the glass analyses for the same experiments confirmed that in every case, they had reached equilibrium as well.

Figure 4.4.5: Time-series of experiments performed at 1300C (the lower of the two temperatures studied) to establish the equilibration time for the Fe-Ir blebs. The errors shown are standard deviations of each cluster of analyses (around 20 were collected per bleb, although fewer could be obtained for the 8 hour experiment). The relatively large size of these errors demonstrates the difficulty associated with analyzing such small and irregularly shaped blebs of metal (see section 4.5.3.2).



4.5 – ANALYTICAL METHODS

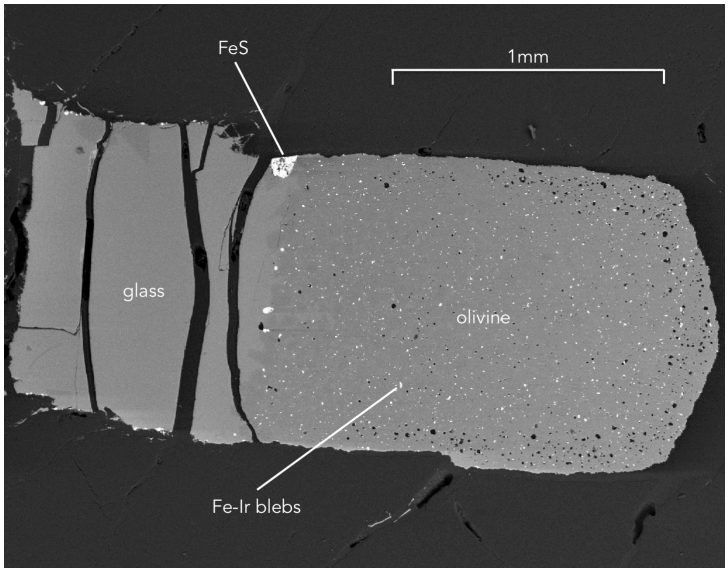
4.5.1 Overview

All experimental products were imaged by scanning electron microscope and analyzed quantitatively (to determine major-element concentrations) by WDS with an electron probe. In the partitioning experimental products, the REE concentrations in the co-existing mineral and glass phases was measured by Laser-Ablation ICP-Mass Spectroscopy. In the sulfur-bearing experiments, the iron concentration of the iridium beads was also measured by EPMA, and the valence of sulfur dissolved in their glasses was determined by X-ray absorption spectroscopy (XANES).

4.5.2 Imaging of run products by SEM

Backscattered electron (BSE) images of every experiment were collected using a JEOL JSA-840A scanning electron microscope. These were used for preliminary identification of phases, and verification that the capsules had remained sealed. In the case of the sulfur-bearing experiments, the size, shape and distribution of the iridium beads was also determined. A typical run product is shown in figure 4.5.2.For the REE-partitioning experiments, BSE images served as maps for selection of laser spots for LA-ICP-MS.

Figure 4.5.2: BSE image of a typical run product from a sulfide-saturated piston-cylinder experiment.



4.5.3 Major-element chemistry and Fe-Ir bleb composition by WDS

4.5.3.1 Analysis of major-elements

The major-element composition of the phases in every experiment was determined using a JEOL-8600 Electron Microprobe, at Oxford University's Research Laboratory for Archaeology and the History of Art. An accelerating voltage of 15kV and beam current of 20nA were used. To minimize sample damage, glasses were analyzed with a defocused beam (10μm diameter). Wollastonite served as the primary standard for Si and Ca, periclase for Mg, hematite for Fe, jadeite for Al and Na, fowlerite for Mn, chromium metal for Cr and rutile for Ti. A well-characterized almandine served as a secondary standard.

4.5.3.2 Analysis of Fe-Ir blebs

Analyses of the Fe-Ir blebs were performed at 20kV with a focused 20nA beam. BSE images of the blebs showed them to be irregular in shape, and typically between 5 and 20 μm in width. Secondary electron (SE) images revealed them to be irregular in the vertical dimension too, having slightly convex-upwards surfaces. This deviation from perfect flatness is an outcome of iridium's greater resistance to polishing than the surrounding material, and is analytically problematic because a fundamental requirement for WDS is flat sample surface geometry. Despite experimenting with various diamond pastes and laps, these couldn't be flattened, and ultimately a combination of quality control (removal of analyses with anomalous totals) and averaging of analyses was employed to overcome it.

The bleb's small size presented challenges for the analysis too. In particular, they demanded a judicious compromise for the acceleration voltage, between the provision a sufficiently high excitation energy (1.5 times the Ir Lα line, at 13.4keV), and the propagation of an excitation volume smaller than a typical bleb. Care was taken to ensure that this latter condition was met in both the vertical and horizontal directions. Simulations performed with the software Casino (Hovington *et al.* 2006) confirmed that a 20kV beam's penetration depth into an Ir layer never exceeds 200nm (iridium being a commendable X-ray attenuator), and silicon was added to the routine to detect any contamination by surrounding material (thereby ensuring that excitation volumes didn't extend laterally beyond bleb margins). Analyses reporting the presence of silicon were discarded. Since the average blob size is smaller than the

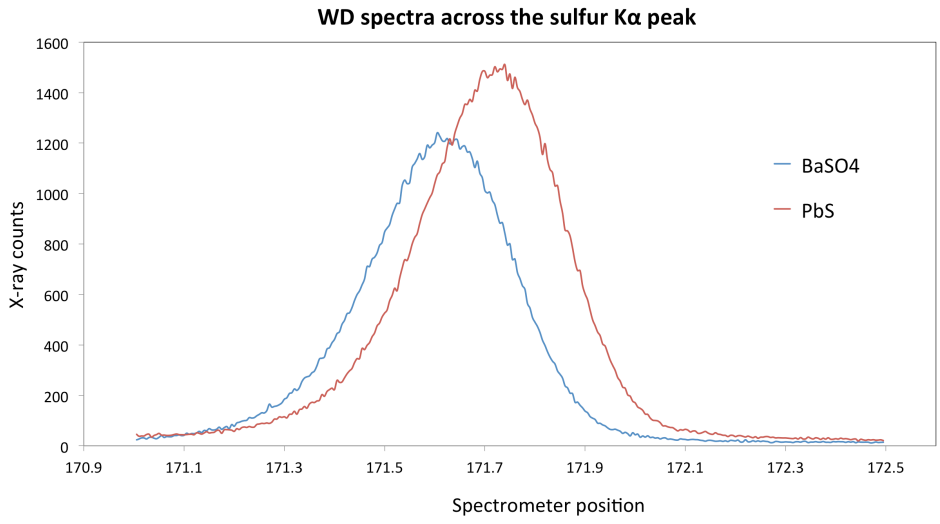
reproducibility of the instrument stage, each analysis had to be performed manually rather than being automated.

Metallic Ir and Fe and wollastonite were used as primary standards. Separate samples of pure Fe and Ir metal were used as secondary standards. This was obviously not ideal since they didn't permit testing of both calibrations during a single analysis, but no well characterized Fe-Ir alloy was readily available.

4.5.3.3 Analysis of sulfur

Sulfur analysis with WDS is complicated by the ~10eV valence-dependent shift in the energy of the sulfur Kα line (Carroll and Rutherford 1987 - see section 3.3.1.2). This shift is illustrated in fig 4.5.3.3, which shows the Kα peaks for the sulfur bearing minerals galena and barite. Materials with mixed sulfur valence exhibit an effective sulfur peak position that is intermediate between those of the oxidized and reduced end-members. Therefore, spectra such as these were collected for the silicate glass produced in every experiment, so that an appropriate peak position could be used for each analysis. A defocused beam was used, and probe current and count times optimized to provide the lowest detection limit without altering the sulfur speciation. Long counting times were required at each energy because the sulfur concentrations were so low (1 wt% or less).

Figure 4.5.3.3: The difference in characteristic X-ray energy for reduced and oxidized sulfur. Shown here are scans across the sulfur Kα peak for oxidized and reduced sulfur (barite and galena respectively). The error in sulfur concentration which results from using the incorrect peak-position is considerable (25% relative).



4.5.4 REE concentrations determined by Mass Spectrometry

A quadrupole mass spectrometer was used to determine REE concentrations in each of the phases present (glass plus one liquidus phase) in the partitioning experiments. Specifically, a Perkin Elmer NexION 400Q ICP-MS was used for the analysis, with sample ablation and delivery performed using a New Wave Research UP213 laser system. This was run in pulse-mode, with a spot diameter of 40μm. Nebuliser gas flow on the ICP-MS was 0.85 l/min, and elements were analyzed in "pulse counting" mode.

Ca^{40} was used to calibrate the instrument, the Ca concentration in each phase having been previously determined by WDS (see section 4.5.3). A NIST610 standard glass was used as the primary standard, with NIST612 and BCR-2G basaltic glass as the secondary. The NIST glasses are alkali-rich glasses doped with ~400μg/g of every known element (Eggins and Shelley 2002, Jochum *et al.* 2011), and were regarded as sufficiently matrix-similar to the experimental products being investigated. BCR-2G is a well characterized natural basalt, which has been characterized by 20 international laboratories using more than three independent analytical procedures (Wilson 1997). Detection limits reported by the instrument were well below the concentration of every element analyzed.

A challenge encountered here was ablating volumes of a single phase with the laser spot, rather than ablating volumes that straddle minerals-melt boundaries. The footprint of each spot was carefully chosen to prevent any surface boundaries being crossed. However, the laser pits had a finite depth (~50μm), so boundaries encountered in the z-direction (beneath the sample surface) were monitored indirectly by examining the time-series of counts for each analysis. Discontinuities in these time-series were taken to indicate contamination by a second phase, rendering the analysis in question erroneous. Ultimately, more than a quarter of the analyses made had to be discarded in this way.

4.5.5 Sulfur valence determined by XANES

The valence of sulfur dissolved in each of the sulfur-bearing glasses was determined by X-ray absorption near-edge spectroscopy (XANES). A comprehensive introduction to this relatively new technique is provided in section 3.5.4.2. The instrument specifications, analytical conditions and standard materials are described in section 3.5.4.4.

Spectra were collected across the Sulfur K-edge, so that the sulfur valence could be estimated for each experiment by comparison with FeS, S or $FeSO_4$ standards. Valence was determined by visual comparison with standards (since these exhibit such different edge energies).

4.6 – RESULTS

4.6.1 REE-partitioning experiments

Following a series of pilot experiments that were used to achieve the desired starting material compositions, three mineral-melt pairs were crystallized in three separate experiments: lower-Ca pyroxene and melt, higher-Ca pyroxene and melt, Fo_{76} olivine and melt. These were the only phases present in each experiment, and their major-element chemistry is presented in table 4.6.1a. Trace element compositions and mineral-melt partition coefficients for the three experiments shown in tables 4.6.1b-d. These are graphed as logs against their ionic radii in figs 4.6.1a-c. For each mineral, the log of the partitioning behaviour exhibits the expected parabolic dependence on ionic radius. Superimposed onto each figure are the particular curves predicted using site-specific data applied to the lattice strain model (ionic radii and elasticities). The errors shown represent one standard deviation on the analyses used to calculate the coefficients. The ionic radii for each element were taken from the compilation of Shannon (1976).

For the higher-calcium pyroxene, all REEs were assumed to partition into the M2 site, assuming 8-fold co-ordination in the mineral structure. The ideal radius (0.996Â) was predicted from the mineral's calcium and aluminium abundances, using the expression proposed in Wood and Blundy (1997). The site elasticity was calculated from the T and P of the experiment, using an expression from the same paper. The resulting parabola is a very close match to the data. A marginally closer fit is obtained with a slightly greater elastic modulus than anticipated (310GPa rather than 271GPa).

As with the higher-calcium pyroxene, the M2 site was the assumed host for REEs partitioning into the lower-calcium pyroxene. The partitioning data for this mineral also satisfy a parabolic relationship, though not over their entire range. The largest ions (neodymium, praseodymium and lanthanum) fall slightly above the parabola's limb; their concentrations in the mineral exceeding the expectations of the lattice strain relationship. This is attributed to contamination of the ablated volume by melt inclusions. Assuming this is the correct explanation for these anomalous points, the remaining data imply a slightly smaller ideal radius (0.968Â) that that predicted by the considerations about the mineral's chemistry (0.978Â).

Table 4.6.1a: major-element compositions of the mineral-melt pairs recovered from the REE-partitioning experiments. Note the two-fold difference in calcium content of the pyroxenes.

		wt % oxides										
Experiment	Phase	SiO2	TiO2	Al2O3	Cr2O3	FeO	MnO	MgO	CaO	Na2O	K2O	TOTAL
WN12-6	glass	44.97	1.10	11.04	0.39	16.45	0.34	10.68	11.39	1.91	0.02	98.29
WN12-6	high-Ca pyx	51.88	0.27	4.10	1.11	10.02	0.30	19.43	11.67	0.46	0.00	99.24
WN13-1	glass	46.81	1.06	11.20	0.46	16.52	0.32	10.96	8.66	2.07	0.02	98.08
WN13-1	low-Ca pxx	51.62	0.31	4.15	0.80	14.11	0.33	22.52	5.42	0.50	0.01	99.77
WN12-8	glass	42.99	1.06	10.51	0.27	17.14	0.37	11.75	12.33	1.81	0.03	98.26
WN12-8	Fo76 ol	38.77	0.03	0.17	0.2	21.72	0.37	38.54	0.51	0.03	0.01	100.35

Table 4.6.1b: Trace element analyses and partition coefficients for the run products of experiment 12-6: a "higher-Ca" pyroxene in equilibrium with the JFR-2 basaltic melt. The 1 standard deviation of each analysis is given, as well as the errors on the partition coefficients calculated from the trace element analyses.

	Higher-Ca pyx + JFR-2 melt					
Element	pyx conc (ppm)	1sd	glass conc (ppm)	1sd	$D^{pyx\text{-}melt}$	err
Si29	242507.50	7751.45	210207.43	6701.62	1.154	0.052
Ca44	80417.18	3028.55	79444.13	2917.73	1.012	0.053
Fe57	77695.04	5122.75	122944.20	7683.70	0.632	0.057
Sc45	76.04	3.92	71.22	3.51	1.068	0.076
Y89	26.09	1.03	97.48	3.58	0.268	0.014
La139	5.66	0.35	228.81	12.28	0.025	0.002
Pr141	14.99	0.61	233.88	8.89	0.064	0.004
Nd146	21.36	1.24	249.25	12.61	0.086	0.007
Sm152	31.46	1.35	219.76	8.54	0.143	0.008
Gd158	24.72	1.30	126.66	5.93	0.195	0.014
Dy163	33.77	1.49	133.85	5.35	0.252	0.015
Yb173	39.57	2.19	139.59	7.05	0.283	0.021

Table 4.6.1c: Trace element analyses and partition coefficients for the run products of experiment 13-1: a "lower-Ca" pyroxene in equilibrium with the JFR-2 basaltic melt. The 1 standard deviation of each analysis is given, as well as the errors on the partition coefficients calculated from the trace element analyses.

	Lower-Ca pyx + JFR-2 melt					
Element	pyx conc (ppm)	1sd	glass conc (ppm)	1sd	$D^{pyx\text{-}melt}$	err
Si29	243068.45	7745.48	215022.08	6854.46	1.130	0.051
Ca44	37631.73	1654.32	60726.17	2543.14	0.620	0.038
Fe57	95303.03	8514.76	126171.50	10357.19	0.755	0.092
Sc45	65.58	4.34	72.85	4.49	0.900	0.081
Y89	19.06	0.86	94.84	3.94	0.201	0.012
La139	9.52	0.73	219.38	15.11	0.043	0.004
Pr141	13.73	0.65	227.54	9.99	0.060	0.004
Nd146	17.08	1.25	246.78	15.82	0.069	0.007
Sm152	20.87	1.05	218.13	9.83	0.096	0.006
Gd158	16.98	1.11	126.08	7.32	0.135	0.012
Dy163	23.83	1.23	133.80	6.23	0.178	0.012
Yb173	35.90	2.52	140.76	8.98	0.255	0.024

Table 4.6.1d: Trace element analyses and partition coefficients for the run products of experiment 12-8: a Fo_{76} olivine in equilibrium with the JFR-2 basaltic melt. The 1 standard deviation of each analysis is given, as well as the errors on the partition coefficients calculated from the trace element analyses.

	Fo_{76} Olivine + JFR-2 melt					
Element	ol conc (ppm)	1sd	glass conc (ppm)	1sd	$D^{ol\text{-}melt}$	err
Si29	181226.23	5818.78	200578.21	6403.16	0.9035	0.0409
Ca44	3100.97	143.87	87326.38	3380.77	0.0355	0.0021
Fe57	161353.45	12343.62	126082.17	8874.24	1.2797	0.1330
Sc45	14.87	0.93	77.94	4.22	0.1907	0.0158
Y89	1.24	0.09	116.10	4.47	0.0107	0.0009
La139	0.73	0.07	235.25	14.05	0.0031	0.0004
Pr141	1.04	0.07	235.00	9.47	0.0044	0.0003
Nd146	0.90	0.12	255.36	14.29	0.0035	0.0005
Sm152	0.72	0.09	221.28	9.14	0.0032	0.0004
Gd158	0.61	0.09	129.77	6.66	0.0047	0.0007
Dy163	1.05	0.11	136.43	5.81	0.0077	0.0009
Yb173	3.86	0.33	143.46	8.00	0.0269	0.0027

Figure 4.6.1a: Comparison of measured partition coefficients for REEs between Fe-rich silicate melt and higher-Ca pyroxene expected to occur in the Martian mantle. The parameters governing the parabola shape are predicted from the mineral chemistry and equilibrium T and P conditions, using the model of Wood and Blundy (1997). The closeness of the fit negates the possibility of any significant influence by melt chemistry.

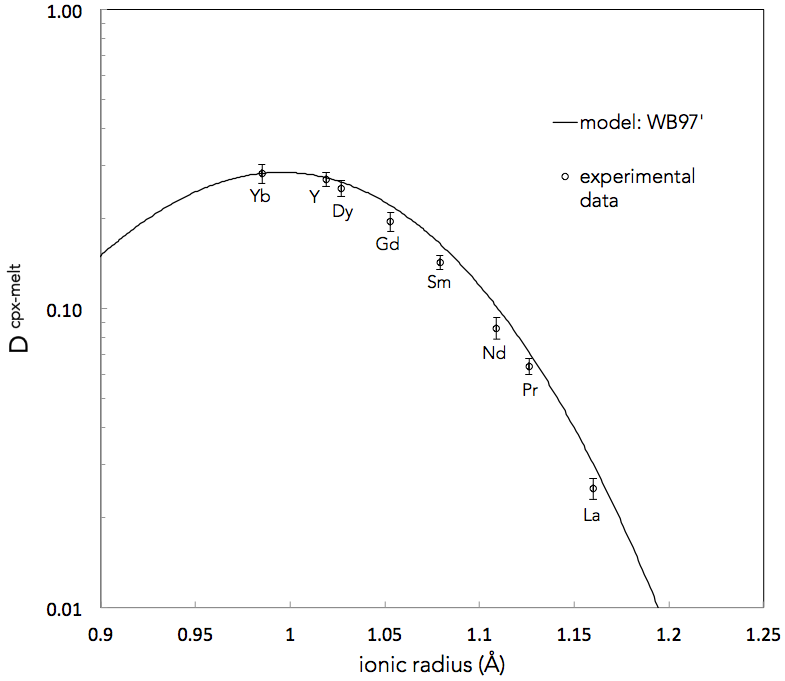


Figure 4.6.1b: Comparison of measured partition coefficients for REEs between Fe-rich silicate melt and lower-Ca pyroxene, also expected to occur in Martian mantle. The fit is very slightly inferior to that for the higher-Ca pyroxene, but nonetheless a close match. Contamination has probably affected the values for Nd, Pr and La.

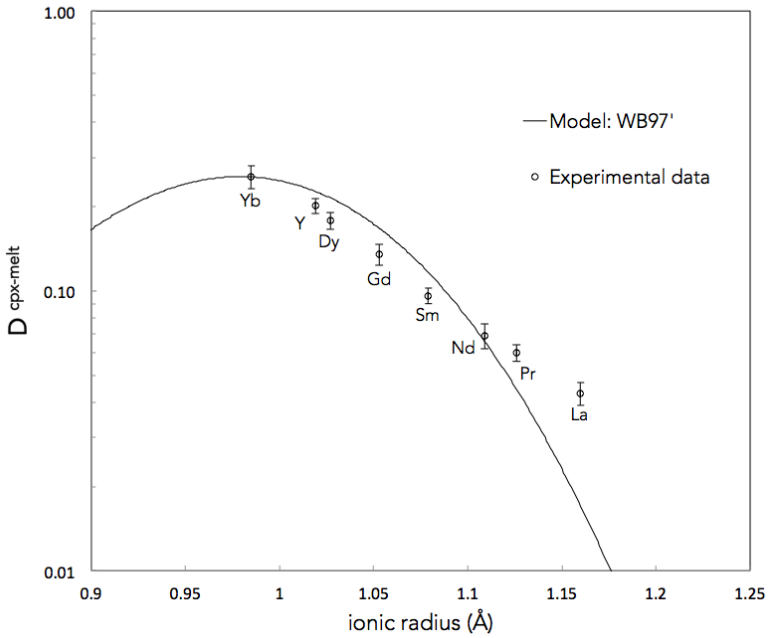
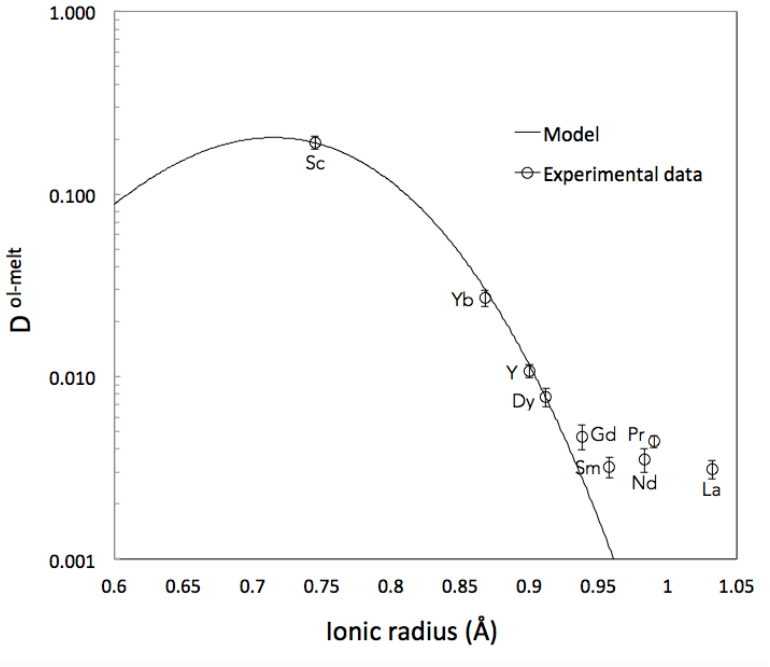


Figure 4.6.1c: Experimental and modelled partitioning data for Fo_{76} olivine in equilibrium with an Fe-rich basaltic melt. The parabola parameters are those predicted by Wood and Blundy (2003), for partitioning into the olivine's M1 site. An excellent fit to the data is obtained, with the exception of the largest ions, whose implied partitioning behaviour has likely been affected by the unavoidable analysis of melt inclusions, trapped inside the olivine.



The olivine data were modelled assuming partitioning into the M1 site (in 6-fold co-ordination). Ideal radii and site elasticity were taken from Wood and Blundy (2003), and fit the data very closely. The best-fit ideal radius was halfway between the 0.7-0.73 range quoted, so the data do not meet the source's suggestion that the value be higher in Fe-rich olivines.

Since the unstrained olivine lattice does not accommodate trivalent species, the measured REE concentrations are lower than those in the pyroxenes by almost an order of magnitude on the average. The five elements with the lowest concentrations actually fall above the parabolic curve. As with the lower-Ca pyroxene, the presence of melt inclusions within the olivine offers the most likely explanation for this unexpected behaviour.

No evidence for any influence over element partitioning by melt chemistry is apparent from any of these three systems. To the extent that the lower-calcium pyroxene deviates from the expected relationship, these deviations are nowhere larger than 0.1 log units.

4.6.2 Sulfur-bearing experiments

The chemical compositions of the glasses and Fe-Ir blebs in each sulfur-bearing experiment are presented in table 4.6.2, with their sulfur concentrations and calculated fO_2s. These data are also presented graphically in figure 4.6.2a. The Fe-Mg olivine-melt K_Ds (Roeder and Emslie 1970, Filiberto and Dasgupta 2011) are included in table 4.6.2 so that the approach to equilibrium can be evaluated.

Figure 4.6.2a: The sulfur concentrations and fO_2 conditions for all of the high-pressure sulfur-bearing experiments conducted in this study. Separate sulfide phases within the experiments performed at FMQ-2 demonstrate that these are sulfide-saturated. No separate sulfate phases were observed in the more oxidizing experiments, so the data shown may not represent SCAS. Note the clustering of fO_2 conditions, rather than the equally spaced range originally desired.

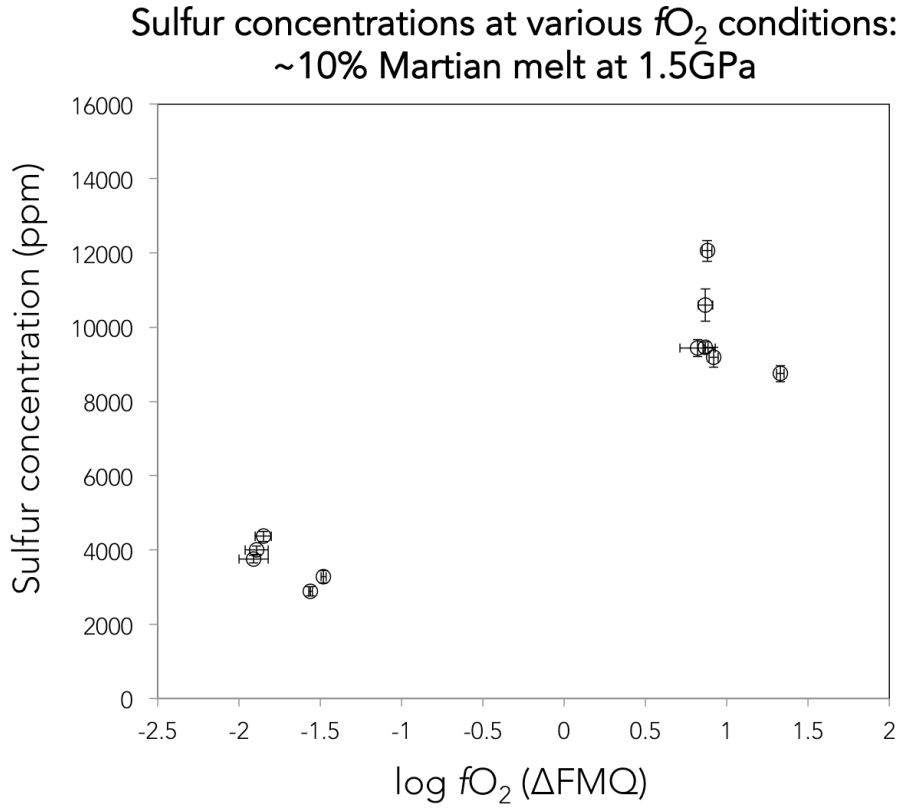


Table 4.6.2: Experimental conditions and results for all of the high-pressure sulfur-bearing experiments conducted in this study.

	Experimental conditions					Silicate glass compositions (wt % oxides)											Fe-Ir alloy composition						
Experiment	T (°C)	P (GPa)	duration (h)	charge composition	capsule material	SiO2	TiO2	Al2O3	Cr2O3	FeO	MnO	MgO	CaO	Na2O	TOTAL	ol-melt K_D	Fe	Ir	N	fO2	fO2 err	S (ppm)	S (1σ)
WN13-14	1400	1.5	2	0.5*JFR-4 + 0.47*Fo72 + 0.03*FeS	graphite	43.58	1.23	11.13	0.13	18.07	0.38	11.82	8.69	3.38	98.41	3.5	0.30	0.70	6	-1.91	0.09	3757	106
WN13-15	1400	1.5	4	0.5*JFR-4 + 0.47*Fo72 + 0.03*FeS	graphite	43.60	1.20	10.42	0.12	19.86	0.31	12.11	7.82	3.10	98.54	3.53	0.30	0.70	7	-1.89	0.07	3998	116
WN13-16	1400	1.5	8	0.5*JFR-4 + 0.47*Fo72 + 0.03*FeS	graphite	43.06	1.11	9.77	0.11	20.49	0.27	12.85	7.28	3.11	98.05	3.5	0.30	0.70	8	-1.85	0.05	4366	143
WN14-3	1300	1.5	1	★ FeSO4	Au-Pd	50.38	0.79	14.11	0.02	12.78	0.40	9.27	7.63	2.89	98.27	-	0.04	0.96	8	0.82	0.11	9434	231
WN13-25	1300	1.5	13	★ FeSO4	Au-Pd	41.53	1.10	8.50	0.01	18.08	0.20	12.61	8.16	2.96	93.15	4.62	0.04	0.96	4		0.0223	14107	223
WN13-26	1300	1.5	12	★ 0.33 FeS : 0.67 FeSO4	Au-Pd	42.42	1.06	8.58	0.02	19.17	0.20	12.09	7.65	2.95	94.12	4.65	0.05	0.95	6	0.88	0.0287	12052	287
WN13-27	1300	1.5	12	★ 0.67 FeS : 0.33 FeSO4	Au-Pd	40.11	0.33	3.40	0.02	18.69	0.10	32.43	3.19	0.99	99.28	1.51	0.08	0.92	4		0.0809	-	809
WN13-28	1300	1.5	12	★ FeSO4	Au-Pd	40.98	1.18	10.22	0.03	19.27	0.24	10.52	8.02	3.13	93.58	4.99	0.06	0.94	5	0.87	0.0438	10596	438
WN14-14	1300	1.5	12	★ 0.6 FeS : 0.4 FeSO4	Au-Pd	48.22	1.03	11.34	0.02	14.37	0.28	9.22	8.71	2.89	96.07	5.07	-	-	0		0.0231	9000	231
WN14-15	1300	1.5	12	★ 0.7 FeS : 0.3 FeSO4	Au-Pd	44.01	1.47	10.41	0.03	16.03	0.24	10.02	9.05	3.16	94.41	3.89	0.03	0.97	4	1.33	0.0226	8746	226
WN14-16	1300	1.5	12	★ 0.8 FeS : 0.2 FeSO4	Au-Pd	45.72	1.39	10.71	0.02	16.17	0.25	10.13	8.48	2.98	95.85	4.19	0.05	0.95	5	0.92	0.0273	9184	273
WN14-17	1300	1.5	12	★ 0.9 FeS : 0.1 FeSO4	Au-Pd	45.84	1.38	10.53	0.02	16.73	0.25	10.57	7.88	2.78	95.97	4.32	0.05	0.95	5	0.87	0.0151	9449	151
WN14-18	1300	1.5	2	0.1*carb, 0.87*decarb + 0.03*FeS	graphite in Pt	42.61	1.36	11.86	0.14	17.27	0.28	9.33	8.34	3.36	94.54	2.79	0.28	0.72	14	-1.56	0.0124	2878	124
WN14-19	1300	1.5	3.25	0.1*carb, 0.87*decarb + 0.03*FeS	graphite in Pt	41.67	1.29	11.35	0.12	18.46	0.22	10.05	7.97	3.06	94.17	2.83	0.27	0.73	14	-1.48	0.0164	3278	164
Timeseries to establish equilibration time for Fe-Ir blebs at 1300°C																							
WN14-20	1300	1.5	2	JFR-4	graphite	46.11	1.33	12.19	0.20	16.01	0.41	8.93	8.71	3.44	97.34	3.03	0.26	0.74	18	-1.56	0.25	4040.3	121.67
WN14-21	1300	1.5	8	JFR-4	graphite	46.29	1.29	12.14	0.19	15.77	0.39	9.01	8.77	3.51	97.35	3.05	0.22	0.78	19	-1.24	0.68		
WN14-22	1300	1.5	4	JFR-4	graphite	45.97	1.25	11.67	0.23	16.14	0.38	9.51	8.52	3.41	97.08	3.02	0.24	0.76	12	-1.37	0.31		
WN14-23	1300	1.5	1	JFR-4	graphite	46.65	1.29	11.54	0.26	16.37	0.37	9.75	8.41	3.23	97.86	3.05	0.25	0.75	19	-1.52	0.39		
WN14-24	1300	1.5	24	JFR-4	graphite	46.39	1.27	11.94	0.19	15.70	0.39	9.07	8.75	3.64	97.33	2.99	0.26	0.74	20	-1.58	0.15		

The decimals accompanying the various components represent their relative abundanes by mass.
In addition to the materials shown, each experiment contained Iridium powder.
Experiments marked with a ★ contain 50:50 mixtures of JFR-4 and Fo72 olivine, in addition to the sulfur compounds listed. In aggregate these additional sulfur compounds represented one tenth of the experimental charge by mass.
"carb" and "decarb" represent carbonated and decarbonated JFR-2 powder respectively. Carbonated mixtures were added in an attempt to raise the fO2 in the capsule.
Fe-Ir alloy analyses are reported as normalized mole fractions. N referes to the number of useable analyses (totals >95%) .

Figure 4.6.2a clearly demonstrates that the use of $FeS/FeSO_4$ mixtures was unsuccessful in providing fO_2 conditions intermediate between those achieved using pure end-members. Rather than forming a disparate array, two clusters of fO_2 conditions are formed by the data, at +2 and -1 log units with respect to the Fayalite-Magnetite-Quartz (FMQ) buffer. Clustering at the lower of these conditions is not surprising, since experiments were performed in graphite capsules, and were therefore almost certainly fixed at the C-CO buffer. The clustering of more oxidized experiments is less easy to explain, since Au-Pd capsules are usually nonbuffering. In the absence of a redox buffer, the fO_2 in an experiment is determined by the chemical potential of oxygen in the most voluminous phases present; in this case, the olivine and melt. The fO_2 reached then probably reflects equilibration between these, which simply swamped the effects of the sulfide and sulfate that had been added. The fO_2 of the cluster of oxidized experiments does coincide with the expected position of the quartz-iron-fayalite (QIF) buffer at these conditions, but no quartz or metallic iron was observed in any of the run products, demonstrating that this is nothing more than a coincidence.

In addition to glass, olivine and metal blebs, many of the experiments performed in graphite capsules contain blebs of FeS, confirming that they are sulfide saturated. The measured sulfur concentrations for these experiments therefore represent SCSS for this melt under these conditions.

Determining whether the more oxidized experiments reached saturation is complicated by the unfortunate response of their capsule materials to compression. Unlike the graphite capsules, which remained rigid and well shaped during each experiment, the Au-Pd capsules frequently suffered deformation, contorting their 3D structure and isolating large volumes of the capsule from observation with a 2D section[2]. So although no separate sulfate-phases were observed in any of these experiments, the small areas accessible for observation might simply have been regions which lacked any sulfate. Previous studies have reported that sulfate is immiscible with silicate melt, and forms single large blebs rather than being distributed evenly throughout the capsule interior. The sulfur concentrations measured in these Au-Pd capsule experiments do cluster relatively closely, suggesting that some limit was

[2] Being also substantially thinner than the graphite capsules, they were prone to opening: two trial experiments (not included in table 4.6.2) exhibited visible breaches of the capsule wall.

reached, but confirmation of this through the detection of a separate sulfate phase was not achieved with these experiments.

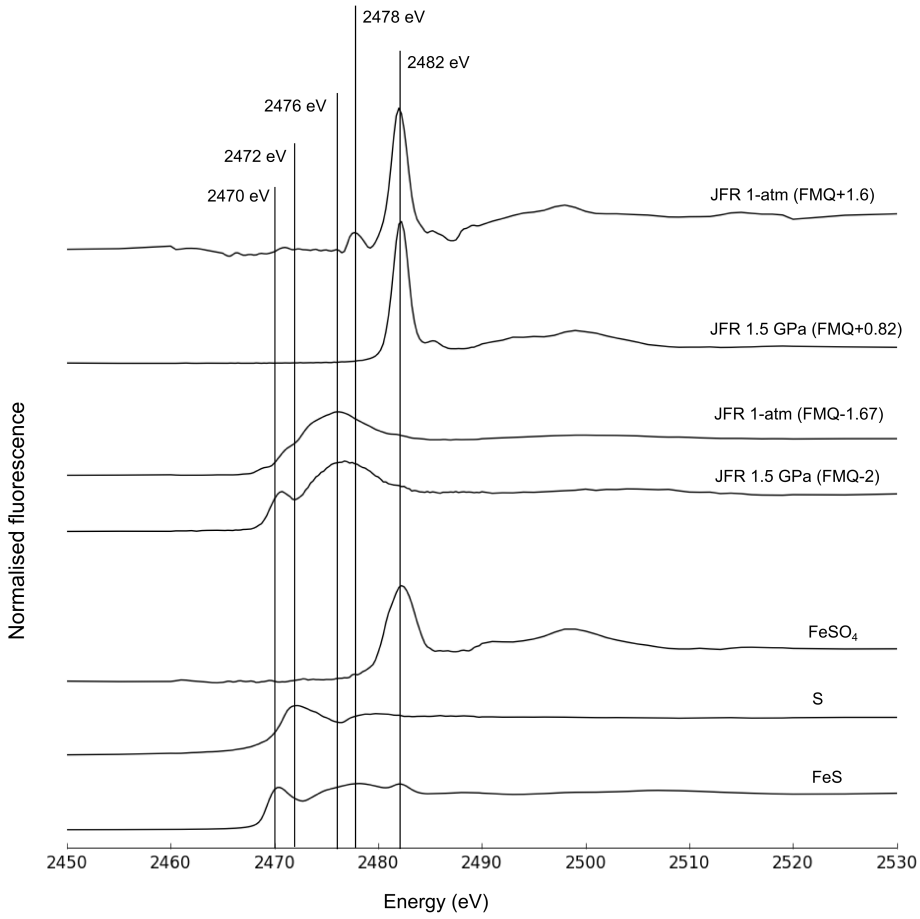
Consistent with the findings of Jugo *et al.* (2005), the measured sulfate concentrations are consistently much higher than the sulfur concentration at sulfide saturation (SCSS): by around factor of 2 on the average. Jugo *et al.* (2005) reported a larger difference, although as explained above, the sulfate concentrations measured here do not necessarily represent SCAS.

Despite the clustering of fO_2 conditions, these results constrain the position of the sulfide-sulfate crossover fO_2 at pressure between the two clusters. These values bracket the position identified by the one-atmosphere experiments described in the previous chapter, sadly neither ruling out nor confirming a pressure-effect on speciation.

XANES spectra were collected for glasses equilibrated under both the most oxidizing and reducing conditions. The white line energies of these fell into two distinct groups: ~2470eV for those below FMQ, and ~2482eV for all of those equilibrated above. Accordingly, all spectra show a close match with either the FeS or $FeSO_4$ standard, confirming that these are the stable species in the glasses.

Spectra representative of the oxidized and reduced experiments are shown in figure 4.6.2b, along with their standards, and their characteristic peak positions labelled for quick reference. For comparison, the most oxidized and reduced members of the 1-atmosphere glasses of chapter 3 are shown as well.

Figure 4.6.2b: Comparison between representative XANES spectra for glasses formed under the most oxidizing and reducing conditions under 1-atmosphere and 1.5GPa pressure. Note the peak at 2470eV within the high-pressure reduced spectrum, indicative of saturation by FeS.



Two features are of particular interest here. The spectrum for the oxidized melts equilibrated at high pressure is extremely clean, containing only the 2482eV peak characteristic of the sulfate ion. This is in contrast to the oxidized spectrum generated at 1-atmosphere, which also features a small peak at 2478eV, associated with the sulfite ion, and known to result from beam-induced damage to the sample. This is potentially explained by the contrasting concentrations of sulfur within these two glasses, also apparent from their noticeably different signal/noise ratios. Assuming that the rate of photo-reduction is limited by factors other than the sulfur concentration (e.g. the diffusion rate between electron donors and sulfur), the glass with the higher concentration would be expected to have a lower sulfite/sulfate ratio after the

same exposure to the beam. The alternative explanation, that the two glasses have different susceptibility to beam damage, is unlikely.

The experiments performed under reducing conditions show a more interesting difference, since it probably reflects a true difference between the chemistry of the two samples (rather than an artefact of the analysis). Both spectra exhibit the broad 2478eV feature characteristic of sulfide bonding in silicates, but in addition, the glass equilibrated at 1.5GPa has a relatively sharp peak at the energy characteristic of sulfide bonding in FeS (see the FeS standard). Since the glass is sulfide saturated, this is almost certainly due to sulfide blebs scattered throughout the glass. Under very high magnification, very small and bright features are visible in backscatter within many reduced samples, consistent with this explanation.

In some respects this is not a very exciting result, for no difference in speciation is observed in the glasses equilibrated at high and low pressure. Such a pressure effect remains plausible however, and has actually been observed by in similar materials, most notably by Matjuschkin *et al.* (2016) who observed a ~1.5 log unit shift in sulfide stability towards more oxidizing conditions for terrestrial arc magmas. A shift of similar size is not observed here, but since the fO_2 conditions explored don't overlap the sulfide-sulfate crossover at 1.5GPa a smaller shift cannot be ruled out.

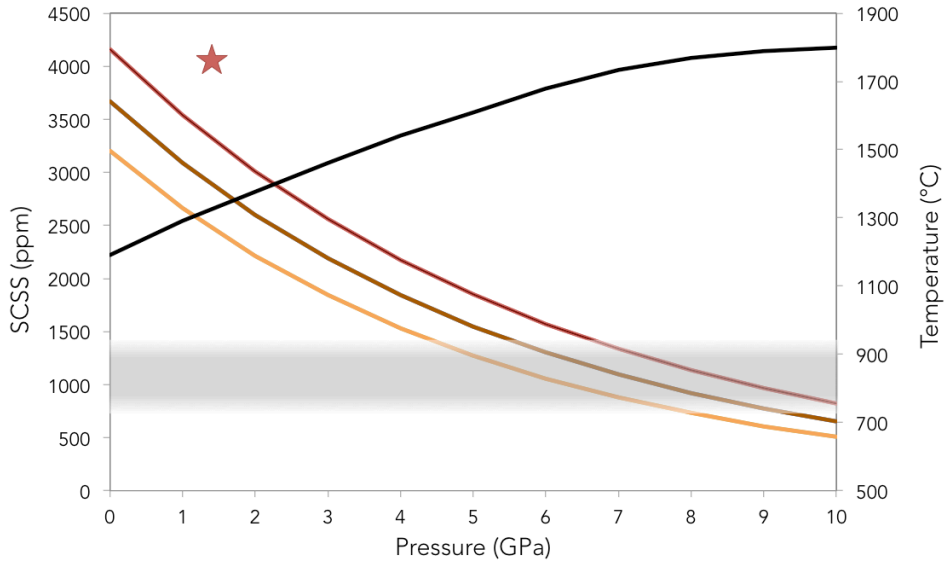
4.7 – DISCUSSION

4.7.1 Evaluation of models for SCSS

Most models for SCSS are founded on the concept of sulfide capacity established initially by Fincham and Richardson (1954) and subsequently developed and adapted for geological applications by Haughton *et al.* (1974), Wallace and Carmichael (1992), O'Neill and Mavrogenes (2002) and others. In general, these models express SCSS in terms of other intensive parameters by combining the so called "Fincham and Richardson relation" (equation 3.3 from the previous chapter) with the equilibrium between sulfur gas and dissolved FeO, and oxygen gas and pure immiscible FeS. The most recent iteration of this approach is that of Smythe *et al.* (2017), which also includes terms for the composition of the sulfide phase. In this scheme, the dependence of SCSS on temperature and pressure are incorporated as well, and arise indirectly, through their influence on both the sulfide capacity, and the activity of FeO in the silicate melt.

Under the conditions investigated here, Smythe *et al.* (2017) predicts a SCSS of 3262ppm for the JFR-4 composition, which is within ~20% of the value of 4040ppm obtained experimentally (the average from the three sulfide-saturated experiments performed). It is interesting that the model under-predicts SCSS by such a significant margin, and this suggests that the effect of FeO might not have been fully accounted for. Modifications are probably necessary before this scheme can be usefully extended to modelling Martian magmatism. Figure 4.7.1 shows the expected SCSS for the JFR-4 melt composition as a function of pressure, for three different temperatures. The SCSS measured here experimentally at 1400°C is indicated by the red star. The strong negative dependence on pressure is conspicuous, unlike the rise in SCSS with temperature (which is more intuitive). The grey band represents measured sulfur concentrations in the Shergottites, which average 1067ppm (Ding *et al.* 2015).

Figure 4.7.1: Modelled SCSS with pressure (Smythe *et al.* 2017). The experiments performed here represent a test of this model, for Fe-rich composition at high pressure. The orange, brown and red lines represent SCSS at 1200°C, 1300°C and 1400°C. The black line is the expected Martian geotherm (Fei *et al.* 2005). The hazy grey band represents the spread of actual sulfur concentrations observed in the Shergottites. Note the discrepancy between the modelled and measured value for SCSS.



4.7.2 A review of Mars' status as a sulfur-rich planet

It is interesting to note that the SCSS determined here for an assumed primary melt is very high compared with the sulfide concentrations in Martian meteorites; more than three times higher than the average. This remains true even if only the most "primitive looking" Shergottites are considered. Furthermore, owing to the exponential decrease in SCSS with pressure, the pressures corresponding to these concentrations imply an unrealistic crustal thickness if they do indeed represent sulfide-saturated assemblages. This potentially undermines the notion that the SNC source rocks were sulfide-saturated during separation from Mars' mantle, because the decompression accompanying their surface-ward migration would only have increased their capacity to carry sulfur. This has potentially has far-reaching implications, because the absence of a separate sulfide phase in the Shergottites' source regions caps the mantle sulfur abundance at whatever concentration is observed in these rocks, and actually implies a much lower value, since melt fractions exceeding ~50% are geophysically unreasonable.

It could be argued that irrespective of the average sulfur concentrations, since the very highest are somewhat closer to the "undegassed" value (~2700ppm in DaG 476), the existence of this sample alone requires a sulfur-rich source. According to this view, lower values are simply attributed to loss in transit through the crust. Although valid, this argument is vulnerable to the possibility that the Shergottites probably experienced fractional crystallization, which would have concentrated sulfur in their residual liquids. Arguing against this however, is the observation that many Shergottites (including DaG476) contain up to 30% cumulus olivine (Filiberto and Dasgupta 2011), which can only have diluted their sulfur concentrations.

The most obvious resolution to this discrepancy is the possibility that the Shergottites have lost sulfur between the mantle and the crust, either by degassing, or leaching by hydrothermal fluids following their crystallization. While there is no clear evidence for the latter possibility, little could be expected for the former had it occurred, since vesicles cannot be preserved during the crystallization process. Some support is offered by evidence for parallel depletions in other volatiles (e.g. water, indicated by pyroxene Li isotope profiles from Beck *et al.* 2004), although these are of limited help because their initial concentrations are similarly unconstrained. Assessing the Shergottites' degassing potential theoretically is a non-starter, since it depends overwhelmingly on the fracture density of the crust, which is effectively an unknown parameter. Comparisons with terrestrial MORBs indicate only that closed-system transport through the crust is possible, since MORBs typically erupt sulfide-saturated (Mathez 1976).

Since the earliest attempts to determine its bulk composition (Dreibus and Wanke 1985), Mars has been regarded as a sulfur-rich planet. This view originated from the recognition of enrichments in other volatiles such as phosphorus and chloride, as well as depletions in mantle siderophile abundances, which, coupled with efforts to satisfy Mars's moment-of-inertia factor, support the notion of a sulfur-rich core. Most recently, a global survey of Mars' surface by the Mars Odyssey Gamma-Ray Spectrometer (GRS) reported an average surface abundance of 4.4wt% SO_3 equivalent (McLennan *et al.* 2010): a value significantly higher than for any other terrestrial planet. However, perhaps the strongest evidence for the Shergottites' parent melts being sulfide-saturated is their low Ni contents. As pointed out by Tuff *et al.* (2013), nickel is around five times less abundant in the Shergottites than in terrestrial MORBs,

implying a subterrestrial nickel abundance for the Martian mantle. However, higher nickel concentrations observed in other Martian basalts, combined with nickel's lithophile partitioning behaviour under the low-pressure conditions of Martian core formation, point to a more Earth-like nickel concentration. The presence of sulfides (into which nickel would strongly partition) elegantly solves this problem. In the absence of an alternative mechanism for depleting primary melts in nickel, sulfide minerals in the Shergottite source regions remain a necessary part of our model of Martian differentiation.

In summary, the use of Shergottite sulfur concentrations for inferring Mars' mantle sulfur abundance is hindered by processes which both act to raise (fractional crystallization) and lower (crystal accumulation, degassing) the sulfur contents of these melts. The sulfur concentrations in the most primitive Shergottites, combined with the SCSS presented here, indicate that either the bulk-silicate portion of Mars is less sulfur-rich than presently assumed, or that the Shergottites have experienced considerable degassing en-route to the surface. Given the additional evidence for Mars's sulfur rich constitution, the latter possibility is considered more likely. This raises the possibility that Mars might have had a more sulfur-rich atmosphere in the past, which offers a means for maintaining the "warm and wet" environment emerging from analysis of sediments and geomorphology.

4.7.3 REE partitioning during Martian mantle melting

The Shergottites' mineralogy implies that their petrogenesis is complex, likely involving more than one episode of partial melting, crystallization and/or possibly mixing. Nonetheless, some of them have been proposed as primary mantle melts (Filiberto and Dasgupta 2011). To establish a baseline for this complexity, simple equilibrium crystallization of the Martian mantle melting was modelled, and the resulting melt and residue concentrations of REEs calculated using the partitioning coefficients presented previously.

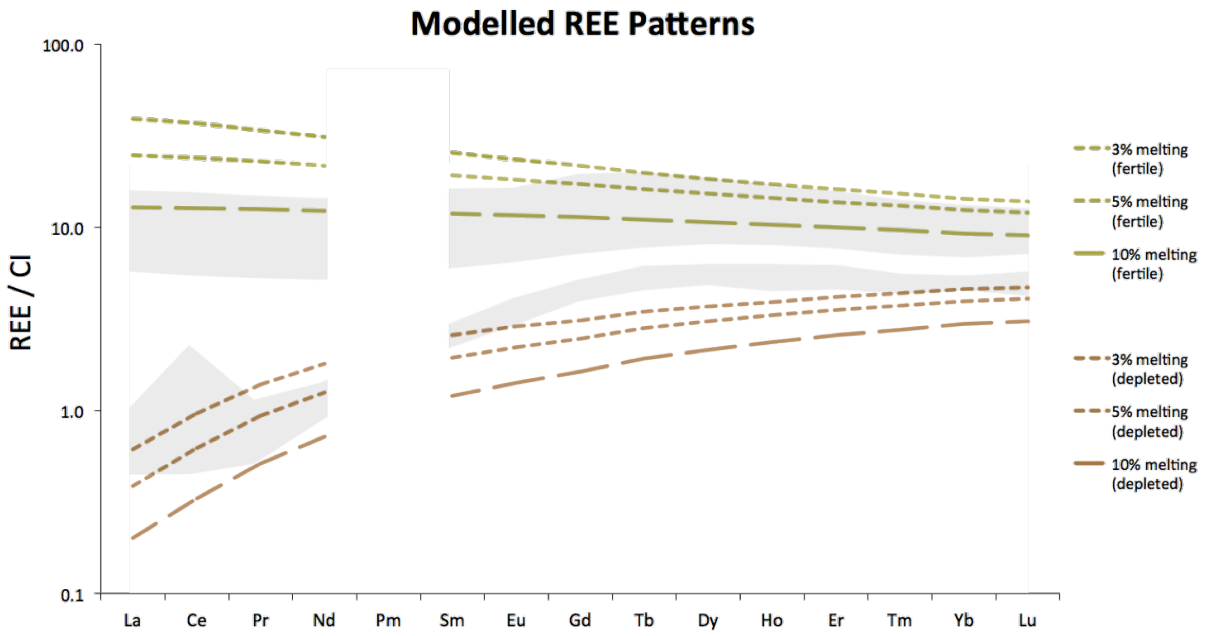
The major element compositions and modes of the phases constituting the DW mantle at 1.5GPa were calculated using Bertka and Holloway's (1994a) experimental data. Their study provided "snapshots" of the partial melting process at 0%, ~10%, and ~30% melting, and a linear change in phase modes was assumed between these to construct a continuous (if simplified) record of the melting process. For each increment of melting, the equilibrium

concentrations were calculated for every element in the coexisting solid and liquid phases. The initial REE abundances were calculated using the average Shergottitic Ca concentration (Dreibus and Wanke 1985) and the chondritic Ca/Yb element ratio (McDonough and Sun, 1994). Consistent with the literature convention, all REE concentration profiles were chondrite-normalized to aid comparisons between them.

Two low-degree melting scenarios were modelled: the first for a "fertile" mantle source (with chondritic abundances of the REEs), and the second for a "depleted" source, corresponding to the residue remaining from the first generation of melting. The REE profiles resulting from 3%, 5% and 10% partial melting of both sources are shown in figure 4.6.3c, overlying a compilation of natural profiles observed in the Shergottites (shown separately in figure 4.2.2).

While the most general differences between the HD and SD shergottites are reproduced, their characteristic features cannot be accounted for by this simple scheme. Consistent with the natural profiles, the chondrite normalized REE abundances for the fertile sourced melts are everywhere higher than those from the depleted source, and have considerably higher La/Lu ratios. However, neither the "lazy-S" shape of the SD Shergottites, nor the "step-like" profile of the HD Shergottites are predicted.

Figure 4.7.3: Observed and modelled chondrite-normalized REE profiles. The green and red lines represent the melt generated from a fertile and depleted mantle source respectively.



In the melting process modelled here, crystal-melt partitioning is dominated by the presence of higher-calcium pyroxene, since it has the largest partitioning coefficients, and undergoes the most dramatic change in modal abundance as melting progresses. The profiles generated are consequently most sensitive to the prevalence of this mineral. As a result, they constitute smooth uniformly sloping curves, which steepen towards the LREE end. By contrast, the natural profiles exhibit an inflection point between neodymium and europium, which is exaggerated for the HD shergottites. This more complex curvature implies the past influence of more than one dominant mineral, since mixing of the melts generated here cannot give rise to such an inflection. The identity of this second mineral (besides the higher-calcium pyroxene of this study) is unknown, but it presumably preferentially hosts LREEs. The leading candidate mineral for chemically segregating mantle at high pressure is garnet, which preferentially sequesters HREEs, rather than LREEs.

The most useful conclusion that emerges from this comparison between modelled and real profiles, is that more than one generation of mantle melting is necessary to reproduce the HD shergottites – there is no melting fraction of the fertile mantle that results in LREE depletion. Furthermore, this modelling effort confirms that neither of the shergottite groups' source regions can have had chondritic REE abundances (if these rocks are indeed primary melts, as some have suggested), supporting the notion that some form of segregation has affected Mars' mantle early in its history, prior to the extraction of the shergottites. This is consistent with the now widespread view that Mars' mantle comprises at least two chemically separate reservoirs, most popularly attributed to fractional crystallization of an early magma ocean (e.g. Borg and Draper 2003). The phase relations involved in crystallization of this magmas ocean remain enigmatic however, since no known mineral is capable of generating the inflections in REE-profile observed in the shergottites.

4.9 REFERENCES

Beck, P., Barrat, J.A., Chaussidon, M., Gillet, P. and Bohn, M. (2004). Li isotopic variations in single pyroxenes from the Northwest Africa 480 shergottite (NWA 480): A record of degassing of Martian magmas? *Geochimica et Cosmochimica Acta*, 68(13), pp.2925–2933.

Bertka, C.M. and Holloway, J.R. (1994a). Anhydrous partial melting of an iron-rich mantle I: subsolidus phase assemblages and partial melting phase relations at 10 to 30 kbar. *Contributions to Mineralogy and Petrology*, 115(3), pp.313–322.

Bertka, C.M. and Holloway, J.R. (1994b). Anhydrous partial melting of an iron-rich mantle II: primary melt compositions at 15 kbar. *Contributions to Mineralogy and Petrology*, 115(3), pp.323–338.

Blinova, A. and Herd, C.D.K. (2009). Experimental study of polybaric REE partitioning between olivine, pyroxene and melt of the Yamato 980459 composition: Insights into the petrogenesis of depleted shergottites. *Geochimica et Cosmochimica Acta*, 73(11), pp.3471–3492.

Blundy, J. and Wood, B.J. (1994). Prediction of crystal-melt partition coefficients from elastic moduli. *Nature*, 372(6505), pp.452–454.

Borg, L.E. and Draper, D.S. (2003). A petrogenetic model for the origin and compositional variation of the martian basaltic meteorites. *Meteoritics and Planetary Science*, 38(12), pp.1713–1731.

Borg, L.E., Nyquist, L.E., Wiesmann, H., Shih, C.Y. and Reese, Y. (2003). The age of Dar al Gani 476 and the differentation history of the martian meteorites inferred from their radiogenic isotopic systematics. *Geochimica et Cosmochimica Acta*, 67(18), pp.3519–3536.

Brice, J.C. (1975). Some thermodynamic aspects of the growth of strained crystals. *Journal of Crystal Growth*, 28(2), pp.249–253.

Bridges, J.C., and Warren, P.H. (2006). The SNC meteorites: basaltic igneous processes on Mars *Journal of the Geological Society of London*, 163 p.229-251.

Buchanan, D. and Nolan, J. (1979). Solubility of sulfur and sulfide immiscibility in synthetic tholeiitic melts and their relevance to Bushveld-complex rocks. *The Canadian Mineralogist*, 17(1979), pp.483–494.

Ding, S., Dasgupta, R., Lee, C-T.A. and Wadhwa, M. (2015). New bulk sulfur measurements of Martian meteorites and modelling the fate of sulfur during melting and crystallization -

Implications for sulfur transfer from Martian mantle to crust-atmosphere system. *Earth and Planetary Science Letters*, 409, pp.157–167.

Eggins, S.M. and Shelley, J.M.G. (2002). Compositional Heterogeneity in NIST SRM 610-617 *Glasses. Geostandards Newsletter,* 26, pp.269–286.

Fei, Y., and Bertka, C. (2005). The Interior of Mars. *Science*, 308 pp.1120-1121.

Filiberto, J. and Dasgupta, R. (2011). Fe^{2+}–Mg partitioning between olivine and basaltic melts: Applications to genesis of olivine-phyric shergottites and conditions of melting in the Martian interior. *Earth and Planetary Science Letters*, 304(3–4), pp.527–537.

Fincham, C.J.B. and Richardson, F.D. (1954). The Behaviour of Sulphur in Silicate and Aluminate Melts. *Proceedings of the Royal Society A: Mathematical, Physical and Engineering Sciences,* 223(1152), pp.40–62.

Haughton, D.R., Roeder, P.L. and Skinner, B.J. (1974). Solubility of sulfur in mafic magmas. *Economic Geology*, 69(4), pp.451–467.

Jayasuriya, K.D., O'Neill, H.S.T., Berry, A.J and Campbell, S.J. (2004). A Mossbauer study of the oxidation state of Fe in silicate melts. *American Mineralogist*, 89, pp.1597-1609.

Jochum, K.P., Weis, U., Stoll, B., Kuzmin, D., Yang, Q., Raczek, I., Jacob, D.E., Stracke, A., Birbaum, K., Frick, D.A., Gunther, D. and Enzweiler, J. (2011). Determination of reference values for NIST SRM 610-617 glasses following ISO guidelines. *Geostandards and Geoanalytical Research*, 35(4), pp.397–429.

Jugo, P.J., Luth, R.W. and Richards, P. (2005). An Experimental Study of the Sulfur Content in Basaltic Melts Saturated with Immiscible Sulfide or Sulfate Liquids at 1300 C and 1.0 GPa. *Journal of Petrology*, 46(4), pp.783–798.

Li, C. and Ripley, E.M. (2005). Empirical equations to predict the sulfur content of mafic magmas at sulfide saturation and applications to magmatic sulfide deposits. *Mineralium Deposita*, 40(2), pp.218–230.

Matjuschkin, V., Blundy, J.D. and Brooker, R.A. (2016). The effect of pressure on sulphur speciation in mid- to deep-crustal arc magmas and implications for the formation of porphyry copper deposits. *Contributions to Mineralogy and Petrology*, 171:66.

Mavrogenes, J.A., and O'Neill, H.S.C. (1999). The relative effects of pressure, temperature and oxygen fugacity on the solubility of sulfide in mafic magmas *Geochimica et Cosmochimica Acta*, 63 (No. 7/8), pp.1173-1180.

McDonough, W.F. and Sun, S. (1994). The composition of the Earth *Chemical geology,* 120, pp. 223-253.

McKay, G., Wagstaff, J, and Yang, A.R. (1986). Clinopyroxene REE distribution coefficients for shergottites: The REE content of the Shergotty melt. *Geochimica et Cosmochimica Acta*, 50(6), pp.927-937.

McSween, H.Y. (1985). SNC meteorites: Clues to Martian petrologic evolution? *Reviews of Geophysics*, 23(4), pp.391-416.

McSween, H.Y. (1994). What we have learned about Mars from SNC meteorites (Invited review). *Meteocritics*, 29, pp.757-779.

Mysen, B.O. (2004). Element partitioning between minerals and melt, melt composition, and melt structure. *Chemical Geology*, 213(1–3), pp.1–16.

O'Neill, H.S.C. and Mavrogenes, J.A. (2002). The Sulfide Capacity and the Sulfur Content at Sulfide Saturation of Silicate Melts at 1400°C and 1 bar. *Journal of Petrology*, 43(6), pp.1049–1087.

Righter, K., Pando, K. and Danielson, L.R. (2009). Experimental evidence for sulfur-rich martian magmas: Implications for volcanism and surficial sulfur sources. *Earth and Planetary Science Letters*, 288(1–2), pp.235–243.

Roeder, P.L., and Emslie, R.F. (1970). Olivine-Liquid Equilibrium *Contributions to Mineralogy and Petrology*, Vol.29 p.275-289.

Rohrbach, A. and Schmidt, M.W. (2011). Redox freezing and melting in the Earth's deep mantle resulting from carbon-iron redox coupling. *Nature,* 472(7342), pp.209–212.

Shannon, R.D. (1976). Revised effective ionic radii and systematic studies of interatomic distances in halides and chalcogenides. *Acta Crystallographica* Section A, 32(5), pp.751–767.

Smythe, D.J., Wood, B.J. and Kiseeva, E. (2017). The S content of silicate melts at sulfide saturation: new experiments and a model incorporating the effects of sulfide composition. *American Mineralogist. In Press* (DOI: 10.2138/am-2017-5800CCBY).

Toplis, M.J. and Corgne, A. (2002). An experimental study of element partitioning between magnetite, clinopyroxene and iron-bearing silicate liquids with particular emphasis on vanadium. *Contributions to Mineralogy and Petrology*, 144(1), pp.22–37.

Tuff, J., Wade, J. and Wood, B.J. (2013). Volcanism on Mars controlled by early oxidation of the upper mantle. *Nature*, 498(7454), pp.342–5.

Wadhwa, M. (2001). Redox state of Mars' upper mantle and crust from Eu anomalies in shergottite pyroxenes. *Science*, 291(5508), pp.1527-1530.

Wallace, P. and Carmichael, I.S.E. (1992). Sulfur in basaltic magmas. *Geochimica et Cosmochimica Acta*, 56(5), pp.1863–1874.

Wendlandt, R.F. (1982). Sulfide saturation of basalt and andesite melts at high pressures and temperatures. *American Mineralogist*, 67(9–10), pp.877–885.

Wilson, S.A. (1997). The collection, preparation and testing of a USGS reference material BCR-2, Columbia River, Basalt, U.S. Geological Survey Open-File Report 98-00x.

Wood, B.J. and Blundy, J.D. (1997). A predictive model for rare earth element partitioning between clinopyroxene and anhydrous silicate melt. *Contributions to Mineralogy and Petrology*, 129(2–3), pp.166–181.

Wood, B.J. and Blundy, J.D. (2003). Trace element partitioning: The influences of ionic Radius, Cation charge, Pressure, Temperature. *Treatise on Geochemistry*, S*econd edition* Vol. 3, pp.421-448.

Woodland, A.B. and O'Neill, H.S.C. (1997). Thermodynamic data for Fe-bearing phases obtained using noble metal alloys as redox sensors. *Geochimica et Cosmochimica Acta*, 61(20), pp.4359–4366.

Chapter 5

Concluding Remarks and Directions for future research

5.1 - OVERVIEW

This thesis has investigated the behaviour of sulfur during Martian igneous processes, with particular emphasis on the implications of its behaviour for the internal structure and chemistry of Mars' mantle. Individual conclusions and discussions accompany the previous chapters, so rather than repeating these here, a synthesis is made of the broader implications of these findings for Martian differentiation, and the likely origin of sulfur in Mars' surface. This is followed by some specific recommendations for further research, based on results or challenges encountered in during each chapter.

5.2 – IMPLICATIONS

5.2.1 The origin of surficial Martian sulfur

As explained in the introduction, the Martian surface is extraordinarily rich in sulfur (McLennan *et al.* 2010), which primarily takes the form of sulfate minerals (Gendrin *et al.* 2005). Whether or not this enrichment is a reflection Mars' bulk chemistry – rather than merely its surface – is critical for understanding Mars formation and internal structure. This is because in addition to being volatile (and therefore potentially a monitor of Mars' condensation from the solar nebula), sulfur is strongly siderophile, and therefore a likely determinant of the size, density and melting point of the Martian core. One way to investigate the origin of this surficial sulfur is to integrate the flux of sulfur from the mantle, and compare the total mass of sulfur obtained with that observed in the surface environment. To do this, it is necessary to know the capacity of melts for delivering sulfur from the mantle, and this was investigated in chapter 4.

The high-pressure experiments performed in chapter 4 indicate that partial melts of Mars putative mantle can dissolve 4040ppm of sulfur before reaching sulfide saturation. This is significantly higher than the value determined for terrestrial basalts (1500ppm; Jugo *et al.* 2005); and is consistent with the well-documented positive influence of FeO on sulfur solubility (e.g. Haughton *et al.* 1974). However, as remarked upon earlier, the measured concentrations of sulfur in Martian meteorites are significantly less than this upper limit. It is reasonable to ask whether the difference between these values corresponds to sulfur that has degassed during melt migration from the mantle, and whether this is the origin of the sulfur that now outcrops in sediments on the surface.

Taking 6.54×10^6 km^3 as an estimate for the erupted volume of magma on Mars (Greeley and Schneid 1991), and multiplying this by the most recent estimate for the density of the Martian crust (3100 kg/m^3; Baratoux et al. 2014) yields a total erupted mass of 20.3×10^{18} kg. Assuming that the fraction of this material that has been lost as gaseous sulfur equals the initial (sulfide saturated) sulfur concentration (4040ppm) minus the average concentration observed in the Shergottites (1067ppm), this yields a total degassed mass of 6.03×10^{16} kg of sulfur. Perhaps the most illuminating way of comparing this with the quantity of sulfur at the surface is by calculating how deep the surficial abundance of sulfur must extend beneath the surface, to correspond to the same total mass. Taking 1.76 wt% as the average surface concentration (McLennan *et al.* 2010), and assuming global coverage of sulfur (the Martian poles are less well sampled but this is probably reasonable nonetheless), the degassed mass of sulfur corresponds to a layer ~8m deep. This is clearly a geologically reasonable number, which demonstrates well the similarity of these two masses. Obviously this result is highly speculative, since the surface abundance of sulfur is heterogeneous and the meteorites only sample a tiny portion of the crust. But the similarity in the order-of-magnitude of the two values is significant. A similar calculation by Righter *et al.* (2009) drew the same conclusion, finding the total masses of degassed and surficial sulfur to be within a factor of two of one another.

In summary, the sulfide concentrations measured as part of this study support the notion that the sulfur observed at Mars' surface can be accounted for by degassing of its mantle, and does not require exogenous delivery of sulfur (such as by a sulfur-rich impactor for example).

5.2.2 The oxidation state of the Martian mantle

The foregoing conclusions consider magmatic sulfur only in its reduced form, as this is how sulfur is present in all Martian meteorites. However, besides its noteworthy abundance, sulfur is of great interest because of its variable valence state and diverse geochemical behaviour. The main finding of this thesis is that the major-element chemistry of silicate melts influences the speciation of their dissolved sulfur. The identification of Fe as the controlling element makes this finding especially relevant to Martian igneous processes, since the bulk silicate portion of Mars is characterized by an FeO concentration approximately twice that of the bulk silicate Earth (Wanke and Dreibus 1994).

According to the results presented in this study, sulfur dissolved in Martian melts undergoes oxidation to sulfate at fO_2 conditions half a log unit higher than in terrestrial melts.

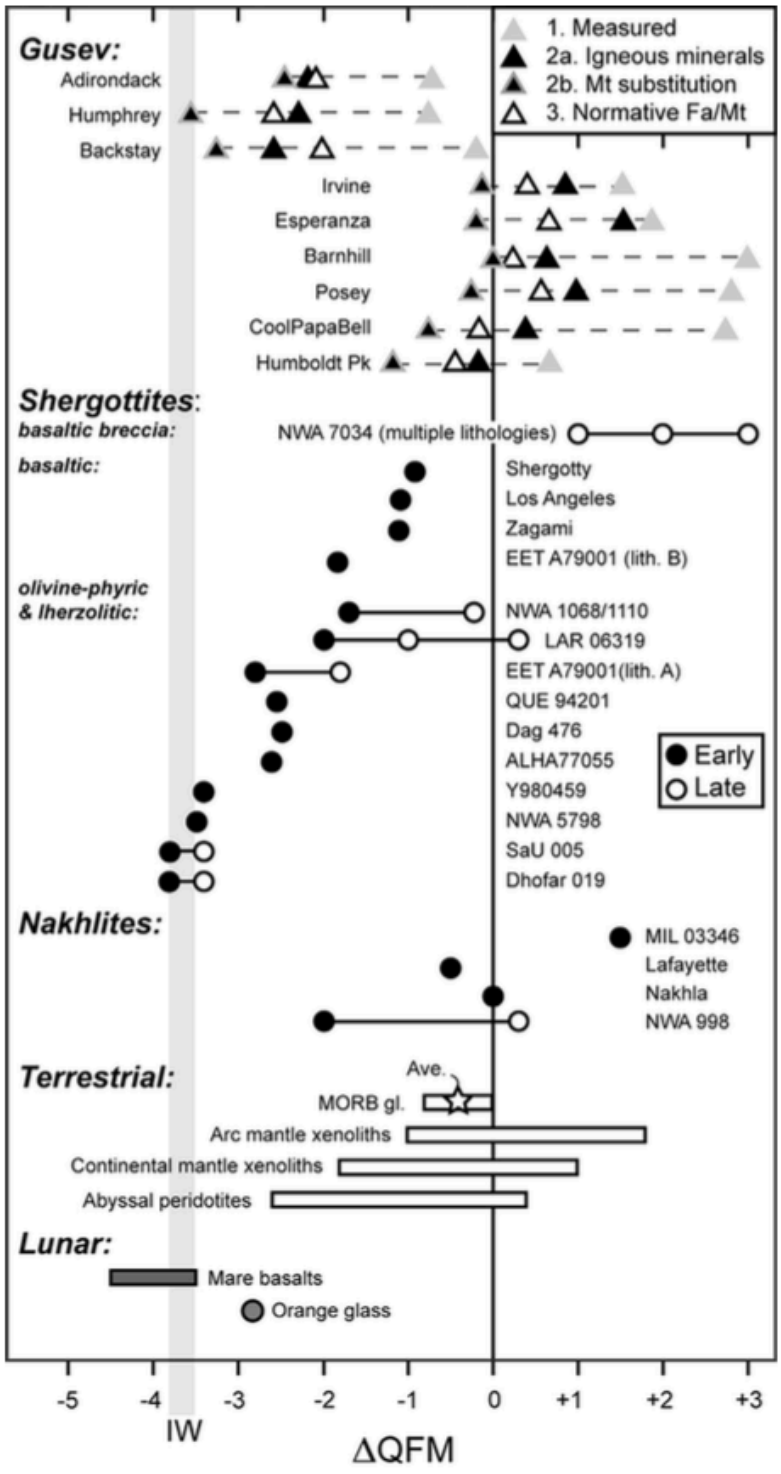
This result is of interest because, as outlined in the introduction, the Shergottite meteorites and Gusev crater basalts exhibit markedly different Ni concentrations, which have been interpreted as evidence for sulfide existing in the Shergottites' source regions and preferentially retaining Ni (Tuff *et al.* 2013). A corollary of this scenario is that these two suites of rock have been derived from source regions with different fO_2 conditions, as this is the simplest explanation for sulfide being stable in one source region (that of the meteorites) but not the other (that of the Gusev basalts). This conclusion is supported by other proxies for the Gusev basalts' oxidation state, such as the presence of magnetite (McSween *et al.* 2004).

The notion that different regions of Mars' mantle exhibit different degrees of oxidation is, in-and-of-itself, exciting. However, the results of this investigation into sulfur speciation enable this difference to be expressed quantitatively, since the silicate melts studied are close approximations to primary melts of Mars' mantle. For sulfate to be the stable species in these FeO rich melts, their primary fO_2 must be greater than or equal to 0.5 log units above the Fayalite-Magnetite-Quartz (FMQ) buffer. This is towards the high end of estimates provided by other oxybarometers (figure 5.2.2).

A pertinent question that remains to be answered definitively however, is whether the oxidized nature of the Gusev rocks truly reflect the conditions of their source regions, or whether this characteristic has been inherited en route towards the surface (for example by assimilation by oxidized crustal material or interaction with water-rich fluids). Resolution of this issue will likely have to await a sample-return mission, so that more detailed analysis can be made of the textural relations in these (or similar) rocks. But assuming the Gusev rocks' oxidized character *is* representative of their source, some mechanism is required to explain the change in redox state of large parts of Mars' mantle. The Gusev rocks' greater ages relative to the Shergottites have been used to argue that oxidation must have taken place very early in Mars' history (Tuff *et al.* 2013). However, from the geochronology alone it is difficult to reject the competing hypothesis that Mars began with an oxidized mantle, large parts of which have subsequently been reduced. The preference for the former scenario comes primarily from the relative scarcity of reduction mechanisms: mechanisms for oxidation being easier to imagine, since hydrogen, a likely by-product, is readily lost to space. Due to its multivalent character, sulfur may actually have

participated in oxidation (for example, by the hydration of iron sulfide to yield iron sulfate and hydrogen gas).

Figure 5.2.2: A compilation of estimates for the fO_2 of Martian igneous rocks. Note the large contrast in fO_2 between the Shergottites and the Gusev basalts. Figure taken from Schmidt *et al.* (2013).



5.2.3 Origins of the Shergottite REE profiles

The notion that Mars' mantle comprises at least two chemically isolated reservoirs has been is relatively well established on the basis of trace element and isotopic data from the Martian meteorites (e.g. Borg *et al.* 2013). One major line of evidence for this is the variation in REE profiles exhibited by the Shergottites (e.g. Bridges and Warren 2006). The nature of these source regions (their location, geologic age, and genetic relation to one another) are, however, unknown. A leading hypothesis is that they represent late stage liquids and cumulates from the crystallization of a magma ocean (Borg and Draper, 2004).

As part of this study, a simpler model was tested, whereby the LREE/HREE-enriched and LREE/HREE-depleted Shergottites are conjectured to be products of successive generations of melting of a single mantle source. This model was unable to reproduce the details of the profiles (in particular their inflections between praseodymium and gadolinium), indicating that it has not captured the essential processes that have given rise to the Shergottites. Future studies should explore the effect of garnet on REE partitioning, since this is relatively unexplored, and Al-depletions in the Shergottites have been suggested to indicate that garnet might have been present in their source regions (see section 1.1.5 of chapter 1).

5.3 – DIRECTIONS FOR FUTURE WORK

5.3.1 Spectroscopic determination of sulfur speciation

While the conclusions concerning sulfur speciation at one atmosphere pressure are robust, they could be extended and strengthened by further work. The greatest uncertainty inherent in this section derives from the assumption that all chemical components retain their valence during the quenching of each silicate melt. This question could be definitively answered through analysis of an in-situ molten silicate at a suitably equipped beamline. Such an experiment calls for some method of containing a molten material under appropriate conditions while exposing it to the X-ray beam. A further improvement concerns the interpretation of the XANES spectra collected. The present interpretations are based on the assumption that the sulfide and sulfate species have similar fluorescence yields, so that their peak amplitudes both scale linearly (and by the same scaling factor) with the concentration of sulfur in the materials studied. Collection of XANES spectra for mechanical mixtures of sulfide and sulfate can be used to measure the accuracy of this approximation, and thereby validate (or invalidate!) the linear combination fitting (LCF) procedure used to estimate the $S^{6+}/\Sigma S$ ratio. By the standards of the proposal made above, this is a very straightforward procedure.

Both the XANES and SIMS analyses were greatly impeded by the very low concentrations of sulfur dissolved in the more oxidized melts. These resulted from limitations placed over the oxygen and sulfur fugacities by the experimental apparatus. Specifically, sulfur fugacity could never exceed the Pt-PtS buffer, and the fugacities of both oxygen and sulfur could only be changed in such as manner as would maintain 1-atmosphere of pressure inside the furnace. Pressure vessels offer one means to exceed this limit, but as with the one-atmosphere furnace, they don't presently allow oxygen and sulfur fugacity to be controlled arbitrarily and independently.

Finally, the linear relationship between log S^{6+}/S^{2-} and log $Fe_2O_3/(FeO)^2$ ratio potentially offers an alternative to measuring S^{6+}/S^{2-} directly in silicate melts. At present however, this relationship is somewhat circumstantial, being heavily biased towards basaltic melts and lacking support from the S^{6+}/S^{2-} obtained using SIMS. A second study following a similar methodology to this one, but with a range of more Fe-poor compositions, and direct measurements of the Fe redox ratio by Mossbauer spectroscopy, should provide a more rigorous test of this relationship.

5.3.2 Measurement of fO_2 with the Fe-Ir sensor

The olivine capsules developed in chapter 2 provide a means to test the calibration for the Fe-Ir fO_2 sensor used in chapter 4, at least across the fO_2 range for which olivine is a stable phase. Performing such a test with the classic wire-loop methods is difficult because of the loops propensity to absorb iridium. The difficulty experienced analyzing these blebs by WDS suggests that larger blebs are necessary (since these are probably more likely to polish to a flat surface), or that some alternative means of analysis (e.g. nanoSIMS) are required.

5.3.3 The role of garnet in the petrogenesis of the Shergottites

Both the major and trace element chemistry of SNCs suggest that crystallization of an Al-rich phase, probably garnet, was involved in their petrogenesis. The presence of garnet might help to explain the contrasting REE profiles of the heavily- and slightly-depleted shergottites presented in chapter 4. Therefore, partition coefficients between appropriate garnet compositions and melts are required. Future work should investigate the compositional effect of REE partitioning into these important phases, in particular, with a view to explaining the inflection seen in both the HD and SD shergottites between praseodymium and gadolinium.

5.4 – REFERENCES

Agee, C.B. and Draper, D.S. (2004). Experimental constraints on the origin of Martian meteorites and the composition of the Martian mantle. *Earth and Planetary Science Letters*, 224(3–4), pp.415–429.

Baratoux, D., Samuel, H., Michaut, C., Toplis, M.J., Monnereau, M., Wieczorek, M., Garcia, R. and Kurita. (2014Petrological constraints on the density of the Martian crust. *Journal of geophysical Research*, 119(7), pp.1707-1727.

Borg, L.E. and Draper, D.S. (2003). A petrogenetic model for the origin and compositional variation of the martian basaltic meteorites. *Meteoritics and Planetary Science*, 38(12), pp.1713–1731.

Bridges, J.C., and Warren, P.H. (2006). The SNC meteorites: basaltic igneous processes on Mars *Journal of the Geological Society of London*. Vol. 163 p.229-251.

Ding, S., Dasgupta, R., Lee, C-T.A. and Wadhwa, M. (2015). New bulk sulfur measurements of Martian meteorites and modelling the fate of sulfur during melting and crystallization - Implications for sulfur transfer from Martian mantle to crust-atmosphere system. *Earth and Planetary Science Letters*, 409, pp.157–167.

Gendrin, A., Mangold, N., Bibring, J-P., Langevin, Y., Gondet, B., Poulet, F., Bonello, G., Guantin, C., Mustard, J., Arvidson, R. and LeMouelic, S. (2005). Sulfates in Martian layered terrains: The OMEGA/Mars Express View. *Science*, 307, pp.1587-1591.

Greeley, R. and Schneid, B.D. (1991). Magma generation on Mars: amounts rates and comparison with Earth, Moon, and Venus. *Science*, 254 pp.996-998.

Haughton, D.R., Roeder, P.L. and Skinner, B.J. (1974). Solubility of sulfur in mafic magmas. *Economic Geology*, 69(4), pp.451–467.

Jugo, P.J., Luth, R.W. and Richards, P. (2005). An Experimental Study of the Sulfur Content in Basaltic Melts Saturated with Immiscible Sulfide or Sulfate Liquids at 1300 C and 1.0 GPa. *Journal of Petrology*, 46(4), pp.783–798.

McSween, H.Y., Arvidson, R.E., Bell, J.F., Blaney, D., Cabol, N.A., Christiensen, P.R., Clark, B.C., Crisp, J.A., Crumpler, L.S., Des Marais, D.J., Farmer, J.D., Gellert, R., Ghosh, A., Gorevan, S., Graff, T., Grant, J., Haskin, L.A., Herkenhoff, K.E., Johnson, J.R., Jolliff, B.L., Klingelhoefer, G., Knudson, A.T., McLennan, S., Milam, K.A., Moersch, J.E., Morris, R.V., Rieder, R., Ruff, S.W., Souze Jr, P.A., Squyres, S.W., Wanke, H., Wang, A., Wyatt, M.B., Yen, A. and Zipfel, J. (2004). Basaltic Rocks Analyzed by the Spirit Rover in Gusev Crater. *Science*, 305(5685), pp.842–845.

McLennan, S.M., Boynton, W.V., Karunatillake, S., Hahn B.C. and Taylor, G.J. (2010). Distribution of sulfur on the surface of Mars determined by the 2001 Mars Odyssey Gamma Ray Spectrometer. *40th Annual Lunar and Planetary Science Conference*, 41, pp.2174.

Righter, K., Pando, K. and Danielson, L.R. (2009). Experimental evidence for sulfur-rich martian magmas: Implications for volcanism and surficial sulfur sources. *Earth and Planetary Science Letters*, 288(1–2), pp.235–243.

Schmidt, M.E., Schrader, C.M. and McCoy, T.J. (2013). The primary fO2 of basalts examined by the Spirit rover in Gusev Crater, Mars: Evidence for multiple redox states in the martian interior. E*arth and Planetary Science Letters*, 384, pp.198–208.

Tuff, J., Wade, J., and Wood, B.J. (2013). Volcanism on Mars controlled by early oxidation of the upper mantle. *Nature*, 498(7454), pp.342–5.

Wanke, H., Dreibus, G. and Wright, I.P. (1994). Chemistry and Accretion History of Mars *Transactions of the Royal Society A: Mathematical, Physical and Engineering Sciences*, 349(1690), pp.285–293.

Appendices

Appendix 1

Mass Flow Controller: principles of operation

The flux of each of the three gases (CO, CO_2, SO_2) through the furnace was set using a mass flow controller (MFC): an electronically controlled valve, which is continuously adjusted in response to the flux reported by a built-in flow sensor.

The flow sensor comprises a capillary tube, through which a small fraction of the gas passing through the MFC's primary conduit is diverted. During normal operation (defined shortly), the flow is laminar through both conduits, courtesy of their specially designed geometry. Both flow rates are therefore proportional to each other, and the flux measured through the capillary tube suitably monitors the flux through the primary conduit.

A pair of heating coils are wound around the capillary tube, longitudinaly displaced from one another. A current passed through these coils heats the gas, and establishes a temperature gradient between the two coils, which in-turn creates a resistance contrast between them. This resistance contrast is linearly proportional to the flow rate, and is used to open/close the value such that the user-specified flow is achieved. The flux measured in this way is a mass flux, so the heat capacity of the gas must be known to determine the volume flux through the MFC (expressed in mL/min).

'Normal operation' refers here to the range of flow rates for which the flow through both the primary conduit and the capillary is laminar. The accuracy of the flux reported reduces if the MFC is used outside this range; the upper limit is equal to the highest setting permitted by the dial, and the lower limit one-tenth of the upper limit.

Appendix 2

Gas mixture calculations

The oxygen and sulfur fugacity during each experiment was controlled by continuously fluxing a mixture of CO, CO_2 and SO_2 gas through the furnace tube. Mixtures of these gases were chosen such that at the prevailing temperature (1300°C) and pressure (1-atmosphere), an equilibrium mixture of new gas species formed, for which the fugacity of O_2 and S_2 had the desired values. In other words, bulk compositions of C, S and O were selected such that their equilibrium position in the furnace (at one atmosphere pressure) dictated the required fugacities of O_2 and S_2.

To select an appropriate mixture, the equilibrium oxygen and sulfur fugacities were calculated for many arbitrary CO-CO_2-SO_2 gas mixtures, which were iteratively adjusted so as to converge on one exhibiting the desired fugacities. Calculation of the equilibrium fO_2 and fS_2 for each candidate gas mixture is simple in principle, entailing a search for the position of equilibrium at the stipulated temperature and pressure, before reading off the coefficients of O_2 and S_2. It is made more complicated however, by the large number of possible species that can be made from C, S an O: CO, CO_2, CO_3, S_2, SO_3, S, S_3, S_4, S_6, S_8, CS, CS_2, O_2, CCO, C_3O_2, O_3, O, C, C_2. A large number of possible combinations of these species satisfy the mas-balance constraints, and the combination with the lowest Gibbs energy must be found.

The guiding equations permitting this process are therefore the additivity of the Gibbs energies and partial pressures of the various species:

$$G_{mixture} = \sum_i G_i \quad \text{(a)}$$

$$P_{total} = \sum_i P_i \quad \text{(a)}$$

The procedure followed was that explained in White *et al.* (1958). The thermodynamics data (entropies and volumes each species) were taken from the JANF tables.

White, W.B., Johnson, S.M. and Dantzig, G.B. (1958) Chemical Equilibrium in Complex Mixtures, *The Journal of Chemical Physics*, 28(5), 751-755.

Appendix 3

A brief introduction to Secondary Ion Mass Spectroscopy (SIMS)

All mass spectrometers perform the same fundamental operation: dispersion of ionic species according to their mass/charge (m/Q) ratios. This dispersion is invariably achieved using electric and/or magnetic fields, but the geometry of the fields and the resulting particle trajectories differ from one instrument design to another, depending on their specific analytical purposes.

The classic mass dispersion method is *magnetic sector* spectrometry, which uses a static magnetic field to deflect ions along a curved trajectory towards a detector. Differences in m/Q yield different amounts of curvature, and the field strength is adjusted to permit the exclusive passage of ions with a particular m/Q ratio. A more recent dispersion method is *quadrupole* spectrometry, which employs four parallel metal rods with adjustable potentials maintained between opposite pairs, to impart oscillatory trajectories to ions travelling between them (parallel to their axis direction). Only ions having the desired m/Q follow trajectories that terminate at the detector, and all the rest being diverted. Quadrupoles are relatively inexpensive, and permit more rapid analysis of groups of elements than magnetic sectors, owing to the speed with which the quadrupole voltages can be changed. However, their focusing geometry limits their mass resolution, which rarely exceeds 1,000[1]. A third popular technique is *time-of-flight* (*TOF*) mass spectrometry, which uses an electric field to accelerate ions through a common electrical potential, dispersing them longitudinally by kinetic energy (and therefore also by mass). The amount of dispersion, and hence the mass difference, is measured by recording their flight time to the detector. Time-of-flight spectrometry offers high mass resolution (in excess of 10,000), but is fairly inflexible with respect to the types of material that can be analyzed.

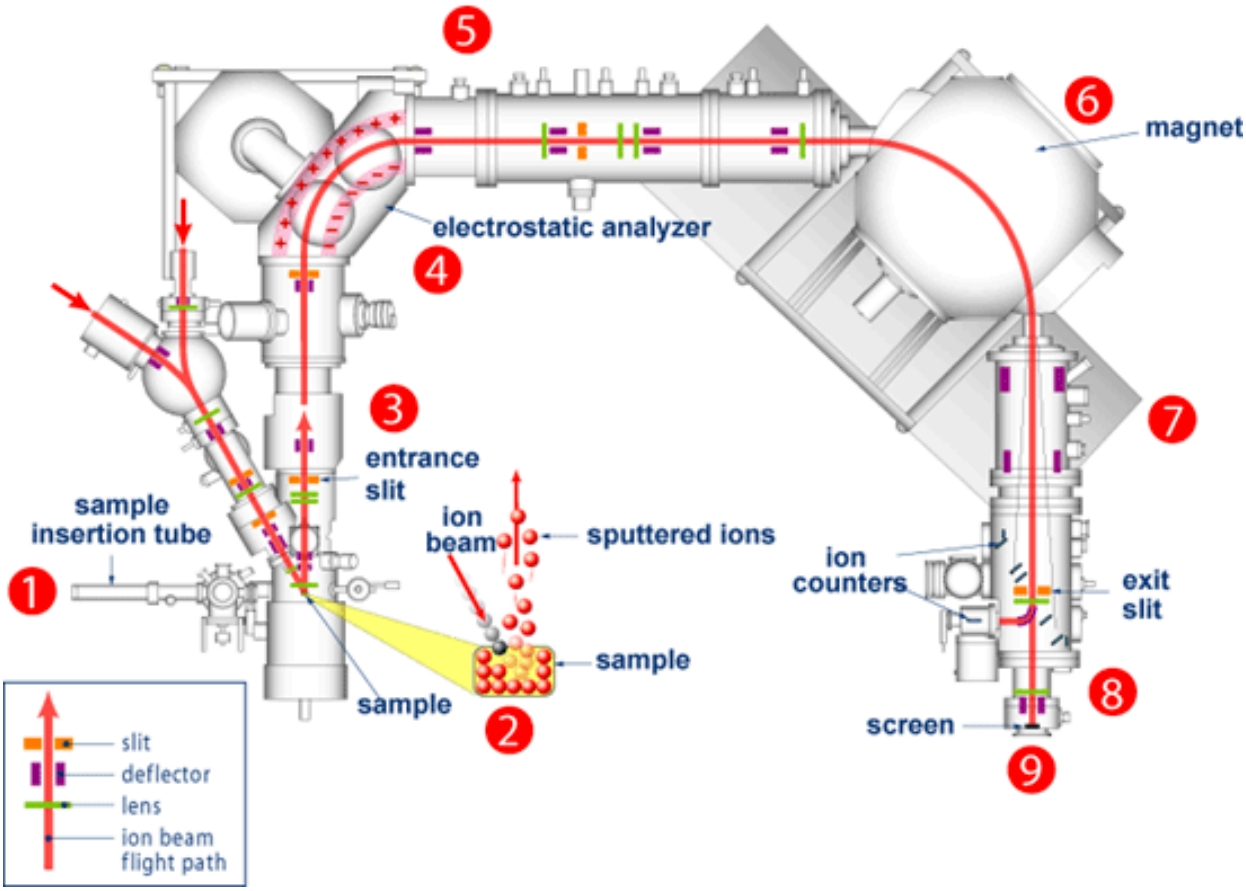
Our choice of spectrometer was dictated by our high mass resolution requirements: in particular, our need to resolve ^{32}S from $^{32}O_2$. We therefore used a magnetic sector technique called secondary ion mass spectrometry (SIMS). Specifically, we used the Cameca 1270 Ion

[1] Mass resolution is quantified by the relation m/Δm, where m is the mass of an ion of interest, and Δm is the mass difference between the two species under study. Personally, I find the inverse figure more intuitive since smaller values correspond to the resolution of smaller mass differences.

Mass Spectrometer at Edinburgh University (the Edinburgh Materials and Micro Analysis Centre, or EMMAC).

The Cameca 1270 is a double-focusing mass spectrometer, meaning that it disperses ionized sample material twice: first using an electric field (to filter the ions by energy) and then with a magnetic field (to filter them by mass). A technical drawing is shown below in figure a. The electric field is generated at the first bend in the instrument tube (a segment called the *ion energy analyzer*), and by dispersing the ions according to their energy it filters out those which lie outside a very narrow energy window. This is necessary to ensure that all of the ions entering the mass spectrometer (at the second bend) do so with the same velocity, since the mechanism for introducing the sample material into the instrument gives rise to a range of secondary ion energies.

Figure a: A schematic of a secondary-ion mass spectrometer, viewer from above. The sample is located at location (2), and the detector at location (9). Figure taken from Jayne Doucette, Woods Hole Oceanographic Centre.



The instrument samples the material under study by bombarding its surface with a focused beam of ions (the *primary ion beam*). Cs^+ ions were employed for our analyses, but Ar^+, Ga^+, O^-, O^{2+} or neutral species are used for analysis of different materials. The primary ions sputter the sample surface, ejecting *secondary ions* from a small volume (in our case, around 5micron wide). These secondary ions are extracted from the sample surface by a 10kv potential, and guided towards the ion energy analyzer by an immersion lens (a tuneable electric field). Before entering the ion energy analyzer, the beam is magnified by a magnetic *transfer lens*, collimated by a series of *entrance slits*, and cropped by a *field aperture*, so as to remove any further aberrations.

The magnetic sector comprises a large electromagnet with an adjustable field strength (it read around 0.04T while my sulfur analyses were being made). To maintain a steady deflection of the secondary ion beam, the field strength must be regulated very precisely. This is achieved with a Hall Probe[2], which continuously monitors and adjustments the current which propagates the magnetic field.

Secondary ions that survive the journey through both bends in the instrument (and therefore have the desired m/Q) strike the detector and are counted. The detector is an *electron multiplier*: a staggered array of electrodes (*dynodes*) maintained at successively higher potentials, which gives rise to a cascade of electrons upon receipt of a secondary ion. This cascade produces a transient voltage large enough to be recorded by a logger. The overall effect is to amplify the tiny voltages imparted by the impact of individual secondary ions.

The propagation of an electron cascade by a single secondary ion and its receipt by the logger takes a finite amount of time, during which the detector is insensitive to any further secondary ions. This period is appropriately termed *dead time*, and must not exceed the average delay between the arrival of successive ions, if accurate count rates are to be obtained. To make sure that our detector wasn't saturated, we obtained count rates for a range of primary ion beam currents, and demonstrated that higher primary beam currents gave rise to higher count rates for the elements.

[2] The Hall effect is the generation of a voltage across a current-carrying conductor located in a magnetic field.

It is crucial that a constant primary ion beam intensity is maintained throughout each analysis. Therefore a second detector is employed to monitor the primary ion beam before and after each analysis (only one detector may be used at a time). This second detector is a *Faraday Cup*: a small hollow grounded electrode that collects incoming ions and experiences a measurable drop in potential as a result. This drop in potential is amplified and related to the ion current (count rate).

Appendix 4

Calculation of sulfide concentrations using the model of Smythe *et al.* 2017

The Smythe *et al.* (2017) model provides sulfur concentrations at sulfide saturation (SCSS) for a range of silicate melts, based on their chemical composition and temperature. Fundamentally, the model combines the "Fincham and Richardson relation" (eqn. 3.3, but repeated below as eqn. a) with the equilibrium between FeS in sulfide and FeO in silicate melts (eqn. b):

$$log\,\mathrm{Cs} \;=\; log[\mathrm{S^{2-}}] \;+\; \tfrac{1}{2} log \frac{f\mathrm{O_2}}{f\mathrm{S_2}} \tag{a}$$

$$\mathrm{FeO}^{silicate} \;+\; \tfrac{1}{2}\mathrm{S_2} \;=\; \mathrm{FeS}^{sulfide} \;+\; \tfrac{1}{2}\mathrm{O_2} \tag{b}$$

This second equilibrium may be expressed in terms of its Gibbs free energy change:

$$\Delta G^{o} \;=\; -\,\mathrm{RT}\, log \frac{f\mathrm{O_2}^{1/2} a_{\mathrm{FeS}}^{sulfide}}{f\mathrm{S_2}^{1/2} a_{\mathrm{FeO}}^{silicate}} \tag{c}$$

…and rearranged to that it contains a term comprising the same ratio of fugacities as that in eqn. a):

$$\frac{\Delta \mathrm{G^o}}{\mathrm{RT}} \;=\; log\, a_{\mathrm{FeO}}^{silicate} \;-\; log\, a_{\mathrm{FeS}}^{sulfide} \;-\; \tfrac{1}{2} log \frac{f\mathrm{O_2}}{f\mathrm{S_2}} \tag{d}$$

Equations a and d may therefore be combined to yield a new expression, which relates the sulfide concentration at saturation (*log*[S^{2-}]) to various other intensive parameters of the melt and coexisting sulfide phase.

$$log[\mathrm{S^{2-}}] \;=\; \frac{\Delta \mathrm{G}^{o}}{\mathrm{RT}} \;+\; log\,\mathrm{C}_s \;+\; log a_{FeS}^{sulfide} \;-\; log a_{FeO}^{silicate} \tag{e}$$

The Gibbs energy change for equilibrium b is calculated from the entropies and volumes of the various components in the melt, and measured activities of FeS and FeO in the sulfide and silicate phases respectively.

This model was used to calculate SCSS for each of the melts, both with their actual (measured) FeO concentrations, and with their intended (but unrealized) concentrations. Since the ratio of these two numbers is a constant, it could be used to scale up the measured sulfur concentrations to which each melt would have exhibited, had they not suffered from loss of Fe

to their platinum loops. Although we are not dealing with sulfide saturated melt (or interested in SCSS specifically), we are exploiting the fact that ratios of SCSS are equal to ratios of sulfide concentration below saturation.